



**HAL**  
open science

# Segmentation of 2D-echocardiographic sequences using level-set constrained with shape and motion priors

Thomas Dietenbeck

► **To cite this version:**

Thomas Dietenbeck. Segmentation of 2D-echocardiographic sequences using level-set constrained with shape and motion priors. Other. INSA de Lyon, 2012. English. NNT : 2012ISAL0128 . tel-00838767

**HAL Id: tel-00838767**

**<https://theses.hal.science/tel-00838767v1>**

Submitted on 26 Jun 2013

**HAL** is a multi-disciplinary open access archive for the deposit and dissemination of scientific research documents, whether they are published or not. The documents may come from teaching and research institutions in France or abroad, or from public or private research centers.

L'archive ouverte pluridisciplinaire **HAL**, est destinée au dépôt et à la diffusion de documents scientifiques de niveau recherche, publiés ou non, émanant des établissements d'enseignement et de recherche français ou étrangers, des laboratoires publics ou privés.



Numéro d'ordre : XXX-XXXX

Année 2012

THÈSE

Délivrée par

L'Institut National des Sciences Appliquées de Lyon

DIPLÔME DE DOCTORAT

(arrêté du 7 aout 2006)

ÉCOLE DOCTORALE: ÉLECTRONIQUE, ÉLECTROTECHNIQUE,  
AUTOMATIQUE  
SPÉCIALITÉ: STIC SANTÉ

Soutenue publiquement le XX XX 2012 par

Thomas DIETENBECK

# Segmentation of 2D-echocardiographic sequences using level-set constrained with shape and motion priors.

Jury

|                           |   |                       |
|---------------------------|---|-----------------------|
| <b>Denis FRIBOULET</b>    | Professeur des Universités, INSA Lyon               | Directeur de thèse    |
| <b>Olivier BERNARD</b>    | Maître de Conférences, INSA Lyon                    | Co-directeur de thèse |
| <b>Isabelle BLOCH</b>     | Professeur, ENST                                    | Rapporteur            |
| <b>Frederik MAES</b>      | Professor, KU Leuven                                | Rapporteur            |
| <b>Jan D'HOOGE</b>        | Associate Professor, KU Leuven                      | Examineur             |
| <b>Alain LALANDE</b>      | Maître de Conférences, Université de Bourgogne      | Examineur             |
| <b>Fabrice MÉRIAUDEAU</b> | Professeur des Universités, Université de Bourgogne | Examineur             |

# Résumé de la thèse

L'imagerie échographique est une des principales modalités d'imagerie cardiaque, dans la mesure où elle permet une acquisition temps réel et non-invasive des structures cardiaques. La segmentation du muscle cardiaque (myocarde) dans ces séquences représente donc un objectif important pour l'analyse de la fonction cardiaque et l'aide au diagnostic. Cette segmentation s'avère cependant particulièrement difficile, du fait des spécificités de la formation de l'image ultrasonore cardiaque qui conduit à des inhomogénéités et à un faible contraste entre le myocarde et les tissus environnants.

Dans cette thèse, nous proposons un algorithme de segmentation du myocarde basé sur le formalisme des ensembles de niveaux. Nous modélisons dans un premier temps le myocarde par un modèle géométrique (hyperquadriques) qui permet de représenter des formes asymétriques telles que le myocarde tout en évitant une étape d'apprentissage. Ce modèle est ensuite inclus dans le formalisme des ensembles de niveaux afin de servir de contrainte de forme lors de la segmentation simultanée de l'endocarde et de l'épicarde. Ce terme d'*a priori* de forme est couplé à un terme local d'attache aux données ainsi qu'à un terme évitant la fusion des deux contours. L'algorithme est validé sur 80 images en fin systole et en fin diastole segmentées par 3 cardiologues.

Dans un deuxième temps, nous proposons de segmenter l'ensemble d'une séquence en utilisant l'information de mouvement. Dans ce but, nous faisons l'hypothèse de conservation des niveaux de la fonction implicite associée à l'ensemble de niveaux et l'exprimons comme une énergie dans un formalisme variationnel. Cette énergie est ensuite ajoutée à l'algorithme décrit précédemment pour la segmentation statique du myocarde afin de contraindre temporellement l'évolution du contour. L'algorithme est alors validé sur 20 séquences échocardiographiques (soit environ 1200 images) segmentées par 2 experts.

# Abstract

Echography is one of the main cardiac imaging technique, since it is non invasive and allows a real time acquisition of cardiac structures. The segmentation of the cardiac muscle (myocardium) in these sequences is thus an important goal for the analysis of the heart function and for diagnosis assistance. However this segmentation turns out to be a difficult task due to the physics of ultrasound acquisition which yield inhomogeneities inside the structures and a poor contrast between the myocardium and the surrounding tissues.

In this work, we propose to segment the myocardium using the a level-set formalism. The myocardium is first approximated by a geometric model (hyperquadrics) which allows to handle asymmetric shapes such as the myocardium while avoiding a learning step. This representation is then embedded into the level-set formalism as a shape prior for the joint segmentation of the endocardial and epicardial borders. This shape prior term is coupled with a local data attachment term and a thickness term that prevents both contours from merging. The algorithm is validated on a dataset of 80 images at end diastolic and end systolic phase with manual references from 3 cardiologists.

In a second step, we propose to segment whole sequences using motion information. To this end, we apply a level conservation constraint on the implicit function associated to the level-set and express this constraint as an energy term in a variational framework. This energy is then added to the previously described algorithm in order to constrain the temporal evolution of the contour. Finally the algorithm is validated on 20 echocardiographic sequences with manual references of 2 experts (corresponding to approximately 1200 images).



# Contents

|   |             |
|---|-------------|
| <b>Résumé de la thèse</b>                           | <b>ii</b>   |
| <b>Abstract</b>                                     | <b>iii</b>  |
| <b>Contents</b>                                     | <b>viii</b> |
| <b>List of Symbols</b>                              | <b>ix</b>   |
| <br>  |             |
| <b>I Introduction</b>                               | <b>1</b>    |
| <b>Introduction générale (in French)</b>            | <b>3</b>    |
| Objectifs de la thèse . . . . .                     | 3           |
| Organisation du manuscrit . . . . .                 | 4           |
| <b>1 General introduction</b>                       | <b>7</b>    |
| 1.1 Objectives . . . . .                            | 7           |
| 1.2 Thesis organization . . . . .                   | 8           |
| <br>  |             |
| <b>II Context</b>                                   | <b>11</b>   |
| <b>Résumé en français (Abstract in French)</b>      | <b>13</b>   |
| Échocardiographie . . . . .                         | 13          |
| Contours actifs variationnels . . . . .             | 15          |
| <b>2 Anatomy and function of the heart</b>          | <b>17</b>   |
| 2.1 Heart anatomy . . . . .                         | 17          |
| 2.2 Cardiac cycle . . . . .                         | 19          |
| 2.2.1 Diastole . . . . .                            | 19          |
| 2.2.2 Systole . . . . .                             | 19          |
| 2.3 Cardiovascular diseases . . . . .               | 20          |
| <b>3 Echocardiography</b>                           | <b>23</b>   |
| 3.1 Ultrasound image formation . . . . .            | 24          |
| 3.1.1 Equipment . . . . .                           | 24          |
| 3.1.2 Interaction between wave and tissue . . . . . | 26          |
| 3.1.3 Speckle . . . . .                             | 27          |
| 3.2 Ultrasound signal representations . . . . .     | 28          |
| 3.2.1 Radio-frequency signal (RF) . . . . .         | 28          |

|            |  |           |
|------------|--|-----------|
| 3.2.2      | Analytic signal . . . . .  | 30        |
| 3.2.3      | Complex envelope signal (IQ) . . . . .   | 30        |
| 3.2.4      | Envelope signal . . . . .  | 31        |
| 3.3        | Imaging modes . . . . .  | 31        |
| 3.3.1      | B-mode echography . . . . .  | 31        |
| 3.3.2      | M-mode echography . . . . .  | 32        |
| 3.3.3      | Doppler echography . . . . .   | 32        |
| 3.4        | Standard B-mode views . . . . .  | 32        |
| 3.5        | Specificities of echocardiographic images for segmentation . . . . .   | 33        |
| 3.6        | Overview of segmentation methods in echocardiographic sequences . . . . .  | 36        |
| <b>4</b>   | <b>Variational active contours</b>   | <b>39</b> |
| 4.1        | Active contour representation . . . . .  | 40        |
| 4.2        | Parametric representation . . . . .  | 42        |
| 4.2.1      | Energy functional . . . . .  | 42        |
| 4.2.2      | Evolution equation . . . . .   | 42        |
| 4.3        | Implicit representation: Level-set methods . . . . .   | 43        |
| 4.3.1      | Formalization of the evolution equation . . . . .  | 43        |
| 4.3.2      | Direct formulation of the energy functional using level-set . . . . .  | 44        |
| 4.4        | Explicit representation . . . . .  | 45        |
| 4.5        | Main families of active contour energy . . . . .   | 45        |
| 4.5.1      | Gradient based model . . . . .   | 46        |
| 4.5.2      | Region based model . . . . .   | 47        |
| 4.5.3      | Local region based model . . . . .   | 47        |
| 4.6        | Numerical implementation of the level-set . . . . .  | 49        |
| 4.6.1      | Discretisation of the evolution equation . . . . .   | 50        |
| 4.6.2      | Choice of the involved implicit function and reinitialization . . . . .  | 51        |
| 4.7        | Conclusion . . . . .   | 52        |
| <b>III</b> | <b>Segmentation of the whole myocardium in echocardiographic images using level-set constrained with shape priors</b>  | <b>55</b> |
|            | <b>Résumé en français (Abstract in French)</b>   | <b>57</b> |
|            | État de l'art . . . . .  | 57        |
|            | Notre contribution: Modèle du myocarde indépendant de la vue . . . . .   | 59        |
|            | Notre contribution: Segmentation du myocarde dans des images échocardiographiques 2D et dans toutes les vues . . . . . | 61        |
| <b>5</b>   | <b>Active contours based on shape prior constraints</b>  | <b>65</b> |
| 5.1        | Shape model . . . . .  | 65        |
| 5.1.1      | Geometric shape model . . . . .  | 65        |
| 5.1.2      | Learned templates . . . . .  | 67        |
| 5.2        | Variational segmentation with shape prior . . . . .  | 69        |
| 5.3        | Constrained segmentation of echocardiographic images . . . . .   | 74        |
| 5.4        | Conclusion . . . . .   | 75        |

|           |   |            |
|-----------|---|------------|
| <b>6</b>  | <b>Our contribution: Modeling of the whole myocardium using hyperquadrics</b>   | <b>77</b>  |
| 6.1       | Hyperquadrics . . . . .   | 77         |
| 6.1.1     | Definition . . . . .  | 77         |
| 6.1.2     | Fitting hyperquadrics on range data . . . . .   | 78         |
| 6.2       | Modeling of the whole myocardium . . . . .  | 80         |
| 6.3       | Shape prior energy . . . . .  | 80         |
| 6.4       | Fast solution to the fitting problem . . . . .  | 82         |
| 6.5       | Model validation . . . . .  | 83         |
| 6.5.1     | Comparison protocol . . . . .   | 83         |
| 6.5.2     | Results . . . . .   | 85         |
| 6.6       | Conclusion . . . . .  | 88         |
| <b>7</b>  | <b>Our contribution: Segmentation of the whole myocardium in any view in 2D-echocardiographic images</b>                            | <b>89</b>  |
| 7.1       | Energy formulation . . . . .  | 89         |
| 7.2       | Data attachment term . . . . .  | 89         |
| 7.3       | Shape prior term . . . . .  | 91         |
| 7.4       | Thickness term . . . . .  | 91         |
| 7.5       | Implementation issues . . . . .   | 94         |
| 7.5.1     | Level-set evolution . . . . .   | 94         |
| 7.5.2     | Image subdivision and ROI definition . . . . .  | 94         |
| 7.5.3     | Initialization procedure . . . . .  | 95         |
| 7.6       | Results . . . . .   | 96         |
| 7.7       | Conclusion . . . . .  | 103        |
| <b>IV</b> | <b>Segmentation of the whole myocardium in echocardiographic sequences using level-set constrained with motion and shape priors</b> | <b>105</b> |
|           | <b>Résumé en français (Abstract in French)</b>  | <b>107</b> |
|           | État de l'art . . . . .   | 107        |
|           | Notre contribution: Segmentation du myocarde dans des séquences échocardiographiques 2D et dans toutes les vues . . . . .           | 109        |
| <b>8</b>  | <b>Active contours using motion constraints</b>   | <b>115</b> |
| 8.1       | Motion as a data . . . . .  | 115        |
| 8.1.1     | Joint motion estimation and sequence segmentation . . . . .   | 115        |
| 8.1.2     | Sequence segmentation using an <i>a priori</i> estimated motion . . . . .   | 118        |
| 8.2       | Motion as a constraint . . . . .  | 119        |
| 8.3       | Echocardiographic sequence segmentation . . . . .   | 123        |
| 8.4       | Conclusion . . . . .  | 128        |
| <b>9</b>  | <b>Our contribution: Segmentation of the whole myocardium in any view in 2D-echocardiographic sequences</b>                         | <b>129</b> |
| 9.1       | Proposed scheme . . . . .   | 129        |
| 9.2       | Motion estimation . . . . .   | 130        |
| 9.2.1     | Review of motion estimation in echocardiographic images . . . . .   | 130        |
| 9.2.2     | Motion estimation using the monogenic signal . . . . .  | 131        |
| 9.3       | Motion term . . . . .   | 132        |



|           |  |            |
|-----------|--|------------|
| 9.3.1     | Hypothesis . . . . .                               | 133        |
| 9.3.2     | Energy formulation . . . . .                       | 134        |
| 9.4       | Implementation issues . . . . .                    | 135        |
| 9.4.1     | Implementation of the evolution equation . . . . . | 135        |
| 9.4.2     | Level-set evolution . . . . .                      | 136        |
| 9.4.3     | ROI tracking . . . . .                             | 136        |
| 9.5       | Results . . . . .                                  | 137        |
| 9.5.1     | Comparison protocol . . . . .                      | 137        |
| 9.5.2     | Evaluation of the proposed scheme . . . . .        | 138        |
| 9.5.3     | Myocardial tracking results . . . . .              | 140        |
| 9.6       | Conclusion . . . . .                               | 144        |
| <b>V</b>  | <b>Conclusion</b>                                  | <b>151</b> |
|           | <b>Conclusions et perspectives (in French)</b>     | <b>153</b> |
|           | Contributions principales . . . . .                | 153        |
|           | Perspectives . . . . .                             | 154        |
| <b>10</b> | <b>Conclusions and perspectives</b>                | <b>157</b> |
| 10.1      | Main contributions . . . . .                       | 157        |
| 10.2      | Perspectives . . . . .                             | 158        |
|           | <b>Appendix</b>                                    | <b>163</b> |
| <b>A</b>  | <b>Derivation of the thickness term</b>            | <b>163</b> |
| <b>B</b>  | <b>Derivation of the motion term</b>               | <b>165</b> |
| B.1       | Notation . . . . .                                 | 165        |
| B.2       | Derivation of the motion term . . . . .            | 165        |
|           | <b>Personal bibliography</b>                       | <b>167</b> |
|           | <b>Bibliography</b>                                | <b>180</b> |

# List of Symbols and abbreviations

## Latin letter

- $\mathbf{p}$  A point of coordinate  $(x, y)$  in 2D or  $(x, y, t)$  in 2D+t  
 $T$  Number of frames in a sequence

## Greek letter

- $\Omega$  Definition domain  
 $\phi$  Level-set function  
 $\Gamma$  Active contour  
 $\tau$  Artificial time-step

## Abbreviations

- SAX Parasternal Short-Axis view  
LAX Parasternal Long-Axis view  
A4C Apical 4 chamber view  
A2C Apical 2 chamber view  
ED End-diastole  
ES End-systole  
 $D^*$  Modified Dice criterion  
MAD Mean Absolute Distance  
HD Hausdorff Distance



# I Introduction

---



---

---

# Introduction générale

---

## Objectifs de la thèse

Les maladies cardiovasculaires sont la première cause de décès dans le monde avec environ 17,3 millions de morts en 2008, soit 30% de la mortalité mondiale totale. 7,3 millions d'entre elles furent causées par une cardiopathie coronarienne et 6,2 millions par un accident vasculaire cérébral <sup>1</sup>.

De nombreuses modalités d'imagerie cardiaque sont mises en œuvre afin d'améliorer le diagnostic et le traitement de telles pathologies. Dans ce contexte, la plus utilisée est l'échographie qui, comparativement à d'autres techniques d'imagerie, présente plusieurs avantages:

- le coût d'un examen (et d'un échographe) est relativement faible;
- aucune préparation du patient n'est nécessaire et l'examen peut avoir lieu au lit du patient;
- elle est non invasive et ne présente aucun risque pour le patient
- la fréquence d'acquisition est élevée.

De par ces caractéristiques, l'échographie est particulièrement bien adaptée à l'application cardiaque, où elle est connue sous le nom d'échocardiographie. En effet, l'acquisition en temps réel des phénomènes dynamiques impliqués dans un cycle cardiaque permet d'extraire des paramètres cliniques (tel que le mouvement cardiaque ou son épaissement) utiles au diagnostic. Notons aussi que l'échographie Doppler permet de mesurer la vitesse du muscle ou du flux sanguin.

L'échocardiographie présente cependant un certain nombre d'inconvénients. Bien que l'échographie 3D soit de plus en plus accessible, une vaste majorité des examens reste 2D. De plus, du fait de la physique de l'acquisition ultrasonore, la qualité des images est relativement faible, présente généralement un faible contraste et des interfaces tissulaires

---

<sup>1</sup>Source: OMS, <http://www.who.int/mediacentre/factsheets/fs317/fr/index.html>

---

floos. Enfin l'échographe, les conditions d'acquisition et l'opérateur influencent eux aussi le résultat d'un examen échographique.

Comme le diagnostic repose essentiellement sur une inspection visuelle faite par des cardiologues, deux directions de recherche dans le domaine de l'échocardiologie ont émergé: recherche sur la physique de l'acquisition et recherche sur les méthodes de traitement du signal et de l'image ultrasonore. Le but de ces recherches n'est cependant pas nécessairement d'améliorer la qualité visuelle des images ultrasonores affichées à l'écran puisque le cardiologue y est habitué et les interprète correctement. Il est plutôt de fournir des outils permettant d'extraire des paramètres cliniques pertinents afin de faciliter le diagnostic.

Parmi les travaux récents dans le domaine de l'échocardiographie, on peut citer l'échographie 3D temps réel, l'élastographie ultrasonore ou encore l'introduction d'oscillations latérales pour l'estimation de mouvement. Des avancées récentes dans le domaine des ultrasons utilisent aussi des ondes ultrasonores à des fins thérapeutiques (ablation de tumeurs, destruction de calculs).

Dans le contexte de l'échocardiographie, l'extraction et l'analyse de l'évolution de paramètres de la fonction cardiaque (tel que le volume du ventricule gauche en fin systole ou en fin diastole, le taux de déformation, ...) au cours du cycle cardiaque représentent un besoin clinique fort et procurent des informations précieuses durant un examen. Cependant, cela suppose de segmenter le myocarde, tâche qui est généralement effectuée manuellement par un cardiologue. Du fait de la faible qualité des données, cela conduit à une interprétation subjective des images et donc à une variabilité inter et intra-opérateur élevée. Des outils de segmentation complètement automatiques sont donc nécessaires afin d'effectuer cette tâche rapidement, objectivement et de manière reproductible.

C'est dans ce contexte que se situe mon travail de thèse qui porte sur la segmentation de séquences échocardiographiques. Il traite les aspects méthodologiques suivants:

- la modélisation du myocarde complet grâce à un *a priori* de forme suffisamment général pour être utilisé dans toutes les vues standards en échocardiographie. Dans cette optique, nous proposons un modèle géométrique basé sur les hyperquadriques.
- la segmentation de séquences échocardiographiques par ensemble de niveaux contraint. Les contraintes sont de deux types: un *a priori* de forme basé sur le modèle géométrique proposé et une contrainte liée au mouvement cardiaque.

## Organisation du manuscrit

Le manuscrit est composé de trois parties. Dans la première partie, nous donnons un bref aperçu de l'anatomie et du fonctionnement du cœur et décrivons les principales maladies cardiovasculaires pouvant être détectées en imagerie échocardiographique. Nous présentons ensuite les bases de la formation d'images ultrasonores et donnons les principales propriétés de ces images. Nous présentons plus en détails les difficultés liées à la segmentation de séquences échocardiographiques et faisons une brève revue des méthodes de segmentation dédiées à cette technique d'imagerie. Dans cet état de l'art, une

---

attention particulière est apportée à la validation de chaque algorithme (nombre d'images, d'experts, etc.). Enfin nous décrivons le cadre général des contours actifs variationnels et de leur implémentation puisqu'il sera utilisé dans cette thèse.

Dans la deuxième partie, nous nous intéressons à la segmentation du myocarde complet dans des images échocardiographiques. Nous proposons de contraindre l'évolution du contour par un *a priori* de forme. Dans un premier temps, nous présentons comment construire un *a priori* de forme de manière soit géométrique soit par un apprentissage. Nous dressons ensuite un état de l'art de techniques générales de segmentation par ensemble de niveaux utilisant un *a priori* de forme puis d'algorithmes dédiés à la segmentation du ventricule gauche en imagerie ultrasonore. Nous proposons ensuite un modèle géométrique basé sur les hyperquadriques qui permet de gérer des formes asymétriques telles que les frontières myocardiques tout en évitant une étape d'apprentissage. Nous comparons cette représentation à d'autres modèles géométriques et montrons qu'il permet de mieux modéliser le cœur dans les quatre vues principales utilisées en routine clinique. Enfin nous incluons cet *a priori* dans un contexte variationnel et l'associons à un terme local d'attache aux données ainsi qu'à un terme d'épaisseur afin de segmenter le myocarde complet dans des images échocardiographiques. Cet algorithme est alors validé sur un jeu de données de 80 images en fin systole et en fin diastole pour lesquelles les références de 3 cardiologues sont disponibles. Il est aussi comparé à une méthode proposée récemment.

Dans la dernière partie, nous proposons de contraindre la segmentation par l'information de mouvement. Nous commençons par dresser un état de l'art des techniques utilisant le mouvement soit explicitement comme une information (et qui nécessitent donc d'estimer le mouvement à un moment donné) ou implicitement comme une contrainte sur l'évolution du contour. Nous proposons ensuite une nouvelle énergie basée sur le mouvement et qui, lors de sa minimisation, force le niveau zéro de la fonction implicite à satisfaire la contrainte du flux optique. Ce terme d'énergie est ajouté au formalisme développé précédemment afin de segmenter des séquences échocardiographiques dans toutes les vues. Les performances de l'algorithme sont ensuite évaluées sur un jeu de données de 20 séquences échocardiographiques segmentées manuellement par deux experts ( $\simeq 1200$  images) et comparées à la même méthode que précédemment.





---

## General introduction

---

### 1.1 Objectives

Cardiovascular diseases are the number one cause of death with an estimate of 17.3 million deaths in 2008, representing 30% of all global deaths. Among these deaths, 7.3 million were due to coronary heart disease and 6.2 million were due to stroke<sup>1</sup>.

Modern technology provides a number of tools to access myocardial function. Amongst them, echography is widely used for the diagnosis of cardiac diseases since it presents several advantages when compared to other imaging techniques:

- the cost of an exam is relatively low;
- no specific preparation of the patient is required and the exam can take place at the patient's bed;
- it is non invasive and does not present any hazard for the patient;
- the acquisition rate is very high.

These characteristics make echography particularly well adapted to the field of cardiology, where it is known as echocardiography. Indeed, since it allows real-time acquisitions of the dynamic processes of the heart, valuable clinical parameters (such as the heart motion or thickening) can be extracted and used for the diagnosis. Also, the technique of ultrasound Doppler enables to measure the velocity of the muscle or of the blood flow.

Echography has however also some drawbacks. Though 3D echography is becoming more available, most of the exams are still 2D in clinical routine. Due to the physics of

---

<sup>1</sup>Source: World Health Organization, <http://www.who.int/mediacentre/factsheets/fs317/en/index.html>

ultrasound acquisition, the image quality is relatively poor, yielding frequently a low contrast and blurred tissular borders. Finally the ultrasound device, the acquisition condition and the operator also influence the result of an echographic scan.

Since the diagnosis relies on a visual inspection by expert cardiologists, two directions of research in the field of echography have emerged: research on the physics of acquisition and research on the methods of ultrasound signal and image processing. The aim of these research is not necessarily to improve the quality of the image displayed since the medical doctors are familiar with echographic scans, but rather to automatically extract clinically relevant parameters to ease the diagnosis. Among recent work in the field of echography, let us cite 3D real time echography, ultrasound elastography and the introduction of lateral oscillations for motion estimation. Recent advances in ultrasound techniques also use ultrasound waves in therapy (tumor ablation, destruction of stones).

In the context of echocardiography, the extraction and analysis of the evolution of heart function parameters (such as the end diastolic/systolic volume, strain rate, ...) throughout the cardiac cycle represent a strong clinical need and provide valuable informations during an exam. However, this relies on the segmentation of the myocardial border which is usually manually drawn by a cardiologist. This yields subjective interpretation of the data as well as high inter and intraobserver variability due the quality of the data. Automatic segmentation tools for echocardiographic data are thus highly needed in order to provide these parameters in an objective, fast and reproducible manner. Consequently, echocardiographic image segmentation is a very active research domain.

This Ph.D work falls within the scope described above and is dedicated to the segmentation of echocardiographic sequences. It addresses the following main methodological aspects:

- Modeling the whole myocardium using a general enough shape prior in order to be able to use it in any of the echocardiographic view used in clinical routine. To this end, we propose a geometric prior based on hyperquadrics.
- Segmentation of echocardiographic sequences using constraint level-set. The constraints are of two kind: a shape prior based on the proposed geometric model and a motion constraint.

## 1.2 Thesis organization

The manuscript is composed of three main parts. In the first part, we give an overview of the anatomy and the functioning of the heart and describe common cardiovascular diseases that can be assessed using echocardiographic images. We then present the physical basis of the ultrasound image formation and give the main properties of the echographic image. We focus on the difficulties to segment echocardiographic sequences and provide a brief review of segmentation methods dedicated to this imaging technique. Particular attention is given in this review to the validation of each algorithm (number of images,

experts, ...). Finally, we describe the general framework underlying variational active contours and their level-set implementation which will be used in this thesis.

The second part is dedicated to the segmentation of the whole myocardium in echocardiographic images. We propose in this work to constrain the evolving curve using a shape prior. Firstly we present how to build a shape prior either through geometrical considerations or through a learning step. We then review general level-set techniques that use a shape prior and more specifically shape constrained techniques dedicated to the segmentation of the left ventricle in ultrasound images. In this context, we propose a geometric prior based on hyperquadrics that allow to handle asymmetrical shapes such as the myocardial borders and to avoid a learning step. We compare this prior to other geometrical priors and show that it allows to have a better modelling of the heart boundaries in any of the four main clinical views. Finally this prior is embedded into a variational framework and coupled to a local data attachment term and a thickness term in order to segment the whole myocardium in echocardiographic images. This algorithm is then validated on a dataset of 80 end-diastolic or end-systolic images with manual references of three experts and compared to a state-of-the-art method.

In the third part, we deal with motion constrained segmentation. We first review existing techniques that use the motion either explicitly as an information (thus requiring to estimate it at some point) or implicitly as a constraint on the contour evolution. We then propose a new energy based on the motion that, when minimized, enforces the zero-level of the implicit function to satisfy the optical flow constraint. This energy term is added to the formalism described in the second part in order to segment complete echocardiographic sequences in any view. The algorithm performance are then evaluated on a dataset of 20 echocardiographic sequences with manual references of two experts ( $\simeq 1200$  images) and compared to the same method as previously.



## II Context

---



---

---

# Résumé en français

---

## Échocardiographie

L'échographie est une modalité d'imagerie aujourd'hui largement utilisée dans le domaine médical et permet d'acquérir en temps réel une image des propriétés acoustiques du milieu étudié. Le principe de l'imagerie échocardiographique repose sur la propagation d'ondes acoustiques ultrasonores dans des tissus biologiques. L'onde incidente émise par la sonde est diffusée, réfléchiée et atténuée sur les différentes structures tissulaires. Une partie de cette onde revient en direction de la sonde qui en effectue l'acquisition. L'intensité de ces échos est ensuite utilisée pour créer une image des tissus.

## Représentation des signaux ultrasonores

L'image affichée à l'écran de l'échographe est généralement obtenue par une succession de traitements de la réponse ultrasonore du milieu. Les propriétés des différents signaux entrant en jeu sont résumées dans le tableau 3.1 et des exemples de ces signaux sont donnés en Fig. 3.6.

Parmi ces différents signaux, les deux présentant le plus d'intérêt sont le signal RF et le signal enveloppe. Le signal RF est obtenu après la conversion de l'onde acoustique en un signal électrique et une étape de formation de voie. Une séquence d'émissions-acquisitions dans différentes directions permet de couvrir une région du corps du patient et de constituer une image RF, résultant de la juxtaposition de plusieurs lignes RF. Le signal enveloppe est obtenu à partir du signal RF après une succession de traitement:

- détection de l'enveloppe par démodulation du signal RF,
- compensation de l'atténuation que subit le signal lors de sa propagation,
- compression logarithmique, pour palier à la dynamique très élevée de l'image.



---

## Les différentes vues échocardiographiques

En échocardiographie classique, il existe plusieurs plans privilégiés d'acquisition ou vues. L'existence d'un nombre restreint de vues s'explique par les difficultés d'accéder au cœur, liées à sa position par rapport à la cage thoracique et aux poumons. Les vues parasternales sont obtenues en positionnant la sonde entre deux os de la cage thoracique et perpendiculairement au grand axe du cœur. Elles permettent d'imager le ventricule gauche suivant son petit axe (vue parasternale petit axe SAx, Fig. 3.9(a)) ou son grand axe (vue parasternale grand axe LAx, Fig. 3.9(b)). Les vues apicales sont obtenues en positionnant la sonde au niveau de l'apex et permettent d'imager le cœur suivant son grand axe. Les deux vues orthogonales habituellement imagées sont les vues apicales 4 chambres (A4C, Fig. 3.10(a)) et 2 chambres (A2C, Fig. 3.10(b)).

## Segmentation de séquences échocardiographiques

Du fait des propriétés des images ultrasonores (présence du speckle, contraste faible et spatialement variant, etc.), la segmentation de ce type d'images est actuellement encore un problème ouvert, qui a fait l'objet de très nombreuses études [Noble and Boukerroui (2006)]. Ces études font appel à des d'approches très diverses, parmi lesquelles les méthodes basées sur les contours actifs ont reçu une attention particulière [Chalana *et al.* (1996), Giachetti (1998), Lin *et al.* (2003), Sarti *et al.* (2005), Dydenko *et al.* (2006), Bernard *et al.* (2007)b]. Il est à remarquer que ces études concernent principalement la segmentation de l'endocarde. Comme le note [Noble and Boukerroui (2006)], très peu d'études ont abordé la segmentation du myocarde complet, qui implique la détection de l'épicarde [Feng *et al.* (1991), Dias and Leitao (1996), Chalana *et al.* (1996)] qui est généralement considérée comme plus complexe.

Concernant la validation de la segmentation, la plupart des techniques ne se focalisent que sur une seule vue (*e.g.* SAx [Chalana *et al.* (1996), Taron *et al.* (2004)], A4C [Lin *et al.* (2003), Carneiro *et al.* (2012)]) et la taille de la base de données utilisée pour la validation est généralement faible (15 à 20 images dans [Sarti *et al.* (2005), Belaid *et al.* (2011)a]). Concernant les études plus poussées, on peut citer [Chalana *et al.* (1996)] qui segmente 44 séquences en SAx avec les références en fin systole et fin diastole de 4 experts. En plus de la comparaison en terme de distance entre les résultats obtenus et la variabilité inter-observateur (IOD), les auteurs effectuent aussi un test de corrélation de Pearson pour montrer la qualité de leurs résultats. [Comaniciu *et al.* (2004)] utilise une base de données de 32 séquences dans 3 vues. Leur algorithme est comparé à 3 autres méthodes en terme de distance absolue moyenne et de moyenne des sommes des distances au carré mais aucune IOD n'est donné. Enfin [Carneiro *et al.* (2012)] réalise sa validation sur une base de données de 14 séquences A4C (soit 80 images segmentées manuellement par 2 cardiologues). Les auteurs se comparent à deux autres méthodes et vérifie que leurs résultats sont cohérents avec l'IOD en calculant l'index de Williams, la "Percent statistic" [Chalana and Kim (1997), Alberola-López *et al.* (2004)] et par une analyse de

---

Bland-Altman [Bland and Altman (1986)].

## Contours actifs variationnels

Le principe général de la segmentation par contours actifs consiste à faire évoluer une interface vers l'objet à détecter. En deux dimensions, cette démarche se traduit par l'évolution d'une courbe initiale dans une image vers la structure à segmenter. Pour les contours actifs variationnels, l'évolution de la courbe résulte de la minimisation d'une fonctionnelle d'énergie traduisant les propriétés de l'objet à segmenter. Cette démarche a été introduite initialement par [Kass *et al.* (1988)] avec le modèle des snakes.

### Représentation du contour

Dans la plupart des cas, le contour est représenté de manière paramétrique (modèle des snakes, [Kass *et al.* (1988)]) ou implicite (ensemble de niveaux, [Osher and Sethian (1988)]). On peut noter que [Duan *et al.* (2010), Barbosa *et al.* (2012)b] ont récemment proposé de représenter le contour explicitement. Un exemple de chaque type de représentation est donné en 4.2.

Dans le cas des ensembles de niveaux, le contour  $\Gamma$  est représenté implicitement comme le niveau zéro d'une fonction lipschitzienne de  $\mathbb{R}^2$ . Cette fonction, généralement notée  $\phi$ , satisfait:

$$\begin{cases} \phi(\mathbf{p}) > 0, & \text{if } \mathbf{p} \in \Omega_i, \\ \phi(\mathbf{p}) < 0, & \text{if } \mathbf{p} \in \Omega_o, \\ \phi(\mathbf{p}) = 0, & \text{if } \mathbf{p} \in \partial\Omega_i = \Gamma(s), \end{cases}$$

où  $\mathbf{p} \in \Omega$ ,  $\Omega \subset \mathbb{R}^2$ ,  $\Omega_i$  est la région intérieure définie par  $\Gamma$  et  $\Omega_o = \Omega \setminus \Omega_i$ .

### Formulation de la fonctionnelle d'énergie et équation d'évolution

[Jehan-Besson *et al.* (2003)] a proposé une écriture générale de la fonctionnelle d'énergie:

$$E(\Gamma) = \int_{\Gamma} K^c(\mathbf{p}) ds + \int_{\Omega_i} K^i(\mathbf{p}) d\mathbf{p} + \int_{\Omega_o} K^o(\mathbf{p}) d\mathbf{p}.$$

Dans cette expression, le premier terme est une intégrale de contour qui fait intervenir  $K^c$ , un descripteur du contour de l'objet à détecter. Les deux autres termes sont des intégrales de régions faisant intervenir des descripteurs des propriétés de la région intérieure et extérieure.

Cette écriture présente cependant l'inconvénient d'avoir à la fois des intégrales de contour et de région, ce qui nécessite lors de la dérivation de cette énergie de transformer les intégrales de région en intégrales de contour. Pour lever cette difficulté, [Chan and Vese (2001)] ont proposé d'exprimer directement la fonctionnelle  $E$  en fonction de  $\phi$  de la

---

façon suivante:

$$E(\phi) = \int_{\Omega} K^c(\mathbf{p})\delta(\mathbf{p})\|\nabla\phi(\mathbf{p})\| d\mathbf{p} + \int_{\Omega} K^i(\mathbf{p})H(\phi(\mathbf{p})) d\mathbf{p} + \int_{\Omega} K^o(\mathbf{p})(1 - H(\phi(\mathbf{p}))) d\mathbf{p},$$

où  $H(\cdot)$  est la fonction de Heaviside et  $\delta(\cdot)$  la distribution de Dirac.

Le calcul de la variation de  $E$  relativement à  $\phi$  permet d'obtenir l'équation d'Euler-Lagrange associée et une descente de gradient fournit alors l'équation d'évolution qui prend la forme suivante:

$$\frac{\partial\phi}{\partial\tau}(\mathbf{p}, \tau) = V(\mathbf{p}, \tau)\delta(\phi(\mathbf{p}, \tau)).$$

### Implémentation numérique de l'ensemble de niveaux

L'implémentation de l'équation d'évolution générale revient à résoudre une équation différentielle dépendant du temps. La très grande majorité des implémentations fait appel à une technique de différences finies. Cette méthode a été développée initialement par [Osher and Sethian (1988), Osher and Fedkiw (2002)] pour assurer la convergence de l'algorithme vers des solutions non oscillatoires et uniques.

On pourra noter cependant que certains auteurs ont très récemment proposé de résoudre cette EDP en utilisant une représentation paramétrique continue de l'ensemble de niveaux. Ainsi [Gelas *et al.* (2007)] utilise une méthode de collocation et une représentation par fonctions de base radiales (RBF). [Bernard *et al.* (2009)] propose d'utiliser une représentation par B-splines directement dans la fonctionnelle, ce qui conduit à une formulation de type filtrage linéaire.

Un problème classique rencontré lors de l'évolution de l'ensemble de niveaux est que des régions très plates ou au contraire des fronts très raides ont tendance à se développer. Ceci peut conduire à des difficultés en termes d'estimation numérique des dérivées partielles et de vitesse de convergence. La stratégie communément utilisée pour résoudre ce problème est d'initialiser la fonction implicite comme la carte de distance signée au contour. Au cours de son évolution, l'ensemble de niveau est périodiquement réinitialisé afin de préserver sa forme de carte de distance. La méthode la plus couramment mise en œuvre pour la réinitialisation consiste à tirer parti de la propriété du gradient de la carte de distance et à appliquer périodiquement au contour l'équation d'évolution auxiliaire suivante [Peng *et al.* (1999), Sussman *et al.* (1998)]:

$$\frac{\partial\phi_0}{\partial\tau}(\mathbf{p}, \tau) = \text{sign}(\phi_0(\mathbf{p}, \tau)) (1 - \|\nabla\phi_0(\mathbf{p}, \tau)\|),$$

où  $\phi_0$  est la fonction à réinitialiser et  $\text{sign}(\cdot)$  est la fonction signe.

---

# Anatomy and function of the heart

---

The vascular system plays a crucial role in the functioning of the living organism, and the heart is at its center. The state of the heart and of the arteries has a direct impact on the quality and on the length of one's life. Consequently, cardiovascular pathologies are a major cause of mortality in industrialized countries. Cardiac health is therefore a public and social issue. In this section we give a brief overview of heart anatomy and its function. We then discuss common cardiovascular diseases that can be diagnosed using echography.

## 2.1 Heart anatomy

The heart is a muscular organ that is located between the lungs in the middle of the chest, behind and slightly to the left of the breastbone (sternum). It is surrounded by a double-layered membrane that is called the pericardium. Its outer layer surrounds the roots of the heart's major blood vessels and is attached by ligaments to the spinal column, diaphragm, and other parts of the body. The heart's muscular walls are called myocardium. Its outer surface is called the epicardium and its inner lining the endocardium.

The heart has four chambers as illustrated in Fig. 2.1. The two upper chambers are called the left and right atria, and the lower chambers are called the left and right ventricles. The atria act as reservoirs for venous blood. They have a small pumping function to assist ventricular filling. The ventricles are the major pumping chambers that deliver blood to pulmonary (right ventricle) and systemic circulations (left ventricle). The wall that separates the left and right atria and the left and right ventricles is called the septum.

The heart muscle, like every other organ or tissue in the body, needs oxygen-rich

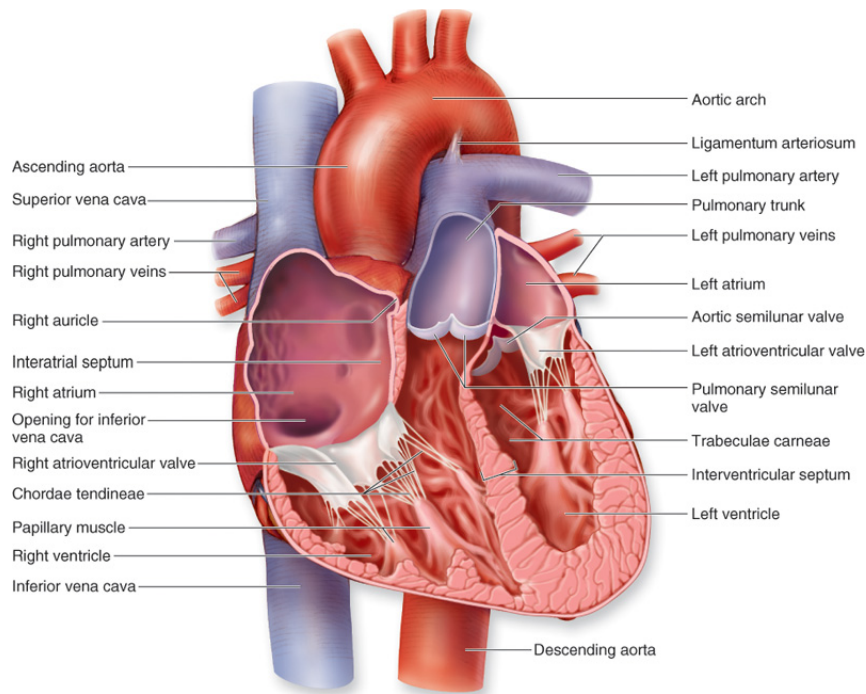
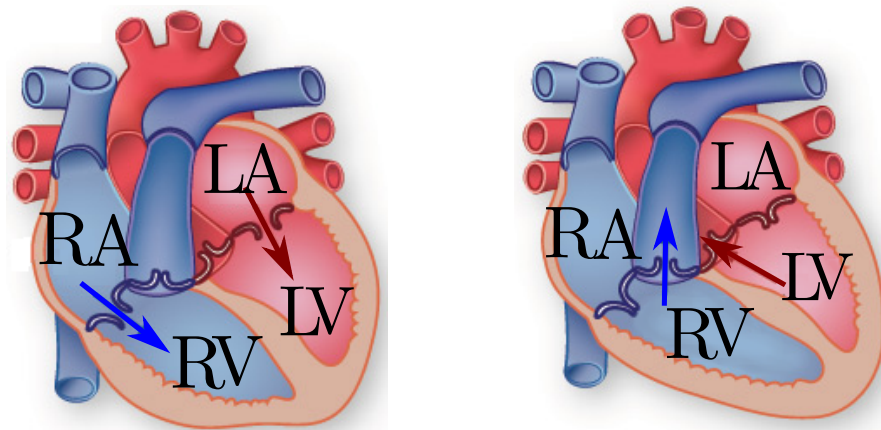


Figure 2.1: Anatomy of the human heart. (Source: [http://academic.kellogg.edu/herbrandsonc/bio201\\_mckinley/cardiovascular%20system.htm](http://academic.kellogg.edu/herbrandsonc/bio201_mckinley/cardiovascular%20system.htm))

blood and vital nutrients to survive. Blood is supplied to the heart by its own vascular system, called coronary circulation. The aorta branches off into two main coronary blood vessels, the so-called *coronary* arteries. These coronary arteries then branch off into smaller arteries, which supply oxygen-rich blood to the entire heart muscle. The right coronary artery supplies blood mainly to the right side of the heart while the left coronary artery mainly supplies blood to the left side of the heart.

Four valves ensure that the blood flows only in one direction and prevent blood from leaking backwards from one chamber to the upstream chamber (valvular regurgitation). The aortic and pulmonary valves are located at the downstream sides of the left and right ventricle, respectively. The two atrioventricular valves, the mitral and tricuspid valve, are located between the atria and ventricles. The leaflets of the atrioventricular valves are connected to the papillary muscles that are, in turn, connected to the walls of the ventricles. The papillary muscles shorten during the contraction of the ventricles in order to prevent a bulging of the atrioventricular valves towards the atria that would lead to regurgitation. Blood is pumped away from the heart through arteries and returns to the heart through veins. The major artery of the body is the *aorta* and the major veins of the body are the *vena cava*.

Because of its function, the left ventricle is the largest and most important chamber in the heart. Given the position of the heart inside the thorax, the left ventricle is oriented slightly backwards with respect to the right ventricle. Consequently, the left ventricle wall which is opposed to the septum is often called the posterior wall.



(a) Diastolic phase

(b) Systolic phase

Figure 2.2: Heart physiology during diastole and systole.

## 2.2 Cardiac cycle

Each cardiac cycle is divided into two alternating periods of diastole (relaxation) and systole (contraction) (see Fig. 2.2).

### 2.2.1 Diastole

During diastole, the atria contract and push the blood into the relaxed ventricles. More precisely, the de-oxygenated blood returning from the body flows from the right atrium into the right ventricle. In parallel, the left atrium pushes the re-oxygenated blood that arrived from the pulmonary veins into the left ventricle. More specifically, the diastole consists of four sub-phases:

1. isovolumetric relaxation: the ventricular pressure decreases, but its volume remains constant prior to opening of the atrioventricular valves;
2. rapid filling: after opening of the atrioventricular valves, the pressure gradient drives blood from each atrium into the respective ventricle;
3. diastasis: the ventricular filling is mainly due to direct blood flow from the veins;
4. atrial systole: the atria contract actively and complete the ventricular filling.

### 2.2.2 Systole

The second part of the heart cycle, the systole, begins when the ventricles are filled and start to contract. The right ventricle pumps the oxygen-poor blood through the pulmonary valve into the pulmonary artery towards the lungs to be re-oxygenated. The left ventricle pushes the oxygen-rich blood through the opened aortic valve into the aorta and further into the body. After the pulmonary and aortic valves have closed, the myocardium performs the reverse motion, causing the ventricles to relax. The lower pressure in the ventricles causes the tricuspid and mitral valves to open, and the cycle begins again.

## 2.3 Cardiovascular diseases

Cardiovascular disease refers to the class of diseases that involve the heart and/or blood vessels (arteries and veins). There are many forms of heart and cardiovascular diseases, and what follows is a description of common diseases that can be assessed using echocardiographic images.

### Ischemic heart disease

Ischemic (or Ischaemic) heart disease is a disease characterized by reduced blood supply to the heart. The coronary arteries supply blood to the heart muscle and no alternative blood supply exists, so a blockage in the coronary arteries reduces the supply of blood to heart muscle. Most ischemic heart disease is caused by atherosclerosis.

### Coronary heart disease

Coronary heart disease, also called coronary artery disease and atherosclerotic heart disease, is the end result of the accumulation of atheromatous plaques within the walls of the arteries that supply the myocardium (see Fig. 2.3). While the symptoms and signs of coronary heart disease are noted in the advanced state of disease, most individuals with coronary heart disease show no evidence of disease for decades as the disease progresses before the first onset of symptoms arise (often a sudden heart attack). After decades of progression, some of these atheromatous plaques may rupture and start limiting blood flow to the heart muscle. The disease is the most common cause of sudden death.

### Myocardial infarction

Acute myocardial infarction, commonly known as a heart attack, is a disease that occurs when the blood supply to a part of the heart is interrupted, causing death of heart tissue. It is the leading cause of death for both men and women all over the world.

### Cardiomyopathy

Cardiomyopathy is a weakening of the heart muscle or a change in the heart muscle. It often occurs when the heart cannot pump as well as it should, or with other heart function problems. Common types of cardiomyopathy include:

- dilated cardiomyopathy (Fig. 2.4(b)): The heart cavity is enlarged and stretched (cardiac dilation), but the wall-thickness remains normal. This results in a diffuse, globally restricted myocardial contraction.
- hypertrophic cardiomyopathy (Fig. 2.4(c)): This genetic disorder causes an abnormal growing of the left ventricular wall thickness. The thickening leads to wall stiffness and might prevent the heart from relaxing during diastole.

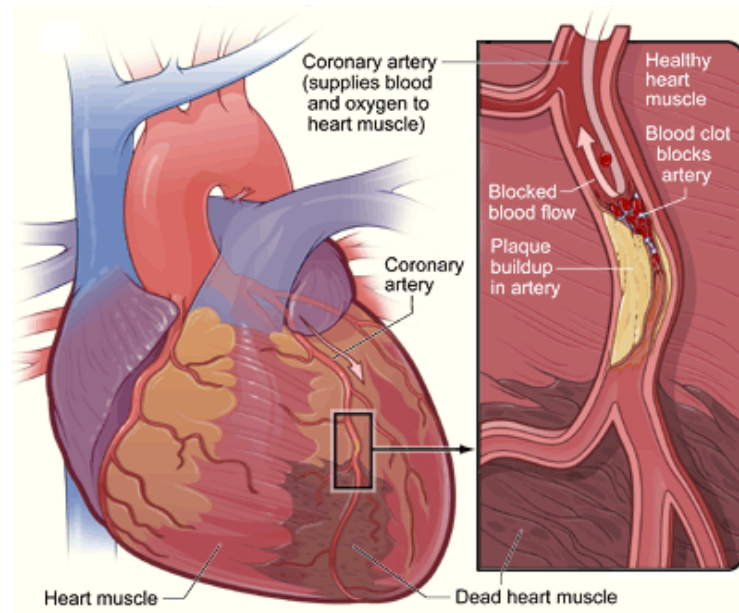


Figure 2.3: Illustration of a Coronary Artery Disease (Source:<http://www.nhlbi.nih.gov/health/health-topics/topics/cad/signs.html>)

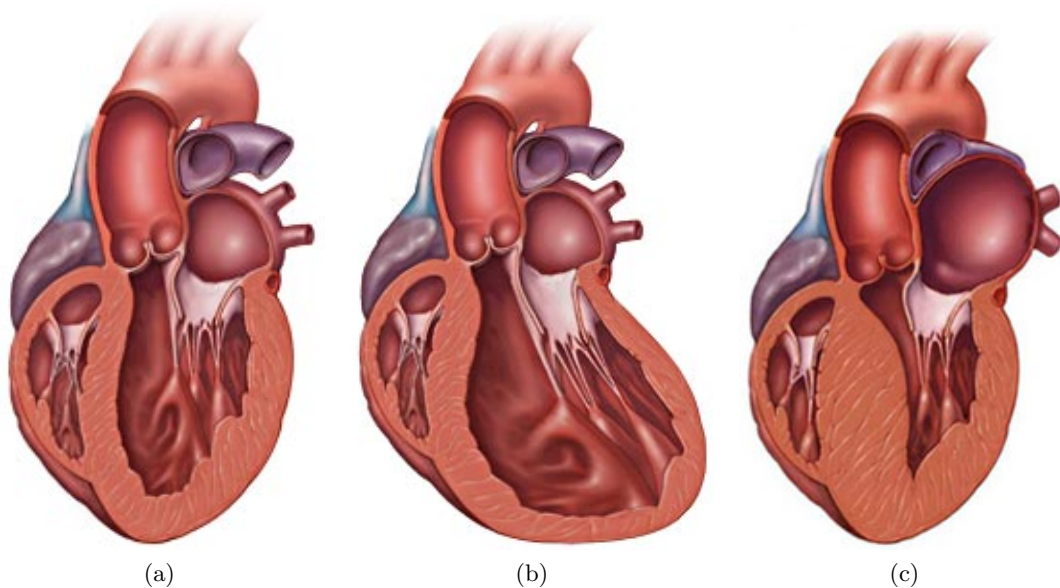


Figure 2.4: Illustration of a cardiomyopathy: (a) normal heart, (b) heart with dilated cardiomyopathy, (c) heart with hypertrophic cardiomyopathy (Source: <http://www.mayoclinic.com/health/cardiomyopathy/DS00519>)





---

# Echocardiography

---

As mentioned in the previous chapter, the heart plays a center role in providing oxygen and nutrients to other tissues and organs. It is thus important to be able to assess this function, thus making heart imaging a valuable tool. Depending on the cardiac activity to observe, different imaging techniques can be used. For example magnetic resonance (MRI) can be used to assess the heart's morphology or functioning. The perfusion as well as infarcted regions can be estimated using MRI and contrast agent. Diffusion tensor imaging allows to get the heart's fibers structure. Angiography is used for the diagnosis of coronarial diseases.

Another popular imaging technique is echography which is nowadays widely used in medical imaging and relies on the propagation of ultrasound in biological tissues. The major reasons for its popularity is that it is relatively cheap, easy to transport (allowing to perform an exam from patient's bedside), safe (as it does not utilise ionizing radiation) and non-invasive. Furthermore it allows real-time acquisition of images of the acoustic properties of the inspected medium.

Since this work deals with the segmentation and tracking of echocardiographic images, we will give more details on this technique in this chapter. We will first explain how an echographic image is obtained as well as the different signals involved. We then describe the different imaging mode use in echography. In a third step, we will deal with the standard views used in clinical practice to image the heart. Finally we will discuss about the segmentation of echocardiographic images and the problems that may arise.

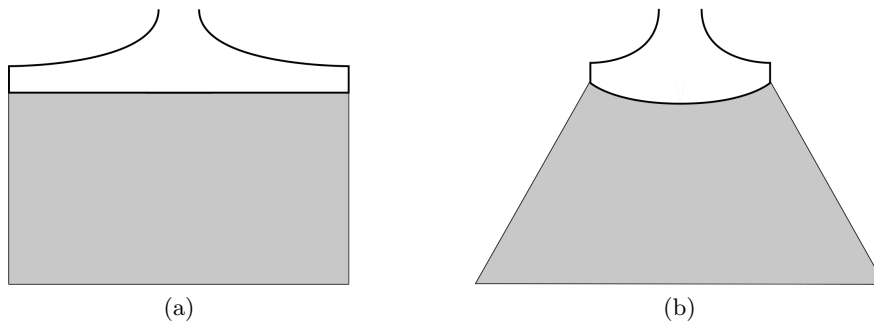


Figure 3.1: Existing acquisition geometry: (a) linear, (b) sectorial

## 3.1 Ultrasound image formation

Echographic imaging relies on the propagation of ultrasound acoustic waves into biological tissues. A high-frequency sound is emitted by a probe into the tissue to be imaged. This probe then listens for the echoes returning from structures within. The intensity of these echoes are used to make an image of the tissue. This section gives some details on the formation of such images.

### 3.1.1 Equipment

#### Transducer

A typical ultrasound system uses a transducer made up of a number of piezoelectric elements to transmit a sound pulse into the tissue. Piezoelectric elements constitute the main part of the transducer as they convert the electrical energy to acoustic energy, and vice versa. Usually the same transducer is used to receive the reflected sound from the insonified medium.

The acquisition is either done using a linear transducer (detection of the thyroid or breast cancer, imaging of the carotid) or a sectorial one (cardiac or fetal imaging). In cardiac imaging, the use of a sectorial transducer is due to the difficult access to the heart (the thoracic cage, the depth) and implies that the emitted waves spread out allowing to image a wide area (Fig. 3.1).

#### Beamforming

To build an echographic image, transducers with multiple piezoelectric elements are used in both emission and transmission mode. The construction principle uses the time-delay law in order to focus the emitted energy in a region of the medium. The *Huygens' principle* is used for this purpose. This principle states that a wavefront can be decomposed into a number of point sources, each being the center of an expanding, spherical wave. Thus, it is possible to form any wavefront by constructing it from point sources. This is the principle used to focus and steer the ultrasound beam to the desired location in space. The piezoelectric elements are considered as point sources. A beamformer is used to send signals with individual time-delay to the piezoelectric elements, which results in

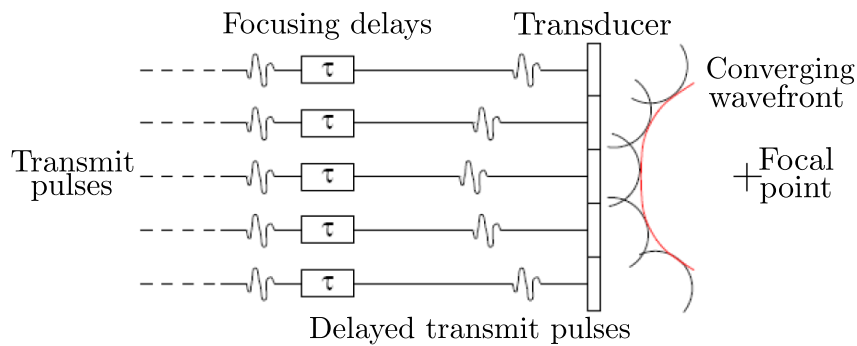


Figure 3.2: Beamformer principle. Each piezoelectric element generates an approximately spherical wave. Adding the waves according to Huygens' principle gives the total, converging wavefront.

the generation of a beam steered and focused toward a point of interest, as illustrated in Fig. 3.2. The same physical system is also used for the conversion of a returned echos into an electrical signal. For more details on beamforming methods, one may refer to [Angelsen (2000), Liebgott (2005)].

## Resolution

The quality of an ultrasound system mainly depends on both axial (direction of propagation) and lateral (direction perpendicular to the previous one, also called transverse direction) resolutions of the acquisition system.

**Axial Resolution** This resolution is defined as the limit in separation of two consecutive echos. This resolution mainly depends on the shape, length, wave length and band-width of the interrogating ultrasound wave. In practice, the frequencies used in echocardiography (which are linked to the wavelength) are about 3-3.5MHz and the axial resolution is about 0.2mm.

**Lateral Resolution** This resolution is defined as the smallest distance where two waves can be separated in a plane perpendicular to the ultrasonic beam. This resolution mainly depends on the beam width of the ultrasound wave: the smaller it is the better the lateral resolution will be. The ultrasound beam first tends to focus and then to spread out as it moves away from the probe. Thus the ultrasound beam does not have the same width all along its path. The focal distance corresponds to the distance between the probe and the point where the beam is the finest. Using the aforementioned beamforming technique, the focal distance can be modified during the exam by the clinician to correspond to the region of interest. It can be noted that using dynamic focusing, it is also possible to focus on multiple points along a certain direction.

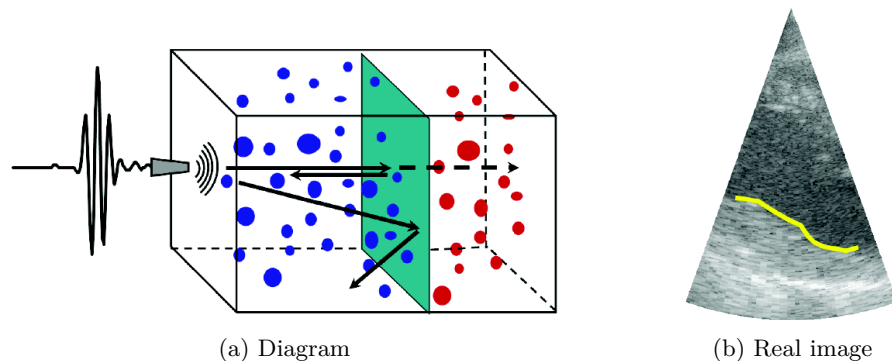


Figure 3.3: Illustration of specular reflection. (a) principle of specular reflection (see text). (b) Parasternal long-axis view: the yellow curve represents the specular interface that separates blood pool from tissue region

### 3.1.2 Interaction between wave and tissue

When an ultrasound beam propagates into the body, the wave is distorted and changed by the physical properties of the tissue through which it travels. The main interactions that take place between the sound wave and its medium are the absorption and the specular and diffuse reflection, the latter yielding to the well-known speckle phenomenon.

#### Reflection

Biological tissue is not homogeneous acoustically, *i.e.* the acoustic impedance is not constant within the medium (the acoustic impedance corresponds to the ratio of sound pressure to particle velocity). Thus, when an ultrasonic beam is incident in the tissue, one part of the ultrasonic wave is reflected at places where there are some discontinuities in the acoustical properties of the medium. Acoustic reflexions are mainly due to two different phenomena: specular reflections and backscatter reflections. The difference is related to the wavelength.

**Specular reflections** (see Fig. 3.3) appear when the transmitted sound-wave reaches boundaries where the size of the inhomogeneities in acoustical impedance is larger than the wavelength of the acoustical signal. The proportion of the ultrasound wave that is reflected (also called reflection coefficient) is linked to the acoustical impedance of the media on both side of the interface. Specular reflections arise when soft tissues are in contact with air (*e.g.* lungs, digestive tract) or mineralized structures (*e.g.* bones). In echocardiography, it allows to visualize boundaries like those which separate blood and tissue.

**Diffuse reflections** (also called diffuse component) and speckle (see Fig. 3.4) appear when a transmitted sound-wave reaches a region containing scatterers whose sizes are smaller than the wavelength. This phenomenon is mainly responsible for the noisy nature

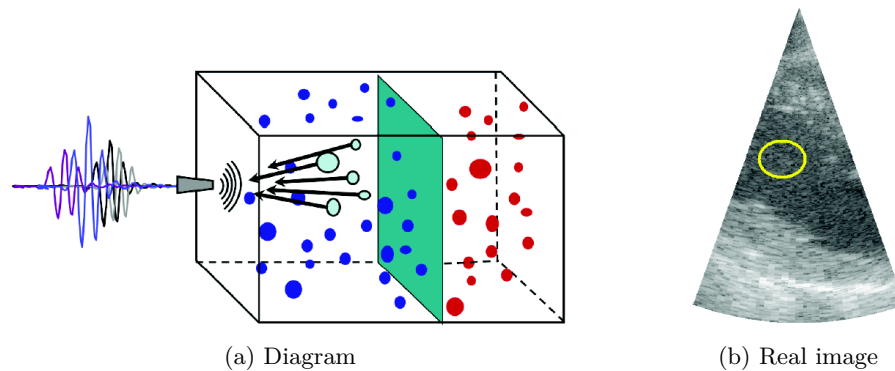


Figure 3.4: Illustration of diffuse reflection. (a) principle of specular reflection (see text). (b) Parasternal long-axis view: the yellow curve delimits a region where we can find some diffuse reflections from blood (granular aspect)

of the ultrasound images. More informations on this phenomenon will be given in the sequel.

### Refraction

When an ultrasonic beam reaches a reflective boundary with a propagation direction that is different than the surface normal, part of the beam is reflected with a reflection angle equal to the incident angle. The transmitted part is refracted by an angle that depends on the ratio of the propagation velocities in the two tissues.

In echography, the interaction between the ultrasound beam and an smooth oblique boundary yields a signal drop-out since no energy is directly reflected to the probe after an oblique reflection and the beam's direction of propagation changes after the refraction.

### Absorption

The ultrasound wave's intensity decreases as it moves away from the source and as it crosses interfaces. This decrease in intensity is linked to the multiple aforementioned interactions (reflexion, refraction) and to the absorption which corresponds to an energy transfer to the medium mainly in the form of heat. Indeed, as the ultrasonic wave propagates, the particle oscillations that it causes, require energy, causing the wave to lose energy. This phenomenon is characterized by the attenuation coefficient which is specific to each medium and increases with the wave frequency.

#### 3.1.3 Speckle

The speckle corresponds to the granular aspect of ultrasound images and leads to an inhomogeneous signal inside homogeneous tissular regions. This texture comes from the diffuse reflexion mentioned previously and can be seen as resulting from both constructive or destructive interferences of the back-propagated waves for small obstacles that the ultrasound beam might encounter. A constructive (*resp.* destructive) interference yields a bright (*resp.* dark) region in the echographic image.

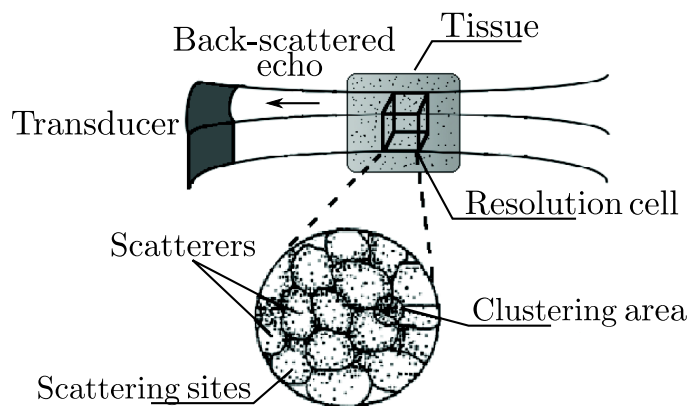


Figure 3.5: Schematic representation of the resolution cell influence

The speckle phenomenon depends on the resolution cell of the echographic equipment. The resolution cell corresponds locally to the size of the point spread function (PSF) of the acquisition system. Given the shape of the ultrasound beam that converges to the focal point and diverges afterward, the size of the resolution cell varies with depth. This phenomenon is limited in practice through the use of dynamic focusing inside the acquisition systems. In echocardiography, the involved frequencies vary between 2-5 MHz and for this range of values, the size of the corresponding resolution cell is about one cubic millimeter.

Speckle can be viewed as the interference phenomenon of the ultrasound waves backscattered from the scatterers present inside the resolution cell (see Fig. 3.5). As a consequence, speckle depends on the nature of the involved scatterers such as their density, their repartition and their echogeneity. When the number of scatterers involved in the resolution cell is high and their repartition is uniform, the speckle is defined as fully developed. This situation in echocardiography can arise for example in blood pool [Wagner *et al.* (1983)]. When the population of scatterers involved inside the resolution cell is lower, the speckle is defined as partially developed. It has been shown that partially developed speckle situation arises in myocardium tissue [Clifford *et al.* (1993), Shankar (1995)].

## 3.2 Ultrasound signal representations

The image usually displayed on the screen of an ultrasound equipment is obtained through successive processing of the original ultrasound response. Fig. 3.6 illustrates the principal steps involved in the formation of the ultrasound imaging. In this section, we give details on these signals. The frequency properties and the mathematical relation between each ultrasound signals are summarized in Table 3.1.

### 3.2.1 Radio-frequency signal (RF)

The transducer converts the acoustical reflected wave into an electrical signal. This signal is then processed by the beamformer. The output corresponds to the radio-frequency

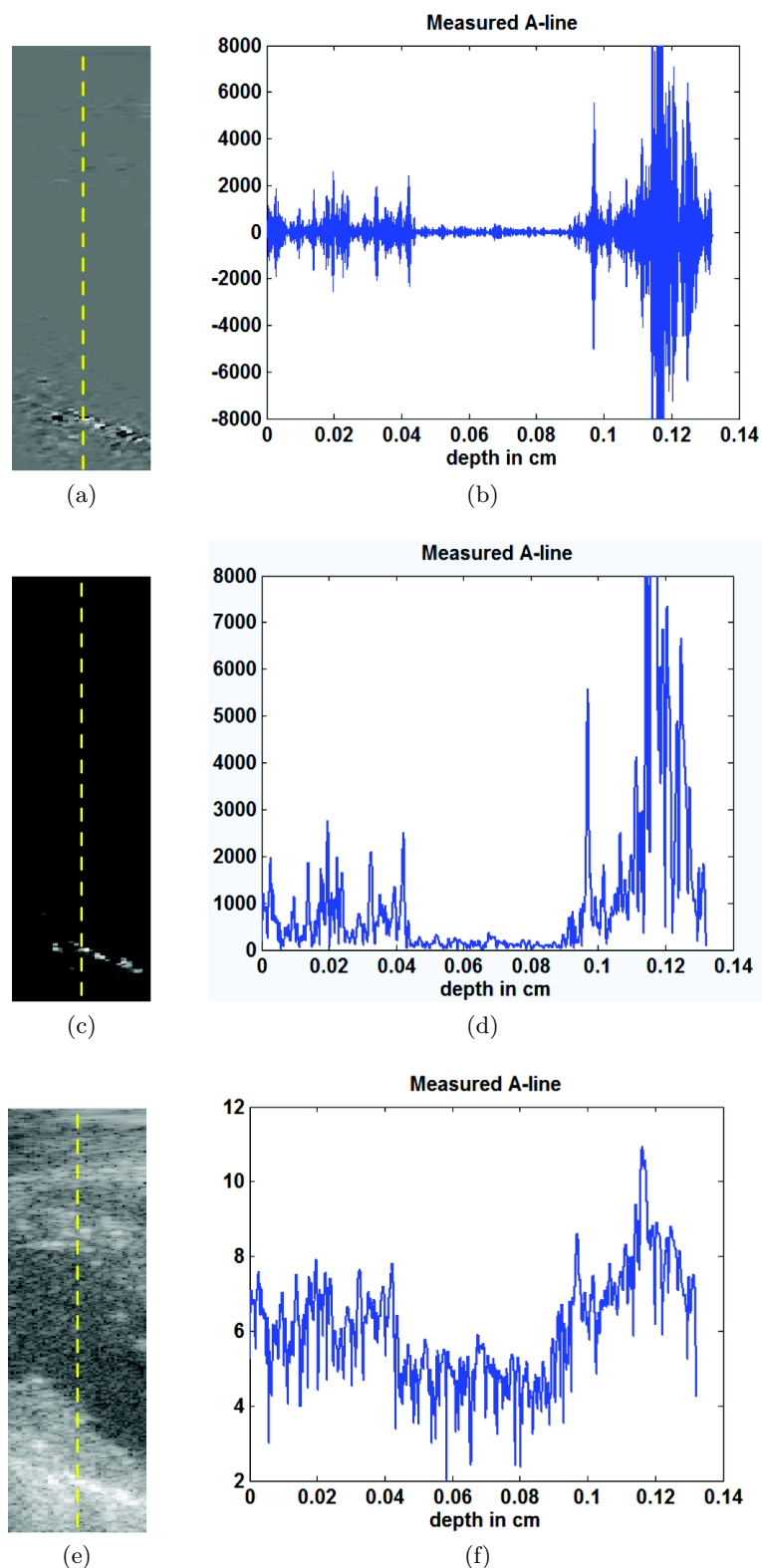


Figure 3.6: Illustration of the ultrasound image formation. From the radio-frequency signal ((a) and (b)), the envelope image ((c) and (d)) and the envelope image with logarithmic compression ((e) and (f)) are successively derived. The final image (e) corresponds to the image displayed on the screen of the ultrasound equipment. For each image, we give the A line signal corresponding to the yellow curve



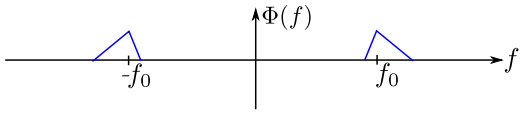
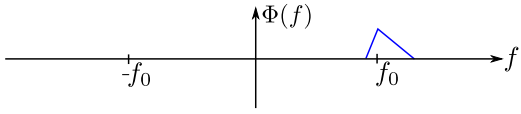
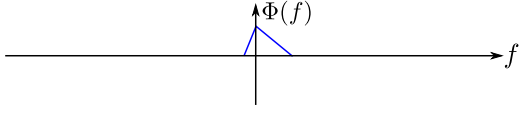
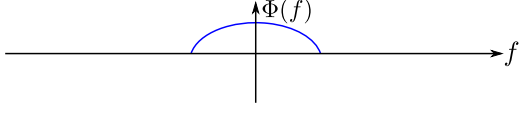
| Signal          | Expression  | Spectrum   |
|-----------------|---|--|
| RF signal       | $rf(t)$   |  |
| Analytic signal | $An(t) = rf(t) + j\mathcal{F}_H(rf(t))$<br>$\mathcal{F}_H$ : Hilbert transformation |  |
| IQ signal       | $IQ(t) = An(t) \exp(-j2\pi f_0 t)$  |  |
| Envelope signal | $env(t) =  IQ(t) $<br>$env(t) =  An(t) $  |  |
| Image           | $Image = \log(env(t) + a)$<br>with $a = \text{constant}$                            |  |

Table 3.1: Relation and properties of the different ultrasound signals

signal. This signal contains a lot of microinformations on the structures that the transmitted sound-wave insonified. The RF signal is a real signal whose central frequency ranges between 2-5 MHz. In order to cover a region of the patient's body, several ultrasound beams are emitted in different direction and the corresponding RF signals are put together to form an RF image (Fig. 3.6(a) and (b)).

### 3.2.2 Analytic signal

The analytic signal is obtained from the RF signal by removing the negative frequency components of the RF Fourier transform (this is generally done using the Hilbert transform operator). Indeed, because the RF signal is real, its corresponding spectrum is symmetric. The negative components can be viewed as a redundant information and thus can be removed without loss of information. The resulting signal is complex.

### 3.2.3 Complex envelope signal (IQ)

The complex envelope (usually called IQ signal for In phase Quadrature signal) is obtained through demodulation of the analytic signal according to its central frequency  $f_0$ . The resulting signal is complex with a spectrum having a maximum frequency value lower than the one of the RF and analytical signals. Thus, the IQ signal has the same amount of useful information but implies a lower sampling frequency than the RF signal.

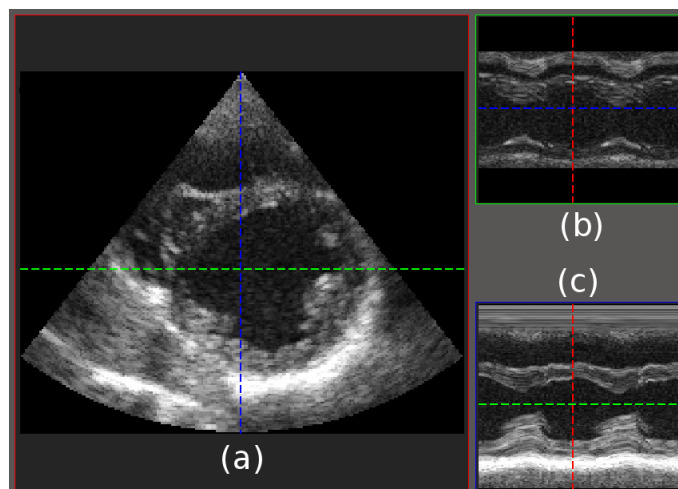


Figure 3.7: B-mode coupled with M-mode. (a) Parasternal short-axis view. (b) M-mode representation of the green horizontal line in (a). (c) M-mode representation of the blue vertical line in (a).

### 3.2.4 Envelope signal

The envelope signal is used for the display of the echographic image. This signal corresponds to the envelope of the RF signal and can be derived either from the RF or the IQ signal (see Fig. 3.6(c) and (d)). A logarithmic compression is applied to the envelope signal in order to compensate for the high dynamics of the image. This last operation allows to obtain the final gray levels used for the display of the image (see Fig. 3.6(e) and (f)). If the image was acquired using a sectorial probe, the image is also converted from polar coordinates  $(\rho, \theta)$  to cartesian coordinates  $(x, y)$ .

## 3.3 Imaging modes

There are 3 main types of echocardiography used clinically: the B-mode (brilliance), the M-mode (motion) and the Doppler echography.

### 3.3.1 B-mode echography

The B-mode is the most frequently used imaging mode. It can be either 2-dimensional or 3-dimensional (due to the recent advances in echographic probes) and thus allows to image both depth and width (in 2D) or thickness (in 3D). This is achieved by repeatedly emitting ultrasound beam with different directions of propagation. The position of a point on an image then depends of the time of flight and the direction of propagation of the ultrasound beam. This acquisition procedure is very fast allowing to achieve a framerate around 50-70 images/s (in 2D) or 20-30 volumes/s (in 3D).

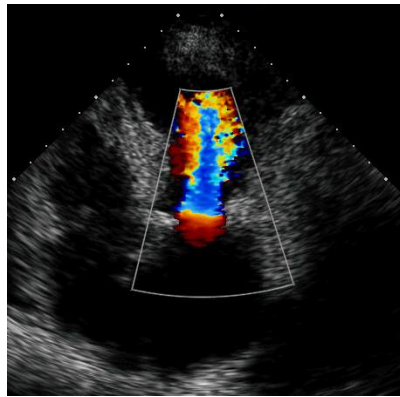


Figure 3.8: 2D Doppler imaging coupled to the B-mode of an apical 4 chamber view (Source: <http://www.cardiodiac.net/EchoCardiographie.htm>)

### 3.3.2 M-mode echography

When an ultrasound beam with a fixed direction of propagation is observed over time, the motions of the objects crossed by the beam induce a variation of the position and amplitude of the echos received by the probe. The representation of these variations of both position and intensity over time yield the M-mode (motion) or TM-mode (time-motion). This mode allows to see very rapid events and to achieve a higher temporal resolution than the B-mode but requires the probe to be placed carefully. An example of a M-mode image along with the corresponding B-mode image is shown in Fig. 3.7.

### 3.3.3 Doppler echography

Doppler imaging allows evaluation of blood flow patterns, direction and velocity. When an ultrasound beam crosses the heart's cavities or a vessel, the reflected echo will have a higher (resp. smaller) wavelength if the object moves away (resp. towards) from the probe. Thus the Doppler probe receives a signal with a shifted frequency with respect to emitted signal. An appropriate signal processing extracts the signal at the Doppler frequency  $f_D$  and the flow direction. It is however important to keep during the exam an constant incident angle of the probe with respect to the vessel axis in order to get a Doppler signal whose frequency's variations are only linked to blood velocities variations.

The exam's output can be either an audio signal or a velocity curve with respect to time. The Doppler echograph also allows a color coding of the blood flows. Usually, positive flow that moves toward the probe are displayed in red and flow moving away from the probe in blue. These flows are superimposed over the classical B-mode image (displayed in gray-level). An example of Doppler exam is shown in Fig. 3.8.

## 3.4 Standard B-mode views

In classical echocardiography, several privileged directions of acquisition or views exist. Indeed due to the particular position of the heart inside the thorasic cage and with respect

to the lungs, the access to the heart is difficult, thus limiting the possible views. It is also one reason why acquisition in sector geometry have to be performed in order to scan a wider region. The classical views used in clinical routines and their relative characteristics are described in the next paragraphs <sup>1</sup>.

**Parasternal short-axis view** (SAx, Fig. 3.9(a)): In this view, the anterior and antero-septum are presented on the top of the image and the posterior and inferior walls are presented in the lower portion of the image. It mainly allows to observe the contractile motion of the myocardium. Other structures such as the mitral valve or the papillary muscle might also be present in this view depending on the level at which the heart is cut.

**Parasternal long-axis view** (LAx, Fig. 3.9(b)): This view provides a reliable picture of the function of the anterior septum and posterior walls. It allows to easily observe the motion of the mitral valve. The view of two of the aortic leaflets shows their rapid systolic opening and a diastolic closed position arising from a position at the base of the anterior mitral leaflet. The apex of the left ventricle is often excluded from the LAx view.

**Apical 4-chamber view** (A4C, Fig. 3.10(a)): The acquisition is performed from the apex and one might see (assuming a wide enough opening) the 4 chambers: the 2 ventricles on top of the image and the 2 atria on the bottom. By convention the left ventricle is displayed to the viewer's right. The interventricular septum and interatrial septum form what is seen as the verticle column of tissue in the middle of the image. This view also offers a symmetric display of the two large atrio-ventricular valves appearing to lie horizontally on the screen.

**Apical 2-chamber view** (A2C, Fig. 3.10(b)): In this view, only the left ventricle and atrium are imaged. It permits evaluation of the motion of the anterior and inferior left ventricular myocardial segments. The mid-portion of the mitral valve motion is also evident.

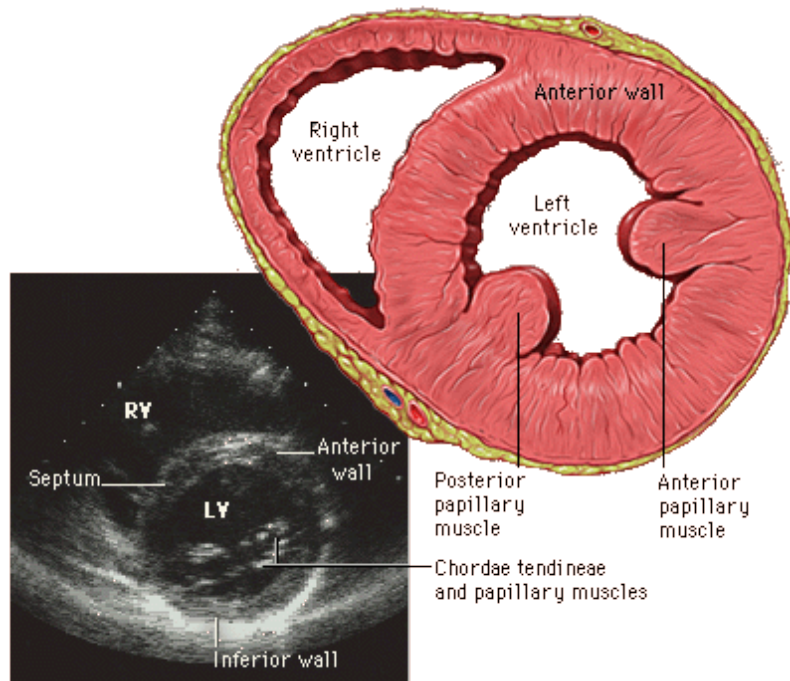
## 3.5 Specificities of echocardiographic images for segmentation

The above described specificities of cardiac anatomy and of the ultrasound image formation make segmentation of echocardiographic images a difficult task. This difficulty is linked to the following elements:

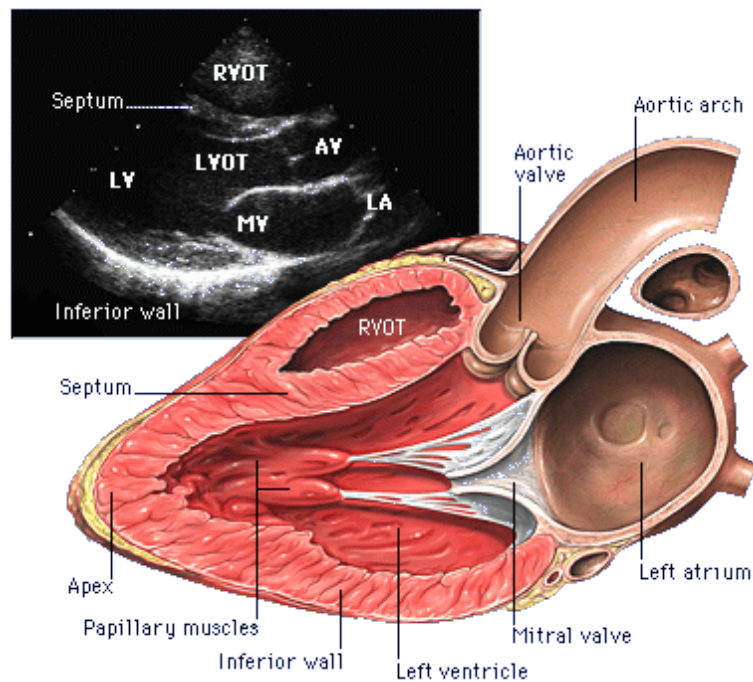
- the major difficulty corresponds to the diffuse reflection component which yields speckle noise in tissular homogeneous regions;

---

<sup>1</sup>More details may be found from the following website: [http://www.yale.edu/imaging/echo\\_atlas](http://www.yale.edu/imaging/echo_atlas)

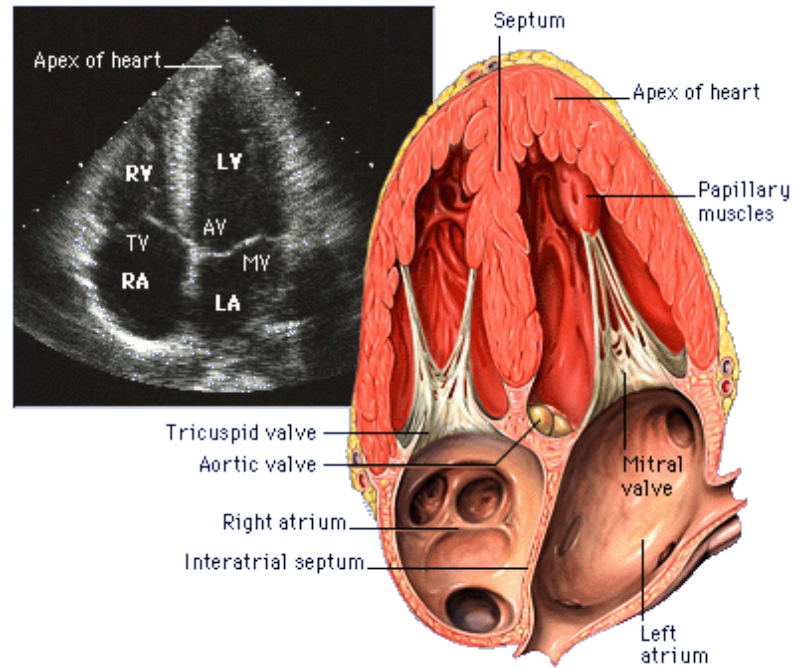


(a) Parasternal short-axis view

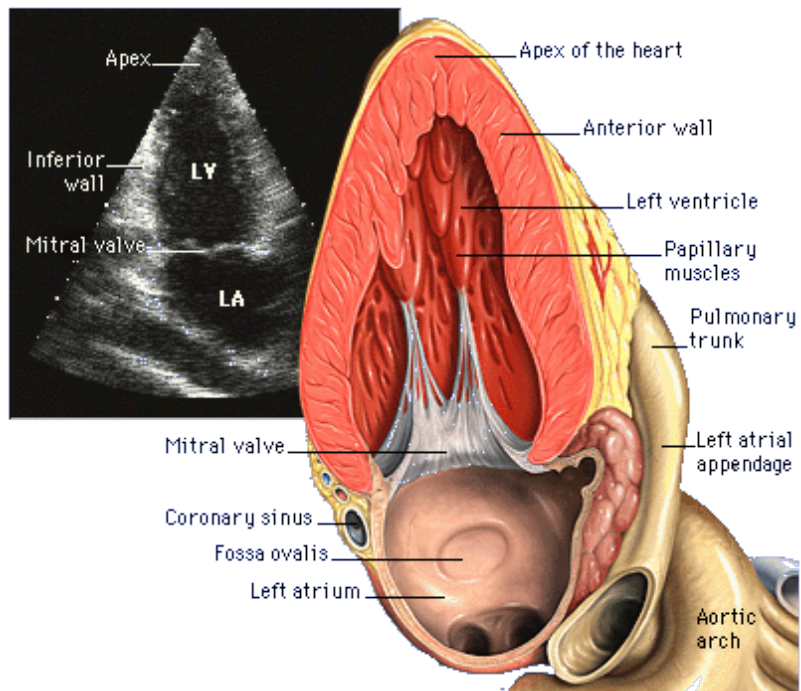


(b) Parasternal long-axis view

Figure 3.9: Parasternal views (Source: [http://www.yale.edu/imaging/echo\\_atlas/views/](http://www.yale.edu/imaging/echo_atlas/views/))



(a) Apical 4-chamber view



(b) Apical 2-chamber view

Figure 3.10: Apical views (Source: [http://www.yale.edu/imaging/echo\\_atlas/views/](http://www.yale.edu/imaging/echo_atlas/views/))

- due to attenuation, the amplitude of the signal varies with depth;
- the intensity of the backscattered signal depends on the position and the orientation of the tissue with respect to the ultrasound probe; in particular, a cardiac wall which is normal to the direction of insonification backscatters a very strong signal due to specular reflection, while a wall which is positioned along the direction of insonification backscatters a weak, diffuse signal; the intensity of the diffuse signal itself depends on the orientation of the tissular scatterers (muscular fibers) with respect to the incident wave;
- because of the limited field of view of the probe and because of the anatomy of the heart, cardiac structures may be positioned partially outside of the field of view of the probe, and consequently, may not appear as separate and well defined objects on the image; during the cardiac cycle, the observed structures may move out of the field of view, either because of lateral in-plane motion or because of their motion out of the plane of acquisition; as a consequence, the number or the topology of the objects to be detected may not be constant through the cycle;
- since we want to segment the myocardium in all the clinical views mentioned in the previous section, we need to be able to handle very different shapes.

### 3.6 Overview of segmentation methods in echocardiographic sequences

Due to the aforementioned difficulties, the segmentation of 2D-echocardiographic sequences is still an open issue, despite the numerous works addressing this problem over the last two decades [Noble and Boukerroui (2006)]. Various approaches were used in these studies such as: fuzzy logic [Feng *et al.* (1991)], Markov field [Friedland and Adam (1989), Herlin *et al.* (1994)], neural network [Binder *et al.* (1999)], image local phase [Mulet-Parada and Noble (2000), Belaid *et al.* (2011)b], active appearance model [Bosch *et al.* (2002)], information fusion [Comaniciu *et al.* (2004)], bayesian approach [Mignotte *et al.* (2001), Boukerroui *et al.* (2003)]. Amongst these approaches, methods based on active contour received a particular attention [Chalana *et al.* (1996), Giachetti (1998), Mikić *et al.* (1998), Lin *et al.* (2003), Sarti *et al.* (2005), Sheng *et al.* (2006), Dydenko *et al.* (2006), Bernard *et al.* (2007)b, Bernard *et al.* (2007)a].

As noted by [Noble and Boukerroui (2006)], most of these methods deal with the segmentation of the endocardium and only a limited literature focus on the segmentation of the whole myocardium which implies to segment the epicardium as well [Dias and Leitao (1996), Chalana *et al.* (1996), Feng *et al.* (1991)]. Indeed the detection of the epicardium is often considered as more complex than the one of the endocardium, since in addition to the aforementioned difficulties, the contrast between the epicardial border and the surrounding tissues is usually weak. It can be noted that [Zhu *et al.* (2007), Zhu *et al.*

(2010)] introduced an incompressibility constraint to segment the whole myocardium in 3D-echocardiography.

As mentioned earlier, an important characteristic of echographic images is the presence of speckle which is intrinsically due to the ultrasound image formation process. This characteristic (granular aspect of the image) makes segmentation based on the use of differential image information (such as gradient information) difficult. In this context, many studies propose to use the statistics of the echocardiographic images as the basic features driving the segmentation process [Lin *et al.* (2003), Sarti *et al.* (2005), Sheng *et al.* (2006), Dydenko *et al.* (2006), Bernard *et al.* (2007)b, Bernard *et al.* (2007)a]. However, due to the phenomena of attenuation, diffraction and beam orientation, the tissue properties vary significantly spatially. As a consequence, global statistics are not sufficient to detect the myocardium and authors have recently proposed to use local statistics to model the myocardium [Alessandrini *et al.* (2009), Alessandrini *et al.* (2011), Belaid *et al.* (2011)a], following the seminal work of [Lankton and Tannenbaum (2008), Li *et al.* (2008)]. Another strategy to deal with the intensity inhomogeneities is to introduce prior knowledge on the shape or motion of the object to recover as will be shown in Chapter 5 and 8.

Regarding the validation of the obtained segmentation, most of the techniques segment only a particular view (*e.g.* SAx [Chalana *et al.* (1996), Taron *et al.* (2004), Tao and Tagare (2007), Alessandrini *et al.* (2011)], A4C [Lin *et al.* (2003), Nascimento and Marques (2008), Zhou (2010), Carneiro *et al.* (2012)]) and the size of the validation dataset is often small (15 to 20 images [Sarti *et al.* (2005), Tao and Tagare (2007), Belaid *et al.* (2011)b]). However some studies [Chalana *et al.* (1996), Bosch *et al.* (2002), Comaniciu *et al.* (2004), Carneiro *et al.* (2012)] perform a more thorough validation and we will detail some of them. In [Chalana *et al.* (1996)], the dataset comprises 44 SAx sequences where both end-systolic and end-diastolic frames were segmented by four different experts. The method was evaluated in terms of Mean Absolute Distance (MAD) computed between the segmentation results and the reference of each expert. The MAD was then compared to the inter-observer (IO) distance and the percentage of cases where the measure was within the IO range was also computed. The authors also performed a Pearson's correlation test between the area enclosed by the segmentation result and the average of the references contours. The authors reported a MAD of 2.8mm and 3.61mm for the epicardium and endocardium respectively while the IO distances were 3.79mm and 2.67mm for the epicardial and endocardial borders respectively. Note however that no comparison is made with other techniques.

[Comaniciu *et al.* (2004)] used a database of 32 sequences (18 SAx and 14 A4C or A2C) having 18 to 90 frames. MAD and Mean Sum of Squared Distance (MSSD) were used to evaluate the global and local behavior of the algorithm respectively. When considering the segmentation of the endocardium on the whole dataset, a MAD and MSSD of 1.7pixel (px) and 8.3px<sup>2</sup> respectively were reported while for the most difficult cases these measures were equal to 4.1px and 25.8px<sup>2</sup>. The algorithm compared favorably to 3 other methods



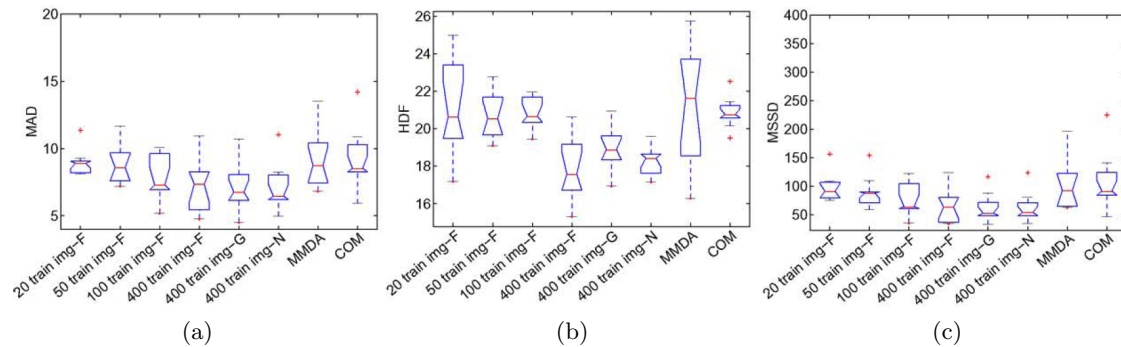


Figure 3.11: Box plot results for varying training set (6 first box plots) and the 2 state-of-the-art methods ( [Nascimento and Marques (2008)] (MMDA) and [Zhou *et al.* (2005)] (COM)) for three different error measures: (a) MAD (in px), (b) HD (in px) and (c) MSSD (in px<sup>2</sup>). Note that all figures are reproduced from [Carneiro *et al.* (2012)].

but no inter-observer measures are given.

[Carneiro *et al.* (2012)] performed their validation on a dataset of 12 A4C sequences of diseased cases and 2 A4C sequences of healthy patients. 80 endocardial reference contours were drawn by two cardiologists, in addition to the one required to train the model (see also 5.3 for more details on the segmentation algorithm). For the comparison, the authors used the MAD, Hausdorff distance (HD), MSSD, the Jaccard distance and the average perpendicular error and compared their results to 2 other state-of-the-art methods. To verify if their results lied inside the inter-observer variability, the authors used the Williams index and the Percent statistics proposed by [Chalana and Kim (1997), Alberola-López *et al.* (2004)] and a Bland-Altman analysis [Bland and Altman (1986)]. Fig. 3.11 shows box plot results for varying training set and the 2 other methods.

---

## Variational active contours

---

The general principle of the segmentation using active contours (also called deformable models) consists in evolving an interface towards the boundaries of the object to be detected. If we consider the 2D case, this can be seen as the evolution of an initial curve in an image towards the desired structure (Fig. 4.1). When using variational active contour, the evolution of the curve is given by the minimization of an energy functional which reflects the property of the object. This framework has been originally proposed by [Kass *et al.* (1988)] with the snake model.

The implementation of this type of approach for a given application requires to consider the following steps and choices:

- Choice of the representation of the active contour. In most of the cases, this representation is either parametric (snakes) or implicit (level-set) though explicit representation have recently been proposed [Vallet *et al.* (2006), Duan *et al.* (2010), Barbosa

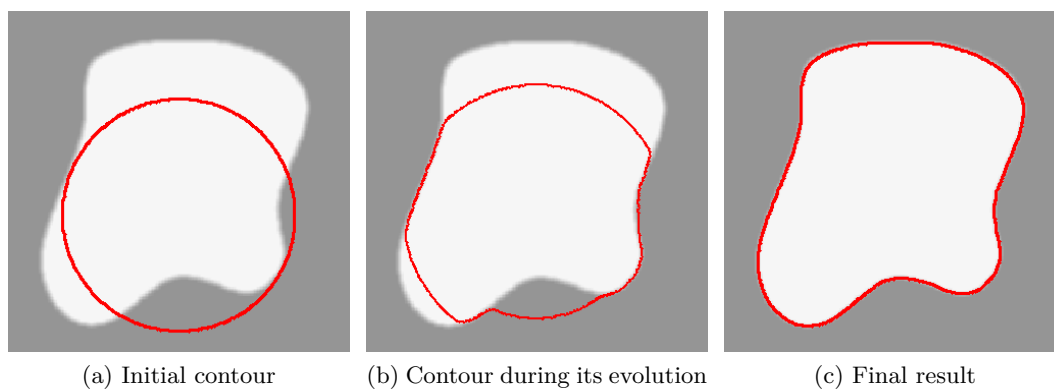


Figure 4.1: 2D example of the evolution of an active contour.

*et al.* (2012b)].

- Energy functional formulation. This step is application dependant since the functional is built to best model the object to be segmented. A local minimum of the functional must thus corresponds to its boundaries.
- Deriving the evolution equation. In this step, mathematical tools (such as Euler Lagrange derivative or shape gradient) are used to derive from the energy criterion a partial differential equation (PDE) that will drive the active contour from its initial position towards the boundaries of the object [Aubert *et al.* (2003)].
- Numerical implementation of the evolution equation. The numerical resolution of this PDE usually involves finite differences techniques applied to the active contour.

In the next section, we will detail those differents steps while focusing more specifically to the level-set formulation since this framework will be used in the sequel.

## 4.1 Active contour representation

### Definition:

The active contour can be represented as a parametric curve  $\Gamma : [0, 1] \mapsto \mathbb{R}^2$ ,  $s \rightarrow \Gamma(s) = (x(s), y(s))$ , where  $s$  is the parameter (Fig. 4.2(a)).

The interface  $\Gamma$  can also be represented as an explicit function. Geometrically, this implies that one of the coordinates of the points of the interface is expressed as a function of the remaining coordinates. For the 2D case, this can be expressed as  $\zeta : \mathbb{R} \mapsto \mathbb{R}$ ,  $x \rightarrow \zeta(x)$  (Fig. 4.2(c)). The contour then corresponds to the set of points where  $y = \zeta(x)$ . As suggested in [Duan *et al.* (2010)], if we associate a function in  $\Omega$  to the contour as

$$\Upsilon(x, y) = \zeta(x) - y, \quad (4.1)$$

the contour may also be represented as  $\Gamma = \{\mathbf{p} = (x, y) | \Upsilon(\mathbf{p}) = 0\}$ . Note than when using this representation, authors usually use a coordinate system different from the cartesian one (*e.g.* the polar coordinate system  $(r, \theta)$ ) in order to be able to represent a closed contour.

In the level-sets formalism, the active contour is represented implicitly as the zero-level of a Lipschitz-continuous function of  $\mathbb{R}^2$  (Fig. 4.2(b)). Let  $\phi(\mathbf{p})$  be this function, where  $\mathbf{p} = (x, y) \in \Omega$  and  $\Omega$  is the subset of  $\mathbb{R}^2$  corresponding to the image domain. This function satisfies

$$\begin{cases} \phi(\mathbf{p}) > 0, & \text{if } \mathbf{p} \in \Omega_i, \\ \phi(\mathbf{p}) < 0, & \text{if } \mathbf{p} \in \Omega_o, \\ \phi(\mathbf{p}) = 0, & \text{if } \mathbf{p} \in \partial\Omega_i = \Gamma(s), \end{cases} \quad (4.2)$$

where  $\Omega_i$  is the inner region defined by the active contour  $\Gamma$ . The outer region noted  $\Omega_o$  is defined as  $\Omega_o = \Omega \setminus \Omega_i$ .

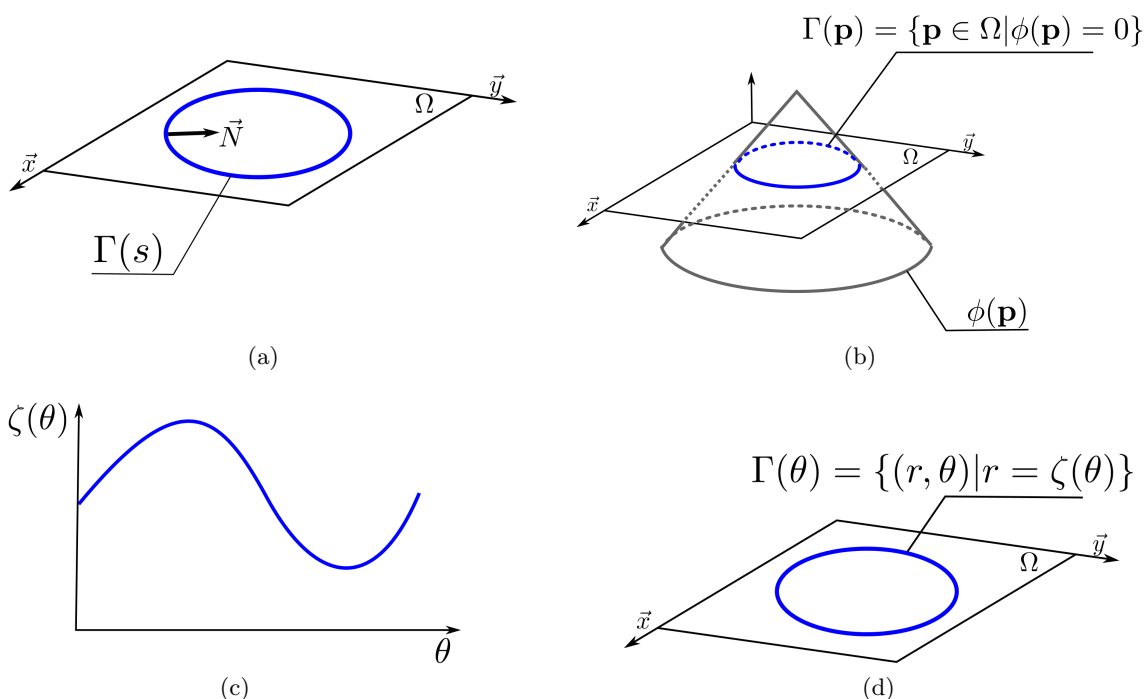


Figure 4.2: Representation of a contour. (a) Parametric representation. (b) Implicit representation: the contour  $\Gamma$  corresponds to the zero-level of the implicit function  $\phi(\mathbf{p})$ . Explicit representation: the contour  $\Gamma$  (d) corresponds to a set of points where one coordinate is defined as a function of the remaining ones (c).

Note that, a parallel can be drawn between the explicit and implicit formulation where the contour is always represented as the set of points corresponding to the zero-level of a function (the associated function  $\Upsilon$  or the implicit function  $\phi$ ), in contrary to the parametric representation where the contour is defined directly.

### Example:

Let  $\Gamma$  be an ellipse of center  $(X_c, Y_c)$  and of radii  $a$  and  $b$  (in the  $x$  and  $y$  direction respectively). Its parametric representation is

$$\begin{aligned} \Gamma : [0, 1] &\mapsto \Omega & (4.3) \\ s \rightarrow \Gamma(s) &= \begin{cases} x = X_c + a \cos(2\pi s) \\ y = Y_c + b \sin(2\pi s). \end{cases} \end{aligned}$$

We can also define this ellipse using the explicit representation. Using the polar coordinates, we have  $\Gamma = \{(r, \theta) | r = \zeta(\theta)\}$ , where  $r = \sqrt{(x - X_c)^2 + (y - Y_c)^2}$ ,  $\theta = \arctan((y - Y_c)/(x - X_c))$  and

$$\begin{aligned} \zeta : [0, 2\pi] &\mapsto \mathbb{R}^+ & (4.4) \\ \theta \rightarrow \zeta(\theta) &= (ab) / \sqrt{(b \cos(\theta))^2 + (a \sin(\theta))^2}. \end{aligned}$$

Finally, we can also represent this ellipse implicitly as

$$\begin{aligned} \phi : \Omega &\mapsto \mathbb{R} \\ \mathbf{p} = (x, y) &\rightarrow \phi(\mathbf{p}) = \frac{(x - X_c)^2}{a^2} + \frac{(y - Y_c)^2}{b^2} - 1 \end{aligned} \quad (4.5)$$

and  $\Gamma = \{\mathbf{p} \in \Omega \mid \phi(\mathbf{p}) = 0\}$ .

## 4.2 Parametric representation

### 4.2.1 Energy functional

Following the work of [Jehan-Besson *et al.* (2003)], a general expression of the energy functional is given by

$$E(\Gamma) = \int_{\Gamma} K^c(\mathbf{p}) ds + \int_{\Omega_i} K^i(\mathbf{p}) d\mathbf{p} + \int_{\Omega_o} K^o(\mathbf{p}) d\mathbf{p} \quad (4.6)$$

where  $d\mathbf{p} = dx dy$  and  $ds$  corresponds to the curve length parameterization.

The first integral of (4.6) depends on the contour and describes the boundary properties of the object. Thus the function  $K^c$  is often based on the gradient of the image (as will be seen in section 4.5.1).

The last two terms of (4.6) correspond to region terms that describe the properties of either the inner region (function  $K^i$ ) or the outer one (function  $K^o$ ). Those functions often exploit the statistical properties of the image (as will be seen in section 4.5.2 and 4.5.3).

### 4.2.2 Evolution equation

Minimizing the energy functional (4.6) is equivalent to canceling the first variation of  $E(\Gamma)$ , that is finding  $\Gamma$  such that

$$\frac{\partial E}{\partial \Gamma} = 0. \quad (4.7)$$

Generally, the expression of  $\frac{\partial E}{\partial \Gamma}$  is explicitly computed using standard calculus of variation (*i.e.* Euler-Lagrange equations) and yield a partial differential equation. Since a parametric representation of the contour has been adopted, the domain integrals of  $E$  have to be transformed into boundary integral using either the Green-Riemann theorem [Zhu and Yuille (1996)] or shape gradients [Jehan-Besson *et al.* (2003)]. This can be a very complex step and one may refer to the review paper from [Aubert *et al.* (2003)] for more information on this topic.

The minimization of  $E$  is then performed using a gradient descent which yields the following evolution equation of the active contour [Caselles *et al.* (1997)]

$$\frac{\partial \Gamma}{\partial \tau}(s, \tau) = V(\mathbf{p}, \tau) \mathbf{N}(s, \tau), \quad (4.8)$$

where  $\mathbf{N}$  is the unit inward normal to the contour,  $V$  is the speed term which depends on the functions  $K^c$ ,  $K^i$  and  $K^o$  and thus of the targetted application. Note that in (4.8), an artificial time step  $\tau$  has been introduced to perform the gradient descent.

It is interesting to note that the active contour's evolution only takes place along its normal direction. Indeed, as shown by [Epstein and Gage (1987)], the component of the speed along the normal controls the contour's deformation while its tangential component does not modify the contour's geometry but only its parameterization. Furthermore, it is important to stress that due to the use of a gradient descent, the obtained optimum after convergence corresponds to a local minimum and is thus dependent of the active contour's initialization.

### 4.3 Implicit representation: Level-set methods

The level-set framework has been first proposed in Physics by [Osher and Sethian (1988)] to solve the problem of front propagation. The modelisation of the contour using this type of representation has then been proposed by [Malladi *et al.* (1995)], though the contour evolution was not due to a variational formulation. This variational formulation has been introduced by [Caselles *et al.* (1997)] and almost simultaneously by [Yezzi *et al.* (1997)].

These research efforts find their origin in the difficulty to handle topologically complex shapes (*e.g.* object having a hole or multiple non connex components) with the parametric formulation of the active contour's evolution. On the contrary, the contour's representation using level-set allows to easily deal with those kind of shapes as well as with splitting and merging of the contour due to its implicit formulation (as can be seen in Fig. 4.3 and Fig. 4.5). Moreover this removes the problem of contour self intersections and the need for control point resampling mechanisms. Another advantage of this representation lies in the fact that it allows to discretize the evolution equation on a regular grid.

#### 4.3.1 Formalization of the evolution equation

From the definition of  $\phi(\mathbf{p})$  and the equation (4.8), it can be shown that the evolution equation for the implicit formulation can be written as follows [Caselles *et al.* (1997)]

$$\frac{\partial \phi}{\partial \tau}(\mathbf{p}, \tau) = V(\mathbf{p}, \tau) \|\nabla \phi(\mathbf{p}, \tau)\|. \quad (4.9)$$

One can notice that the level-set evolution is linked to the velocity term  $V$  (that depends on the object characteristics) and to its gradient. On a formal level, this expression corresponds to a time-dependant partial differential equation.

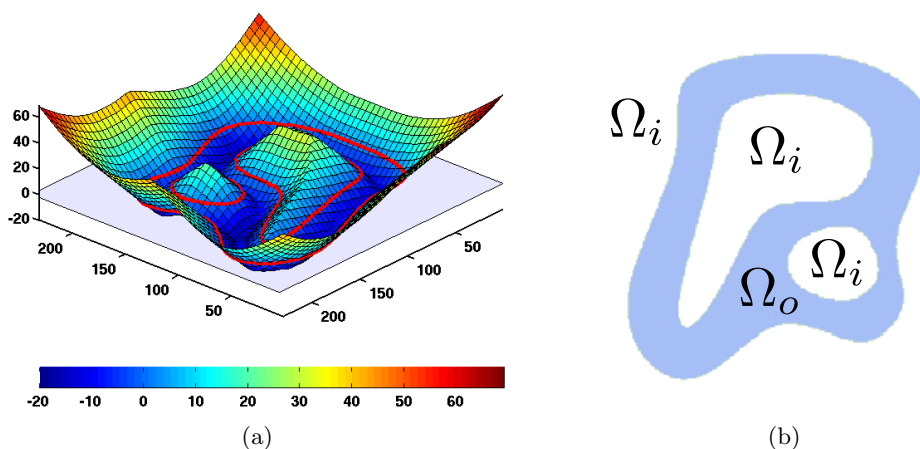


Figure 4.3: (a) Level-set function  $\phi(\mathbf{p})$  represented as a signed distance function; the red curve corresponds to the contour  $\Gamma$  defined as the zero-level-set. (b) The contour  $\Gamma$  divides the domain  $\Omega$  into an inner region  $\Omega_i$  and an outer one  $\Omega_o$ .

### 4.3.2 Direct formulation of the energy functional using level-set

As mentioned earlier, a difficult step consists in handling the region terms which can imply complex calculus to express the functional variation (transformation of the domain integrals into boundary integrals). In their seminal work, [Chan and Vese (2001)] described an approach allowing to tackle this difficulty. It consists in expressing the energy functional directly using the implicit representation of the active contour. This way, the parametric formulation is taken out of the picture.

Considering the step function  $H(\cdot)$  (also called Heaviside function) and the Dirac distribution  $\delta(\cdot)$ , the functional can be written as

$$E(\phi) = \int_{\Omega} K^c(\mathbf{p})\delta(\mathbf{p})\|\nabla\phi(\mathbf{p})\| d\mathbf{p} + \int_{\Omega} K^i(\mathbf{p})H(\phi(\mathbf{p})) d\mathbf{p} + \int_{\Omega} K^o(\mathbf{p})(1 - H(\phi(\mathbf{p}))) d\mathbf{p}. \quad (4.10)$$

One may notice that, in this expression, all the integrals are applied on the whole definition domain  $\Omega$ .

The Euler-Lagrange equation is obtained through the calculus of variation of  $E$  with respect to  $\phi$  and a gradient descent then provides the evolution equation that writes as follow

$$\frac{\partial\phi}{\partial\tau}(\mathbf{p}, \tau) = V(\mathbf{p}, \tau)\delta(\phi(\mathbf{p}, \tau)). \quad (4.11)$$

Note that some authors proposed a modified version of the evolution equation where the dirac distribution  $\delta(\phi)$  is replaced by the norm of the gradient  $\|\nabla\phi\|$  [Zhao *et al.* (1996)], which should not change the solution after convergence [Marquina and Osher (2000), Tsai and Osher (2003)].

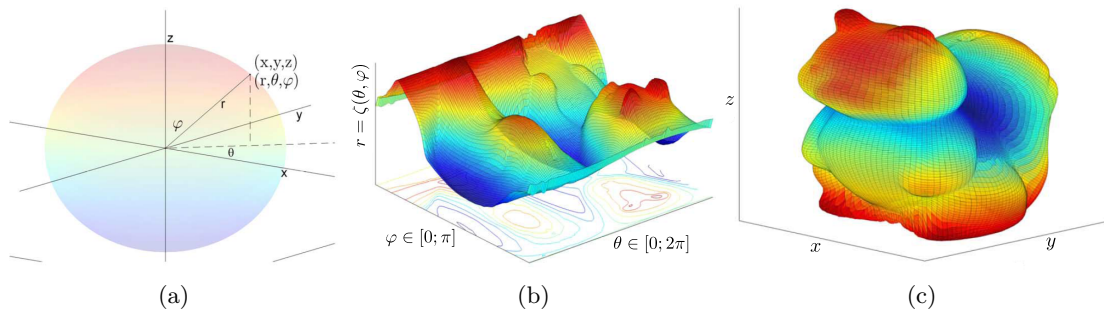


Figure 4.4: Illustrative 3-D surface compact representation through an explicit function in the spherical domain. (a) Correspondence between the Cartesian and spherical domains. (b) Explicit function in the spherical domain. (c) Explicit function converted to the Cartesian space (from [Barbosa *et al.* (2012)b]).

## 4.4 Explicit representation

In [Duan *et al.* (2010)], the authors adopted an energy formulation close to the one described in 4.2 where they have both domain and boundary integrals. Following the work of [Vallet *et al.* (2006)], the minimization of the energy is performed using a Newton downhill method.

[Barbosa *et al.* (2012)b] proposed recently to exploit the associated function  $\Upsilon$  defined in (4.1) to easily define inner and outer region in a level-set-like manner. This allows to take advantage of the substantial litterature on region based energy initially proposed for level-set and to apply it to the explicit formulation of the contour.

It is also important to stress that in contrary to the implicit representation that allows a topological flexibility, a consequence of using explicit formulation is that it can only represent simple-connected object. This may be seen as a mild constraint in many applications, such as medical imaging (*i.e.* when the goal is to segment one simply-connected object and thus where the topological flexibility of level-sets is not desired or at least not always needed). Note that due to the dimension reduction of the problem, this formulation provides fast algorithm that can run real-time (as mentionned in [Duan *et al.* (2010), Barbosa *et al.* (2012)b]). An example of explicit representation of a squirrel is shown in Fig. 4.4.

## 4.5 Main families of active contour energy

Substantial litterature deals with image segmentation using level-set models and we will give here three classical examples. An interested reader may refer to the following review papers for a more complete overview [Osher and Paragios (2003), Suri *et al.* (2002), Tsai and Osher (2003), Cremers *et al.* (2007)].



### 4.5.1 Gradient based model

In an article that is now considered to have initiated this kind of methods, Caselles *et al.* proposed an active contour allowing to segment objects characterized by high gradients on their boundaries while preserving the smoothness of the solution [Caselles *et al.* (1997)].

The object descriptor is based on the following function

$$g(I) = \frac{1}{1 + \|\nabla G_\sigma * I\|^p}, \text{ with } p = 1 \text{ or } 2 \quad (4.12)$$

where  $I$  represents the image to be segmented,  $G_\sigma$  is a Gaussian with standard deviation  $\sigma$ . The function thus depends on the gradient of the image smoothed by a Gaussian. It varies from 0 for high gradient to 1 for low gradient.

The energy functional used does not have any region term and correspond to the following descriptor

$$K^c = \alpha \|\Gamma(s)\|^2 + \lambda g^2(I(\Gamma(s))) \quad (4.13)$$

where  $s$  correspond to some parameterization of the curve.

This descriptor yields an energy functional that writes

$$E(\Gamma) = \alpha \int_0^1 \|\Gamma(s)\|^2 ds + \lambda \int_0^1 g^2(I(\Gamma(s))) ds. \quad (4.14)$$

The first part of the energy minimizes the contour length and acts thus as a regularization term (imposing a smooth curve). The second term is a data attachment term that aims at maximizing the gradient along the contour. The hyperparameters  $\alpha$  and  $\lambda$  weight the influence of each term.

The evolution equation is then given in a parametric formulation as

$$\frac{\partial \Gamma}{\partial \tau}(\tau) = (g(I)\kappa - \nabla g(I) \cdot \mathbf{N})\mathbf{N}, \quad (4.15)$$

where  $\kappa$  is the curvature of  $\Gamma$ . In this equation, the term depending on the curvature controls the curve smoothness while the other part controls the evolution towards high gradient's areas.

Using (4.9), the evolution equation can be rewritten in an implicit formulation as

$$\frac{\partial \phi}{\partial \tau}(\tau) = \left( g(I)\kappa - \nabla g(I) \cdot \frac{\nabla \phi}{\|\nabla \phi\|} \right) \|\nabla \phi\| = g(I)\kappa \|\nabla \phi\| - \nabla g(I) \cdot \nabla \phi, \quad (4.16)$$

Since this seminal work, many other contour based segmentation approaches have been proposed where the data attachment term depends on the gradient vector flow rather than the gradient itself [Paragios *et al.* (2004)].

### 4.5.2 Region based model

In their reference work, [Chan and Vese (2001)] were interested in segmenting objects with weak edges for whom the gradient information is not appropriated. To tackle this problem, the proposed functional makes use of the characteristics of the inner and outer region ( $\Omega_i$  and  $\Omega_o$  respectively) defined by the active contour. The corresponding descriptors are the following

$$\begin{cases} K^c = \mu, \\ K^i = \nu + \lambda_1(I - c_i)^2, \\ K^o = \lambda_2(I - c_o)^2. \end{cases} \quad (4.17)$$

The energy functional is then defined using the implicit representation of the active contour and writes as

$$\begin{aligned} E(\phi) = & \mu \int_{\Omega} \delta(\phi(\mathbf{p})) \|\nabla\phi(\mathbf{p})\| d\mathbf{p} + \nu \int_{\Omega} H(\phi(\mathbf{p})) d\mathbf{p} \\ & + \lambda_1 \int_{\Omega} (I(\mathbf{p}) - c_i)^2 H(\phi(\mathbf{p})) d\mathbf{p} + \lambda_2 \int_{\Omega} (I(\mathbf{p}) - c_o)^2 (1 - H(\phi(\mathbf{p}))) d\mathbf{p}. \end{aligned} \quad (4.18)$$

The two first terms of the functional correspond respectively to the length of the zero-level and to the area of the inner region weighed by  $\mu$  and  $\nu$ . Their minimization thus allows to impose a smoothness constraint on the contour.

The two last terms weighed by  $\lambda_1$  and  $\lambda_2$  corresponds data attachment terms and involve the means of the inner region ( $c_i$ ) and of the outer one ( $c_o$ ). The minimization of those terms thus yields to the separation of the image into two homogeneous regions with different means. Note that the data attachment terms are inspired by the Mumford-Shah functional [Mumford and Shah (1989)].

The evolution equation is then given by

$$\frac{\partial\phi}{\partial\tau}(\tau) = \left( \mu \operatorname{div} \left( \frac{\nabla\phi}{\|\nabla\phi\|} \right) - \nu - \lambda_1(I - c_i)^2 + \lambda_2(I - c_o)^2 \right) \delta(\phi). \quad (4.19)$$

We can notice that the minimization of the contour length yields the term  $\operatorname{div} \left( \frac{\nabla\phi}{\|\nabla\phi\|} \right)$  which corresponds to the euclidian curvature of the active contour.

An illustration of this approach is given in Fig. 4.5 where the evolution of the level-set according to eq.(4.19) is shown on a simulated image containing two homogeneous regions with complex topology.

### 4.5.3 Local region based model

Recently, [Lankton and Tannenbaum (2008)] proposed a framework to segment inhomogeneous objects where both the gradient and region data attachment terms may provide misleading informations. This is done by considering that though the properties of the

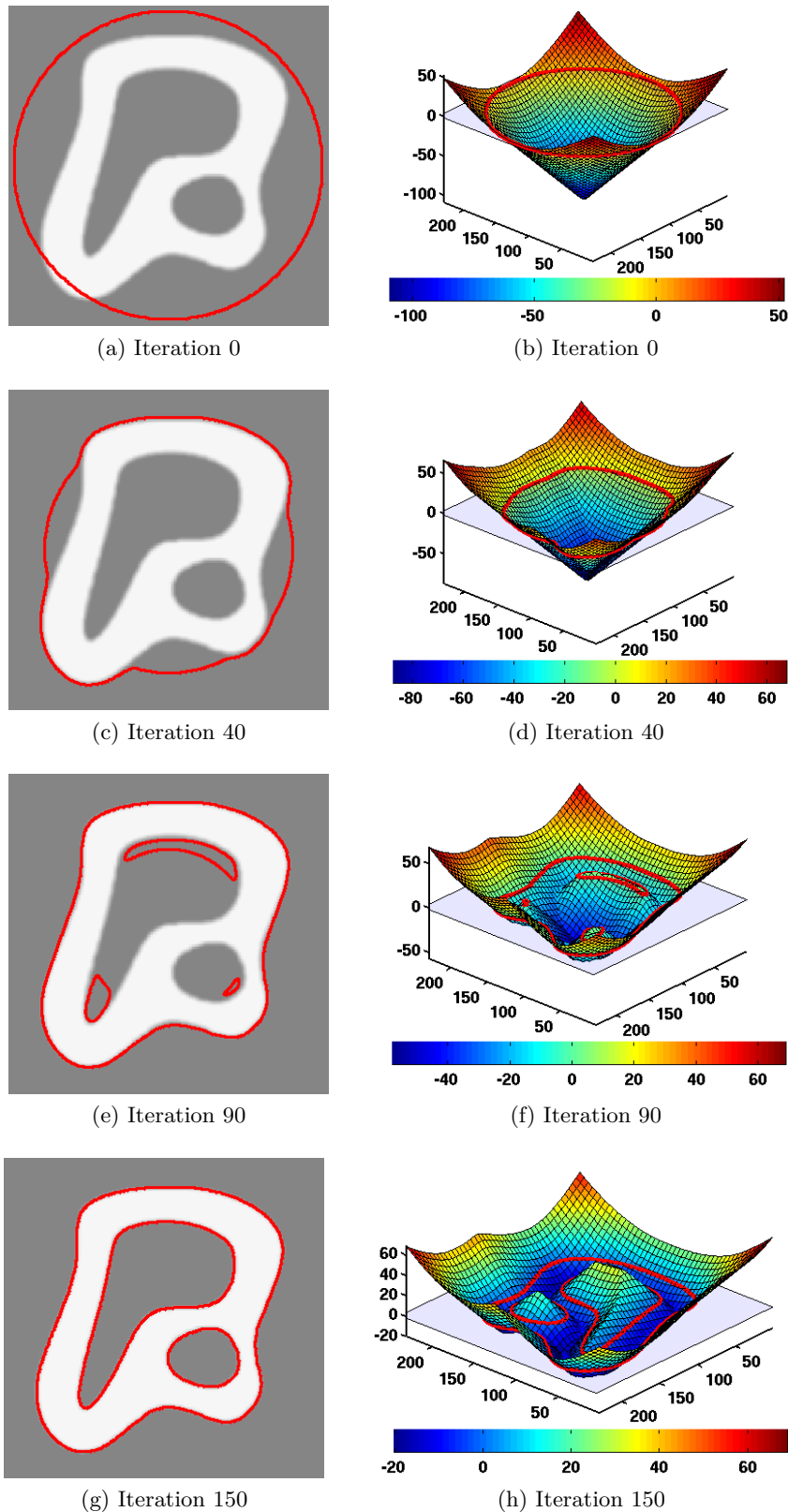


Figure 4.5: Evolution of the implicit function using Chan and Vese method on a simulated image (b, d, f, h). The zero-level is shown in red. (a, c, e, g) The corresponding image with the contour shown in black.

object may vary spatially, they remain consistent on a local scale. This yields the following descriptors

$$\begin{cases} K^c = \mu, \\ K^i(\mathbf{p}) = \delta(\phi(\mathbf{p}))\lambda_1 \int_{\Omega} B(\mathbf{p}, \mathbf{q}) F_i(I, \phi) d\mathbf{q}, \\ K^o(\mathbf{p}) = \delta(\phi(\mathbf{p}))\lambda_2 \int_{\Omega} B(\mathbf{p}, \mathbf{q}) F_o(I, \phi) d\mathbf{q}, \end{cases} \quad (4.20)$$

where  $B(\mathbf{p}, \mathbf{q})$  corresponds to a neighborhood centered on the point  $\mathbf{p}$  and of size  $R$  and  $F_i$  and  $F_o$  are some region descriptors (such as the one described in (4.17)). Note that the contour descriptor  $K^c$  is the same as the one used in 4.5.2 and that the region descriptors are now computed locally due to the function  $B(\cdot)$ .

The energy functional is then defined using the implicit representation of the active contour and writes as

$$\begin{aligned} E(\phi) = \mu \int_{\Omega} \delta(\phi(\mathbf{p})) \|\nabla \phi(\mathbf{p})\| d\mathbf{p} + \lambda_1 \int_{\Omega} \delta(\phi(\mathbf{p})) \int_{\Omega} B(\mathbf{p}, \mathbf{q}) F_i(I, \phi) d\mathbf{q} d\mathbf{p} \\ + \lambda_2 \int_{\Omega} \delta(\phi(\mathbf{p})) \int_{\Omega} B(\mathbf{p}, \mathbf{q}) F_o(I, \phi) d\mathbf{q} d\mathbf{p}. \end{aligned} \quad (4.21)$$

Note that in this energy, only the points belonging to the zero-level contribute to the energy due to the presence of the Dirac  $\delta(\mathbf{p})$  in the energy term.

The authors showed that the following evolution equation can be derived from (4.21)

$$\begin{aligned} \frac{\partial \phi}{\partial \tau}(\mathbf{p}, \tau) = -\delta(\phi(\mathbf{p})) \left( \operatorname{div} \left( \frac{\nabla \phi(\mathbf{p})}{\|\nabla \phi(\mathbf{p})\|} \right) + \int_{\Omega} B(\mathbf{p}, \mathbf{q}) \nabla_{\phi} F_i(I, \phi) d\mathbf{q} \right. \\ \left. + \int_{\Omega} B(\mathbf{p}, \mathbf{q}) \nabla_{\phi} F_o(I, \phi) d\mathbf{q} \right). \end{aligned} \quad (4.22)$$

From this equation, one may notice that the presence of the Dirac forces the evolution of the contour to only take place along the zero-level. Nevertheless, [Li *et al.* (2008)] proposed a very similar framework that handles local properties of the inner and outer region while allowing an evolution over the whole domain.

## 4.6 Numerical implementation of the level-set

The implementation of the general evolution equation given in eq.(4.9) is equivalent to solving a time-dependant partial differential equation (PDE). A vast majority of the implementations use finite differences techniques to perform this minimization. These numerical schemes have been introduced by Osher [Osher and Sethian (1988), Osher and Fedkiw (2002)] and allow to obtain accurate and unique solutions, and involve upwind differencing, essentially non oscillatory schemes borrowed from the numerical solutions of conservation laws and Hamilton Jacobi equations.

It can however be noted that some authors recently proposed to solve this PDE by

using a continuous and parametric representation of the level-set. [Gelas *et al.* (2007)] used a collocation method and radial basis functions (RBF) to represent the level-set. [Bernard *et al.* (2009)] proposed to use a B-Splines representation of the level-set which once introduced in the energy functional yields a linear filtering formulation of the problem. Note that the idea of using B-Spline to represent the level-set has also been recently applied to the explicit representation by [Barbosa *et al.* (2012)b].

#### 4.6.1 Discretisation of the evolution equation

The partial derivatives of the level-set function are discretized using the following finite differences schemes:

$$D_x^+ \phi(x, y) = (\phi(x + \Delta x, y) - \phi(x, y)) / \Delta x \quad (4.23)$$

$$D_x^- \phi(x, y) = (\phi(x, y) - \phi(x - \Delta x, y)) / \Delta x \quad (4.24)$$

$$D_x^0 \phi(x, y) = (\phi(x + \Delta x, y) - \phi(x - \Delta x, y)) / (2\Delta x) \quad (4.25)$$

$$D_{xx}^0 \phi(x, y) = (\phi(x + \Delta x, y) - 2\phi(x, y) + \phi(x - \Delta x, y)) / \Delta x^2 \quad (4.26)$$

$$D_{xy}^0 \phi(x, y) = (\phi(x + \Delta x, y + \Delta y) + \phi(x - \Delta x, y - \Delta y) - \phi(x - \Delta x, y + \Delta y) - \phi(x + \Delta x, y - \Delta y)) / (4\Delta x \Delta y) \quad (4.27)$$

$$(\alpha)^+ = \max(\alpha, 0) \quad (4.28)$$

$$(\alpha)^- = \min(\alpha, 0) \quad (4.29)$$

The speed term involved in eq.(4.9) can take the following general form:

$$V(\mathbf{p}) = -\mathbf{A}(\mathbf{p}) \cdot \frac{\nabla \phi(\mathbf{p})}{\|\nabla \phi(\mathbf{p})\|} + P(\mathbf{p}) + C(\mathbf{p}) \operatorname{div} \left( \frac{\nabla \phi(\mathbf{p})}{\|\nabla \phi(\mathbf{p})\|} \right), \quad (4.30)$$

where  $\mathbf{A}(\mathbf{p})$  is a vector field and  $P(\mathbf{p})$  and  $C(\mathbf{p})$  are scalar fields.

Introducing the velocity (4.30) in eq.(4.9) yields the following general evolution equation:

$$\frac{\partial \phi}{\partial \tau} = \mathbf{A} \cdot \nabla \phi - P(\mathbf{p}) \|\nabla \phi\| - C(\mathbf{p}) \|\nabla \phi(\mathbf{p})\| \operatorname{div} \left( \frac{\nabla \phi(\mathbf{p})}{\|\nabla \phi(\mathbf{p})\|} \right). \quad (4.31)$$

The three term of the right hand side of eq.(4.31) correspond to a pure convection term, a propagation term and a regularization term based on mean curvature, respectively. Each of these terms are usually implemented using dedicated numerical methods.

#### Advection force:

This term tries to move the surface  $\phi$  in a given direction and allows thus to guide the level-set evolution. Its numerical implementation is performed using the following Upwind scheme

$$\mathbf{A} \cdot \nabla \phi = (A_x)^+ D_x^- \phi + (A_x)^- D_x^+ \phi + (A_y)^+ D_y^- \phi + (A_y)^- D_y^+ \phi, \quad (4.32)$$

where  $\mathbf{A} = (A_x, A_y)$ .

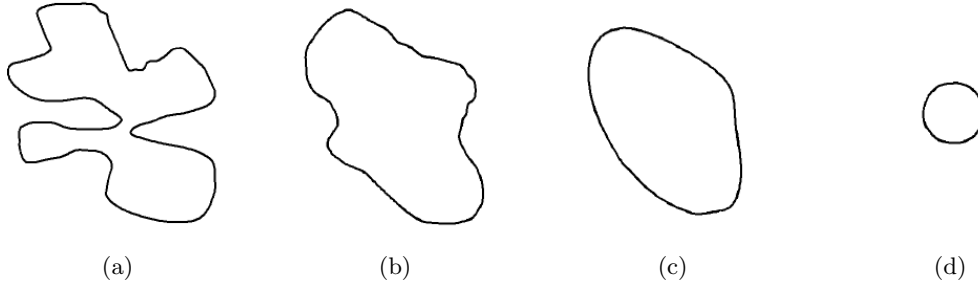


Figure 4.6: 4 successive steps of the evolution of the implicit function using only the curvature term.

### Propagation force:

This term depends on the region's characteristics of the object to be segmented. It acts as a pressure force that allows  $\phi$  to expand or contract until the target is reached. Its approximation using Upwind schemes writes

$$-P\|\nabla\phi\| = (-P)^+\Delta^-\phi + (-P)^-\Delta^+\phi, \quad (4.33)$$

with

$$\begin{cases} \Delta^+\phi = \sqrt{((D_x^-\phi)^+)^2 + ((D_x^+\phi)^-)^2 + ((D_y^-\phi)^+)^2 + ((D_y^+\phi)^-)^2} \\ \Delta^-\phi = \sqrt{((D_x^-\phi)^-)^2 + ((D_x^+\phi)^+)^2 + ((D_y^-\phi)^-)^2 + ((D_y^+\phi)^+)^2}. \end{cases} \quad (4.34)$$

### Regularization force:

This term is proportionnal to the curvature. It smoothes the surface  $\phi$  to avoid irregularities or discontinuities which might appear during the evolution. The effect of this term are shown in Fig. 4.6. Several approaches to compute the mean curvature exist [Deriche and Monga (1988)] but the one used the most frequently is based on the first and second derivatives of  $\phi$  ( $\phi_x$ ,  $\phi_y$ ,  $\phi_{xx}$ ,  $\phi_{yy}$ ,  $\phi_{xy}$ ). In 2D, the curvature can be expressed as

$$\kappa = \operatorname{div} \left( \frac{\nabla\phi}{\|\nabla\phi\|} \right) = \frac{\phi_{xx}\phi_y^2 - 2\phi_{xy}\phi_x\phi_y + \phi_{yy}\phi_x^2}{(\phi_x^2 + \phi_y^2)^{3/2}}. \quad (4.35)$$

Using this equation, we can deduce the the expression of the regularization term used in the level-set's evolution equation

$$C\|\nabla\phi\|\operatorname{div} \left( \frac{\nabla\phi}{\|\nabla\phi\|} \right) = C \frac{D_{xx}^0\phi(D_y^0\phi)^2 - 2D_{xy}^0\phi D_x^0\phi D_y^0\phi + D_{yy}^0\phi(D_x^0\phi)^2}{((D_x^0\phi)^2 + (D_y^0\phi)^2)^{1/2}}. \quad (4.36)$$

## 4.6.2 Choice of the involved implicit function and reinitialization

A classical problem encountered during the implementation of the schemes described in the previous section is the following: during its evolution, the level-set usually develops

very flat or steep fronts [Osher and Fedkiw (2002), Malladi *et al.* (1995)], which may lead to difficulties for the numerical estimation of the partial derivatives as well as for the convergence speed. A commonly adopted strategy to tackle this problem is the following:

1. The level-set is initialized as a signed distance function. Note that such a choice yields the interesting property that  $\|\nabla\phi(\mathbf{p})\| = 1, \forall \mathbf{p} \in \Omega$  meaning there are no steep or flat front.
2. During its evolution, the level-set is periodically reinitialized to keep a signed distance function.

A first way to implement such a strategy is to extract the contour's points (corresponding to the current zero-level) and to compute explicitly the corresponding signed distance map. However such a method requires a lot of computational time. Thus the usually chosen method to perform the reinitialization consists in taking advantage of the property of the gradient and to periodically apply to the level-set the following auxiliary evolution equation [Peng *et al.* (1999), Sussman *et al.* (1998)]:

$$\frac{\partial\phi_0}{\partial\tau}(\mathbf{p}, \tau) = \text{sign}(\phi_0(\mathbf{p}, \tau)) (1 - \|\nabla\phi_0(\mathbf{p}, \tau)\|), \quad (4.37)$$

where  $\phi_0$  is the function to reinitialize and  $\text{sign}(\cdot)$  is the sign function.

However if  $\phi_0$  is not smooth, the zero-level corresponding to the implicit function obtained from eq.(4.37) may not match the one of the original function. To tackle this problem, [Li *et al.* (2005)] recently proposed to add a term in the energy functional

$$E(\phi) = \int_{\Omega} \frac{1}{2} (\|\nabla\phi(\mathbf{p})\| - 1)^2 d\mathbf{p}. \quad (4.38)$$

This regularization term penalises the level-set if it differs too much from a signed distance map. This method thus allows to keep signed distance map's properties without having to explicitly reinitialize the level-set function.

Finally, we will note that, in order to have lower computational time, most of the implementations do not compute the evolution equation on the whole domain but only on a narrow band around the zero-level [Malladi *et al.* (1995)]. Unfortunately, this type of implementation has the drawback of making the algorithm more sensitive to the initialization.

## 4.7 Conclusion

Variational active contours are now a well established class of segmentation methods. Their principle is based on the minimization of an energy functional obtained either through a contour oriented formulation or a formulation using directly the level-set. The minimization is obtained from this energy through a gradient descent. The minimization process leads to a partial differential equation corresponding to the evolution equation of

the level-set. In this work, the use of such technique is interesting because it provides a general framework to embed a priori knowledge of the structures to be recovered, as it will be shown in the next chapters.





III Segmentation of the whole  
myocardium in echocardiographic images  
using level-set constrained with shape  
priors

---



---

---

## Résumé en français

---

Du fait de la faible qualité d'image, la segmentation de séquences échocardiographiques est un domaine de recherche très actif en particulier en ce qui concerne l'intégration d'information *a priori*. En effet, ces *a priori* rendent la segmentation plus robuste à des informations de bas niveau peu fiables dûes au bruit ou à une occlusion partielle de l'objet par exemple. Dans cette partie, nous faisons tout d'abord un état de l'art des techniques utilisant des *a priori* de formes. Nous proposons ensuite un nouveau modèle *a priori* pour représenter le myocarde. Enfin, nous décrivons comment inclure ce modèle dans un formalisme variationnel et présentons un algorithme de segmentation du myocarde complet en fin systole et en fin diastole quelle que soit la vue.

### État de l'art

#### Construction du modèle *a priori*

Avant de contraindre la segmentation par un *a priori* de forme, il faut tout d'abord choisir une manière de représenter la forme désirée. Cette représentation peut être obtenue de deux manières: soit par des considérations géométriques, soit par un apprentissage. Un modèle géométrique consiste à représenter la forme souhaitée par une fonction mathématique. L'adaptation de la forme à l'objet au cours du processus de segmentation est généralement réalisée au moyen d'une adaptation au sens des moindres carrés. Cette représentation présente plusieurs avantages. Elle ne nécessite aucune étape d'apprentissage et représente généralement la forme par un nombre restreint de paramètres  $\lambda$ . De plus aucun alignement n'est nécessaire entre la forme à représenter et le modèle puisque les paramètres de pose sont intrinsèques au modèle. En revanche, ce type de représentation suppose de définir une fonction mathématiques bien adaptée à la représentation de la forme souhaitée, ce qui n'est pas toujours évident pour des formes complexes. Parmi les modèles géométriques proposés dans la littérature, citons les ellipses [Taron *et al.* (2004), Alessandrini *et al.* (2011)], les super-ellipses [Gong *et al.* (2004), Saroul *et al.* (2008)] ou encore les hyperboles de degré 3 [Hamou and El-Sakka (2010)].

---

Une autre manière de représenter une forme est de le faire par apprentissage. Celui-ci nécessite de disposer d'un ensemble de formes de référence qui peuvent être soit des courbes [Chen *et al.* (2002)], des cartes de distance signées [Leventon *et al.* (2000)] ou un masque binaire [Rousson and Paragios (2002)]. Dans un premier temps, ces formes sont alignées de sorte à éliminer d'éventuelles variations dans les formes dues à des différences de pose (*i.e.* translation, rotation et échelle). La représentation des variations de forme issues de l'ensemble d'apprentissage est le plus souvent réalisée au moyen d'une analyse en composantes principales (ACP) [Leventon *et al.* (2000), Tsai and Osher (2003), Cremers and Soatto (2005), Bresson *et al.* (2006)] mais d'autres solutions ont été proposées comme l'utilisation du contour moyen [Chen *et al.* (2002), Chen *et al.* (2007)], d'une carte de probabilité [Rousson and Paragios (2002)] ou encore des moments [Foulonneau *et al.* (2006)].

## Segmentation par ensembles de niveaux contraints par *a priori* de forme

Une des premières approches pour intégrer la contrainte de forme dans une segmentation de type contour actif correspond aux modèles actifs de formes [Cootes *et al.* (1995)] et à la démarche similaire décrite par [Leventon *et al.* (2000)] pour des ensembles de niveaux et utilisent un *a priori* décrit au moyen d'une ACP. Dans ces 2 cas, l'approche n'est cependant pas variationnelle, puisque la contrainte de forme est dans ces 2 cas intégrée directement dans les termes d'évolution du contour actif.

D'autres approches expriment la contrainte de forme selon une approche variationnelle, ce qui implique la définition d'un terme d'énergie permettant d'évaluer une distance entre le contour actif courant et l'*a priori* de forme. Différentes énergies ont été proposées dans ce contexte, soit en calculant la différence des fonctions implicites représentant le contour actif et l'*a priori* de forme [Rousson and Paragios (2002)], soit en comparant les régions délimitées par les 2 contours [Chan and Zhu (2005)] ou encore en calculant la distance séparant les points du contour actif de l'*a priori* de forme [Chen *et al.* (2002), Bresson *et al.* (2006), Alessandrini *et al.* (2011)] de la manière suivante:

$$E(\phi, \psi) = \int_{\Omega} \psi^2(\mathbf{p}) \|\nabla \phi\| \delta(\phi(\mathbf{p})) d\mathbf{p}.$$

Dans cette expression,  $\phi$  est l'ensemble de niveaux,  $\psi$  l'*a priori* de forme et  $\delta(\cdot)$  est la distribution de Dirac permettant de sélectionner le niveau zéro de l'ensemble de niveaux. Cette énergie a l'avantage de ne pas comparer directement les 2 contours, ce qui permet de définir  $\psi$  comme une fonction implicite quelconque.

## Segmentation contrainte d'images échocardiographiques

Dans le cadre de la segmentation d'images échocardiographiques en vue apicale 4 chambres, [Lin *et al.* (2003)] a proposé un formalisme multi-échelle basé sur les ensembles de niveaux. L'image est tout d'abord segmentée en utilisant des informations de régions et

---

de contour à une faible résolution. Par la suite, le résultat obtenu à la faible résolution sert à la fois d'initialisation et de contrainte de forme à la résolution supérieure.

[Taron *et al.* (2004)] a proposé d'exprimer la fonction implicite directement comme une ellipse et de minimiser une énergie par rapport aux paramètres de cette représentation afin de segmenter l'endocarde en vue parasternale petit axe.

Enfin, [Carneiro *et al.* (2012)] a décrit une méthode de segmentation de l'endocarde en vue apicale 4 chambres basée sur les réseaux de neurones et 2 classifieurs: un rigide et un non rigide. Le classifieur rigide cherche tout d'abord la région où le cœur est présent et estime les paramètres de pose. Le classifieur non rigide est ensuite appliqué afin de détecter la position la plus probable du contour.

## Notre contribution: Modèle du myocarde indépendant de la vue

Notre première contribution est de proposer un modèle du myocarde suffisamment flexible pour pouvoir le représenter dans les quatre vues utilisées en routine clinique. Ce modèle est basé sur un modèle géométrique afin d'éviter d'avoir à effectuer un apprentissage. De plus, la plupart des modèles géométriques proposés ne permettant pas de représenter des formes asymétriques, nous proposons d'utiliser un nouveau modèle basé sur les hyperquadriques.

### Modélisation du myocarde complet par des hyperquadriques

Les hyperquadriques ont été proposées par [Hanson (1988), Han *et al.* (1993)] et sont définies dans le cas 2D comme suit

$$\varphi(\mathbf{p}) = \sum_{i=1}^{N_h} |A_i x + B_i y + C_i|^{\gamma_i},$$

où  $N_h$  correspond au nombre de termes et  $\boldsymbol{\lambda} = \{A_i, B_i, C_i, \gamma_i, \forall i = 1 \dots N_h\}$  est l'ensemble des paramètres à estimer. La forme correspond alors à l'ensemble des points  $\mathbf{p}$  tels que  $\varphi(\mathbf{p}) = 1$ , ce qui correspond au niveau zéro de la fonction implicite  $\Psi(\mathbf{p}, \boldsymbol{\lambda}) = \varphi(\mathbf{p}) - 1$ . On peut noter que, au niveau du contour, comme tous les termes sont positifs et que leur somme vaut 1 et que de plus  $\gamma_i > 0$ , on a  $|A_i x + B_i y + C_i| \leq 1 \forall i$ . Ainsi, chaque terme hyperquadrique décrit une paire de lignes bornant le contour et le contour final est donc englobé par un polygone. La figure 6.1 montre un exemple de représentation d'un nuage de points par une hyperquadrique ainsi que le polygone englobant. On peut noter que, pour  $N_h = 2$ , le contour obtenu est symétrique, ce qui n'est plus le cas pour des valeurs plus élevées de  $N_h$ .

Bien que la fonction  $\varphi$  puisse être utilisée comme mesure d'erreur lors de l'estimation des paramètres des hyperquadriques, cette solution présente l'inconvénient d'avoir de nombreux minima globaux et locaux correspondant à des solutions dégénérées. De ce fait, [Ku-

mar *et al.* (1995)] a proposé d'ajouter des contraintes sur la distance entre les paires de lignes englobantes de sorte à ce qu'elle soit liée aux dimensions minimum et maximum de l'objet à représenter. Ces contraintes sont ensuite exprimées comme des fonctions de pénalités et ajoutées à la mesure d'erreur initiale. La minimisation de la nouvelle mesure d'erreur se fait par la méthode d'optimisation non linéaire de Levenberg-Marquardt [Press *et al.* (1992)].

On propose de modéliser chaque interface du myocarde (*i.e.* l'endocarde et l'épicarde) par une hyperquadrique et on cherche donc une représentation permettant d'intégrer ces 2 contours dans une seule fonction implicite. Cette représentation doit de plus permettre de résoudre efficacement le problème d'estimation lié à la mise à jour des paramètres au cours de la segmentation. En nous appuyant sur les travaux de [Berg (1998)], l'*a priori* de forme est défini de la manière suivante

$$\psi(\mathbf{p}, \boldsymbol{\lambda}) = \max(\Psi(\mathbf{p}, \boldsymbol{\lambda}_{out}), -\Psi(\mathbf{p}, \boldsymbol{\lambda}_{in})),$$

où  $\boldsymbol{\lambda} = [\boldsymbol{\lambda}_{in}, \boldsymbol{\lambda}_{out}]$  et  $\boldsymbol{\lambda}_{in}$  et  $\boldsymbol{\lambda}_{out}$  correspondent aux paramètres de l'hyperquadrique intérieure et extérieure respectivement. Une illustration de la fonction  $\psi$  est donnée en figure 6.2.

## Énergie d'*a priori* de forme

En nous basant sur les travaux de [Caselles *et al.* (1997), Chen *et al.* (2002)], nous proposons de contraindre l'évolution de l'ensemble de niveaux en minimisant l'énergie d'*a priori* de forme suivante

$$E_{shape}(\phi, \boldsymbol{\lambda}) = \int_{\Omega} \psi^2(\mathbf{p}, \boldsymbol{\lambda}) \cdot \|\nabla\phi(\mathbf{p})\| \cdot \delta(\phi(\mathbf{p})) d\mathbf{p}.$$

Cette expression peut s'interpréter comme la recherche d'une géodésique dans un espace riemannien dérivant de l'*a priori*, à savoir  $\psi^2(\mathbf{p})$  et est minimale lorsque le niveau zéro de l'ensemble de niveaux correspond exactement à celui de  $\psi$ . La minimisation de cette contrainte se fait en deux temps. Tout d'abord, on suppose  $\boldsymbol{\lambda}$  constant et on fait évoluer l'ensemble de niveaux  $\phi$  selon le terme d'évolution suivant:

$$\frac{\partial\phi}{\partial\tau}(\mathbf{p}) = \delta(\phi(\mathbf{p})) \cdot \left( \frac{\langle \nabla\psi(\mathbf{p}, \boldsymbol{\lambda}), \nabla\phi(\mathbf{p}) \rangle}{\|\nabla\phi(\mathbf{p})\|} + \psi^2(\mathbf{p}, \boldsymbol{\lambda}) \cdot \kappa \right),$$

où  $\kappa$  correspond à la courbure et  $\langle \cdot, \cdot \rangle$  au produit scalaire.

Dans un second temps, en considérant  $\phi$  fixe et comme on réinitialise l'ensemble de niveaux en carte de distance à chaque itération, la minimisation par rapport à  $\boldsymbol{\lambda}$  peut s'écrire en discret:

$$\boldsymbol{\lambda} = \arg \min_{\boldsymbol{\lambda}'} \sum_{\mathbf{p} \in \Gamma} \psi^2(\mathbf{p}, \boldsymbol{\lambda}').$$

On montre que la minimisation de cette équation est équivalente à l'adaptation séparée

---

de deux hyperquadriques au sens des moindres carrés. L'algorithme d'estimation des paramètres de la contrainte de forme est résumé dans l'Alg. 1.

## Validation du modèle

Pour évaluer la capacité de notre modèle à représenter les formes myocardiques, nous avons réalisé l'adaptation des hyperquadriques décrite ci-dessus sur des contours myocardiques de référence tracés par des cardiologues et comparé la distance entre l'hyperquadrique obtenue et la référence. Dans ce but, trois cardiologues ont manuellement segmenté le myocarde dans 80 images réparties sur les 4 vues principales en échocardiographie. Pour chaque image, un contour moyen est calculé à partir des références des experts [Chalana and Kim (1997)] et notre modèle est estimé séparément sur l'endocarde et l'épicarde. On propose d'évaluer l'influence du nombre de termes hyperquadriques  $N_h$  en comparant les résultats pour  $N_h = 4$  ou 6. Notre modèle est aussi comparé à deux autres modèles géométriques: une ellipse [Taron *et al.* (2004), Alessandrini *et al.* (2011)] et les hyperboles de degré 3 [Hamou and El-Sakka (2010)].

Les résultats obtenus sont résumés dans les Tableaux 6.2 et 6.1 et des exemples de résultats d'estimation pour les différents modèles sont donnés en figure 6.5. On constate que les hyperquadriques avec  $N_h = 4$  sont capables de modéliser avec une bonne précision les contours de l'endocarde et de l'épicarde et ce quelle que soit la vue (par exemple, le MAD est inférieur à 0.2mm pour l'endocarde pour les deux vues parasternales). On observe aussi que l'ajout de termes hyperquadriques modifie peu les résultats. En effet, soit les mesures d'erreur pour les deux valeurs de  $N_h$  sont proches, soit les hyperquadriques avec  $N_h = 4$  produisent de meilleurs résultats et la différence est statistiquement significative. Comparé aux autres modèles géométriques, les hyperquadriques avec  $N_h = 4$  donnent toujours de meilleurs résultats et les différences observées sont statistiquement significatives excepté pour l'endocarde dans les vues apicales.

Pour la segmentation contrainte du myocarde, nous utiliserons donc notre modèle d'hyperquadriques avec  $N_h = 4$  ce qui correspond à un bon compromis entre la précision de l'estimation et le temps de calcul nécessaire à l'estimation.

## Notre contribution: Segmentation du myocarde dans des images échocardiographiques 2D et dans toutes les vues

### Formulation énergétique

Notre seconde contribution est de proposer un algorithme basé sur les ensembles de niveaux contraints par *a priori* de forme afin de segmenter le myocarde dans des images échocardiographiques. La plupart des travaux traitant de la segmentation contrainte par *a priori* de forme minimisent une énergie définie comme la somme de deux termes: un terme d'attache aux données et un terme de contrainte [Leventon *et al.* (2000), Chen *et al.*



---

(2002)]. Dans notre cas, comme nous nous intéressons à la segmentation simultanée de l'endocarde et de l'épicarde, nous ajoutons un terme évitant la fusion des deux contours. L'énergie utilisée prend donc la forme générale suivante:

$$E = E_{data} + E_{shape} + E_{thickness},$$

où  $E_{data}$  est un terme d'attache aux données,  $E_{shape}$  le terme de contrainte décrit précédemment et  $E_{thickness}$  un terme empêchant la fusion des contours en imposant une épaisseur minimale.

### Terme d'attache aux données

Les images échocardiographiques présentent fréquemment des inhomogénéités le long du myocarde (*cf.* Fig. 7.1). [Lankton and Tannenbaum (2008)] ont récemment proposé un formalisme général permettant de localiser un terme d'attache aux données afin de gérer ces variations d'intensité. Dans ce formalisme, le terme d'attache aux données s'écrit:

$$E_{data}(\phi) = \int_{\Omega} \delta(\phi(\mathbf{p})) \int_{\Omega} B(\mathbf{p}, \mathbf{q}) F(I, \phi, \mathbf{q}) d\mathbf{q} d\mathbf{p},$$

où  $F(I, \phi, \mathbf{q}) = H(\phi(\mathbf{q})) \cdot (I(\mathbf{q}) - u_x)^2 + (1 - H(\phi(\mathbf{q}))) \cdot (I(\mathbf{q}) - v_x)^2$  est le terme de [Chan and Vese (2001)] et  $\delta(\cdot)$  la distribution de Dirac. La fonction  $B(\cdot)$  est un masque binaire défini comme suit

$$B(\mathbf{p}, \mathbf{q}) = \begin{cases} 1, & \text{si } \mathbf{q} \in N(\mathbf{p}) \\ 0, & \text{sinon} \end{cases}$$

où  $\mathbf{q}$  est un point de  $\Omega$  et  $N(\mathbf{p})$  correspond à un voisinage du point  $\mathbf{p}$ .  $u_x$  et  $v_x$  correspondent aux moyennes intérieure et extérieure mesurées localement dans la fenêtre  $N(\mathbf{p})$ .

### Terme d'épaisseur

Comme nous souhaitons segmenter l'ensemble du myocarde avec un seul ensemble de niveaux, il peut arriver que les contours de l'endocarde et de l'épicarde évoluent vers une même caractéristique de l'image, ce qui peut conduire à la fusion des deux contours. Il est donc important d'empêcher cette fusion puisqu'elle conduit à des résultats incorrects. Dans le même temps, il faut aussi s'assurer que la solution retenue n'affectera pas la segmentation dans les zones où il n'y a pas de risques de fusion. Nous proposons donc un nouveau terme d'épaisseur agissant localement sur le contour et uniquement si la distance entre les contours intérieur et extérieur est inférieure à une distance prédéfinie  $R_T$ . Ce terme s'écrit de la façon suivante:

$$E_{thickness}(\phi) = \int_{\Omega} \phi(\mathbf{p} + R_T \mathbf{N}) \cdot H(\phi(\mathbf{p} + R_T \mathbf{N})) \cdot \delta(\phi(\mathbf{p})) d\mathbf{p},$$

où  $\mathbf{N}$  correspond à la normale intérieure à un point  $\mathbf{p} \in \Gamma$ . Cette énergie est nulle lorsque tous les points à une distance  $R_T$  suivant la normale intérieure au contour sont des points

---

intérieurs. Le principe de ce terme est illustré en Fig. 7.2 et un exemple de segmentation avec et sans ce terme d'épaisseur sur une image de simulation est donné en Fig. 7.3.

## Implémentation

### Région d'intérêt

Dans les vues parasternale grand-axe et apicales, l'endocarde et l'épicarde ne correspondent pas à des contours fermés et une partie du myocarde peut être en dehors du champ imagé. On définit donc trois régions en fonction de la présence ou non du myocarde comme suit: présence possible du myocarde dans le secteur imagé (zone 1 de Fig. 7.4), présence possible du myocarde hors du secteur imagé (zone 2 de Fig. 7.4) et absence du myocarde (zone 3 de Fig. 7.4). En fonction de la zone, tous les termes d'évolution (zone 1) ou seuls les termes de forme et d'épaisseur (zone 2) sont utilisés. Pour définir ces trois zones, on demande à l'utilisateur de placer deux points correspondant à la position des valves. Enfin, notons que pour les images parasternales petit-axe, l'utilisateur n'a pas à placer ces points puisque la zone 3 n'est pas utilisée.

### Initialisation

L'utilisation d'un terme localisé d'attache aux données nécessite une initialisation assez proche du résultat souhaité. Nous utilisons donc la procédure suivante pour initialiser notre algorithme. L'utilisateur place cinq points près de l'épicarde et un point sur l'endocarde. À partir des cinq premiers points, une ellipse est estimée et le dernier point permet d'estimer une 2<sup>ème</sup> ellipse concentrique.

## Résultats

La base de données utilisée pour évaluer les performances de notre algorithme de segmentation est la même que celle ayant servi à la validation du modèle *a priori*. La qualité de la segmentation est évaluée au travers de trois mesures de distances entre le contour de référence et le contour fourni par la segmentation: le critère de Dice, la distance absolue moyenne (MAD) et la distance de Hausdorff (HD). Les tableaux 7.1 et 7.2 donnent les valeurs moyennes et les écarts-types obtenus par notre algorithme (3 colonnes centrales), les distances inter-observateur (IOD, 3 colonnes de gauche) et une autre méthode proposée récemment et proche de l'approche décrite ici [Hamou and El-Sakka (2010)] (3 colonnes de droite). Les figures 7.8 et 7.9 montrent des résultats de segmentation pour chaque vue en fin diastole et en fin systole respectivement.

On observe que pour les vues parasternales, les résultats obtenus pour l'endocarde et l'épicarde sont proches de la variabilité inter-observateur voire meilleurs. Par exemple pour la vue parasternale petit-axe, les MAD obtenus par notre méthode sont de 1.07mm et 1.25mm pour l'épicarde et l'endocarde respectivement, alors qu'ils sont de 1.41mm et 1.46mm pour l'IOD. On constate cependant que les résultats sont meilleurs pour l'épicarde que pour l'endocarde car la segmentation de l'endocarde nécessite d'exclure les muscles

---

papillaires. Cependant la même observation peut être faite pour les valeurs de l'IOD traduisant un comportement similaire.

Concernant les vues apicales, on observe que les valeurs d'erreur augmentent par rapport à celles obtenues en parasternal. Ceci s'explique par la qualité d'image qui est généralement moins bonne dans les vues apicales, où l'apex est flou car dans la zone de champ proche et où une partie de la paroi latérale est souvent manquante. Là encore, on peut noter que l'IOD augmente aussi comparativement aux vues parasternales traduisant cette difficulté à segmenter le myocarde dans ces vues.

Enfin, comparés aux résultats de l'algorithme proposé par [Hamou and El-Sakka (2010)], nos résultats sont généralement 25% meilleurs, ce qui correspond à une diminution du MAD d'environ 0.5mm et de la distance de Hausdorff de 1.5mm. Ceci peut être expliqué par le fait que notre modèle *a priori* est plus adapté aux formes cardiaques que celui proposé par [Hamou and El-Sakka (2010)] (basé sur les hyperboles de degré 3) comme il a été montré dans le chapitre 6.

---

# Active contours based on shape prior constraints

---

Due to low image quality, segmentation of echocardiographic sequences has been a field of active research in the domain of incorporation of prior information. Indeed this was shown to make the segmentation process robust to misleading low-level information caused by noise, background clutter or partial occlusion of the object of interest. In this chapter, we give an overview of the different way of incorporating shape prior information to constrain the evolution of active contour models. We first describe how the shape model is built either through geometrical consideration or through learning. The two next sections detail approaches specifically dedicated to echocardiographic image sequences and methods which incorporate constraints into a variational active contour framework.

### 5.1 Shape model

Before being able to constraint the segmentation using a shape prior, one must first think of how to represent the desired shape. Building a shape model can be done using either geometrical consideration of the target object or through learning. These two approaches are described in the next sections.

#### 5.1.1 Geometric shape model

A geometric shape model represents the object using mathematical functions. The advantage of geometric prior is that it does not involve a training step and usually rep-

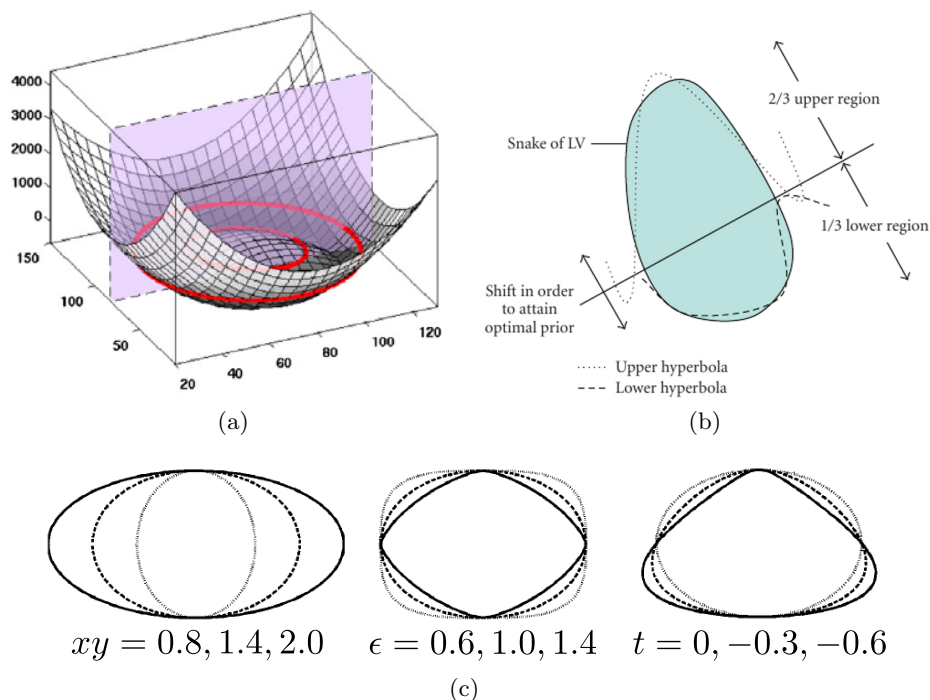


Figure 5.1: Example of geometric priors: (a) annular prior (from [Alessandrini *et al.* (2011)]); (b) 3<sup>rd</sup> order hyperbola (from [Hamou and El-Sakka (2010)]) and (c) superellipses (from [Gong *et al.* (2004)]).

resents the prior with a small number of parameters  $\lambda$ . Another advantage is that no alignment step is required (in opposition to learned templates) since the pose parameters are included in the model parameters. Finally, if the shape prior energy is well chosen, the estimation problem often leads to a simple least square fitting of the model on range data as in [Alessandrini *et al.* (2011), Hamou and El-Sakka (2010)]. The drawback of this representation is that one has to know a geometrical function allowing to represent the targetted object along with its variability. As a consequence, the representation of complex shapes often requires model with a high number of parameters which may lead to high computational cost for the fitting problem.

In [Alessandrini *et al.* (2011)], the authors propose to constrain the segmentation of annular-like objects using two ellipses one inside the other. The model can be represented using 10 parameters  $\lambda = \{Xc_{(i)}, Yc_{(i)}, a_{(i)}, b_{(i)}, \theta_{(i)}, Xc_{(o)}, Yc_{(o)}, a_{(o)}, b_{(o)}, \theta_{(o)}\}$ , where  $(Xc_{(\cdot)}, Yc_{(\cdot)})$  is the center of the inner ( $i$ ) or outer ( $o$ ) ellipse,  $a_{(\cdot)}$  and  $b_{(\cdot)}$  its radii and  $\theta_{(\cdot)}$  its orientation. This model was applied to several real objects (such as the eye, the rings of Saturn) and then validated on the segmentation of the whole myocardium in short-axis view in MRI or in parasternal short-axis view in echocardiography. An example of the shape representation is given in Fig. 5.1(a).

Superellipse has been proposed to model the prostate in echographic scans in [Gong *et al.* (2004), Saroul *et al.* (2008)]. This geometric function corresponds to a generalization of ellipses and can model a large variety of natural shapes, including ellipse, rectangles, parallelograms and pinched diamonds, by changing a small number of parameters. In

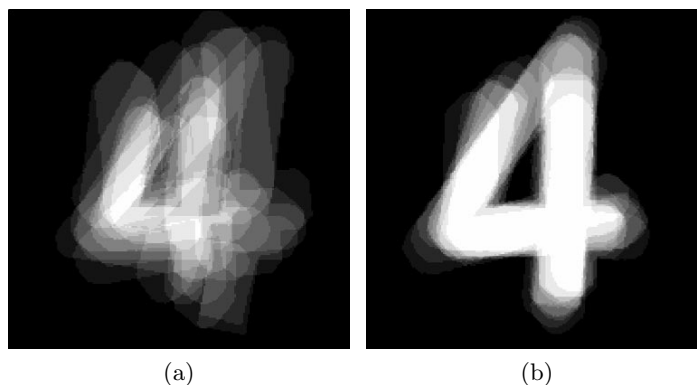


Figure 5.2: Example of a realignment step: Amount of shape overlap in the “four” database (a) before alignment and (b) after alignment (from [Tsai *et al.* (2003)]).

in addition to the 5 parameters of an ellipse, superellipses are also parameterized by their squareness  $\epsilon$  and tapering  $t$ , yielding  $\lambda = \{Xc, Yc, a, b, \theta, \epsilon, t\}$ . Example of superellipses and the effect of some parameters are shown in Fig. 5.1(c) where  $xy = a/b$  is the aspect ratio.

[Hamou and El-Sakka (2010)] suggested to use two 3<sup>rd</sup> order hyperbola, one fitted on the 2/3 upper part of the evolving contour and the other one on the 1/3 lower part as a shape prior in their snake based segmentation algorithm. This shape prior was then applied to the segmentation of the endocardium in apical 4-chamber views in echocardiographic images. The parametric model used is shown in Fig. 5.1(b).

### 5.1.2 Learned templates

Another way of building a shape prior is through learning. In that case, example shapes which corresponds to different representation of the target object are provided. Let  $\Psi = \{\psi_1, \psi_2, \dots, \psi_N\}$  be the set of these shapes. Different representation have been proposed for  $\psi_i$  such as a curve [Chen *et al.* (2002), Chen *et al.* (2007)], a signed distance function [Leventon *et al.* (2000), Chan and Zhu (2005), Bresson *et al.* (2006)] or a binary mask [Rousson and Paragios (2002), Lynch *et al.* (2006), Foulonneau *et al.* (2006)].

A realignment step of the set of shapes  $\Psi$  is generally required to remove any variations in shape due to pose differences (*i.e.* translation, rotation or scaling). Matching geometric shapes is an open and complex issue in computer vision and we refer the interested reader to the review paper of [Zhang and Lu (2004)] for more details on shape-matching algorithms. An example of realignment is shown in Fig. 5.2.

Once the shapes are aligned, one may learn its prior using different techniques:

**Principal Component Analysis (PCA)** has been widely used to learn shape model and aims at capturing the main variations of a training set while removing redundant information [Leventon *et al.* (2000), Tsai *et al.* (2003), Chan and Zhu (2005), Cremers *et al.* (2006), Bresson *et al.* (2006)]. [Cootes and Taylor (1999)] have used this technique on parametric contours to segment different kind of objects. In [Leventon *et al.* (2000)],

the authors applied the PCA not on the parametric geometric contours but on the signed distance functions of these contours.

More formally, a mean shape  $\mu$  is first computed by taking the mean of the shapes,  $\mu = \frac{1}{N} \sum_{i=1}^N \psi_i$ .  $\mu$  is then subtracted from each  $\psi_i$  to create a mean-offset map  $\hat{\psi}_i$ . Each such map  $\hat{\psi}_i$  is placed as a column vector in a matrix  $M$ . Using Singular Value Decomposition (SVD), the covariance matrix  $\frac{1}{N}MM^T$  is decomposed as:

$$U\Sigma U^T = \frac{1}{N}MM^T \quad (5.1)$$

where  $U$  is a matrix whose column vectors represent the set of orthogonal modes of shape variation and  $\Sigma$  is a diagonal matrix of corresponding singular values.

An estimate of a novel shape  $\psi$  of the same class of object can be represented by  $k$  principal components in a  $k$ -dimensional vector of coefficients  $\alpha = U_k^T(\psi - \mu)$ , where  $U_k$  is a matrix consisting of the  $k$  first columns of  $U$  that is used to project a surface into the eigen-space. Given the coefficients  $\alpha$ , an estimate of the shape  $\psi$ , namely  $\tilde{\psi}$ , is reconstructed from  $U_k$  and  $\mu$ :

$$\tilde{\psi} = \mu + \alpha U_k. \quad (5.2)$$

**Mean curve** can be seen as doing PCA with  $k = 0$  that is considering only  $\mu$ . It was proposed by [Chen *et al.* (2002)] who then extended this representation in [Chen *et al.* (2007)] to also include the intensity profile along the mean curve. A drawback of this representation is that the shape is more constrained than when using PCA since variations along the principal components are forbidden. However the computational cost is also lower since the coefficients  $\alpha$  do not have to be estimated after the realignment step.

**Probabilistic maps** were used by [Rousson and Paragios (2002)] to model the shape image  $\psi_M$  as well as local degrees of shape deformations  $\sigma_M$ . A Gaussian density at each pixel  $\mathbf{p}$  describes the shape model as:

$$p^M(\psi, \mathbf{p}) = \frac{1}{\sqrt{2\pi}\sigma_M(\mathbf{p})} \exp\left(-\frac{(\psi(\mathbf{p}) - \psi_M(\mathbf{p}))^2}{2\sigma_M^2(\mathbf{p})}\right). \quad (5.3)$$

The estimation of  $\psi_M$  and  $\sigma_M$  is then performed through a variational framework by seeking for the maximum likelihood of the local densities with respect to these parameters:

$$E(\psi_M, \sigma_M) = -\nu \sum_{i=1}^N \int_{\Omega} \log(p^M(\psi, \mathbf{p})) d\mathbf{p} + (1 - \nu) \int_{\Omega} \|\nabla \sigma_M(\mathbf{p})\|^2 d\mathbf{p}, \quad (5.4)$$

where the first term can be seen as a data attachment term that aims at recovering a representation that best accounts for the training samples and the second one as a regularization term enforcing the local variations  $\sigma_M$  to vary smoothly.  $\nu$  is a blending parameter between the two energy terms.

**Moments** have been used recently in [Foulonneau *et al.* (2006)] to represent the learned shape. Indeed, any shape discretized on a sufficiently fine grid, may be reconstructed from

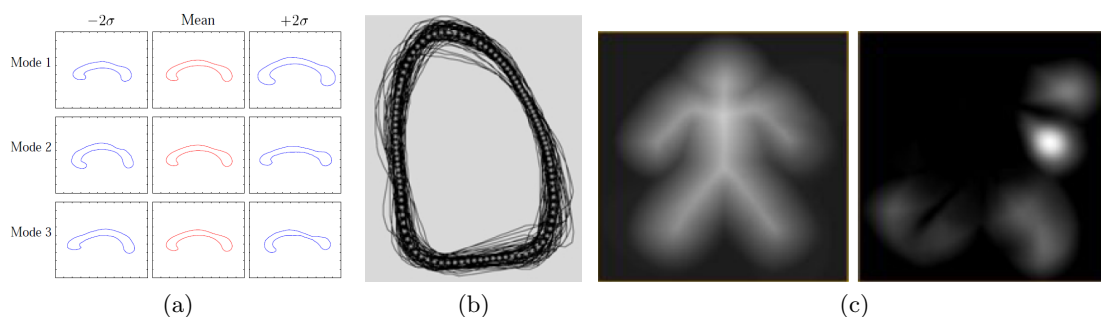


Figure 5.3: Example of learned priors: (a) PCA, the mean curve and the 3 principal modes of variation are shown (from [Leventon *et al.* (2000)]); (b) the aligned curves as well as the mean curve (from [Chen *et al.* (2002)] and (c) the probabilistic map and shape variability (from [Rousson and Paragios (2002)]).

its infinite set of moments though in practice only a limited number of moments are computed. Considering that  $\Omega_{in}$  corresponds to the inner region of  $\psi_i$ , the geometric moments  $M_{u,v}$  of  $\psi_i$  are given by

$$M_{u,v} = \int \int_{\Omega_{in}} x^u y^v dx dy, \quad (5.5)$$

where  $(u, v) \in \mathbb{N}^2$  and  $(u + v)$  is called the order of the moment. To avoid the alignment step, [Foulonneau *et al.* (2006)] proposed to describe the shape with Legendre moments  $\lambda_{p,q}$  since they are invariant by affine transformation (*i.e.* translation, scaling and rotation):

$$\lambda_{p,q} = C_{pq} \int \int_{\Omega_{in}} P_p(x) P_q(y) dx dy, \quad (x, y) \in [-1, 1] \times [-1, 1], \quad (5.6)$$

where the normalizing constant is:  $C_{pq} = (2p + 1)(2q + 1)/4$  and

$$P_p(x) = \sum_{k=0}^p a_{pk} x^k = \frac{1}{2^p p!} \frac{d^p}{dx^p} (x^2 - 1)^p, \quad x \in [-1, 1]. \quad (5.7)$$

## 5.2 Variational segmentation with shape prior

[Cootes *et al.* (1995)] proposed a method known as Active Shape Model (ASM) for the segmentation of specific objects whose shape properties have been previously learned from a training dataset using Principal Component Analysis technique (PCA). The database is composed of a set of shape manually drawn by a specialist, each shape being represented by a set of points. The approach is based on the computation of a Point Distribution Model. This model gives the average position of the points and the PCA provides a number of parameters which control the main modes of shape variation found in the training set. The method consists in finding the parameter values which give the best fit of the model to the processed image using feature matching techniques (such as border detection). The final result allows to extract an object in the image whose shape can be described in the model



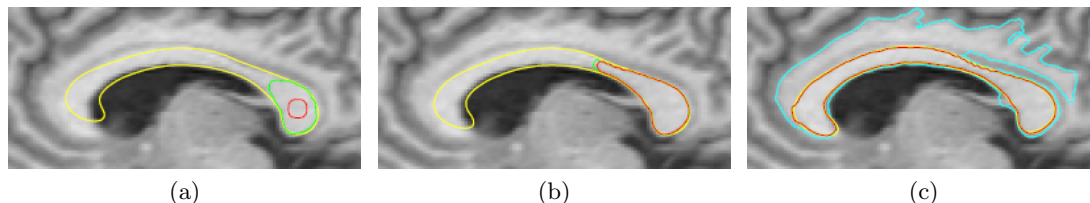


Figure 5.4: Three steps in the segmentation of a corpus callosum. The red curve is the zero level-set of  $\phi$ . The green curve is the next step in the curve evolution. The yellow curve is the MAP estimate of the shape prior. In (c), the cyan contour corresponds to the segmentation result without prior knowledge (from [Leventon *et al.* (2000)]).

space. The authors applied their method for the detection of the left ventricle cavity in apical four chambers views.

[Leventon *et al.* (2000)] were the first to couple a data attachment term and a shape prior in the evolution equation of a level-set. The shape prior was built using PCA on the signed distance function of the references shape. Note that this approach is not variational since the shape prior evolution term does not come from the minimization of an energy. The complete evolution term is given by

$$\frac{\partial \phi}{\partial \tau} = \lambda_1 [g(c + \kappa) \|\nabla \phi\| + \nabla \phi \cdot \nabla g] + \lambda_2 (\psi - \phi), \quad (5.8)$$

where  $\phi$  corresponds to the evolving level-set,  $g$  is a positive decreasing function,  $c$  is a positive constant acting as a balloon force,  $\lambda_1$  and  $\lambda_2$  are two hyperparameters and  $\psi$  is the shape prior. The first term in the righthand side of (5.8) corresponds to the classical geodesic active contour term from [Caselles *et al.* (1997)]. The second term drives the active contour  $\phi$  in the direction of shape prior. After each iteration, the shape prior parameters (its pose and the PCA coefficients  $\alpha$ ) relative to the evolving contour  $\phi$  are estimated through a maximum *a posteriori* framework. This method was successfully applied on both simulated and real medical 2D and 3D data.

Fig. 5.4 shows the result they obtained on a corpus callosum image. For this particular example their training set was composed by 49 examples. The red curve is the zero level-set of the evolving surface  $\phi$ . The green curve is the next step in the curve evolution. The yellow curve is the MAP estimate of the shape prior. The final segmentations with (red curve) and without (cyan) prior knowledge are shown in the last frame.

[Tsai *et al.* (2003)] use the PCA-based shape prior proposed by [Leventon *et al.* (2000)] and propose to perform constrained segmentation in the shape space derived from the training set. In this framework, a shape is represented through the set of parameter  $\{\alpha, \mathbf{v}_p\}$ , where:

- the shape vector  $\alpha$  provides the coordinates of the shape in the shape space derived from the training set.
- the pose vector  $\mathbf{v}_p$  provides the pose of the shape (*i.e.* translation, rotation and scale);

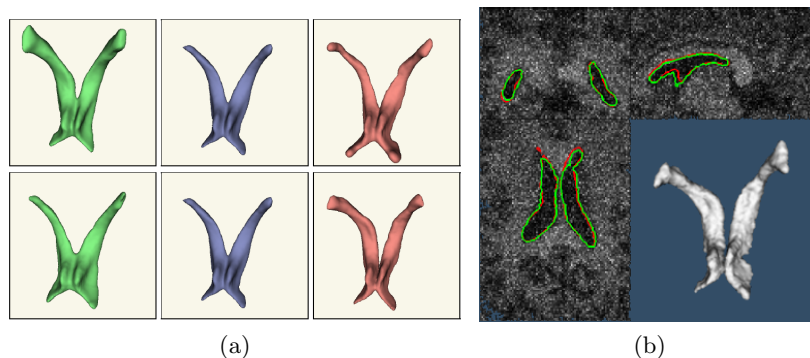


Figure 5.5: (a) Shape model with the most important shape of variations. (b) Segmentation of lateral brain ventricles with shape prior. Green: segmentation result, red: shape prior (from [Rousson *et al.* (2004)]).

The constrained segmentation phase then consists in minimizing an image-based functional in this parameter space. In [Tsai *et al.* (2003)], the authors use either the Chan and Vese region-based functional [Chan and Vese (2001)] or the mean model [Yezzi *et al.* (1997)]. The two parameter vectors  $\{\alpha, \mathbf{v}_p\}$  that optimized the proposed functional are calculated using a gradient descent method. The method has been applied for the segmentation of simulated data and MRI data of the heart and prostate.

In order to ensure the existence of a global minima, variational approaches have been developed where the constraint is directly expressed on the level-set function. To do so, the minimized energy becomes the sum of two terms: a data attachment term and a shape prior one that writes:

$$E(\phi, \psi) = \int_{\Omega} (\phi(\mathbf{p}) - \psi(\mathbf{p}))^2 d\mathbf{p}. \quad (5.9)$$

where  $\phi$  is the level-set and  $\psi$  corresponds to the shape prior, both functions being represented implicitly as signed distance functions. After each evolution iteration, the parameters of the prior (*e.g.* the PCA coefficients  $\alpha, \lambda$  for geometric priors) are re-estimated. For learned priors, the prior and the curve are also aligned in order to estimate the pose parameters (translation, rotation and scaling). This alignment step is often performed by minimizing (5.9) with respect to each pose parameter while keeping  $\phi$  fixed.

The energy formulation (5.9) has initially been proposed by [Paragios *et al.* (2002), Rousson and Paragios (2002)] who describe their prior using probabilistic maps and applied it on synthetic data and real images as well as medical images (in [Rousson *et al.* (2004)], Fig. 5.5). [Cremers *et al.* (2003)] added a label term to this approach allowing to restrict the effect of the shape prior to a subdomain  $\Omega_L \in \Omega$ . In [Cremers *et al.* (2006)], the label term was further extended for the simultaneous segmentation of objects using multiple shape priors.

The shape prior energy given by equation (5.9) has several drawbacks. Since this term relies on the square difference between  $\phi$  and  $\psi$ , it implies that both functions correspond to the same distance measure with respect to the zero level, in order the comparison to hold. To maintain this property, one need to re-initialize as a signed distance function the

level-set function  $\phi$  on its whole definition domain  $\Omega$  during its evolution. Moreover this formulation restricts the type of prior that can be used. Indeed since the weighted sum of signed distance function does not necessarily corresponds to a signed distance function, one has to ensure that a prior obtained through PCA keeps distance properties. This also holds for geometric priors where the shape is usually represented using the algebraic distance. As shown in [Sampson (1982), Harker and O’Leary (2006)], if we denote by  $\psi_a$  the algebraic distance to the contour then  $\psi_e = \frac{\psi_a}{\|\nabla\psi_a\|}$  corresponds to the first order approximation of the euclidian distance which only holds near the zero-level of  $\psi_a$ .

To overcome these problems, [Chan and Zhu (2005)] proposed the following shape prior energy

$$E(\phi, \psi) = \int_{\Omega} (H(\phi(\mathbf{p})) - H(\psi(\mathbf{p})))^2 d\mathbf{p}. \quad (5.10)$$

where  $H$  is the Heaviside function which allows to use any representation for both  $\phi$  and  $\psi$ . Note that in the initial work of [Chan and Zhu (2005)], a label term similar to the one used by [Cremers *et al.* (2003)] is also included in the energy term to restrict the influence of the prior on a subdomain of  $\Omega$ . This approach has been applied to real images where the targetted object presented occlusions.

Another way to overcome these distance problems has been proposed in [Chen *et al.* (2002)], where the prior term corresponds to the distance between points of the active contour and the shape prior. In the level-set formalism, this yield the following energy:

$$E(\phi, \psi) = \int_{\Omega} \delta(\phi(\mathbf{p})) \psi^2(\mathbf{p}) \|\nabla\phi\| d\mathbf{p}. \quad (5.11)$$

Since the two functions  $\phi$  and  $\psi$  are not directly compared,  $\psi$  can be defined as any distance, thus the possible prior representation are not restricted.

In [Chen *et al.* (2002)], the shape prior  $\psi$  is represented as the mean curve of  $\Psi$  and is defined as

$$\psi(\mathbf{p}) = d(\mu R\mathbf{p} + T, C^*), \quad (5.12)$$

where  $d$  corresponds to the euclidian distance between a point  $\mathbf{p}$  to the mean curve  $C^*$ .  $\mu$ ,  $R$  and  $T$  are the pose parameters (scaling, rotation and translation respectively) used to align the zero level of  $\phi$  with the prior  $\psi$ . As for (5.9), this formulation also allows to estimate the pose parameters by minimizing (5.11).

This method was applied to simulated data, the segmentation of the epicardium in 2D echocardiographic images acquired in apical 4-chamber view and to the segmentation of the corpus callosum in MRI. It has been extended in [Chen *et al.* (2007)] where multiple segmentations with different weighting of the shape prior term were run. The intensity profile along the segmentation result was then compared to a learned intensity profile in order to choose the best weighting parameter and thus the best contour. The method was applied to apical 2-chamber scans and two segmentation results as well as the shape prior obtained from 12 training images can be seen in Fig. 5.6.

The same energy was used by [Bresson *et al.* (2006)] and [Alessandrini *et al.* (2011)].

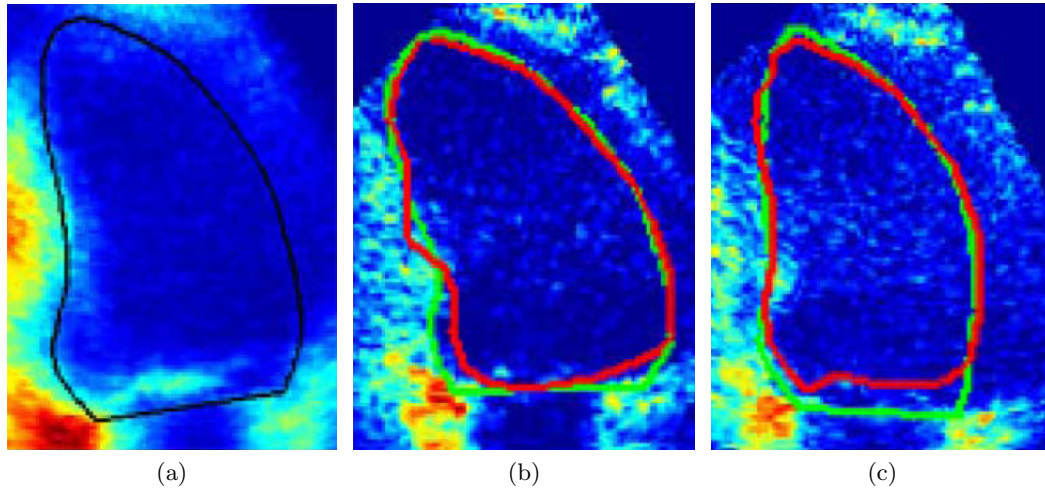


Figure 5.6: (a) Average endocardium with associated intensity profiles generated from the training shapes and images. (b) and (c) Segmentation result (solid, red) compared with the expert's borders (dotted, green). Note that all figures are reproduced from [Chen *et al.* (2007)].

In [Bresson *et al.* (2006)], instead of using the mean curve, the authors built their prior using PCA on the signed distance allowing them to represent  $\psi$  implicitly. The energy (5.11) was coupled with a data attachment term containing both boundary and region information to segment synthetic data and the left brain ventricle in MRI data using 45 shapes to learn the shape model.

In [Alessandrini *et al.* (2011)], the shape is represented geometrically as 2 ellipses, one inside the other and the implicit representation of ellipses based on the algebraic distance was used to obtain  $\psi$ . The energy is then minimized in 2 steps. First by keeping  $\lambda$  fixed, the level-set  $\phi$  is evolved according to the local data attachment term described in (4.21) and the shape prior term. In a second step, by keeping  $\phi$  fixed, the authors showed that the estimation of the prior parameters was equivalent to a least square fitting of the parameters on the zero-level of the implicit function  $\phi$ . The method was used to segment real data and the whole myocardium in MRI and echocardiographic scans acquired in parasternal short-axis view.

Finally, let us note the approach of [Foulonneau *et al.* (2006)] where the shape prior is represented using its Legendre moments which are then compared to the level-set moments. In contrary to the constrain energy (5.9)-(5.11) which can be used with a wide choice of prior, their energy is specifically designed for priors based on moments. The evolution equation is obtained using shape gradient derivatives and the method has been applied to the segmentation of road signs.

### 5.3 Constrained segmentation of echocardiographic images

The ASM model proposed by Cootes *et al.* has been designed for the segmentation of objects whose shape has been previously learned from an off-line training process. However, as noted by many authors [Giachetti (1998), Malassiotis and Srintzis (1999), Lin *et al.* (2003)], the corresponding learned shape template can only be used to segment a specific class of image with similar boundary shape. For the particular task of segmentation of echocardiographic sequences, this model seems to be difficult to be used for two reasons. Firstly, for each specific image view (for example the parasternal long-axis view), the cardiac motion yields a variability of the shape of the myocardial region and the ventricle cavity which is not taken into account in conventional PCA. Moreover, these shapes depend on the probe angle (a small variation on the acquisition angle has an influence on the resulting shape). Thus, in order to be representative of the different shapes involved in one specific image view during the whole cardiac cycle, the corresponding training data set should be composed of a large number of images. In this framework, some authors proposed to modify the PCA model initially proposed by Cootes in order to adapt the shape space to the analysis of temporal sequences.

[Lin *et al.* (2003)] described a multi-scale level-set framework for the segmentation of the endocardium in apical 4-chamber view. The authors first pointed out that at higher levels of a Gaussian pyramid, the intensity distribution of an ultrasound image can be approximately modeled by Gaussian. At this coarse scale level, region and boundary-based information are used to guide a level-set to extract boundary information. At finer scale levels, these coarse boundaries are used to both initialise boundary detection and serve as a shape prior where the minimized energy corresponds to (5.11).

In order to avoid shape learning, [Taron *et al.* (2004)] proposed a method for the recovery of the endocardium in parasternal short-axis view using a geometric model. This approach relies on the assumption that the endocardial contour in a parasternal short-axis view can be reliably modelled as an ellipse. The contour evolution then corresponds to deforming an ellipse according to its parameters, so it is attracted to the desired image features. Though this method does not require any learning step, the shape prior used might be too strong and cannot be applied to other views where the myocardial border does not correspond to an ellipse.

[Zhou (2010)] presented a machine learning approach called shape regression machine (SRM) for the segmentation of the endocardial border. The SRM first performs a statistical learning of the interrelations among shape, appearance and anatomy using an annotated database. The segmentation process is then performed in two stages. First it estimates a rigid shape to solve an automatic initialization problem, which can be seen as an alignment problem to find the pose parameters. Secondly the nonrigid shape is estimated through a learned nonlinear regressor to directly associate nonrigid shape with image appearance. To perform both stages, the authors proposed a method called image-based boosting ridge regression that enables multivariate, nonlinear modeling. The authors validated their

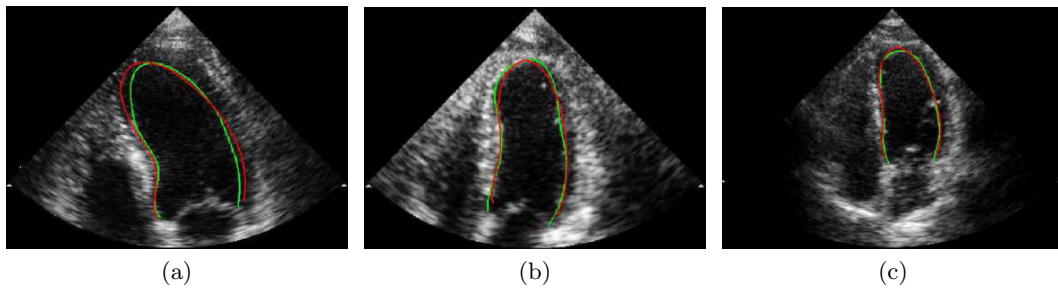


Figure 5.7: Segmentation results using the SRM method (red contour) and ground truth (red). Note that all figures are reproduced from [Zhou (2010)]

method by segmenting the endocardium in 77 end-diastolic apical 4-chamber images using a model trained on 450 references frames.

[Carneiro *et al.* (2012)] described a deep learning method for the segmentation of the endocardium that was applied to apical 4-chamber sequences. Their method relied on a special kind of artificial neural network called deep belief network to build two classifiers: a rigid and a non-rigid one. The rigid classifier is trained using patches that fully contain (or not) the left ventricle. In the segmentation process, it finds the region where the left ventricle is present and estimates the pose parameters to align this region in a canonical coordinate system. The non-rigid classifier learns intensity profiles along lines perpendicular to references contour which are then used in the segmentation process to estimate the most likely position of the contour. To remove noisy results from the non-rigid classifier, the contour is then represented using a PCA model. Note that though their method is applied to the segmentation of sequences, no dynamic model is used, the segmentation of each frame being independant of the other.

## 5.4 Conclusion

As shown in this chapter, most of the shape constrained segmentation techniques use learned templates as shape prior. As mentioned in [Lin *et al.* (2003)], though it can take place off-line, this learning step is very time consuming and requires experts to manually outline the target object in a data-set. Consequently, the learned prior is dependent on the expert as well as on the orientation in the case of 2D segmentation. Indeed due to the shape variability, a prior built on parasternal short-axis images cannot be used to constrain the segmentation in apical 4-chamber scans. Furthermore, one has to be very careful in the dataset construction in order not to give too much weight to a particular shape while ensuring that the training set is representative enough to cope with the variability of the shapes to be segmented. For example, when learning a shape prior for a medical application, one has to consider both healthy and pathological subjects in correct proportion to make sure that both cases can be handled. This can quickly increase the number of shapes to include in the learning process since pathological cases can heavily differ from healthy ones.

Regarding the geometrical priors, most of the works have used them to restrict the set of possible results [Taron *et al.* (2004), Gong *et al.* (2004)] rather than as a constraint allowing local variations around the model [Alessandrini *et al.* (2011)]. Finally, most of the geometrical functions proposed in the literature can only handle symmetrical shapes which is often not the case for the myocardium.

In this context, we propose a new geometric prior based on hyperquadrics to model the myocardium in any view. Hyperquadrics can handle asymmetrical shapes and are thus well suited to represent the heart border as it will be shown in the next chapter. This model will then be included into a variational active contour framework to segment the whole myocardium in any of the 4 views used in clinical routine.

---

# Our contribution: Modeling of the whole myocardium using hyperquadrics

---

As mentioned in the previous chapter, the introduction of a shape prior into a segmentation algorithm is done in two steps: first one needs to build a prior model and then to define an energy that enforces the contour to remain close to the prior. In this chapter, we focus on finding a general enough prior able to model the myocardium in any view. Though this problem is not new, authors generally proposed either learned priors that are thus only valid for a specific view or geometric priors unable to handle asymmetries. To tackle these two problems, we introduce a new model based on hyperquadric. This model is then fitted to manual references of cardiologists and compared to other geometrical priors proposed in the literature.

## 6.1 Hyperquadrics

### 6.1.1 Definition

Hyperquadrics were first proposed for computer graphics applications by [Hanson (1988), Han *et al.* (1993), Cohen and Cohen (1996)]. They are obtained by considering a sum of an arbitrary number of linear terms raised to powers and generate convex shapes bounded by a polygon. While even a small number of terms allows to represent a large variety of shapes, increasing this number allows to better approximate complex shapes, making the model very flexible. Moreover hyperquadrics can model shapes that are not necessarily symmetric. This property is interesting in our application since the



shape of the endocardium or the epicardium may involve asymmetries (this is illustrated in the results shown in Fig. 6.5).

In the case of a 2D shape, a hyperquadric implicit function is given by

$$\varphi(\mathbf{p}) = \sum_{i=1}^{N_h} |A_i x + B_i y + C_i|^{\gamma_i}, \quad (6.1)$$

where  $N_h$  is the number of hyperquadrics terms and  $\boldsymbol{\lambda} = \{A_i, B_i, C_i, \gamma_i, \forall i = 1..N_h\}$  is the set of parameters to be fitted with  $(A_i, B_i, C_i, \gamma_i) \in \mathbb{R}^3 \times \mathbb{R}^{*+}$ . The modelled shape corresponds to the set of points  $(x, y)$  that satisfies  $\varphi(x, y) = 1$  and can be represented as the zero level of the implicit function

$$\Psi(\mathbf{p}, \boldsymbol{\lambda}) = \varphi(\mathbf{p}) - 1, \quad (6.2)$$

where  $\Psi$  can be considered as a distance from a point to the hyperquadric.

Each term in the summation (6.1) is positive and the terms add to one. Therefore, no individual term can ever exceed one. Since the  $\gamma_i$ s are positive, this implies that  $|A_i x + B_i y + C_i| \leq 1 \forall i = 1, 2, \dots, N_h$ . Thus each term gives a pair of parallel bounding lines. The parameters  $A_i$  and  $B_i$  in term  $i$  give the slope of the lines corresponding to that term. The distance  $S_i$  between the bounding lines is given by  $2/\sqrt{A_i^2 + B_i^2}$ .

Fig. 6.1 shows hyperquadrics contours fitted on range data for different values of  $N_h$  and the bounding lines. It can be noted that for  $N_h = 2$ , the fitted shape is symmetric which is not the case for higher  $N_h$ . It can also be noticed that higher  $N_h$  leads to better fit results as well as more flexibility for the represented shape.

Despite the flexibility of the hyperquadrics and their ability to model asymmetrical shapes, they cannot model contours with concavities. To tackle this problem, [Ohuchi *et al.* (2003)] proposed to replace the bounding lines by other functions (*e.g.* hyperbolas, paraboloids).

### 6.1.2 Fitting hyperquadrics on range data

To fit a hyperquadric to range data, we first define an error-of-fit (EoF) function to measure the difference between a modelled shape and the given data set. Though the distance defined in (6.2) could be used, the minimization of this EoF function often leads to incorrect results as the EoF function presents multiple global or local minima. Indeed, by setting  $A_i = B_i = 0 \forall i = 1, \dots, N_h$ , the equation (6.1) can still be satisfied by infinitely many choices of  $C_i$  and  $\gamma_i$  irrespective of the value of  $(x, y)$  yielding global minima. However those global minima do not correspond to meaningful solutions but rather to degenerate solutions where the distance between a pair of bounding lines described in 6.1.1 becomes very large.

Thus, following the work of [Kumar *et al.* (1995)], the hyperquadrics parameters are

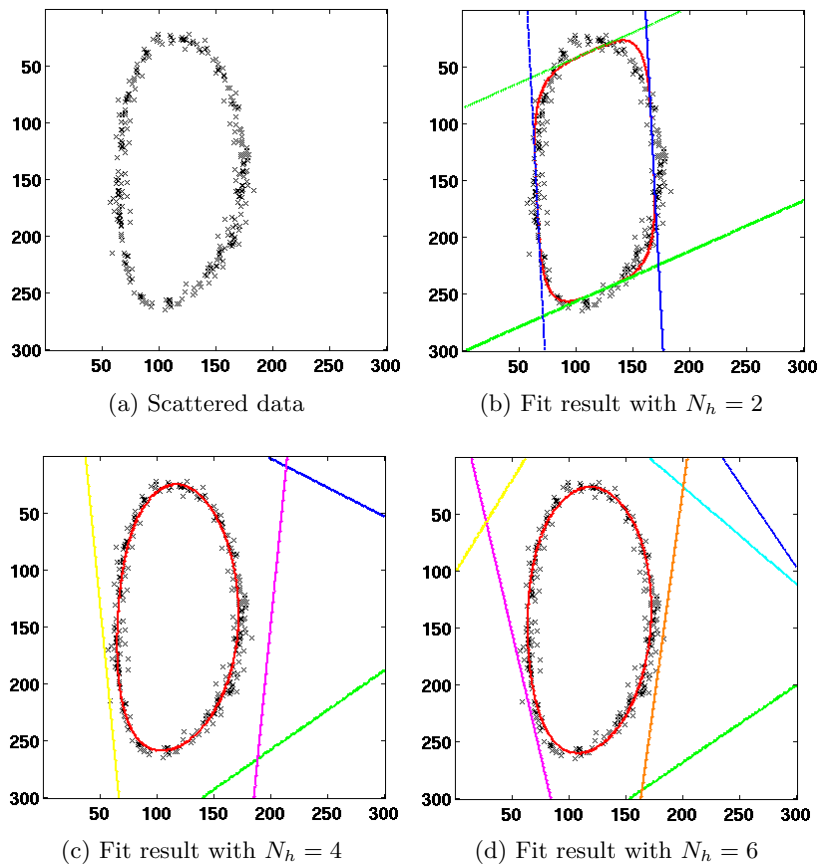


Figure 6.1: Illustration of hyperquadrics fitted on range data with different  $N_h$ . For each fit, the bounding lines are also displayed (one color per pair). Note that for (c) and (d) the distance between bounding lines was too important and thus all the lines are not displayed.

fitted by minimizing the following EoF function

$$EoF = \sum_{i=1}^{N_{data}} \frac{1}{\|\nabla F_{io}(\mathbf{p}_i)\|^2} (1 - F_{io}(\mathbf{p}_i))^2 + \nu \sum_{i=1}^{N_h} P_i, \quad (6.3)$$

where  $F_{io}(\mathbf{p}) = (\varphi(\mathbf{p}))^p$ ,  $P_i$  is a penalty allowing to avoid degenerate solutions and  $N_{data}$  is the number of points used to fit the hyperquadrics. Equation (6.3) thus corresponds to a constrained minimization problem including a data attachment term and a penalization term weighted by  $\nu$ .

As shown in [Kumar *et al.* (1995)],  $P_i$  is directly related to the minimum and maximum dimension of the object considered for the fitting. Indeed we have seen that degenerate solutions might appear if the distance between a pair of bounding lines  $S_i$  is too large. Thus we constraint the upper limit on  $S_i$  to be slightly larger than the maximum diameter  $S_{max}$  of the object. Another, dual, degenerate case arises when the bounding lines get too close to each other, *i.e.* when the inter-lines distance is close to zero. This may be again avoided by setting a lower limit,  $S_{min}$ , to the inter-lines distance.

$$k_2 S_{min} \leq S_i \leq k_1 S_{max} \quad \Leftrightarrow \quad \mu_1 \leq A_i^2 + B_i^2 \leq \mu_2, \quad (6.4)$$

where  $\mu_1 = (1/(k_1 S_{max}))^2$  and  $\mu_2 = (1/(k_2 S_{min}))^2$  with  $k_1$  and  $k_2$  some constants greater than 1. In our application the dimensions  $S_{max}$  and  $S_{min}$  have been chosen as the minimum and maximum extent of the myocardium in the echographic images.

Using the penalty method, the constraint (6.4) is then rewritten as a penalty function  $P_i$  for each term:

$$P_i(\boldsymbol{\lambda}) = (\max[0, \mu_1 - (A_i^2 + B_i^2)])^2 + (\max[0, A_i^2 + B_i^2 - \mu_2])^2. \quad (6.5)$$

Regarding the weighting term  $\nu$ , it can be shown that the solution to the constrained problem (6.3) coincides with the least square problem when  $\nu$  tends to infinity. In practice, a correct result is obtained for a sufficiently large value of  $\nu$ . In all our experiments,  $\nu$  is set to  $10^8$  so that the penalization term is on the same order than the data attachment term.

The minimization of (6.3) is accomplished by the Levenberg-Marquardt non-linear optimization method [Press *et al.* (1992)].

## 6.2 Modeling of the whole myocardium

As will be shown in Section 6.5.2, each of the myocardial boundaries (*i.e.* the endocardium and the epicardium) can be modelled by a single hyperquadric. We are thus searching for a shape representation that allows:

1. to model these two contours through a single implicit representation,
2. to solve efficiently the fitting problem to update the shape parameters.

Let us call  $\psi$  this representation. A trivial choice for  $\psi$  could consist in the pointwise product between two distance functions. However, the resulting representation would no longer be a distance function [Berg (1998)] and, further, it would not allow an optimized solution to the fitting problem, as the one we are presenting in the sequel. Following the work presented in [Berg (1998)], the shape prior is thus defined as:

$$\psi(\mathbf{p}, \boldsymbol{\lambda}) = \max(\Psi(\mathbf{p}, \boldsymbol{\lambda}_{out}), -\Psi(\mathbf{p}, \boldsymbol{\lambda}_{in})), \quad (6.6)$$

where  $\boldsymbol{\lambda} = [\boldsymbol{\lambda}_{in}, \boldsymbol{\lambda}_{out}]$  and  $\boldsymbol{\lambda}_{in}$  and  $\boldsymbol{\lambda}_{out}$  represent the parameters of the inner and outer shapes. The function  $\Psi(\cdot)$  corresponds to the distance from a point  $\mathbf{p} = (x, y)$  to a hyperquadric (equation (6.2)). Fig. 6.2 gives an illustration of the parametric implicit function  $\psi$  adopted in the proposed framework.

## 6.3 Shape prior energy

Inspired by the framework proposed in [Caselles *et al.* (1997), Chen *et al.* (2002)], we define a new shape constraint into our level-set framework by minimizing the following

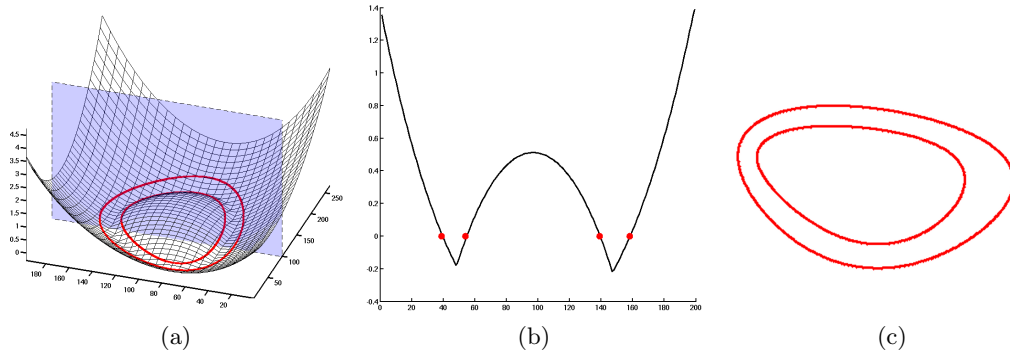


Figure 6.2: Illustration of the parametric implicit function  $\psi$ . The zero level is represented in red. (a) 3-D representation. (b) Visualization of a 2-D profile corresponding to the color plane given in (a). (c) Visualization of the zero-level of  $\psi$

shape prior energy:

$$E_{shape}(\phi, \boldsymbol{\lambda}) = \int_{\Omega} \psi^2(\mathbf{p}, \boldsymbol{\lambda}) \cdot \|\nabla\phi(\mathbf{p})\| \cdot \delta(\phi(\mathbf{p})) d\mathbf{p}, \quad (6.7)$$

where  $\psi(\mathbf{p}, \boldsymbol{\lambda})$  is the implicit function representing the distance of a point  $\mathbf{p}$  to the myocardial shape defined by the parameters  $\boldsymbol{\lambda}$ . Clearly (6.7) reads as a measure of the distance between the active contour and the shape prior, and therefore imposes a similarity between the segmentation result and the prior itself.

The minimization of energy (6.7) may be interpreted as finding a geodesic zero level-set in a Riemannian space derived from the shape prior content. As compared to the initial work of [Caselles *et al.* (1997)] and derived approaches [Chen *et al.* (2002)], the arc length function of (6.7) is no longer weighted by an image based information but by our shape prior term. From the observation that the minimum of this expression is reached when the zero level of  $\phi$  perfectly fits the zero level of the parametric implicit function  $\psi$ , one can anticipate that the minimization of this energy criterion will drive the level-set toward a shape composed of two hyperquadrics.

The minimization of (6.7) is addressed in a two phase scheme. Specifically, keeping  $\boldsymbol{\lambda}$  fixed,  $\phi$  is evolved according to the level-set equation:

$$\frac{\partial\phi}{\partial\tau}(\mathbf{p}) = \delta(\phi(\mathbf{p})) \cdot \left( \frac{\langle \nabla\psi(\mathbf{p}, \boldsymbol{\lambda}), \nabla\phi(\mathbf{p}) \rangle}{\|\nabla\phi(\mathbf{p})\|} + \psi^2(\mathbf{p}, \boldsymbol{\lambda}) \cdot \kappa \right), \quad (6.8)$$

where  $\kappa$  is the curvature of the evolving interface and  $\langle \cdot, \cdot \rangle$  denotes the scalar product. Then, keeping  $\phi$  fixed,  $\boldsymbol{\lambda}$  is updated according to the following fitting problem:

$$\boldsymbol{\lambda} = \arg \min_{\boldsymbol{\lambda}'} \oint_{\Gamma} \psi^2(\mathbf{p}, \boldsymbol{\lambda}') d\mathbf{p}. \quad (6.9)$$

As detailed in the next chapter, we impose  $\phi$  to be a signed distance map [Osher and Fedkiw (2002)]. Thus  $\|\nabla\phi\| = 1$  and (6.9) corresponds to the exact minimization of (6.7) w.r.t.  $\boldsymbol{\lambda}$ . In the next section, we propose a fast solution to the fitting problem in (6.9), which can be employed for implementing efficiently the parameters update step.

Note that, as the image space is in practice discrete, eq.(6.9) can be rewritten as:

$$\boldsymbol{\lambda} = \arg \min_{\boldsymbol{\lambda}'} \sum_{\mathbf{p} \in \Gamma} \psi^2(\mathbf{p}, \boldsymbol{\lambda}'). \quad (6.10)$$

## 6.4 Fast solution to the fitting problem

Considering (6.6), we can rewrite the sum in (6.10) as:

$$J(\mathbf{p}, \boldsymbol{\lambda}) = \sum_{\mathbf{p} \in \Gamma_{in}} \Psi^2(\mathbf{p}, \boldsymbol{\lambda}_{in}) + \sum_{\mathbf{p} \in \Gamma_{out}} \Psi^2(\mathbf{p}, \boldsymbol{\lambda}_{out}), \quad (6.11)$$

where the partition  $\Gamma = \{\Gamma_{in}, \Gamma_{out}\}$  has been introduced

$$\Gamma_{in}(\boldsymbol{\lambda}_{in}, \boldsymbol{\lambda}_{out}) = \{\mathbf{p} \in \Gamma \mid \Psi(\mathbf{p}, \boldsymbol{\lambda}_{out}) < -\Psi(\mathbf{p}, \boldsymbol{\lambda}_{in})\}, \quad (6.12)$$

$$\Gamma_{out}(\boldsymbol{\lambda}_{in}, \boldsymbol{\lambda}_{out}) = \{\mathbf{p} \in \Gamma \mid \Psi(\mathbf{p}, \boldsymbol{\lambda}_{out}) \geq -\Psi(\mathbf{p}, \boldsymbol{\lambda}_{in})\}. \quad (6.13)$$

From this formulation, we observe that (6.11) can be minimized by fitting two separate hyperquadrics on  $\Gamma_{in}$  and  $\Gamma_{out}$ , for which fast direct solvers exist (eq.(6.3), [Kumar *et al.* (1995)]). Consequently we propose to minimize  $J$  by alternatively fitting the two hyperquadrics and updating  $\Gamma_{in}$  and  $\Gamma_{out}$  according to (6.12) and (6.13). The resulting algorithm is summarized in Alg. 1. By doing so, the energy  $J$  is ensured to decrease at each step. In Alg. 1 we call `fitHQ` the function performing the hyperquadric fitting as described in [Kumar *et al.* (1995)].

---

### Algorithm 1: Hyperquadric fitting algorithm

---

**Input:**  $\Gamma, \hat{\boldsymbol{\lambda}}_{in}^{(0)}, \hat{\boldsymbol{\lambda}}_{out}^{(0)}$   
 $\epsilon$ .  
**Output:**  $\hat{\boldsymbol{\lambda}}_{in}, \hat{\boldsymbol{\lambda}}_{out}$

$k = 1;$   
 $\Delta J = \infty;$   
 $J^{(0)} = \text{EoF}(\Gamma, \hat{\boldsymbol{\lambda}}_{in}^{(0)}, \hat{\boldsymbol{\lambda}}_{out}^{(0)});$   
 $[\Gamma_{in}^{(0)}, \Gamma_{out}^{(0)}] = \text{findInOut}(\Gamma, \hat{\boldsymbol{\lambda}}_{in}^{(0)}, \hat{\boldsymbol{\lambda}}_{out}^{(0)});$   
**while**  $\Delta J > \epsilon$  **do**

|  |
|--|
| $\hat{\boldsymbol{\lambda}}_{in} = \text{fitHQ}(\Gamma_{in}^{(k-1)});$   |
| $\hat{\boldsymbol{\lambda}}_{out} = \text{fitHQ}(\Gamma_{out}^{(k-1)});$   |
| $[\Gamma_{in}, \Gamma_{out}] = \text{findInOut}(\Gamma, \hat{\boldsymbol{\lambda}}_{in}, \hat{\boldsymbol{\lambda}}_{out});$ |
| $J^{(k)} = \text{CompEoF}(\Gamma, \hat{\boldsymbol{\lambda}}_{in}, \hat{\boldsymbol{\lambda}}_{out});$                       |
| $\Delta J = \ J^{(k)} - J^{(k-1)}\  / \ J^{(k-1)}\ ;$  |
| $k = k + 1;$   |

---

We remark that, within the segmentation flow, Alg. 1 is used to fit the points on the evolving contour. In this case, at every time step, the adopted initialisation consists in

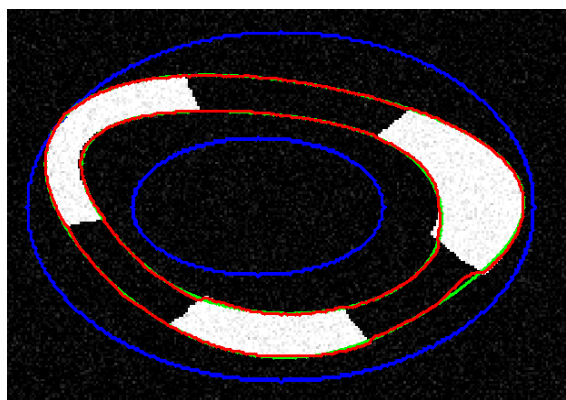


Figure 6.3: Illustration of the evolution of a level-set when minimizing the proposed shape prior energy and the classical Chan & Vese data attachment term [Chan and Vese (2001)]. In blue, the initial contour; in red, the final contour; in green, the shape prior.

the two hyperquadrics obtained from fitting the active contour at the previous time step. Since in this interval the displacement of the active contour is expected to be small, such initialisation allows often the convergence to be reached in one single iteration.

In Fig. 6.3, we show an example of evolution of a level-set using two evolution terms: a data attachment term and the one proposed in (6.8). Since the image to be segmented is a binary mask with a small gaussian noise, there is no need for a sophisticated data attachment term and we thus use the classical Chan & Vese term [Chan and Vese (2001)]. The image contains an object whose boundaries correspond to two hyperquadrics. Though three parts of the object were occluded, we can see that the evolving contour is able to recover the whole object by filling the missing boundaries.

## 6.5 Model validation

In this section, we evaluate the ability of our model to represent the myocardial shape. To this end, we fit our model on reference shapes of cardiologists and compute error measures between the fitting results and the reference.

### 6.5.1 Comparison protocol

#### Experimental data

The reference dataset is composed of 80 images acquired from 20 healthy volunteers and taken at End-Diastole (ED) and End-Systole (ES), which are the instants in the cardiac cycle used by cardiologists in routine echocardiography for the diagnosis of pathologies. The data are distributed as follows:

- 7 ED and 8 ES images in parasternal short-axis view,
- 13 ED and 11 ES images in parasternal long-axis view,
- 13 ED and 12 ES in apical 4-chamber view,
- 8 ED and 8 ES images in apical 2-chamber view.

The images in parasternal short-axis views were acquired using a Toshiba Powervision 6000 (Toshiba Medical Systems Europe, Zoetermeer, the Netherlands) equipped with a 3.75 MHz-probe, while the scans from the other views were acquired using a GE Vivid E9 system equipped with a 2.5 MHz M5S probe (GE Vingmed Ultrasound, Horten, Norway).

### Fitting procedure

Following [Chalana and Kim (1997)], the mean myocardial shape was computed from the manual references drawn by three expert cardiologists. Then for each of the so-obtained reference, the model was fitted separately on the endocardium and the epicardium. Note that since part of the myocardium might lie outside of the field of view or since it does not correspond to a closed contour (in parasternal long-axis, apical 4-chamber or apical 2-chamber views), we only considered points inside a ROI for the fitting. This ROI is the same as the one defined in 7.5.2.

The model is also compared with two other geometrical priors proposed recently for the segmentation of the heart. In [Hamou and El-Sakka (2010)], the prior is obtained by fitting two  $3^{rd}$  order hyperbola, one on the  $2/3$  upper part of the contour and the other one on the  $1/3$  lower part. Our prior is also compared to ellipses which have been proposed by [Taron *et al.* (2004), Alessandrini *et al.* (2011)] to model the heart in parasternal short-axis views.

### Error measures

To evaluate the model, we measured the correspondence between the fitted models and the mean myocardial shape. In particular we adopt three different metrics, *i.e.* the Dice coefficient  $D$  [Dice (1945)], the Mean Absolute Distance  $MAD$  (expressed in mm) [Comaniciu *et al.* (2004)] and the Hausdorff distance  $HD$  (expressed in mm) [Huttenlocher *et al.* (1993)]. If we call with  $R$  and  $S$  the reference contour and the fitted one, and introduce the generic points  $\mathbf{r}$  and  $\mathbf{s}$  belonging to  $R$  and  $S$  respectively, then the Mean Absolute Distance and the Hausdorff distance are defined as:

$$MAD(R, S) = \frac{1}{N_S} \sum_{\mathbf{s} \in S} |d(\mathbf{s}, R)|, \quad (6.14)$$

and

$$HD(R, S) = \max \left( \sup_{\mathbf{r} \in R} d(\mathbf{r}, S); \sup_{\mathbf{s} \in S} d(\mathbf{s}, R) \right) \quad (6.15)$$

where  $d(\mathbf{p}, A)$  represents the shortest distance from the point  $\mathbf{p}$  to the curve  $A$  and  $N_S$  is the number of points in the contour  $S$ . While the MAD measures a global correspondence between the two contours, the Hausdorff distance is well suited for evaluating the local behavior of the algorithm. Moreover, by defining  $\Omega_S$  and  $\Omega_R$  the sets of pixels within the

|                        | Hyperquadrics, $N_h = 4$                                 |                            |                            | Hyperquadrics, $N_h = 6$                                 |                            |                          |
|------------------------|--|----------------------------|----------------------------|--|----------------------------|--------------------------|
|                        | $D^*$  | MAD                        | HD                         | $D^*$  | MAD                        | HD                       |
| Parasternal short-axis | $8.64 \cdot 10^{-3}$<br>( $4.9 \cdot 10^{-3}$ )          | 0.244<br>(0.189)           | 0.731<br>(0.409)           | $6.43 \cdot 10^{-3}$<br>( $2.39 \cdot 10^{-3}$ )         | 0.168<br>(0.089)           | 0.599<br>(0.224)         |
| Parasternal long-axis  | $4.78 \cdot 10^{-3}$<br>( $2.17 \cdot 10^{-3}$ )         | 0.11<br>(0.058)            | 1.15<br>(0.593)            | $7.65 \cdot 10^{-3}\dagger$<br>( $5.11 \cdot 10^{-3}$ )  | 0.179 $\dagger$<br>(0.12)  | 1.7 $\dagger$<br>(0.968) |
| Apical 4-chamber       | $9.42 \cdot 10^{-3}$<br>( $4.71 \cdot 10^{-3}$ )         | 0.266<br>(0.119)           | 1.73<br>(0.888)            | $1.65 \cdot 10^{-2}$<br>( $2.37 \cdot 10^{-2}$ )         | 0.498<br>(0.814)           | 2.67<br>(2.89)           |
| Apical 2-chamber       | $8.51 \cdot 10^{-3}$<br>( $2.77 \cdot 10^{-3}$ )         | 0.258<br>(0.078)           | 1.54<br>(0.6)              | $1.43 \cdot 10^{-2}\dagger$<br>( $1.55 \cdot 10^{-2}$ )  | 0.442 $\dagger$<br>(0.442) | 2.4 $\dagger$<br>(2.16)  |
|                        | Ellipse  |                            |                            | $3^{rd}$ order hyperbola                                 |                            |                          |
|                        | $D^*$  | MAD                        | HD                         | $D^*$  | MAD                        | HD                       |
| Parasternal short-axis | $1.21 \cdot 10^{-2}\dagger$<br>( $3.94 \cdot 10^{-3}$ )  | 0.321 $\dagger$<br>(0.161) | 0.974 $\dagger$<br>(0.379) | $3.58 \cdot 10^{-2}\dagger$<br>( $5.16 \cdot 10^{-3}$ )  | 0.963 $\dagger$<br>(0.386) | 3.41 $\dagger$<br>(1.12) |
| Parasternal long-axis  | $1.13 \cdot 10^{-2}\dagger$<br>( $4 \cdot 10^{-3}$ )     | 0.269 $\dagger$<br>(0.104) | 2.63 $\dagger$<br>(1.11)   | $1.38 \cdot 10^{-2}\dagger$<br>( $4.04 \cdot 10^{-3}$ )  | 0.316 $\dagger$<br>(0.111) | 2.29 $\dagger$<br>(0.75) |
| Apical 4-chamber       | $1.54 \cdot 10^{-2}\dagger$<br>( $5.11 \cdot 10^{-3}$ )  | 0.442 $\dagger$<br>(0.176) | 2.3 $\dagger$<br>(1.08)    | $3.24 \cdot 10^{-2}\dagger$<br>( $5.48 \cdot 10^{-3}$ )  | 0.91 $\dagger$<br>(0.207)  | 4.6 $\dagger$<br>(0.895) |
| Apical 2-chamber       | $1.87 \cdot 10^{-2} \dagger$<br>( $3.99 \cdot 10^{-3}$ ) | 0.573 $\dagger$<br>(0.118) | 2.54 $\dagger$<br>(0.617)  | $3.36 \cdot 10^{-2} \dagger$<br>( $5.94 \cdot 10^{-3}$ ) | 1 $\dagger$<br>(0.223)     | 5.86 $\dagger$<br>(1.29) |

Table 6.1: Results of the fit of the different priors on the mean curve of the epicardial border in term of modified Dice criterion ( $D^*$ ), Mean Absolute Distance (MAD) and Hausdorff distance (HD). The given values correspond to the mean (Standard deviation). HD and MAD are given in mm.  $\dagger$  indicates that the difference was found significant ( $p < 0.001$ ) when compared to hyperquadrics with  $N_h = 4$ .

segmented and the reference region, the Dice coefficient writes as:

$$D(\Omega_R, \Omega_S) = \frac{2Area(\Omega_S \cap \Omega_R)}{Area(\Omega_R) + Area(\Omega_S)}. \quad (6.16)$$

This coefficient measures the correspondence between the two regions, and varies from 0 to 1: it is 1 when the two regions are coincident and 0 when they have null intersection. Note that all these measures are only computed inside the ROI. We decided to display a modified version of the Dice coefficient  $D^* = 1 - D$  so that a value  $D^* = 0$  corresponds to a perfect fit and  $D^* = 1$  to the case of two shapes with no intersection.

## 6.5.2 Results

To validate the choice of our shape prior, we fitted four different models (hyperquadrics with  $N_h = 4$  and 6 terms, ellipses and the  $3^{rd}$  order hyperbola model of [Hamou and El-Sakka (2010)]) on the mean curve of the manual references drawn by three expert cardiologists on the dataset. The mean curve is obtained following the method described in [Chalana and Kim (1997)]. The results are given in Table 6.1 and 6.2 while Fig. 6.4 shows them visually. Some examples of fits are displayed in Fig. 6.5.

From these two tables, we can see that the proposed hyperquadric with  $N_h = 4$  is able



|                        | Hyperquadrics, $N_h = 4$                          |                   |                   | Hyperquadrics, $N_h = 6$                          |                   |                  |
|------------------------|---|-------------------|-------------------|---|-------------------|------------------|
|                        | $D^*$   | MAD               | HD                | $D^*$   | MAD               | HD               |
| parasternal short-axis | $8.78 \cdot 10^{-3}$<br>( $2.87 \cdot 10^{-3}$ )  | 0.142<br>(0.063)  | 0.496<br>(0.168)  | $9.05 \cdot 10^{-3}$<br>( $1.95 \cdot 10^{-3}$ )  | 0.149<br>(0.058)  | 0.52†<br>(0.128) |
| parasternal long-axis  | $1.04 \cdot 10^{-2}$<br>( $6.39 \cdot 10^{-3}$ )  | 0.195<br>(0.115)  | 1.52<br>(0.669)   | $1.65 \cdot 10^{-2}†$<br>( $1.18 \cdot 10^{-2}$ ) | 0.309†<br>(0.212) | 2.21†<br>(1.08)  |
| apical 4-chamber       | $2.62 \cdot 10^{-2}$<br>( $1.79 \cdot 10^{-2}$ )  | 0.515<br>(0.341)  | 2.14<br>(1.17)    | $7.82 \cdot 10^{-2}†$<br>( $5.54 \cdot 10^{-2}$ ) | 1.62†<br>(1.1)    | 5.84†<br>(3.06)  |
| apical 2-chamber       | $3.97 \cdot 10^{-2}$<br>( $1.93 \cdot 10^{-2}$ )  | 0.809<br>(0.339)  | 3.1<br>(1.21)     | $9.36 \cdot 10^{-2}†$<br>( $5.04 \cdot 10^{-2}$ ) | 2.03†<br>(0.951)  | 6.8†<br>(2.87)   |
|                        | Ellipse   |                   |                   | $3^{rd}$ order hyperbola                          |                   |                  |
|                        | $D^*$   | MAD               | HD                | $D^*$   | MAD               | HD               |
| parasternal short-axis | $1.62 \cdot 10^{-2}†$<br>( $5.45 \cdot 10^{-3}$ ) | 0.281†<br>(0.157) | 0.872†<br>(0.434) | $3.7 \cdot 10^{-2}†$<br>( $4.25 \cdot 10^{-3}$ )  | 0.604†<br>(0.206) | 2.17†<br>(0.84)  |
| parasternal long-axis  | $1.63 \cdot 10^{-2}†$<br>( $6.17 \cdot 10^{-3}$ ) | 0.322†<br>(0.137) | 2.65†<br>(1.09)   | $3.69 \cdot 10^{-2}†$<br>( $2.94 \cdot 10^{-2}$ ) | 0.674†<br>(0.473) | 3.46†<br>(1.97)  |
| apical 4-chamber       | $2.59 \cdot 10^{-2}$<br>( $9.19 \cdot 10^{-3}$ )  | 0.514<br>(0.198)  | 2.18<br>(0.597)   | $3.91 \cdot 10^{-2}†$<br>( $1.12 \cdot 10^{-2}$ ) | 0.789†<br>(0.296) | 4.23†<br>(1.79)  |
| apical 2-chamber       | $4.32 \cdot 10^{-2}$<br>( $9.84 \cdot 10^{-3}$ )  | 0.901<br>(0.22)   | 3.43†<br>(0.866)  | $6.72 \cdot 10^{-2}†$<br>( $2.74 \cdot 10^{-2}$ ) | 1.49†<br>(0.706)  | 8.7†<br>(4.93)   |

Table 6.2: Results of the fit of the different priors on the mean curve of the endocardial border in term of modified Dice criterion ( $D^*$ ), Mean Absolute Distance (MAD) and Hausdorff distance (HD). The given values correspond to the mean (Standard deviation). HD and MAD are given in mm. †indicates that the difference was found significant ( $p < 0.001$ ) when compared to hyperquadrics with  $N_h = 4$ .

to model the heart boundaries with a good accuracy. Indeed the MAD values are always below 0.9mm for the endocardial fit and below 0.3mm for the epicardial fit, which shows that the prior is on average really close to the cardiologist’s references. If we consider the Hausdorff distance, which is more sensitive to local errors, it can be observed that the maximal fitting error is never larger than 3.1mm for the endocardial border and 1.8mm for the epicardial border. This indicates that even locally, our model is close to the experts’ boundaries.

Table 6.1 and 6.2 also indicate that the hyperquadrics with  $N_h = 4$  always performs better than the one proposed by [Hamou and El-Sakka (2010)]. The Hausdorff distance and MAD values associated to the proposed prior are on average 30% lower, which shows that our prior is better suited for the modelling of heart boundaries. This can be explained by the fact that hyperquadrics can model asymmetries which is not the case for the  $3^{rd}$  order hyperbola as it can be observed in Fig. 6.5. Note that the above mentioned differences were found to be statistically significant for any view with a level  $p = 0.001$  using the Friedman rank test.

If we now compare hyperquadrics with  $N_h = 4$  to ellipses, we can draw almost the same conclusion except for the endocardial border in apical 2 and 4-chamber views, where hyperquadrics and ellipse yield almost the same results. In particular, it may be noted that

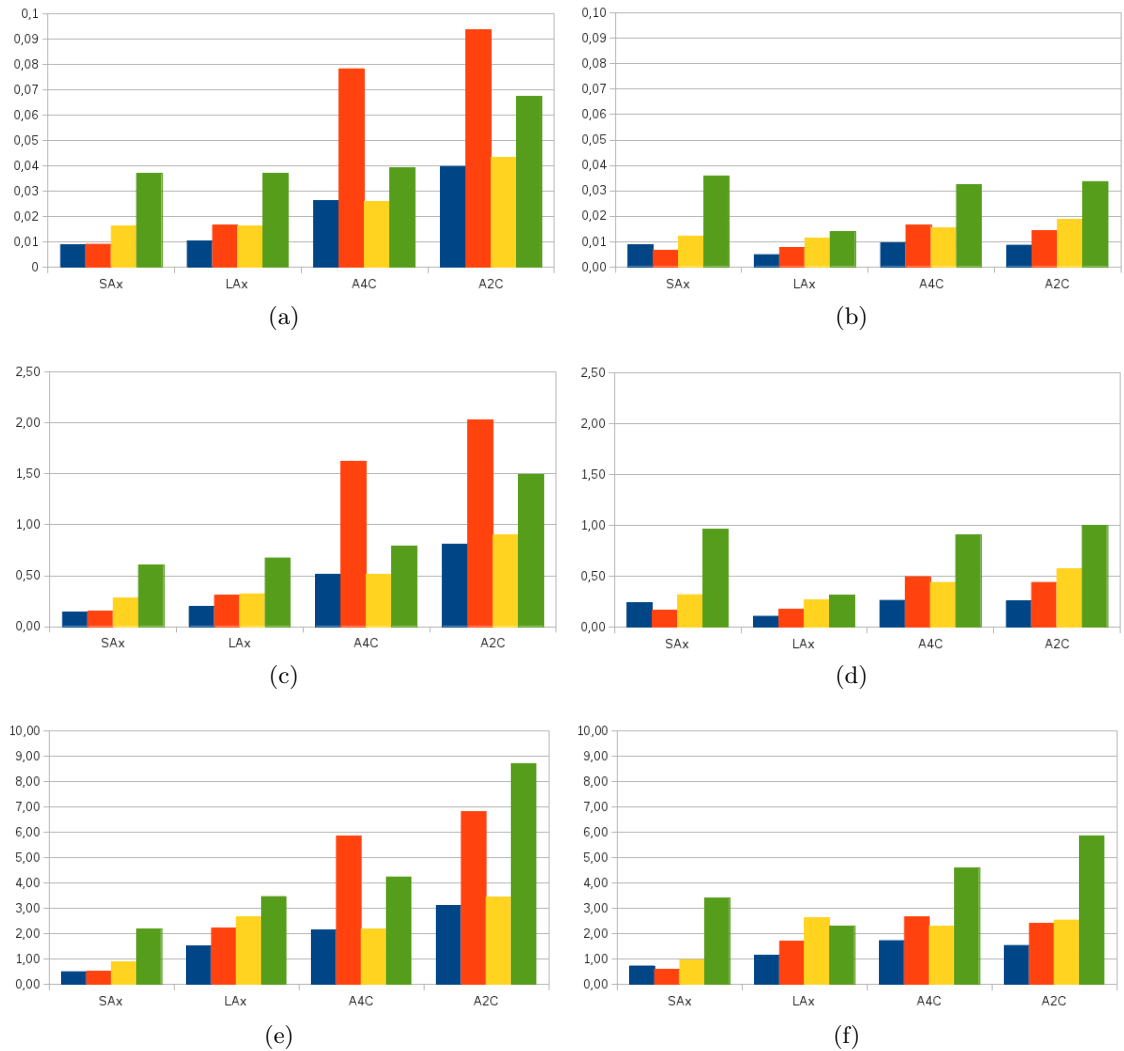


Figure 6.4: Results of the prior fitting on the endocardial (first column) and epicardial (last column) borders in terms of modified Dice coefficient (first row), MAD (second row) and Hausdorff distance (third row). The MAD and Hausdorff distance are given in mm. Blue: Hyperquadrics with  $N_h = 4$ ; Red: Hyperquadrics with  $N_h = 6$ ; Yellow: Ellipse; Green:  $3^{rd}$  order hyperbola.

even in parasternal short-axis views, where the heart boundaries are usually approximated by ellipses, our model provides better results than ellipses. Since even in this view the expert contours are not exactly ellipses, an elliptical prior will not be able to exactly fit the small deviation from this model while hyperquadrics will.

Finally we can see that using hyperquadrics with  $N_h = 4$  allows to better model the heart shape than when using  $N_h = 6$ : the results are indeed either very close (i.e. no significant statistical difference at a level  $p = 0.001$ ) or hyperquadrics with  $N_h = 4$  performs better when the difference is significant. Note also that  $N_h = 6$  has the drawback to yield a higher computational load since more parameters have to be estimated.

As a conclusion, we will set  $N_h = 4$  for the segmentation experiments to be described in the next sections, which is a good compromise between approximation accuracy and the computational load of the algorithm.

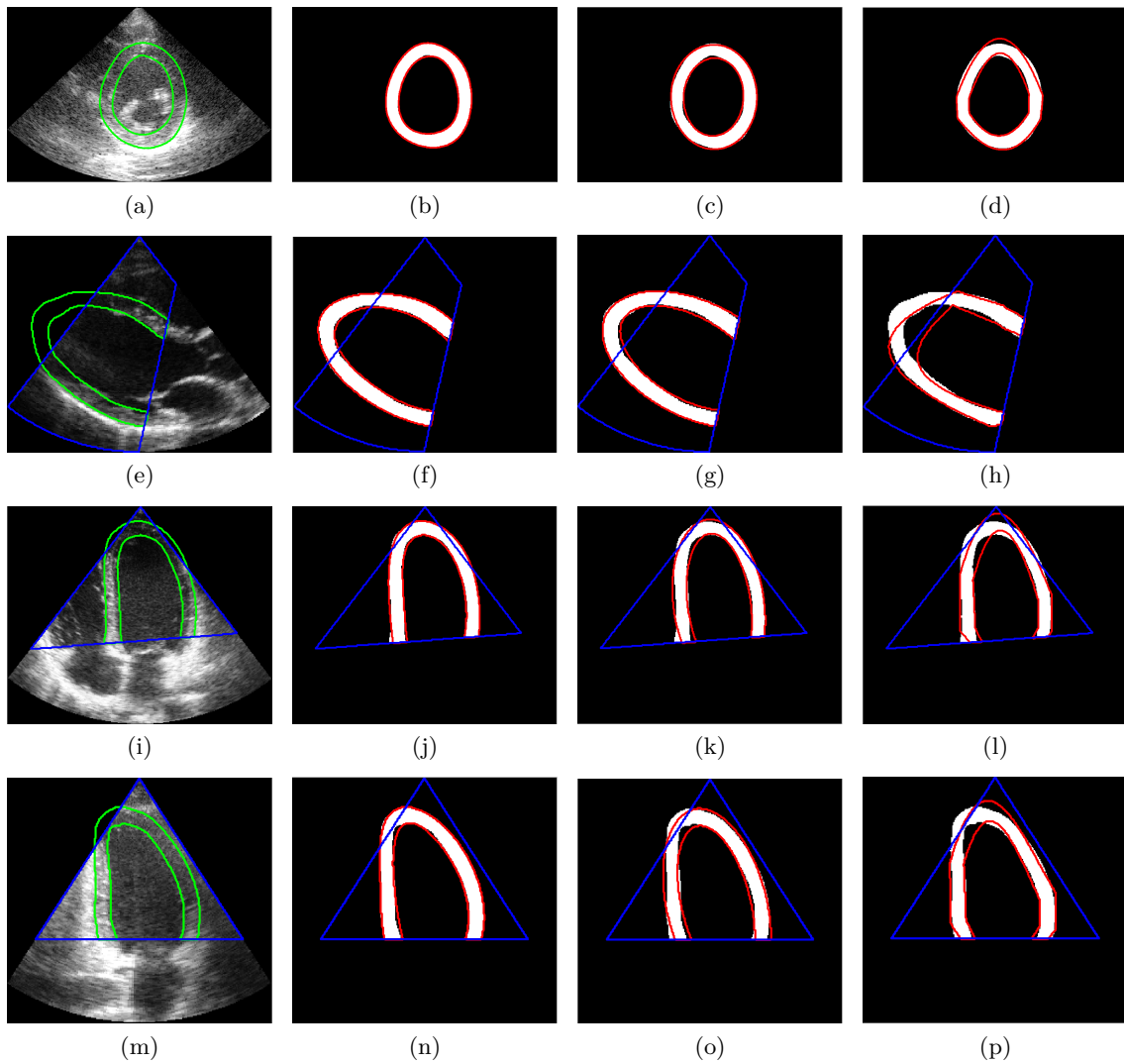


Figure 6.5: Example of results of fits of the different models with the mean expert curve for the 4 main views (from top to bottom: parasternal short-axis, parasternal long-axis, apical 4-chamber, apical 2-chamber). The fitted model is (from left to right) a hyperquadric with  $N_h = 4$ , an ellipse and a  $3^{rd}$  order hyperbola. The blue contour corresponds to the ROI, the green to the reference and the red to the fit result.

## 6.6 Conclusion

In this chapter, we proposed to model the whole myocardium by two hyperquadrics one inside the other. We showed that this model is able to represent the myocardial shape in any of the main clinical views and performs better than other models proposed in the literature. In the next chapter, we will see how to use this prior to constrain the evolution of the level-set through a variational approach.

---

# Our contribution: Segmentation of the whole myocardium in any view in 2D-echocardiographic images

---

## 7.1 Energy formulation

As mentioned in Chapter 5, many energy functionals have been proposed in literature to incorporate shape priors into the level-set formulation. Usually, the authors sum two energy terms: a data attachment term and the shape prior one [Leventon *et al.* (2000), Chen *et al.* (2002), Alessandrini *et al.* (2011)]. Here, since we consider the simultaneous segmentation of two unconnected contours, we also include an anti-collision term. We thus adopt the following general expression for the energy functional:

$$E = E_{data} + E_{shape} + E_{thickness}, \quad (7.1)$$

where  $E_{data}$  represents the chosen data attachment term,  $E_{thickness}$  is a term that prevents the contours from merging by imposing locally a minimum thickness and  $E_{shape}$  embeds the shape prior described in the previous chapter.

## 7.2 Data attachment term

Intensity inhomogeneities often appear along the myocardial boundaries as shown in Fig. 7.1. In Fig. 7.1(a), due to a loss of contrast, intensity inhomogeneity appears between

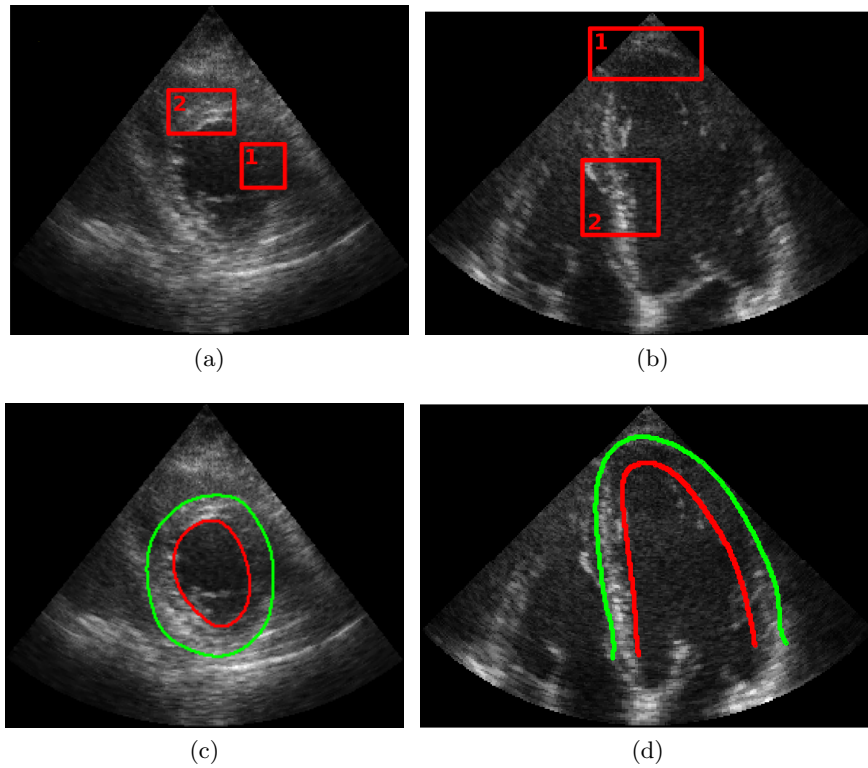


Figure 7.1: Examples of the intensity inhomogeneities occurring along the myocardium borders. Top row: parasternal short-axis view (left) and apical 4-chamber view (right). Bottom row: same images with the cardiologist's reference epicardial (green) and endocardial contours (red).

the lateral wall (area 1) and the anterior wall (area 2). In Fig. 7.1(b), the apex (area 1) is blurred and less contrasted than the septum wall (area 2) because it is located in the near field of the probe.

In order to cope with these intensity inhomogeneities, [Lankton and Tannenbaum (2008)] recently proposed a general framework to localize the data attachment term. Though more sophisticated attachment terms could be used, we adopt the localized version of the Chan-Vese model [Chan and Vese (2001)], as data attachment term  $E_{data}$  and computed directly from the B-mode scan. This formulation handles local statistics and is therefore well suited for segmenting objects whose boundaries are discontinuous or heterogeneous, where standard region based methods that use global statistics fail.

Using the general framework described in [Lankton and Tannenbaum (2008)], the data attachment term  $E_{data}$  can be written as

$$E_{data}(\phi) = \int_{\Omega} \delta(\phi(\mathbf{p})) \int_{\Omega} B(\mathbf{p}, \mathbf{q}) F(I, \phi, \mathbf{q}) d\mathbf{q} d\mathbf{p}, \quad (7.2)$$

where  $F(I, \phi, \mathbf{q}) = H(\phi(\mathbf{q})) \cdot (I(\mathbf{q}) - u_x)^2 + (1 - H(\phi(\mathbf{q}))) \cdot (I(\mathbf{q}) - v_x)^2$  and  $\delta(\cdot)$  is the Dirac function. The function  $B(\cdot)$  is a binary mask defined as

$$B(\mathbf{p}, \mathbf{q}) = \begin{cases} 1, & \text{if } \mathbf{q} \in N(\mathbf{p}) \\ 0, & \text{otherwise} \end{cases} \quad (7.3)$$

where  $\mathbf{q}$  is a spatial variable that represents a single point in  $\Omega$  and  $N(\mathbf{p})$  corresponds to a user-defined neighborhood of point  $\mathbf{p}$ . The quantities  $u_x$  and  $v_x$  correspond to the localized version of the inside and outside average intensity values measured in the window  $N(\mathbf{p})$ .

Minimizing  $E_{data}$  (7.2) with respect to  $\phi$  leads to the following level-set equation:

$$\frac{\partial \phi}{\partial \tau}(\mathbf{p}) = -\delta(\phi(\mathbf{p})) \cdot \int_{\Omega} B(\mathbf{p}, \mathbf{q}) \nabla_{\phi} F(I, \phi, \mathbf{q}) d\mathbf{q}. \quad (7.4)$$

From eq.(7.4), it is apparent that,  $N(\mathbf{p})$  defines to which extent the algorithm is localized: at each point  $\mathbf{p}$  of the interface, the term driving the evolution is computed only in the neighbourhood  $N(\mathbf{p})$  surrounding  $\mathbf{p}$  (instead of being computed from the whole image, as in the usual level set formulation).

As indicated in [Lankton and Tannenbaum (2008)] the size of  $N(\mathbf{p})$  is mainly linked to the size of the object to recover: it should be small enough so that the interface is not attracted by nearby structures that are not to be detected (in the limit, if  $N(\mathbf{p})$  is very large, the algorithm is then equivalent to the usual Chan-Vese algorithm and will perform a global segmentation). Conversely if  $N(\mathbf{p})$  is too small, there is a risk that the interface will not move since it is too far from the object borders.

### 7.3 Shape prior term

As described in Chapter 6, the shape prior  $\psi$  is based on hyperquadrics, as defined in equation 6.6. This is done by minimizing the energy  $E_{shape}$  defined in (6.7) which we recall hereunder:

$$E_{shape}(\phi, \boldsymbol{\lambda}) = \int_{\Omega} \psi^2(\mathbf{p}, \boldsymbol{\lambda}) \cdot \|\nabla \phi(\mathbf{p})\| \cdot \delta(\phi(\mathbf{p})) d\mathbf{p}, \quad (7.5)$$

This minimization is performed in two steps: first with respect to  $\phi$  yielding the following evolution equation:

$$\frac{\partial \phi}{\partial \tau}(\mathbf{p}) = \delta(\phi(\mathbf{p})) \cdot \left( \frac{\langle \nabla \psi(\mathbf{p}, \boldsymbol{\lambda}), \nabla \phi(\mathbf{p}) \rangle}{\|\nabla \phi(\mathbf{p})\|} + \psi^2(\mathbf{p}, \boldsymbol{\lambda}) \cdot \kappa \right). \quad (7.6)$$

Then keeping  $\phi$  fixed, the energy is minimized with respect to the hyperquadrics parameters  $\boldsymbol{\lambda}$  using the fitting algorithm 1 described in Section 6.4.

### 7.4 Thickness term

Since we are dealing with the evolution of a shape bounded by two contours, it might happen that they are both attracted by the same image feature, leading to the merging of both contours. In our experiments, we observed that this happened in about 15% of the segmentations. It is thus important to prevent both contours from merging since this

leads to results that are not meaningful. However it is also important to ensure that this will not modify the behavior of the algorithm when there is no merging problem. This is done in our approach by locally constraining the level-set to have a minimum thickness.

The idea of using such a local thickness term to constrain level-set segmentation has been initially proposed by [Zeng *et al.* (1998)] for cortex segmentation in MR. This initial approach has then been used for 2D cardiac images in US by [Paragios (2002)], in MR by [Lynch *et al.* (2006)] and tested against incompressibility constraint for 3D cardiac US data in [Zhu *et al.* (2010)]. In these works, the object to be segmented is modelled as two distinct level-sets and the constraint is directly introduced in the evolution equation as a term coupling the two level-sets. Our approach is different due to the fact that the two contours are represented as a single implicit function. This allows expressing the constraint as an energy to be minimized and thus deriving the corresponding evolution in a variational framework, which depends only on the level-set  $\phi$ . Let us note that [Chen *et al.* (2008)] also recently described a thickness constraint as an energy to be minimized. However, in this formulation the object is modelled as two distinct level-sets and the constraint essentially acts as a global term minimizing the overall deviation from the average thickness of the myocardium. In our formulation the constraint is applied locally, stopping the evolution in the region of the interfaces where the minimum thickness is not met.

Formally, we define the energy term such that it will allow the level-set to evolve only if the distance between the inner and outer contour is lower than a predefined thickness  $R_T$ .

$$E_{thickness}(\phi) = \int_{\Omega} \phi(\mathbf{p} + R_T \mathbf{N}) \cdot H(\phi(\mathbf{p} + R_T \mathbf{N})) \cdot \delta(\phi(\mathbf{p})) d\mathbf{p}, \quad (7.7)$$

where  $\mathbf{N}$  corresponds to the inward normal of a point  $\mathbf{p} \in \Gamma$ . From (7.7), it is clear that this energy is null when all the point at a distance  $R_T$  along the inward normal of the contours are inside points. Minimizing this energy thus guarantees that the thickness of the contour will be at least  $R_T$  but do not put any constraint on the maximal thickness between the two contours.

The evolution term is obtained by deriving the equation (7.7) with respect to  $\phi$  and writes as:

$$\frac{\partial \phi}{\partial \tau}(\mathbf{p}) = -H(\phi(\mathbf{p} + R_T \mathbf{N})) \cdot \delta(\phi(\mathbf{p})). \quad (7.8)$$

The complete derivation of this term is given in A.

Fig. 7.2 illustrates the principle of this term. In Fig. 7.2(a), we show a simulated image composed of two disks, one inside the other. The centers of the disks are not the same and thus the thickness of the object is not homogeneous. The left part of the object has been occluded in order to mimic a loss of contrast that may occur in echocardiographic scans. We also show the zero-level of  $\phi$  at a point in the evolution process where the inner and outer contour are about to merge. Fig. 7.2(b) shows a 1D profile of  $\phi$  along the yellow line seen in Fig. 7.2(a) while Fig. 7.2(c) shows the corresponding Heaviside function  $H(\phi)$ . In Fig. 7.2(c), at point  $\mathbf{p}_2$ , the distance between the two contours (red points) is higher than  $R_T$ . Thus  $\mathbf{p}_2 + R_T \mathbf{N}$  is an inside point,  $H(\phi(\mathbf{p}_2 + R_T \mathbf{N}))$  is equal to 0 and so is

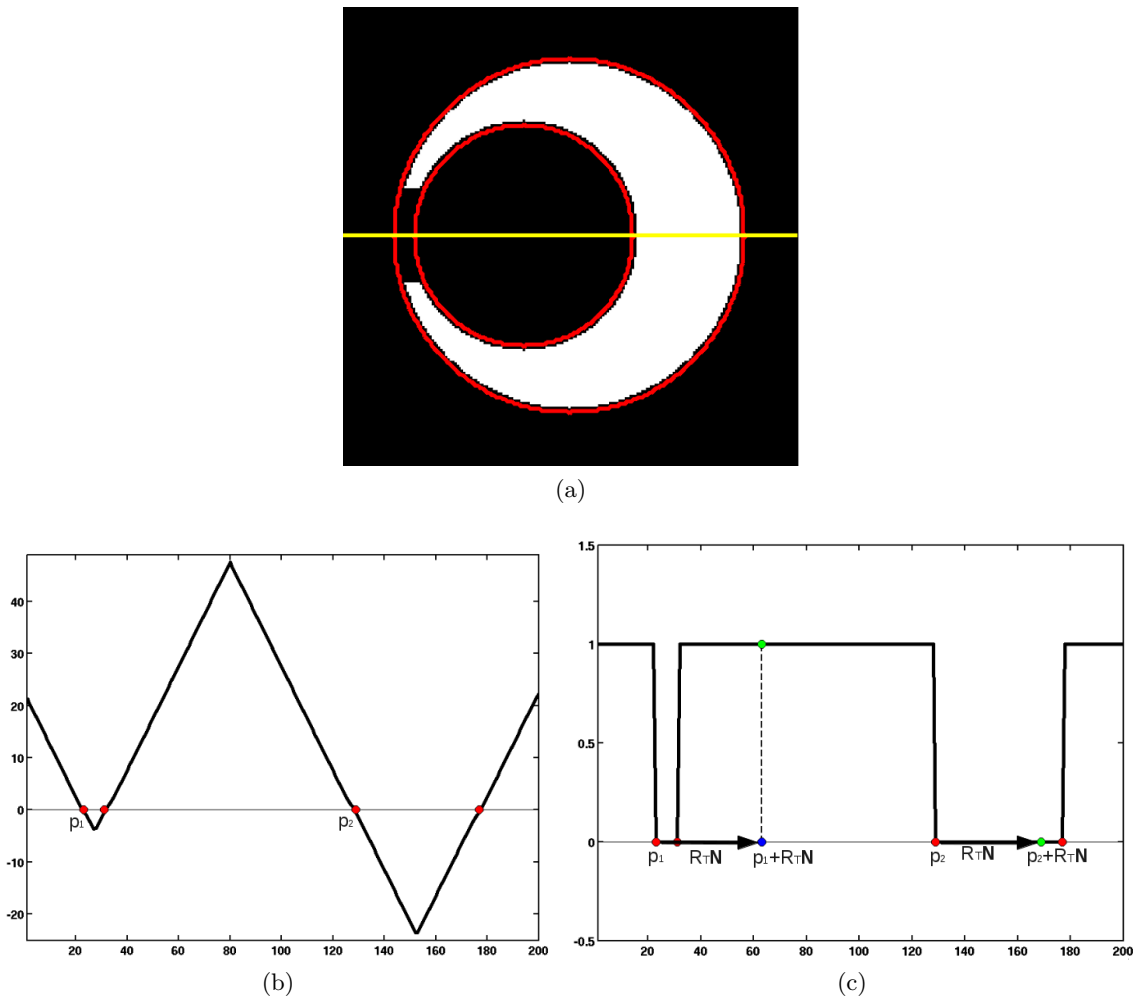


Figure 7.2: Principle of the thickness term: (a) simulated image with the zero-level of an evolving level-set  $\phi$  shown in red; (b) 1D-profile of  $\phi$  along the yellow line of (a); (c)  $H(\phi)$ . In (b) and (c) the red dots corresponds to the zero-level of  $\phi$ . The blue points in (c) correspond to points at a distance  $R$  from  $\mathbf{p}_1$  and  $\mathbf{p}_2$  with their respective value of  $H(\phi)$  shown as the green dots.

the thickness evolution term (7.8). On the opposite for the point  $\mathbf{p}_1$ , the two contours are too close, the value of  $H(\phi(\mathbf{p}_2 + R_T \mathbf{N}))$  is equal to 1, and the level-set will thus evolve according to (7.8). It is therefore apparent that the energy (7.7), will be minimized (and equal to 0) when the distance between the contours is at least  $R_T$ .

Fig. 7.3 shows the final segmentation of the image shown in Fig. 7.2(a). In this illustrative binary image example, we use the classical Chan-Vese data attachment term [Chan and Vese (2001)] and no shape prior. Fig. 7.3(a) gives the result obtained without the thickness term. In that case, since the left part of the image is occluded, the two evolving contours merge, leading to an unsatisfactory segmentation result. On the contrary, by including the thickness term in the evolution equation, the merging of the two contours does not occur yielding the desired segmentation (Fig. 7.3(b)).



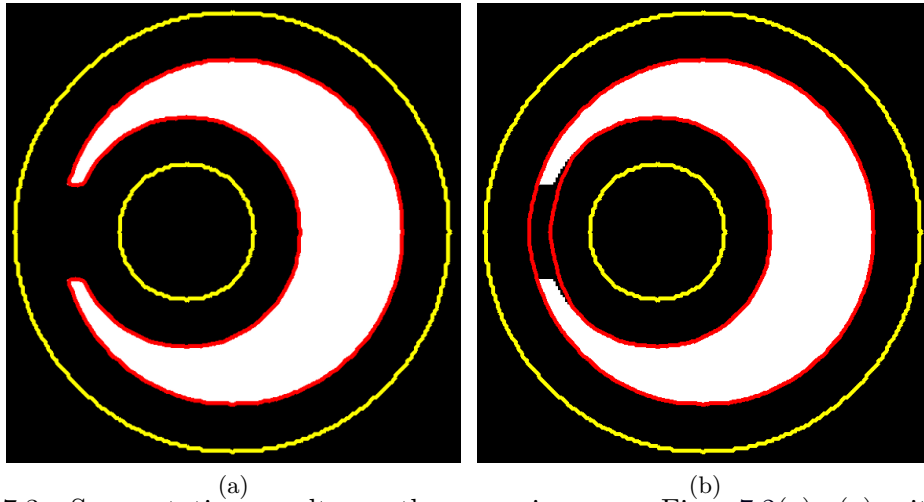


Figure 7.3: Segmentation results on the same image as Fig. 7.2(a), (a) without the thickness term and (b) with the thickness term. The initialisation is shown in yellow and the segmentation result in red.

## 7.5 Implementation issues

### 7.5.1 Level-set evolution

We implemented our level-set evolution equation using standard finite difference scheme [Osher and Fedkiw (2002)], where the implicit function is represented by a signed distance function  $\phi$ . In order to improve efficiency, we only compute values of  $\phi$  in a narrow band around the zero level-set.

Consequently, we re-initialize  $\phi$  every iteration using a fast marching scheme [Sussman *et al.* (1998)]. In order to perform segmentation with a shape prior, the level-set evolves according to the following equation:

$$\frac{\partial \phi}{\partial \tau}(\mathbf{p}) = f(\mathbf{p}) + g(\mathbf{p}) + h(\mathbf{p}), \quad (7.9)$$

where  $f(\cdot)$  is the data attachment term given in equation (7.4),  $g(\cdot)$  is the shape prior term given in equation (7.6) and  $h(\cdot)$  is the thickness term given in equation (7.8).

As in [Lankton and Tannenbaum (2008)] the neighbourhood  $N(\mathbf{p})$  defining the localization of the algorithm is chosen in our case as a circular neighbourhood, with radius  $R_N$  (*i.e.* we assume isotropic image properties). Given that we use a close initialisation (*i.e.* assumed to be on the order of  $R_N$  pixels apart from the desired border),  $R_N$  was thus chosen as the average thickness of the myocardium, *i.e.* 15 pixels in our case. In the same way, the value of  $R_T$  in the thickness term (7.7) was chosen to be set to 5 pixels.

### 7.5.2 Image subdivision and ROI definition

In parasternal long-axis or apical images, the endocardium or epicardium are not closed contours and are only defined on the left or top side of the image respectively (see

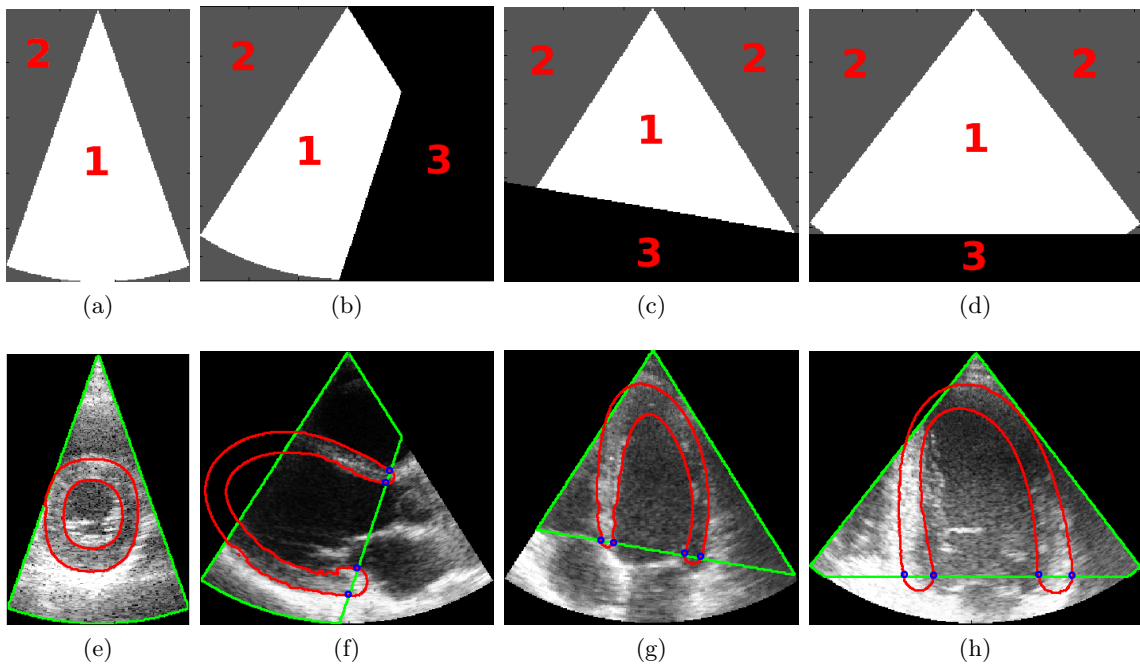


Figure 7.4: Definition of the ROI mask. ROI mask for a parasternal short-axis (a), parasternal long-axis (b), apical 4-chamber (c) and apical 2-chamber (d) views and the corresponding image (e), (f), (g) and (h). The evolving curve is shown in red, the ROI in green and the intersection points used for the fit of the two semi-circles are the blue dots.

Fig. 7.4(f)-7.4(h)). It is thus necessary to define different regions according to the presence or absence of the left ventricle and of image information. The user is thus asked to give two points corresponding to the position of the valves and a mask is then created. This mask defines 3 regions as follows:

- possible presence of the left ventricle and image information is available (for example area 1 in 7.4(b)). In this region both the data attachment term and the shape prior term are used for the evolution of the level-set function.
- possible presence of the left ventricle but outside of the imaged sector (for example area 2 in 7.4(b)). In this region only the shape prior term is used for the evolution of the level-set function.
- left ventricle is absent (for example area 3 in 7.4(b)). Two half circles are fitted on the 4 intersection points between the evolving curve and the ROI (blue points in 7.4(b)), in order to get a closed contour with similar shape as the left ventricle.

Note that in the particular case of parasternal short-axis views, the area 3 is not used (as shown in Fig. 7.4(a) and 7.4(e)).

### 7.5.3 Initialization procedure

Finally, let us note that the adoption of a localized framework of [Lankton and Tannenbaum (2008)] imposes an initialisation not too far from the desired solution, in order

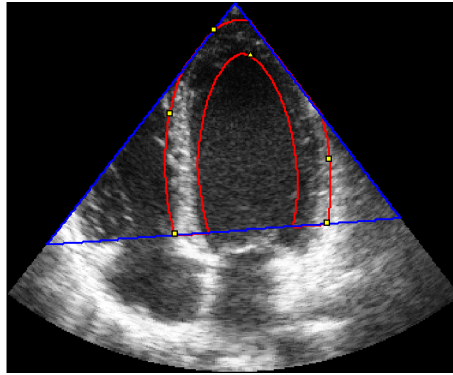


Figure 7.5: Example of initialisation. Yellow dots: Initial points; Red: Corresponding ellipses; Blue: ROI

to obtain meaningful results. The following procedure is thus considered to initialize our algorithm. The user is asked to position only six points. Five points are first positioned near the epicardium. These 5 points are used to fit an initial ellipse (one ellipse is uniquely defined by 5 points). Note that for parasternal long-axis and apical views the two first points are also used to define the ROI as explained in section 7.5.2. One last point is then positioned near the endocardium and is used to obtain a second concentric ellipse. The accuracy to which these initial points have to be placed to yield a satisfactory segmentation corresponds to the size of the local data-attachment term of Lankton’s energy functional and thus to the radius  $R_N$  of the localizing mask  $N(\mathbf{p})$ . As mentioned in the previous sections,  $R_N$  is set to 15 pixels in our application. These initial points are displayed in yellow in the segmentation examples given in the result section. Fig. 7.5 shows an apical 4-chamber view with the 6 points given by the user and the corresponding initial ellipses.

Note that providing 6 points is still a reasonable interaction, since the cardiologist usually inputs 30 points (on average) to draw the references. Thus this procedure divides the user interaction by 5. Furthermore cardiologists do not have to be as accurate as they would have to be if they were drawing the final contour. It can also be noted that the proposed algorithm will be used as an initialisation for the tracking algorithm proposed in Chapter 9, reducing thereby the user-interaction (for instance 18 points are required to initialize the tracking of the endocardium in [Comaniciu *et al.* (2004)]).

## 7.6 Results

We evaluate in this section the performance of our segmentation algorithm. The dataset as well as the manual references are the same than the one described in 6.5.1. The segmentation results are compared to the mean myocardial shape obtained from the three manual references by following the procedure described in [Chalana and Kim (1997)]. The inter-observer distance (IOD) corresponds to the mean of the distances computed between the references of each expert. The segmentation was performed using the parameters given

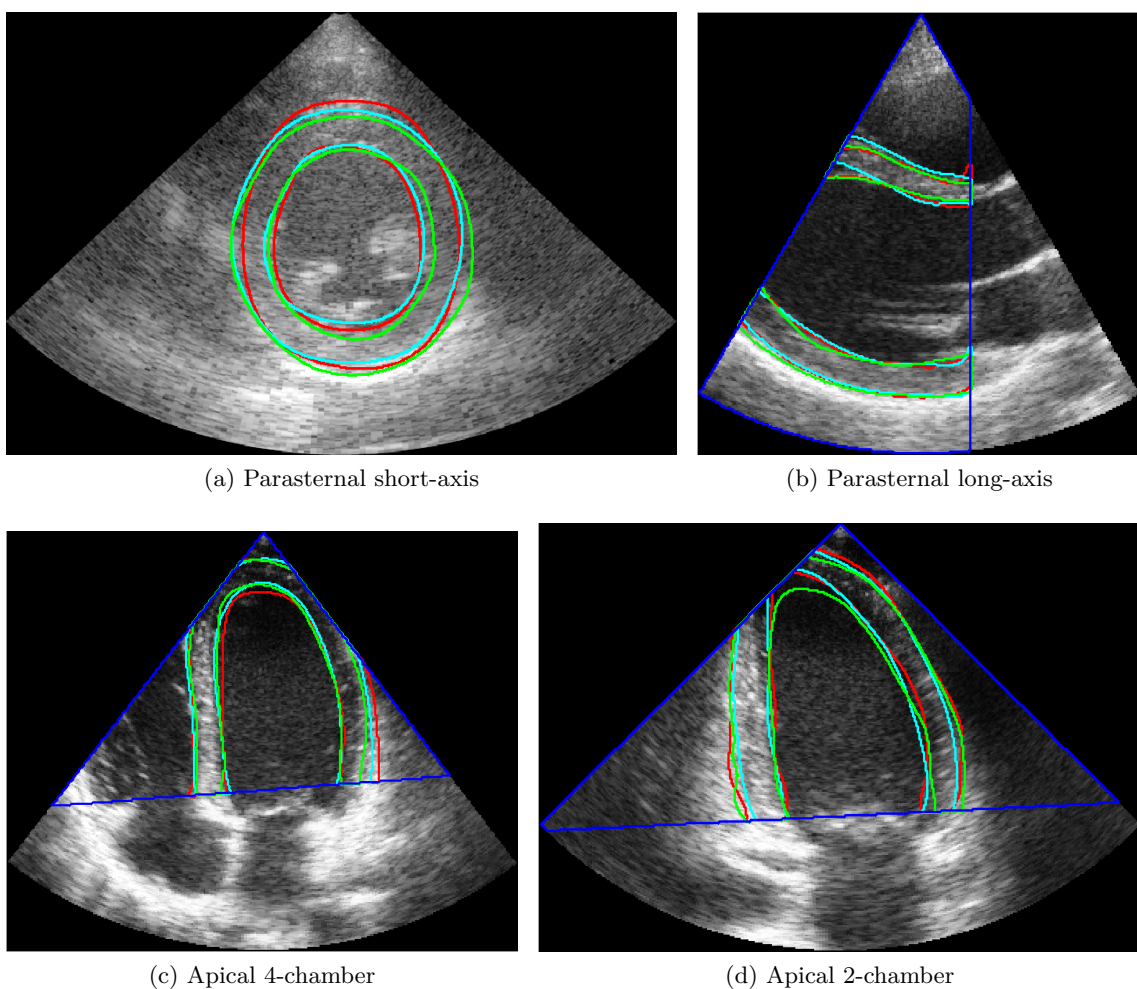


Figure 7.6: References from the three expert cardiologists in the different views. In red: expert 1, in green: expert 2, in cyan: expert 3 and in blue the region of interest.

in section 7.5 and the 6 points required for the initialisation were provided by a fourth cardiologist.

In Fig. 7.6, we show an example of the references from the three experts in order to illustrate the inter-observer variability. We show in Fig. 7.8 and Fig. 7.9 the corresponding segmentation results, the reference contour and the error measures on end-diastolic (ED) and end-systolic (ES) images respectively.

Table 7.1 and 7.2 provide the mean and standard deviation of the error measures obtained for the complete data set on epicardial and endocardial borders, respectively. In each table, we give for each measures (modified Dice, MAD, Hausdorff) the IOD (three first columns), the error measures associated to the proposed method (three middle columns) and to Hamou’s method (three last columns). Fig. 7.7 allows to visually compare these results in every view and for each border.

Concerning the proposed approach, the segmentation of the epicardial border in the parasternal short-axis view (first line in Table 7.1) yields small values for the modified Dice ( $3.89 \cdot 10^{-2}$ ) and the MAD (1.07mm). While the modified Dice and MAD allow evaluating the global quality of the segmentation, the HD provides an upper bound on the error and

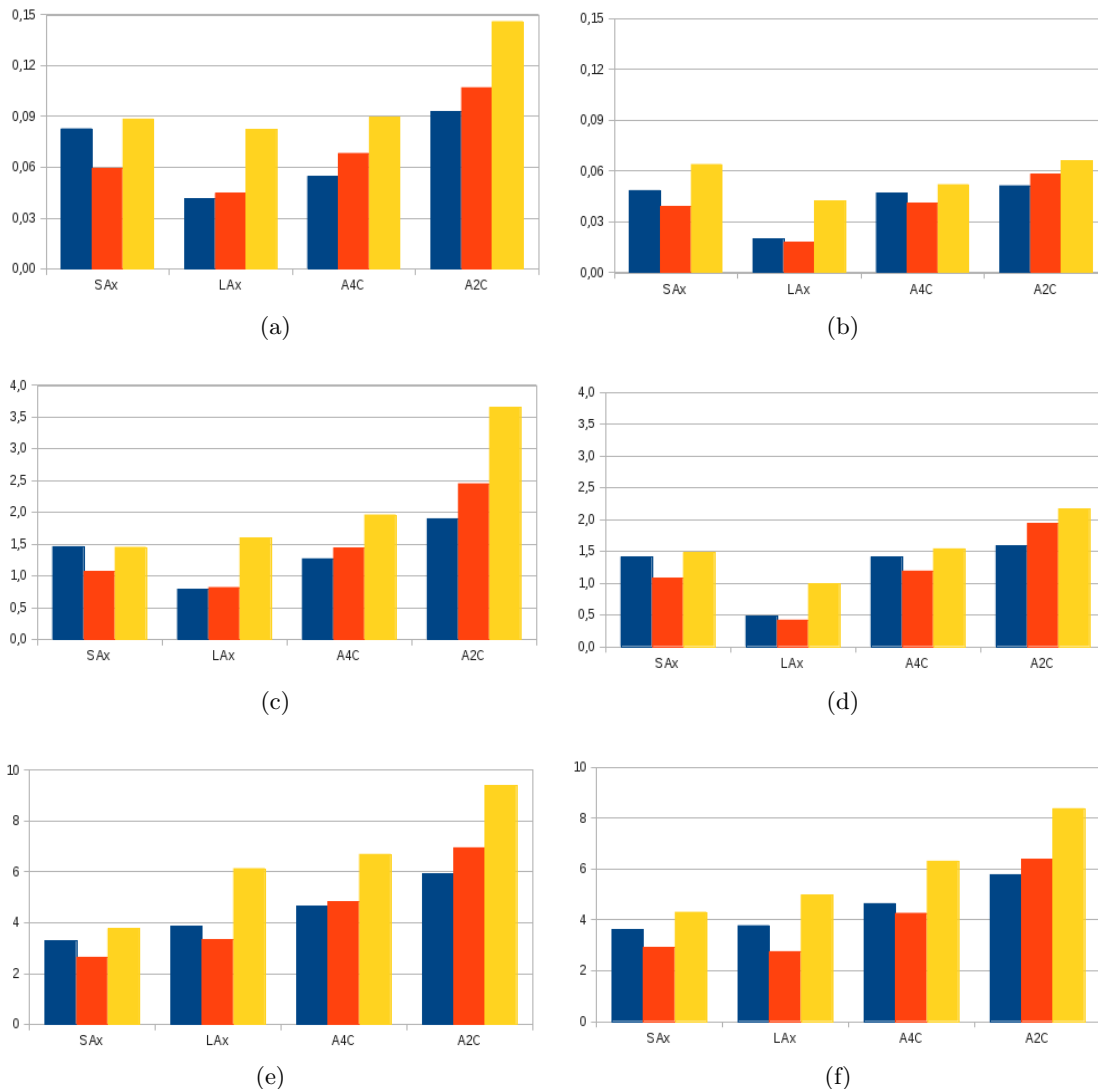


Figure 7.7: Results of the segmentation of the endocardial (first column) and epicardial (last column) borders in terms of modified Dice coefficient (first row), MAD (second row) and Hausdorff distance (third row). The MAD and Hausdorff distance are given in mm. Blue: Inter-Observers Distance; Red: results of our method; Yellow: results of [Hamou and El-Sakka (2010)].

is 2.96mm for this orientation. The comparison of these values with the corresponding IOD (three first columns in Table 7.1) allows interpreting them in a relative perspective. For the parasternal short-axis view, it may be observed that the values obtained using the proposed method are slightly lower than the inter-observer ones ( $4.85 \cdot 10^{-2}$ , 1.41mm and 3.62mm for the modified Dice, the MAD and the HD respectively). This thus indicates that the segmentation provides consistent results in the sense that the difference with the experts' reference is comparable to or even smaller than the distance between experts.

|                        | IOD  |                  |                | Our method                                       |                 |                 | Hamou  |                               |                             |
|------------------------|--|------------------|----------------|--|-----------------|-----------------|--|-------------------------------|-----------------------------|
|                        | $D^*$  | MAD              | HD             | $D^*$  | MAD             | HD              | $D^*$  | MAD                           | HD                          |
| Parasternal short-axis | $4.85 \cdot 10^{-2}$<br>( $1.33 \cdot 10^{-2}$ ) | 1.41<br>(0.754)  | 3.62<br>(1.86) | $3.89 \cdot 10^{-2}$<br>( $1.04 \cdot 10^{-2}$ ) | 1.07<br>(0.518) | 2.96<br>(1.23)  | $6.39 \cdot 10^{-2}$<br>( $3.27 \cdot 10^{-2}$ ) | 1.51 <sup>†</sup><br>(0.387)  | 4.35 <sup>†</sup><br>(1.23) |
| Parasternal long-axis  | $1.99 \cdot 10^{-2}$<br>( $0.6 \cdot 10^{-2}$ )  | 0.484<br>(0.197) | 3.77<br>(1.96) | $1.78 \cdot 10^{-2}$<br>( $0.6 \cdot 10^{-2}$ )  | 0.418<br>(0.13) | 2.75<br>(0.686) | $4.22 \cdot 10^{-2}$<br>( $3.25 \cdot 10^{-2}$ ) | 0.991 <sup>†</sup><br>(0.651) | 4.98 <sup>†</sup><br>(2.43) |
| Apical 4-chamber       | $4.71 \cdot 10^{-2}$<br>( $1.8 \cdot 10^{-2}$ )  | 1.41<br>(0.679)  | 4.64<br>(2.06) | $4.11 \cdot 10^{-2}$<br>( $1.15 \cdot 10^{-2}$ ) | 1.18<br>(0.287) | 4.41<br>(1.15)  | $5.2 \cdot 10^{-2}$<br>( $1.62 \cdot 10^{-2}$ )  | 1.54 <sup>†</sup><br>(0.435)  | 6.23 <sup>†</sup><br>(1.59) |
| Apical 2-chamber       | $5.13 \cdot 10^{-2}$<br>( $1.4 \cdot 10^{-2}$ )  | 1.59<br>(0.691)  | 5.78<br>(1.83) | $5.82 \cdot 10^{-2}$<br>( $2.34 \cdot 10^{-2}$ ) | 1.85<br>(0.694) | 6.06<br>(1.38)  | $6.6 \cdot 10^{-2}$<br>( $2.22 \cdot 10^{-2}$ )  | 2.06 <sup>†</sup><br>(0.543)  | 7.74<br>(2.02)              |

Table 7.1: Results of the segmentation of the epicardial border. The results of our method and the one described in [Hamou and El-Sakka (2010)] as well as the Inter-Observers Distance (IOD) are shown in term of modified Dice criterion ( $D^*$ ), Mean Absolute Distance (MAD) and Hausdorff distance (HD). The given values correspond to the mean (Standard deviation). HD and MAD are given in mm. † indicates that the difference was found significant ( $p < 0.05$ ) when compared to our method.

|                        | IOD  |                 |                | Our method                                       |                  |                | Hamou  |                             |                             |
|------------------------|--|-----------------|----------------|--|------------------|----------------|--|-----------------------------|-----------------------------|
|                        | $D^*$  | MAD             | HD             | $D^*$  | MAD              | HD             | $D^*$  | MAD                         | HD                          |
| Parasternal short-axis | $8.27 \cdot 10^{-2}$<br>( $2.85 \cdot 10^{-2}$ ) | 1.46<br>(0.658) | 3.28<br>(1.35) | $5.94 \cdot 10^{-2}$<br>( $2.14 \cdot 10^{-2}$ ) | 1.25<br>(0.693)  | 2.87<br>(1.4)  | $8.85 \cdot 10^{-2}$<br>( $3.17 \cdot 10^{-2}$ ) | 2.01 <sup>†</sup><br>(1.24) | 4.33 <sup>†</sup><br>(1.71) |
| Parasternal long-axis  | $4.14 \cdot 10^{-2}$<br>( $1.63 \cdot 10^{-2}$ ) | 0.792<br>(0.41) | 3.85<br>(1.62) | $4.46 \cdot 10^{-2}$<br>( $3.53 \cdot 10^{-2}$ ) | 0.818<br>(0.559) | 3.32<br>(1.49) | $8.24 \cdot 10^{-2}$<br>( $5.09 \cdot 10^{-2}$ ) | 1.6 <sup>†</sup><br>(0.778) | 6.13 <sup>†</sup><br>(2.08) |
| Apical 4-chamber       | $5.46 \cdot 10^{-2}$<br>( $1.63 \cdot 10^{-2}$ ) | 1.27<br>(0.535) | 4.66<br>(2)    | $6.82 \cdot 10^{-2}$<br>( $2.29 \cdot 10^{-2}$ ) | 1.48<br>(0.554)  | 4.88<br>(1.47) | $8.94 \cdot 10^{-2}$<br>( $3.86 \cdot 10^{-2}$ ) | 2.2 <sup>†</sup><br>(1)     | 7.82 <sup>†</sup><br>(3.46) |
| Apical 2-chamber       | $9.29 \cdot 10^{-2}$<br>( $3.29 \cdot 10^{-2}$ ) | 1.9<br>(0.871)  | 5.91<br>(2.16) | 0.107<br>( $5.24 \cdot 10^{-2}$ )                | 2.44<br>(0.946)  | 6.77<br>(1.71) | 0.146 <sup>†</sup><br>( $5.79 \cdot 10^{-2}$ )   | 3.83 <sup>†</sup><br>(1.53) | 10.6 <sup>†</sup><br>(4.31) |

Table 7.2: Results of the segmentation of the endocardial border. The results of our method and the one described in [Hamou and El-Sakka (2010)] as well as the Inter-Observers Distance (IOD) are shown in term of modified Dice criterion ( $D^*$ ), Mean Absolute Distance (MAD) and Hausdorff distance (HD). The given values correspond to the mean (Standard deviation). HD and MAD are given in mm. † indicates that the difference was found significant ( $p < 0.05$ ) when compared to our method.

The results associated with the endocardial borders in the same parasternal short-axis view (first line in Table 7.2), show that the errors are in the same order and slightly larger:  $5.94 \cdot 10^{-2}$  for the modified Dice, 1.25mm for the MAD and 2.87mm for the HD. These values are also in the same order and slightly better than the corresponding IOD ( $8.27 \cdot 10^{-2}$  for the modified Dice, 1.46mm for the MAD and 3.28mm for the HD). This is linked to the fact that the segmentation of the endocardial border is generally less smooth than the epicardial one and moreover implies exclusion of the papillary muscles present in the image.

Considering now the 3 other orientations (lines 2 to 4 in Table 7.1 and 7.2), a variation in the performances may be observed. The results obtained for the parasternal views are better than the results corresponding to the apical view: considering the MAD and the epicardial border (Table 7.1, fifth column), the observed values are 1.07mm and 0.418mm for the parasternal short-axis and long-axis views, whereas they are 1.18mm and 1.85mm for the apical 4-chambers and 2-chambers views. The same trend holds for the endocardial border (Table 7.2, fifth column) and the other error measures (modified Dice and HD, fourth and sixth columns). This situation is linked to the variations in image quality and content, as illustrated in Fig. 7.8 and 7.9: while the regions corresponding to the myocardium are well-defined in parasternal views (Fig. 7.8(a), 7.8(b), 7.9(a) and 7.9(b)), in the apical views the region of the apex is commonly located in the near field of the probe (Fig. 7.8(c), 7.8(d), 7.9(c) and 7.9(d)) and is thus usually blurred, yielding missing boundaries of significant size. In these cases, the shape prior is able to cope with this missing information and to provide meaningful results, but induces a lower accuracy.

The standard deviation for the epicardial border varies between  $6 \cdot 10^{-3}$  and  $2.34 \cdot 10^{-2}$  for the modified Dice criterion, 0.13 and 0.694 for the MAD and 0.686 and 1.38 for the HD. These values are in the same order than the standard deviation obtained for the experts' outline boundaries, showing that the segmentation results do not deviate from the mean value more than the experts' outlined boundaries do. The same conclusion can be drawn for the endocardial detection where the standard deviation varies between  $2.14 \cdot 10^{-2}$  and  $5.24 \cdot 10^{-2}$  for the modified Dice criterion, 0.554 and 0.946 for the MAD and 1.4 and 1.71 for the HD.

To illustrate the quality of the results, we show in Fig. 7.10 one of the best and one of the worst results of the algorithm, along with the corresponding error measures (MAD and Hausdorff) and the inter-observer variability. The good result was obtained from a parasternal long-axis image with a good image quality and where both borders can clearly be seen. Indeed the contrast between the myocardium muscle and the blood pool or the surrounding tissue is very high (area 1 of Fig. 7.10(a)), there is no shadowing artifact, yielding a proper segmentation.

On the other hand, when dealing with an image of bad quality, where part of the myocardium is occluded (area 1 of Fig. 7.10(b)) or in the near field area of the probe (area 2 of Fig. 7.10(b)), the segmentation is worsened as can be seen in the apical 2-chamber view (Fig. 7.10(d)). Indeed in those area, the statistics of the inside and outside

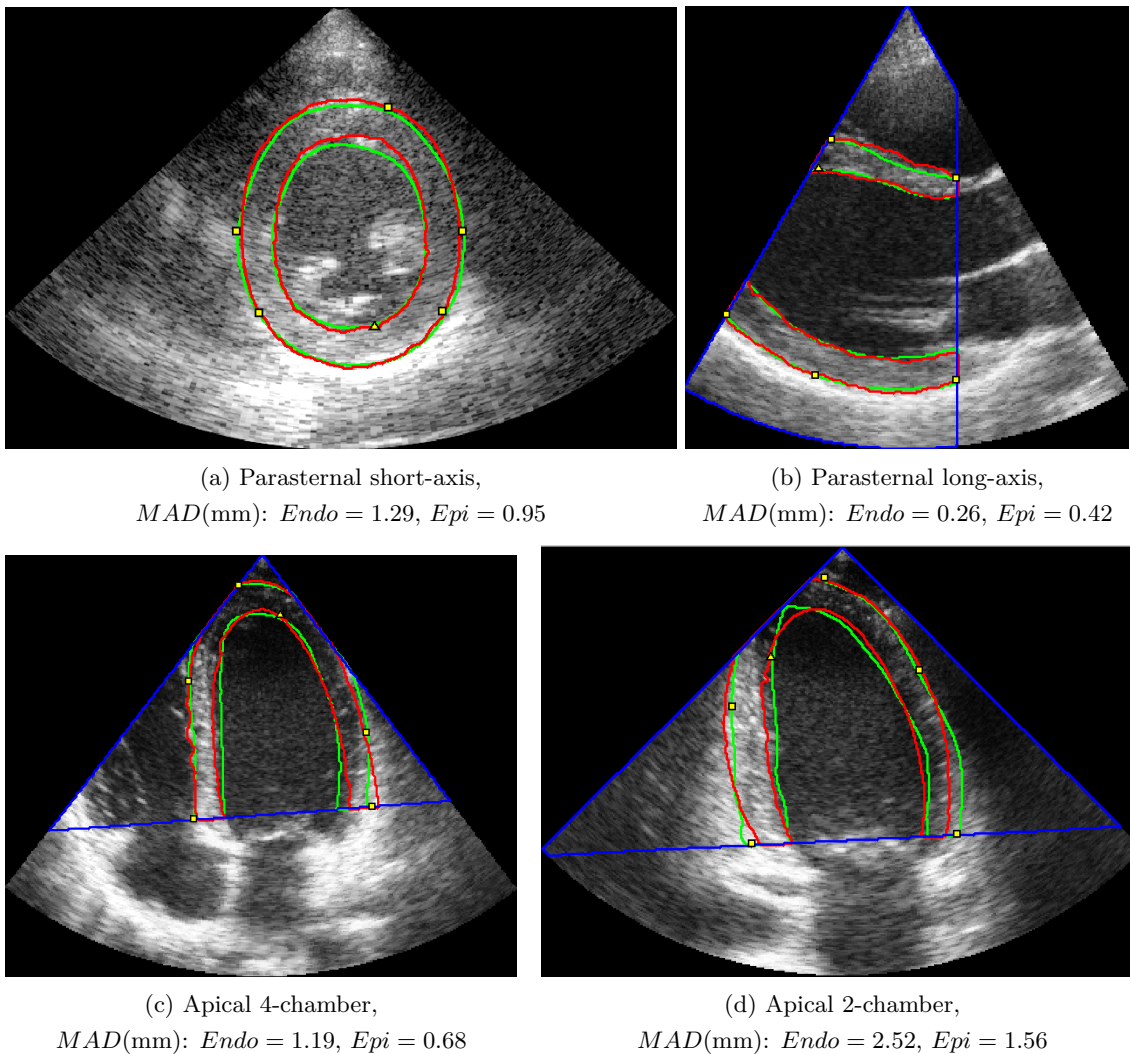


Figure 7.8: Results of segmentation of our method on end-diastolic images. In blue the region of interest, in green the mean reference of the cardiologists, in red our contour. The yellow dots are the 6 points given by a third expert. For each view, the MAD (in mm) computed between the segmentation result and the mean contour is given.

are identical and thus the level set does not evolve. Moreover, the contour has been attracted to an intensity variation inside the septum wall (area 3 of Fig. 7.10(b)), that is greater than the intensity difference between the septum wall and the blood pool.

Consistently, it may be observed that the errors measures are higher for the bad quality image. It is also to be noted that these errors are on the same order than the inter-observer variability, confirming the difficulty of such image and showing that the algorithm provides results with an accuracy comparable to the one associated to the cardiologists.

The results provided in the last three columns in Tables 7.1 and 7.2 allow comparing the performance of the proposed method and Hamou’s method. These results show that our method always yields better performance. Considering the mean differences between the error measures associated with the two approaches, the HD of our method is 1.5mm lower and the MAD is 0.5mm lower which corresponds to at least a 25% improvement of the result. This can be explained by the fact that our shape prior is better suited for



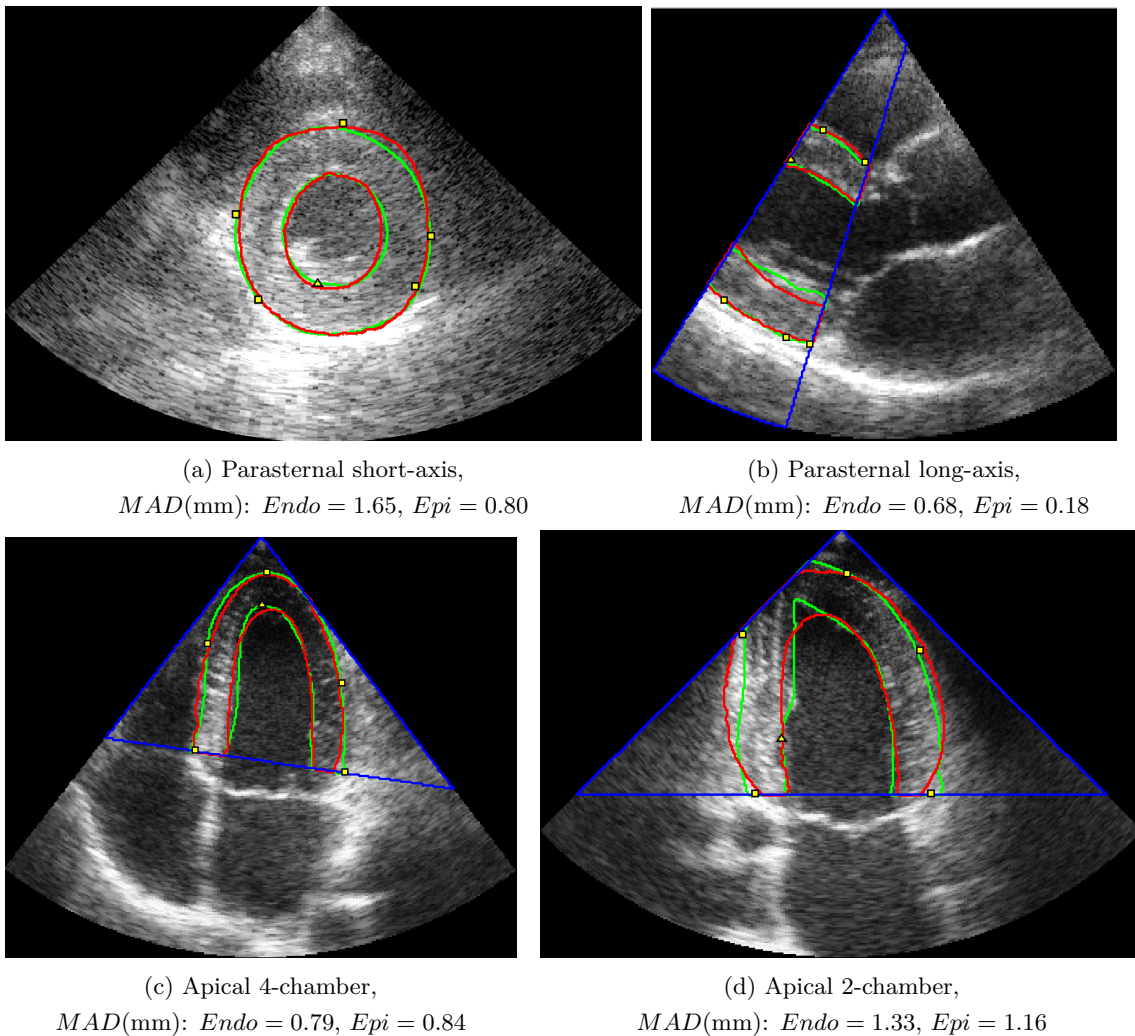


Figure 7.9: Results of segmentation of our method on end-systolic images. In blue the region of interest, in green the mean reference of the cardiologists, in red our contour. The yellow dots are the 6 points given by a third expert. For each view, the MAD (in mm) computed between the segmentation result and the mean contour is given.

the modelling of the heart boundaries as was shown in Section 6.5.2. This allows our segmentation algorithm to better handle missing boundaries or intensity inhomogeneities inside the myocardium. Note that all these differences have been found to be statistically significant at a level  $p = 0.05$  using the Friedman rank test, except for the Hausdorff distance evaluated on the epicardial contour in the apical 2-chamber view, where the two methods performs similarly.

It has to be noted that the six points used for the initialisation of the algorithm often belong to the segmentation results (as shown in Fig. 7.8 and 7.9. This can be simply explained by the fact that the initial points are generally put by experts in regions where it is easy to delineate the myocardial border, which corresponds to regions with high contrast. Thus the evolving contour does not move far away from those points.

As a final remark, let us note that the computational time required for one segmentation varies between 30 seconds and 1 minute, with a non optimized Matlab implementation ran on a 3.06 GHz Core Duo laptop, with 3.9 GB RAM running Fedora 14.

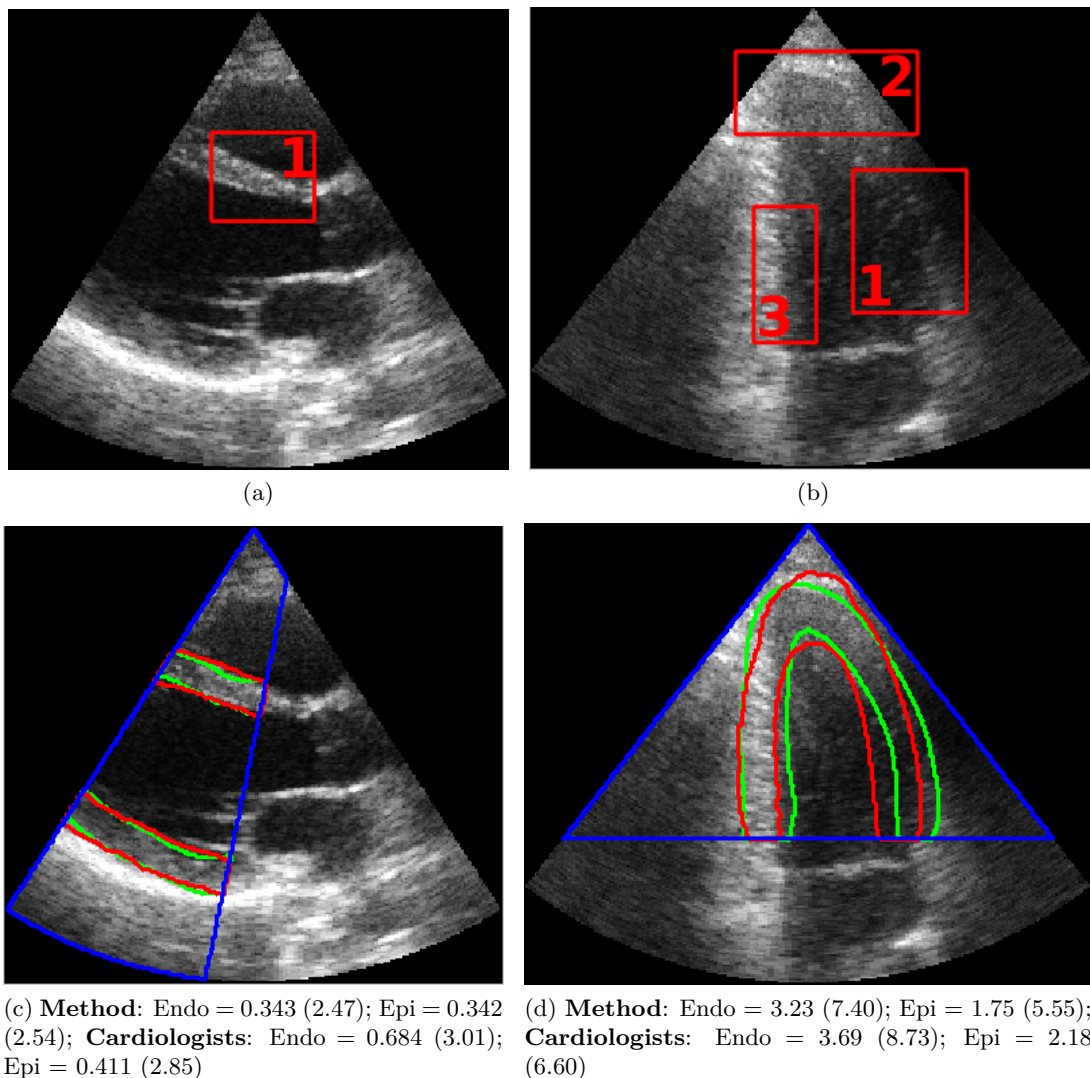


Figure 7.10: Top row: Parasternal long-axis and apical 2-chamber view images; Bottom row: Segmentation result on the same image as (a) and (b). Red: Segmentation result; Green: Mean reference contour; Blue ROI. For each segmentation result, we give the MAD (HD) value in mm for the proposed method and the cardiologists.

## 7.7 Conclusion

In this chapter, we proposed an algorithm to segment the whole myocardium in any of the classical views used in clinical routine. To deal with intensity inhomogeneities and signal drop-out encountered in echographic images, it combines a local data attachment term and the hyperquadric shape prior term proposed in the previous chapter. Moreover to avoid the merging of the endocardial and epicardial contours, a thickness term is added that imposes locally a minimal thickness. We showed that the segmentation results were consistent with the references of 3 experts cardiologists and that our method compared favorably with an algorithm recently proposed.



IV Segmentation of the whole  
myocardium in echocardiographic  
sequences using level-set constrained with  
motion and shape priors

---



---

---

## Résumé en français

---

Le traitement de séquences d'images offre la possibilité de tirer parti du mouvement de la structure à détecter pour améliorer et rendre plus rapide la segmentation. Si certaines approches se proposent d'utiliser le mouvement comme une information permettant de détecter la structure d'intérêt, d'autres intègrent celui-ci sous la forme d'une contrainte supplémentaire. Dans cette partie, nous faisons tout d'abord un état de l'art des techniques utilisant le mouvement lors de la segmentation. Nous décrivons ensuite une nouvelle énergie basée sur l'hypothèse de conservation des niveaux de la fonction implicite et incluons celle-ci dans l'algorithme décrit dans la partie précédente. Nous validons ensuite la méthode sur une base de données de 20 séquences échocardiographiques (soit environ 1200 images).

### État de l'art

#### Mouvement utilisé en tant qu'information de détection

Une première approche consiste à utiliser le mouvement, estimé conjointement avec la segmentation ou avant la segmentation, comme une information permettant de détecter la structure, au même titre que les informations issues de l'intensité des images. De façon similaire à l'information image, une telle démarche implique donc que le mouvement de l'objet présente des propriétés d'homogénéité permettant de le séparer des autres structures présentes dans la séquence. Les travaux décrits dans [Brox *et al.* (2006), Cremers and Soatto (2005), Ehrhardt *et al.* (2008)] empruntent cette démarche en réalisant de façon conjointe la segmentation et l'estimation de mouvement. On trouvera dans les références [Papin *et al.* (2000), Unal *et al.* (2005), Herbulot *et al.* (2006)] l'application de cette démarche appliquée cette fois à des séquences d'images où le mouvement est estimé *a priori*, à savoir avant la phase de segmentation proprement dite.

---

## Mouvement utilisé en tant que contrainte

D'autres d'auteurs ont abordé la segmentation de séquence d'images en exprimant le mouvement comme une contrainte. L'expression de la contrainte passe souvent par une phase de modélisation réalisée via une ACP. Ainsi, [Kohlberger *et al.* (2006)] aborde la segmentation de séquence d'images tridimensionnelles en réalisant une ACP en 4D et en utilisant une représentation implicite des surfaces considérées. [Cremers (2006)] développe quant à lui une approche qui se situe dans le même esprit que [Jacob *et al.* (1999)] mais est formalisée dans un cadre variationnel et utilise une représentation implicite. Une ACP est réalisée sur chaque image d'un ensemble de séquences d'apprentissage et la modélisation de la dynamique de l'a priori ainsi obtenue est réalisée en représentant l'évolution des paramètres de l'ACP au travers d'un modèle autorégressif d'ordre 2.

Un certain nombre d'autres travaux basés sur une formulation variationnelle ne tirent pas parti d'une modélisation par ACP, mais expriment des contraintes très spécifiques à l'application visée. En imagerie cardio-pulmonaire par IRM, [Zhang and Pless (2005)] utilisent une technique d'apprentissage de variété pour intégrer un a priori de mouvement dans une démarche de segmentation par ensemble de niveaux. L'apprentissage de variété est appliqué à des séquences IRM avant la segmentation afin de représenter les variations temporelles de l'image selon 2 degrés de liberté correspondant aux phases du mouvement cardiaque,  $u$ , et aux phases du mouvement respiratoire,  $v$ . Cet apprentissage conduit les auteurs à introduire un terme d'énergie supplémentaire permettant de contraindre la variation de l'ensemble de niveaux selon les 2 dimensions  $u$  et  $v$  de la variété.

[Zhu *et al.* (2007), Zhu *et al.* (2010)] proposent d'utiliser l'incompressibilité du myocarde pour contraindre la segmentation de séquences d'images échocardiographiques 3D. Dans cette approche, le myocarde est représenté à l'aide de 2 surfaces implicites correspondant à l'endocarde et à l'épicarde, ce qui permet d'exprimer immédiatement le volume myocardique. Le problème est alors formalisé dans un cadre Bayésien où le terme d'attache aux données fait l'hypothèse d'une distribution de Rayleigh et où la variation du volume myocardique autour de la moyenne est modélisée au travers d'une distribution Gaussienne.

## Segmentation contrainte de séquences échocardiographiques

L'approche proposée par [Bosch *et al.* (2002)] constitue une généralisation des modèles actifs d'apparence (AAM) et est appliquée en imagerie échocardiographique ultrasonore. La construction du modèle est réalisée à partir de l'ensemble des images des séquences d'apprentissage et de même la phase de segmentation est appliquée à l'ensemble de la séquence cardiaque à traiter. [Casero and Noble (2008)] proposent quant à eux une généralisation des modèles de forme actifs (ASM) où la dimension temporelle est explicitement prise en compte grâce à l'utilisation d'une ACP à noyau, qui correspond à une forme non-linéaire de l'ACP. Dans une étude récente, [Leung *et al.* (2011)] propose de définir la contrainte en appliquant une ACP au mouvement lui-même. Cette ACP est réalisée

---

en approchant le mouvement inter-image au moyen d'une transformation affine. Ce modèle de mouvement est alors utilisé pour contraindre une estimation de mouvement basée sur le flux optique classique. La connaissance du contour initial dans la séquence et du mouvement ainsi estimé permet alors de segmenter l'ensemble des images de la séquence.

Dans [Malassiotis and Srinatzis (1999)], un modèle de forme est construit via une ACP appliquée à la volée sur les données à traiter: le contour détecté dans une image est ainsi utilisé pour mettre à jour l'ACP et traiter l'image suivante. Un filtrage de Kalman est utilisé pour fusionner l'information fournie par un contour actif de type "snake" dans l'image courante (étape de mesure du filtre) et l'application d'un simple système dynamique d'ordre 0 aux paramètres de l'ACP fournit l'étape de prédiction. Dans le même esprit, [Jacob *et al.* (1999)] utilise également une approche basée sur une ACP et un filtrage de Kalman. Dans ces travaux, l'étape de mesure du filtre de Kalman correspond à l'évaluation du gradient de l'image ou à l'opérateur de phase développé par [Mulet-Parada and Noble (2000)]. L'aspect dynamique est pris en compte en exprimant l'évolution des paramètres du modèle de forme au moyen d'un modèle autorégressif d'ordre 2 dont les paramètres sont estimés sur une séquence d'apprentissage. L'application de ce modèle dynamique permet alors de réaliser la phase de prédiction du filtre. [Comaniciu *et al.* (2004)] a quant à lui formulé la segmentation d'une séquence comme un problème de fusion d'information, basée sur un filtre de Kalman et une forme particulière de l'ACP, nommée ACP fortement adaptée APC-FA. Pour une séquence à traiter, cette dernière consiste à mettre à jour l'ACP avec le contour initial de la séquence, de façon à prendre en compte les variations de forme qui pourraient ne pas être reflétées par l'ACP standard. Dans cette approche, un contour initial est fourni puis est propagé en tenant compte à la fois du mouvement estimé et du modèle de forme. La robustesse de la démarche tient au fait que l'étape de fusion du filtre de Kalman prend en compte les 3 sources d'incertitudes, liées à la dynamique du système d'état associé, au modèle de forme fourni par l'ACP et à la mesure du champ de mouvement. Dans cette approche un système dynamique d'ordre 0 est utilisé.

## **Notre contribution: Segmentation du myocarde dans des séquences échocardiographiques 2D et dans toutes les vues**

Notre dernière contribution consiste à inclure l'information de mouvement dans le formalisme variationnel des ensembles de niveaux afin de segmenter des séquences échocardiographiques. Comme mentionné dans l'état de l'art, ceci peut être fait en considérant le mouvement soit comme une donnée soit comme une connaissance *a priori*. Cependant dans notre cas, la seconde option n'est pas vraiment envisageable puisqu'elle nécessiterait une étape d'apprentissage afin de générer un modèle dynamique du mouvement myocardique, ce qui s'avère très difficile du fait de la complexité du mouvement cardiaque, du fait que ce mouvement est partiellement accessible en 2D et du fait que la généralité de l'approche



---

nécessiterait un tel apprentissage séparé pour les 4 vues échocardiographiques envisagées ici.

Nous avons donc choisi de considérer le mouvement comme une donnée estimée avant la segmentation. L'avantage de cette solution est qu'elle est flexible puisqu'elle permet d'utiliser la méthode d'estimation du mouvement ayant les meilleures performances tout en gardant l'algorithme de segmentation inchangé. Par exemple, l'introduction d'oscillations latérales [Liebgott *et al.* (2009), Guo *et al.* (2012)] proposée récemment, offre la perspective d'une meilleure estimation du mouvement transverse ce qui est une limitation des méthodes actuelles d'estimation.

## Estimation du mouvement

De nombreuses approches ont été proposées pour estimer le mouvement dans des séquences échocardiographiques. Elles reposent sur l'analyse locale du speckle [Mailloux *et al.* (1987), Baraldi *et al.* (1996)], l'analyse multi-échelle du speckle [Behar *et al.* (2004), Sühling *et al.* (2005)] ou des techniques de mise en correspondance de blocs [Strintzis and Kokkinidis (1997), Basarab *et al.* (2008)]. Ces méthodes utilisent l'image mode B pour estimer le mouvement, mais d'autres auteurs ont proposé d'utiliser le signal RF afin de tirer profit de la meilleure résolution axiale dans celui-ci [Lubinski *et al.* (1999), D'hooge *et al.* (2002)]. Une étude intéressante de [Yu *et al.* (2006)] compare ces deux types d'approches. Notons aussi les travaux de [Touil *et al.* (2010)] qui suggèrent de réaliser l'estimation du mouvement en coordonnées polaires. En effet, l'acquisition des séquences par une sonde sectorielle induit un échantillonnage plus faible loin de la sonde.

La méthode retenue pour l'estimation du mouvement a été décrite récemment par [Alessandrini *et al.* (2012)a] et est basée sur le signal monogénique. Ce signal étend le concept du signal analytique à des signaux de plusieurs dimensions [Felsberg and Sommer (2001)]. Tout comme dans [Felsberg (2004)], l'hypothèse de conservation de l'intensité est remplacée par celle de la conservation de la phase monogénique qui est plus robuste. Une approche multi-échelle est aussi utilisée afin de pouvoir estimer précisément des mouvements de grande amplitude. Le mouvement est supposé localement affine et estimé pour plusieurs tailles de voisinage en utilisant la phase monogénique. L'estimation donnant la plus faible erreur résiduelle est retenue et utilisée pour compenser le mouvement inter-image avant de réestimer le mouvement à une échelle plus faible. L'algorithme 2 décrit cette procédure d'estimation.

## Contrainte de mouvement

### Hypothèse

La contrainte de mouvement proposée s'inspire de la théorie du flux optique [Horn and Schunk (1981), Lucas and Kanade (1981)] mais est appliqué au niveau de la fonction implicite  $\phi$  plutôt qu'à l'intensité de l'image. Dans la théorie du flux optique classique, en

supposant que l'intensité d'un pixel reste constante au cours du temps et que le déplacement entre deux instants est faible, on obtient l'équation

$$I_x u + I_y v + I_t = 0 \Leftrightarrow \nabla I \cdot \mathbf{V} + I_t = 0,$$

où  $I$  est la séquence dans laquelle on souhaite estimer le mouvement,  $\mathbf{V} = (u, v)$  est le mouvement et  $I_\alpha = \partial I / \partial \alpha$ . Lors de l'estimation du mouvement, on obtient donc un système sous déterminé d'une équation à deux inconnues (les deux composantes de  $\mathbf{V}$ ) et différentes solutions ont été proposées pour résoudre ce problème (variations lentes du champ de mouvement [Horn and Schunk (1981)], mouvement localement constant [Lucas and Kanade (1981)]).

Dans notre cas, nous faisons l'hypothèse de conservation du niveau de la fonction implicite. Cela se traduit par l'équation suivante:

$$\phi_x u + \phi_y v + \phi_t = 0 \Leftrightarrow \nabla \phi \cdot \mathbf{V} + \phi_t = 0.$$

Comme le mouvement est supposé connu ainsi que la segmentation de la première image, on a donc un système d'une équation à une inconnue  $\phi$  lequel a donc une solution unique.

### Formulation énergétique

Afin de contraindre l'évolution de  $\phi$  à respecter l'hypothèse de conservation des niveaux, nous proposons de minimiser l'énergie suivante:

$$E_{motion}(\phi) = \int_{\Omega} \delta(\phi(\mathbf{p})) (\nabla \phi(\mathbf{p}) \cdot \mathbf{V}(\mathbf{p}) + \phi_t(\mathbf{p}))^2 d\mathbf{p}.$$

Remarquons que dans cette équation, seul le niveau zéro de l'ensemble de niveaux est contraint afin que  $\phi$  conserve des propriétés de carte de distance.

L'équation d'évolution est obtenue en dérivant cette énergie par rapport à  $\phi$ :

$$\frac{\partial \phi}{\partial \tau} = - \frac{\partial E}{\partial \phi} = 2\delta(\phi(\mathbf{p})) (\mathbf{V}^T \mathcal{H}(\phi) \mathbf{V} + \nabla \phi^T \mathcal{J}(\mathbf{V}) \mathbf{V} + \text{Tr}(\mathcal{J}(\mathbf{V})) \nabla \phi^T \mathbf{V}),$$

où  $\tau$  est un temps artificiel,  $\mathcal{H}(\phi)$  la matrice hessienne de  $\phi$ ,  $\mathcal{J}(\mathbf{V})$  la matrice jacobienne de  $\mathbf{V}$  et  $\text{Tr}(A)$  la trace de  $A$ .

Pour segmenter des séquences échocardiographiques, nous proposons d'ajouter ce terme à l'algorithme décrit dans la partie précédente. L'énergie minimisée est alors:

$$E = \nu_d E_{data} + \nu_s E_{shape} + \nu_t E_{thickness} + \nu_m E_{motion},$$

où  $E_{data}$  est le terme local d'attache aux données,  $E_{shape}$  l'*a priori* de forme,  $E_{thickness}$  le terme anti-collision et  $E_{motion}$  la contrainte de mouvement.  $\nu_i$  avec  $i = \{d, s, t, m\}$  sont des hyperparamètres permettant de pondérer l'influence de chaque terme.

---

## Implémentation

### Équation d'évolution

Afin d'éviter d'éventuelles instabilités numériques, les dérivées de  $\phi$  ne peuvent être calculées via des schémas spécifiques appelés schémas Upwind [Osher and Sethian (1988)]. Dans notre cas, ces schémas requièrent de calculer la dérivée temporelle avant, ce qui nécessite d'avoir accès à  $\phi(t + 1)$ . Une solution pour résoudre ce problème serait de considérer un ensemble de niveaux 3D:  $\phi : \mathbb{R}^2 \times \mathbb{R}^+ \mapsto \mathbb{R}$  mais cela impliquerait que l'ensemble de la séquence est disponible et empêcherait une utilisation en routine clinique de l'algorithme.

Nous proposons donc de calculer une approximation de  $\phi$  à  $t + 1$  à partir de  $\phi(t - 1)$  et du mouvement. À partir de la segmentation à  $t - 1$ , le myocarde est suivi grâce au mouvement en  $t - 1$  et  $t$  afin d'obtenir une prédiction de  $\phi$  en  $t + 1$ , laquelle est utilisée pour le calcul des dérivées.

### Évolution de l'ensemble de niveaux

Les pondérations apparaissant dans l'énergie minimisée sont fixées empiriquement et conservées pour toutes les segmentations:  $\nu_d = 0.5$ ,  $\nu_s = 1$ ,  $\nu_t = 5$ . La pondération du terme de mouvement est fixée à 1.5 pour l'endocarde et 1 pour l'épicarde du fait de leurs caractéristiques différentes dans l'image. En effet, l'endocarde est généralement moins lisse que l'épicarde et nécessite d'exclure les muscles papillaires. Notons aussi qu'une valeur importante a été donnée au terme d'épaisseur afin qu'il soit prépondérant si les deux contours sont sur le point de fusionner.

L'algorithme est initialisé de la manière suivante: la procédure d'initialisation décrite dans la partie précédente est utilisée sur la première image de la séquence, puis cette image est segmentée par l'algorithme proposée dans le Chapitre 7. Les autres images de la séquence sont alors segmentées par l'algorithme proposé dans cette partie.

### Suivi de la ROI

Pour les vues parasternale grand-axe et apicales, il est nécessaire de mettre à jour la région d'intérêt pour qu'elle corresponde à la partie de l'image où le myocarde est visible. Cette procédure est illustrée en Fig. 9.5 et est effectuée comme suit: les quatre points d'intersection  $\mathbf{p}_t$  entre le résultat de segmentation et la ROI sont calculés et leur position approximative à  $t + 1$  est obtenue à l'aide du mouvement. On estime par moindres carrés la droite la plus proche de ces points, puis un masque est créé à partir de cette droite de manière similaire à celle décrite dans la partie précédente.

## Résultats

### Évaluation de la solution proposée

Le modèle hyperquadrique proposé dans la partie précédente n'a été validé que pour des images en fin systole et en fin diastole. Nous proposons donc de le valider pour

---

des séquences entières et estimons le modèle sur des références de cardiologues pour 5 séquences par vues (soit environ 1200 images). Les résultats obtenus sont résumés dans le tableau 9.1. On constate que les valeurs des erreurs pour les séquences sont plus élevées que pour l'estimation sur des images, ce qui s'explique par une plus grande variabilité dans les formes au cours de la séquence. Néanmoins, l'erreur reste relativement faible puisque le MAD est toujours inférieur à 1mm, ce qui montre que le modèle estimé reste proche des références des cardiologues.

Nous montrons aussi l'importance du mouvement pour guider la segmentation en comparant sur une séquence apicale 4 chambres les résultats de notre méthode, d'un suivi du contour et d'une segmentation multistatique utilisant l'algorithme décrit précédemment. Les résultats obtenus sont résumés dans le tableau 9.2 et le test de rang de Friedman est utilisé pour comparer les résultats obtenus par les différentes méthodes. On observe que la méthode proposée donne toujours de meilleurs résultats que les deux autres algorithmes et que les différences observées sont toujours statistiquement significatives, démontrant l'importance de l'utilisation du mouvement.

### Segmentation du myocarde complet dans des séquences échocardiographiques

Pour évaluer les performances de notre algorithme, deux experts ont segmenté manuellement 5 séquences pour chaque vue (correspondant à un total d'environ 1200 images) et un contour moyen a été calculé à partir de ces références suivant le protocole décrit par [Chalana and Kim (1997)]. Ce contour est utilisé comme référence pour la comparaison avec les résultats de segmentation. En plus de la comparaison avec les références des experts, notre algorithme est aussi comparé à la méthode proposée par [Hamou and El-Sakka (2010)] qui est dans le principe proche de notre méthode puisqu'elle utilise un contour actif évoluant à partir d'une information extraite du flux optique et d'un *a priori* de forme.

Les résultats obtenus sont résumés dans les tableaux 9.3 et 9.4, où les 3 premières colonnes correspondent à la distance inter-observateur (IOD), les 3 colonnes suivantes aux résultats obtenus par notre méthode et enfin les 3 dernières colonnes aux résultats obtenus par la méthode décrite par [Hamou and El-Sakka (2010)]. Les figures 9.7 à 9.10 montrent des exemples de suivi pour deux séquences par vue.

On observe que pour les vues parasternales, les résultats obtenus pour l'endocarde et l'épicarde sont proches de la variabilité inter-observateur voire parfois meilleurs. Par exemple pour la vue parasternale petit-axe, les MAD (HD) obtenus par notre méthode sont de 0.83mm (2.2mm) et 0.85mm (2.15mm) pour l'épicarde et l'endocarde respectivement, alors qu'ils sont de 0.85mm (2.43mm) et 1.46mm (3.27mm) pour l'IOD, ce qui montre que notre algorithme est capable de produire des résultats cohérents à la fois globalement (MAD) et localement (HD). On constate cependant que, tout comme pour la segmentation statique, les résultats sont meilleurs pour l'épicarde que pour l'endocarde car la segmentation de l'endocarde nécessite d'exclure les muscles papillaires. Cependant la même observation peut être faite pour les valeurs de l'IOD traduisant un comportement similaire.

---

Concernant les vues apicales, on observe que les valeurs d'erreur augmentent par rapport à celles obtenues en parasternal (MAD de 1.9mm en apicale 4 chambres contre 0.83mm en parasternal petit axe pour l'épicarde). Ceci s'explique par la qualité d'image qui est généralement moins bonne dans les vues apicales, où l'apex est flou car situé dans la zone de champ proche et où une partie de la paroi latérale est souvent manquante. De ce fait, peu d'informations image ou liées au mouvement peuvent être extraites pour guider le contour. Celui-ci n'évolue donc quasiment pas depuis sa position initiale conduisant à des erreurs plus élevées. On peut noter que l'IOD augmente aussi comparativement aux vues parasternales traduisant cette difficulté à segmenter le myocarde dans ces vues.

Enfin, comparés aux résultats de l'algorithme proposé par [Hamou and El-Sakka (2010)], nos résultats sont toujours meilleurs (et la différence est statistiquement significative) sauf pour l'endocarde en parasternal grand-axe où les résultats sont proches pour  $D^*$  et le MAD. En moyenne, notre MAD est inférieure d'1.5mm (0.6mm) à celui obtenu pour [Hamou and El-Sakka (2010)] et la distance d'Hausdorff est inférieure de 3.2mm (2.9mm) pour l'épicarde (endocarde), ce qui correspond à une amélioration des résultats de 44% (24%) environ. Ceci peut être expliqué par le fait que notre modèle *a priori* est mieux adapté aux formes myocardiques comme il a été montré dans le Chapitre 6, mais aussi par le fait que notre terme de mouvement est plus précis que l'hypothèse classique de flux optique appliquée aux images B-mode.

---

# Active contours using motion constraints

---

When segmenting sequences and tracking an object over time, the knowledge of the underlying motion may bring valuable information and help improving segmentation results and speed. Indeed parts of the object that are occluded in a frame might be visible in another one; temporal coherence implies that contours in successive frames have similar shapes. In this chapter, we do a brief review of available techniques that include these constraints to help guiding the segmentation. We first focus on algorithms using motion as an information and that often perform jointly motion estimation and segmentation. We then present methods where the evolving contour is constrained by a motion model (*e.g.* a temporal shape prior). Finally tools specifically designed for the segmentation of echocardiographic sequences are described.

### 8.1 Motion as a data

When considering motion as a data, one can either estimate the motion prior to the segmentation or perform a joint motion estimation and segmentation. In the latter, the authors usually make the assumption of the intensity conservation (optical flow OF): the intensity of an object remains constant over time.

#### 8.1.1 Joint motion estimation and sequence segmentation

[Paragios and Deriche (1999), Paragios and Deriche (2005)] proposed to derive their Geodesic Active Region model for the detection and tracking of non-rigid moving object. In addition to the OF hypothesis, they also assume that a reference background image is

available to derive a composite energy functional:

$$E = F_D + F_I + F_C. \quad (8.1)$$

In this functional,  $F_I$  is based on low-level image statistics, in order to favour regions having constant intensities properties.  $F_D$  applies to the difference between the reference background and the current frame.  $F_D$  is based on classical combined gradients and intensity homogeneity criteria and thus allows to segment mobile regions. Finally  $F_C$  is a motion-based term, favouring interframe motion that minimize the optical flow constraint, evaluated through the sum of square differences measure. A motion prior is introduced at this level by constraining the computed optical flow to correspond to an affine transformation. The obtained evolution was implemented using level-set approach. The model has been successfully applied to the tracking of video sequences.

[Cremers (2003), Cremers and Soatto (2005)] note that the OF constraint holds if the spatio-temporal gradient of the image is orthogonal to the velocity field. Expressing this information in a Bayesian framework and assuming a piecewise parametric motion, they showed that the problem of joint estimation and segmentation could be expressed in a similar manner as the Mumford-Shah problem. In the case of two-phase segmentation, the energy functional writes as:

$$E(\phi, \mathbf{V}) = \int_{\Omega} \left( \frac{(\mathbf{V}_i(\mathbf{p})^T \nabla I(\mathbf{p}))^2}{|\mathbf{V}_i(\mathbf{p})|^2 |\nabla I(\mathbf{p})|^2} H(\phi(\mathbf{p})) + \frac{(\mathbf{V}_o(\mathbf{p})^T \nabla I(\mathbf{p}))^2}{|\mathbf{V}_o(\mathbf{p})|^2 |\nabla I(\mathbf{p})|^2} (1 - H(\phi(\mathbf{p}))) \right) d\mathbf{p}, \quad (8.2)$$

where the indices  $i$  and  $o$  indicates the inner and outer region respectively and  $\mathbf{V} = \{\mathbf{V}_i, \mathbf{V}_o\}$ ,  $\mathbf{V}_{(\cdot)}$  is the velocity on the domain  $\Omega_{(\cdot)}$  which is defined as  $\mathbf{V}_{(\cdot)}(\mathbf{p}) = M(\mathbf{p})\boldsymbol{\lambda}_{(\cdot)}$ .  $M$  is a matrix depending only on space and time and  $\boldsymbol{\lambda}_{(\cdot)}$  is the parameter vector associated with each region. In [Cremers and Soatto (2005)], the authors model the motion as affine yielding the following matrix  $M$ :

$$M(\mathbf{p}) = \begin{pmatrix} x & y & 1 & 0 & 0 & 0 & 0 \\ 0 & 0 & 0 & x & y & 1 & 0 \\ 0 & 0 & 0 & 0 & 0 & 0 & 1 \end{pmatrix}. \quad (8.3)$$

The energy is then minimized in two steps, first with respect to  $\phi$  to refine the segmentation and then with respect to the motion parameters  $\boldsymbol{\lambda}_{(\cdot)}$  for the motion estimation. The method was validated on traffic scenes sequences (Fig. 8.1).

A drawback of this method is that the estimated motion is constant within a region which might not always be the case. To tackle this problem, [Brox *et al.* (2004)] proposed

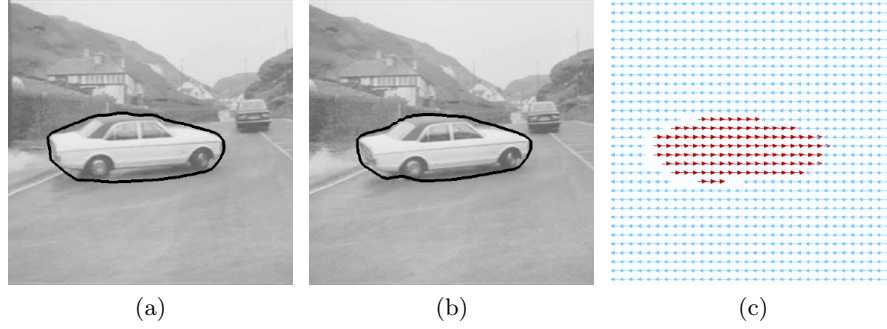


Figure 8.1: Segmentation of the Avengers sequence: (a) and (b) Segmentation obtained for two consecutive frames and (c) Motion estimation on (a) (from [Cremers (2003)]).

a variational framework to estimate the motion where the following energy is minimized:

$$\begin{aligned}
 E(\phi, \{\mathbf{V}\}, N) = & \sum_{i=1}^N \int_{\Omega} H(\phi_i) \left( (I(\mathbf{p} + \mathbf{V}_i) - I(\mathbf{p}))^2 + \gamma (\nabla_2 I(\mathbf{p} + \mathbf{V}_i) - \nabla_2 I(\mathbf{p}))^2 \right) d\mathbf{p} \\
 & + \alpha \sum_{i=1}^N \int_{\Omega} (|\nabla_3 u_i|^2 + |\nabla_3 v_i|^2) d\mathbf{p}, \quad (8.4)
 \end{aligned}$$

$\mathbf{V}_i = (u_i, v_i)$ ,  $\nabla_2$  is the spatial gradient,  $\nabla_3$  the spatio-temporal gradient and  $N$  the number of regions. The first term of (8.4) corresponds to the OF constraint and assumes a gray value consistency. The second term imposes a gradient consistency to deal with changes of brightness which might happen in natural scenes. The last term forces the estimated motion field to vary smoothly inside a given spatio-temporal region. In [Brox *et al.* (2006)], Eq.(8.4) is included into a joint motion estimation and multiphase level-set segmentation framework and modified to consider color sequences.

In the context of liver segmentation in 4D-CT, [Ehrhardt *et al.* (2008)] used a very similar variational framework as the one described by eq.(8.4). However, since they are dealing with CT images, the problem of illumination changes is not relevant and they thus only consider the gray level consistency and regularization terms of (8.4) (1rst and 3rd terms) for the motion estimation and segmentation. Moreover, as opposed to [Brox *et al.* (2006)] where the inter-frame motion was estimated, the motion is computed with respect to a reference frame  $t_{ref}$ . A reference shape  $\psi$  is also available in this frame and is used as a shape prior. The complete energy writes as follows:

$$\begin{aligned}
 E(\phi, \mathbf{V}) = & \lambda_1 \int_{\Omega} -H(\phi(\mathbf{p})) \log(p_{bg}(I(\mathbf{p}))) - (1 - H(\phi(\mathbf{p}))) \log(p_{obj}(I(\mathbf{p}))) d\mathbf{p} \\
 & + \lambda_2 \int_{\Omega} \delta(\phi(\mathbf{p})) \|\nabla \phi(\mathbf{p})\| d\mathbf{p} + \lambda_3 \int_{\Omega} (I(\mathbf{p}) - I_{ref}(\mathbf{p} - \mathbf{V}(\mathbf{p})))^2 d\mathbf{p} \quad (8.5) \\
 & + \frac{\lambda_4}{2} \int_{\Omega} \|\nabla u\|^2 + \|\nabla v\|^2 d\mathbf{p} + \lambda_5 \int_{\Omega} \delta(\phi(\mathbf{p})) (\phi(\mathbf{p}) - \psi(\mathbf{p} - \mathbf{V}(\mathbf{p})))^2 d\mathbf{p},
 \end{aligned}$$

where  $\mathbf{p} = (x, y, t)^T$ ,  $\mathbf{V} = (u, v)^T$  and  $\lambda_i$ ,  $i = \{1, \dots, 5\}$  are hyperparameters weighing the influence of each term. In (8.5), the first term is a data attachment term separating the



object from the background according to the intensity distribution of both regions ( $p_{obj}$  and  $p_{bg}$ ), the second term minimizes the length of the curve thus having a regularization effect. The third and fourth terms correspond to the use of motion for the segmentation. The last term is the shape prior term enforcing the curve to remain close to the reference shape.

### 8.1.2 Sequence segmentation using an *a priori* estimated motion

Approaches described in this section assume that the motion is estimated prior to the segmentation and corresponds to an input of the algorithm. This assumption has the advantage of allowing to choose the motion estimation algorithm that is the best suited for the application.

In order to track and characterize cloud structures, [Papin *et al.* (2000)] proposed a two-steps level-set segmentation algorithm. First the level-set evolves according to a motion term that allows estimating the coarse position of the cloud in the next frame. The corresponding evolution term is

$$\frac{\partial \phi}{\partial \tau}(\mathbf{p}) = -(\xi_{\mathbf{V}}(\mathbf{p})F_{A1} \mathbf{V}(\mathbf{p}) \cdot \mathbf{N} - \epsilon\kappa)\|\nabla \phi(\mathbf{p})\|, \quad (8.6)$$

where  $\mathbf{V}$  is the estimated motion,  $\xi_{\mathbf{V}}$  is a stopping criterion,  $F_{A1}$  is a constant greater than one used to speed up the convergence and  $\epsilon$  weights the influence of the regularization induced by the curvature  $\kappa$ . The stopping criterion  $\xi_{\mathbf{V}}$  measures the shift  $\Delta$  applied to the evolving contour at a given point  $\mathbf{p}$ . It is one when the value of  $\Delta(\mathbf{p})$  is lower than  $\|\mathbf{V}(\mathbf{p})\|$  and zero otherwise expressing the fact that the interframe shift must be bound by the magnitude of the corresponding estimated motion. Once the motion evolution reached convergence, the authors applied an evolution term based on the intensity information of thermal infrared images to refine the contour.

A two-steps method was also proposed by [Unal *et al.* (2005)] in the context of fish sequence segmentation. The authors first do a prediction step where the normal component of the motion with respect to the contour is applied to the active contour in order to respect optical flow constraint. They then perform a correction step where the resulting contour is refined using a data attachment term based on global statistics [Chan and Vese (2001), Yezzi *et al.* (1997)]. Those two-steps are first expressed in the context of level-set segmentation and then transcribed into an active polygons framework, where the evolving contour is represented as a polygon of  $n$  vertices. The evolution equation of a vertex of the polygon is then obtained by averaging the deformation accumulated along the edges the vertex is connected to.

A drawback of the two previous techniques is that the evolution does not come from an energy minimization and thus does not guarantee that a global minima will be reached. A variational approach was proposed by [Herbulot *et al.* (2004), Herbulot *et al.* (2006)] where the segmentation of video sequences is performed using the histogram distribution of the velocity vectors. In this case, the motion is estimated prior to the segmentation and

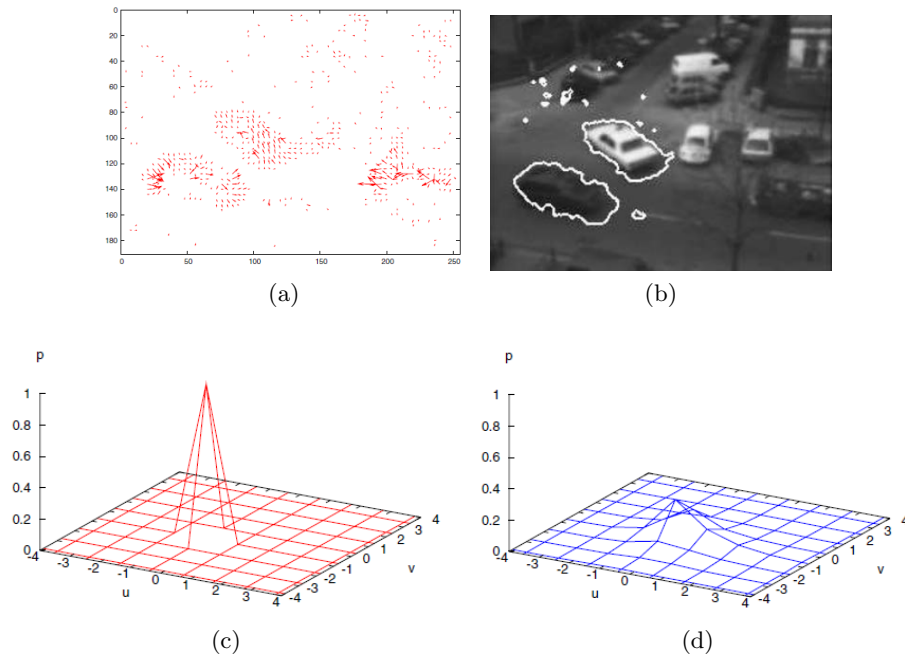


Figure 8.2: Segmentation of the “Taxi” sequence. (a) Optical flow estimation of the motion, (b) Segmentation result using eq.(8.7) and histogram distribution of the velocity in the background (c) and the object (d) (from [Herbulot *et al.* (2006)]).

the motion of the background is eventually compensated. The segmentation is performed by minimizing the following energy:

$$E(\phi) = \int_{\Omega_i} \varphi(q(\mathbf{V}(\mathbf{p}), \Omega_i)) d\mathbf{p} + \int_{\Omega_o} \varphi(q(\mathbf{V}(\mathbf{p}), \Omega_o)) d\mathbf{p}, \quad (8.7)$$

$\varphi$  is either the entropy ( $\varphi(q) = -q(\mathbf{V}(\mathbf{p}), \Omega_{(\cdot)}) \ln(q(\mathbf{V}(\mathbf{p}), \Omega_{(\cdot)}))$ ) or the log-likelihood ( $\varphi(q) = -\frac{1}{|\Omega_{(\cdot)}|} \ln(q(\mathbf{V}(\mathbf{p}), \Omega_{(\cdot)}))$ ) and  $q$  is the probability distribution of the velocity and is estimated using the Parzen window method. The evolution equation is then obtained using shape gradient derivatives and the method is applied to color images and video sequences (Fig. 8.2).

## 8.2 Motion as a constraint

Another way to take advantage of the motion is to use it as a prior. In this case the constrain is implicit since motion is never estimated and never appears in the evolution equation. This prior can be introduced either through a dynamical shape prior [Cremers (2006), Kohlberger *et al.* (2006), Leung *et al.* (2011)] or by constraining the variations of the level-set function  $\phi$  [Zhang and Pless (2005), Lynch *et al.* (2008)].

Generalizing the approach of [Tsai *et al.* (2003)], [Kohlberger *et al.* (2006)] proposed to learn a dynamical shape prior by performing the PCA in 4D. The reference shapes correspond to manual segmentation of 3D sequences, where the time dimension is treated as

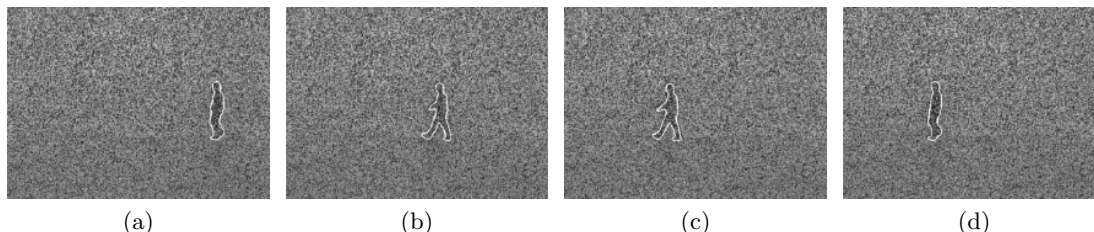


Figure 8.3: Segmentation of a walking person at 75 percent of noise (from [Cremers (2006)]).

a fourth dimension. The shape model is then incorporated into a variational framework by minimizing a data attachment term and the shape prior described in (5.9). The algorithm was applied to the segmentation of the whole myocardium in cardiac 4D SPECT data. Note that as in [Tsai *et al.* (2003)], the energy is directly minimized in the PCA parameter space.

[Cremers (2006)] proposed to build a dynamical shape prior by taking into account the estimated shape prior at the previous frame to update the shape model in the current one. The dynamical shape prior is learned in two steps:

1. PCA is applied on a sequence of training shape (1 shape per frame). This step allows computing the mean shape and the main modes of variation.
2. The same training sequence is then used to estimate the temporal shape dynamics. For each frame, the PCA coefficients  $\alpha$  of the corresponding shape are computed. The dynamics is then modeled as a  $2^{nd}$  order auto-regressive model applied to the temporal series  $\alpha$  and the pose parameters.

This dynamical model is then embedded in a variational process through a Bayesian framework where the AR model is applied to the new sequence to update the PCA coefficients  $\alpha$  for each frame. The method was applied to the segmentation and tracking of a walking person and was able to successfully recover the moving target even in the presence of noise as can be seen in Fig. 8.3.

[Zhang and Pless (2005)] used manifold learning to embed a motion prior into their level-set segmentation algorithm. Manifold learning is applied on MRI cardiac sequences prior to segmentation to represent the image variation through time along two main degrees of freedom (*i.e.* cardiac phase  $u$  and pulmonary phase  $v$ ). The authors observed that when moving along the respiratory phase  $v$ , the resulting motion of the heart corresponds to a global translation of velocity  $\mathbf{V} = (\omega_x, \omega_y)$ , while when moving along the cardiac phase  $u$ , the heart's motion can be approximated by a dilation or expansion (*i.e.* adding or subtracting a constant value  $\omega_u$  to the level-set function). These observations yield two motion prior terms accounting for the variations of  $\phi$  along each dimension of the manifold:

$$E(\phi) = \eta_1 \int_{\Omega} \left( \frac{\partial \phi}{\partial x} \omega_x + \frac{\partial \phi}{\partial y} \omega_y + \frac{\partial \phi}{\partial v} \right)^2 d\mathbf{p} + \eta_2 \int_{\Omega} \left( \frac{\partial \phi}{\partial u} - \omega_u \right)^2 d\mathbf{p}, \quad (8.8)$$

where  $\phi : \mathbb{R}^4 \mapsto \mathbb{R}$ ,  $(x, y, u, v) \rightarrow \phi(x, y, u, v)$ ,  $x$  and  $y$  being the image coordinates. The

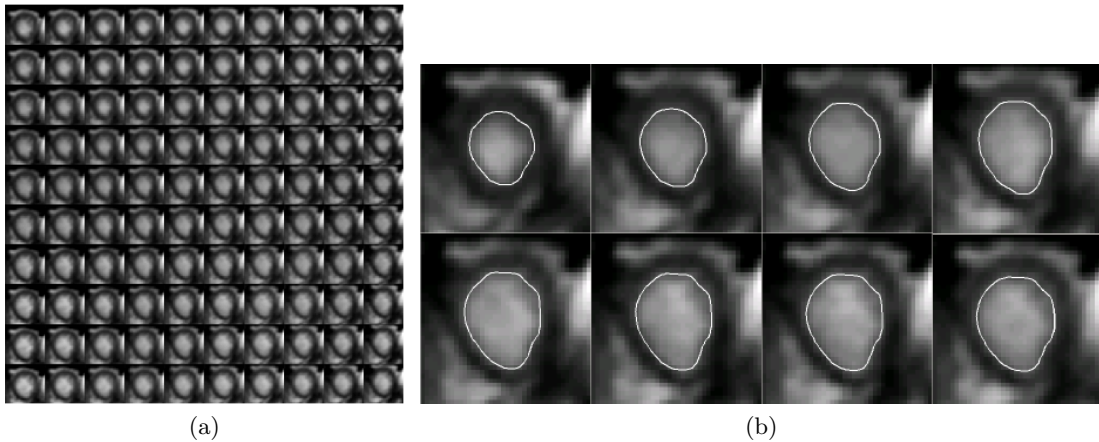


Figure 8.4: (a) Example of manifold learning. (b) Segmentation examples of cine-MRI images (from [Zhang and Pless (2005)]).

first term corresponds to variations of  $\phi$  along the respiratory phase and enforces rigid changes in shape by penalizing regions of  $\phi$  where the  $x$ ,  $y$  and  $v$  derivatives are not consistent with the translation motion. The second term penalizes the overall mean translational motion of the heart, which is minimal when motion is caused only by the heartbeat. In addition to the motion prior terms, the authors also used the region terms of the classical Chan & Vese algorithm (see also [Chan and Vese (2001)] and Section 4.5.2) in the segmentation process.

An alternating scheme is then used to minimize the energy. First the inside and outside intensity's means for the Chan & Vese algorithm as well as  $\omega_x$ ,  $\omega_y$  and  $\omega_u$  are estimated and then  $\phi$  is evolved according to:

$$\begin{aligned} \frac{\partial \phi}{\partial \tau} = & \delta(\phi) \left( -(I - c_i)^2 + (I - c_o)^2 + \lambda \kappa \right) + 2\eta_2 \left( \frac{\partial^2 \phi}{\partial u^2} - \frac{\partial \omega_u}{\partial u} \right) \\ & + 2\eta_1 \left( \frac{\partial^2 \phi}{\partial x^2} \omega_x^2 + \frac{\partial^2 \phi}{\partial y^2} \omega_y^2 + \frac{\partial^2 \phi}{\partial v^2} + 2 \frac{\partial^2 \phi}{\partial x \partial y} \omega_x \omega_y + 2 \frac{\partial^2 \phi}{\partial x \partial v} \omega_x + 2 \frac{\partial^2 \phi}{\partial y \partial v} \omega_y \right). \end{aligned} \quad (8.9)$$

In the context of endocardial segmentation in 3D echocardiography, [Leung *et al.* (2011)] proposed a motion model based on PCA. Their training set is composed of manual references drawn on several 3D sequences and 2 alignment steps are performed:

1. all end-diastolic (ED) contours are aligned in order to remove acquisition variability;
2. all subsequent contours of a sequence are aligned on the ED contours to eliminate variations that are not related to anatomical changes.

Once the contours are aligned, Procrustes analysis [Gower (1975)] is performed in order to obtain the inter-frame motion for all frames of all the sequences. A first prior is introduced at this point, since the motion is supposed to be an affine transformation (represented by a set  $\lambda$  of 12 parameters). Thus assuming that each sequence has  $F$  frames, a set  $\mathbf{\Lambda}$  of  $12(F-1)$  parameters is computed. PCA is then applied on the sets  $\mathbf{\Lambda}$  in order to learn the average transformation  $\mu$ , the PCA eigenvectors and the PCA parameters  $\alpha$  as in (5.2).

This PCA motion model is then introduced in the optical flow equation with the assumption that the parameters  $\alpha$  are constant in small regions around the contour (similar

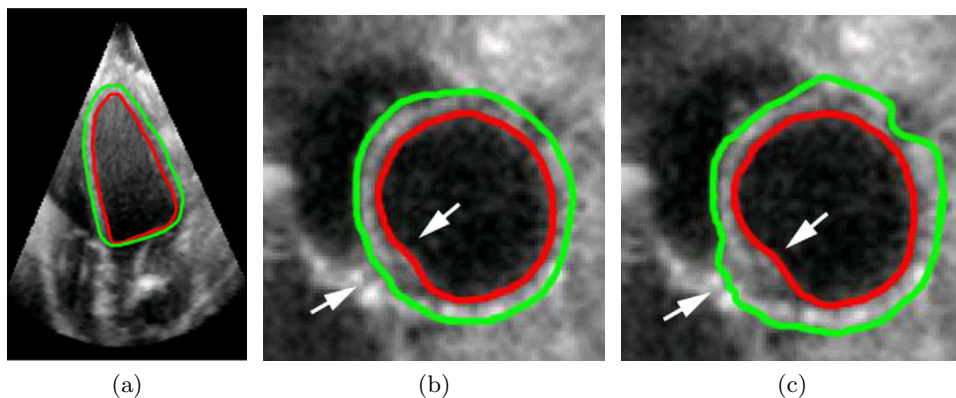


Figure 8.5: (a) Long-axis view of segmented endocardial and epicardial contours. Comparison of the myocardial segmentation results (b) with the incompressibility constraint or (c) without constraint (from [Zhu *et al.* (2010)]). Green: epicardium, red: endocardium.

to the approach of [Lucas and Kanade (1981)]. When segmenting a new sequence, the ED contour is first manually drawn and then the optical flow equation is minimized in order to obtain the affine parameters  $\mathbf{\Lambda}$  of the motion. The motion is then applied to the ED contour frame by frame to get the segmentation result. This method was applied on 35 3D-sequences in a leave one out fashion: 34 sequences were used for the training and the remaining sequence was segmented.

Recently some authors proposed motion constraints specifically dedicated to the segmentation of the heart. [Zhu *et al.* (2007)] introduced an incompressibility constraint in their active contour framework to segment the whole myocardium in 3D echography. Using two active contours  $\phi_i$  and  $\phi_o$ , the myocardial volume  $V = \int_{\Omega} (H(\phi_o(\mathbf{p})) - H(\phi_i(\mathbf{p}))) d\mathbf{p}$  is modelled as a gaussian distribution:

$$p(V) = \frac{1}{\sqrt{2\pi}\sigma} \exp\left(-\frac{(V - V_0)^2}{2\sigma^2}\right), \quad (8.10)$$

where  $V_0$  and  $\sigma$  are the mean and standard deviation of the gaussian model. This term was coupled to a region based data attachment term separating both regions according to the statistics of the BMode image. The intensity distribution of both regions was modelled through a Rayleigh distribution. The method was then applied to 22 3D echocardiographic sequences and gave promising results. In [Zhu *et al.* (2010)], after comparing four intensity distributions (Rayleigh, K-distribution, Rice and Nakagami), the authors used the incompressibility constraint and a data attachment term based on Nakagami distribution to segment synthetic data and 11 3D sequences of canine hearts (see Fig. 8.5). Note that since this motion prior is based on the myocardial volume, it cannot be applied to 2D echocardiography.

[Lynch *et al.* (2008)] suggested to globally constrain the segmentation of MRI cardiac sequences by modelling the left ventricular cavity volume variations. Linking these variations to the boundary motion, the authors expressed the temporal evolution of each point

of the level-set  $\phi$  as a gaussian function:

$$\psi(t) = A + B \exp\left(-\frac{(t - \mu)^2}{2\sigma^2}\right), \quad (8.11)$$

where  $A, B, \mu$  and  $\sigma$  are the gaussian parameters and  $t$  represents the time dimension. This model is directly introduced into the evolution equation which is a modified version of the gradient based evolution equation of [Caselles *et al.* (1997)] (see also Section 4.5.1):

$$\frac{\partial \phi}{\partial \tau} = g(\|\nabla I\|)(\epsilon \kappa + \mathbf{K} + c)\|\nabla \phi\| + \beta \nabla \phi \cdot \nabla I, \quad (8.12)$$

where  $\kappa$  is the curvature,  $c$  a balloon force and  $\beta$  and  $\epsilon$  are hyperparameters weighting the influence of the different terms.  $\mathbf{K}$  represents the normalized difference between the expected value using the model (8.11) and the actual value of  $\phi$ . The evolution is then performed in two steps: first by evolving  $\phi$  using (8.12) and keeping the gaussian's parameters fixed and in a second step by estimating the model by keeping  $\phi$  fixed. The authors also proposed a coupled segmentation algorithm where they first segment the endocardium and then the epicardium. Two different gaussian models are applied as motion constraints and the epicardium is initialized 5 pixels away from the endocardium result. Note however that no thickness term is used and thus nothing forbid the epicardial segmentation to converge to the same boundary than the endocardium.

One may also remark that this motion constraint does not correspond to an incompressibility constraint since the model is linked to the left ventricle (blood) volume variation and not to the myocardial volume. Also since the prior is directly included into the evolution equation and not driven through a minimization process, there is no proof of convergence to a global minima.

It can be noted that Kalman filtering can also be used to introduce prior knowledge on the motion. Such approaches are described in the next section in the context of echocardiographic sequence segmentation.

### 8.3 Echocardiographic sequence segmentation

[Dias and Leitao (1996)] proposed a framework to segment the whole myocardium in parasternal short-axis views using an explicit representation of the contours. Stating the problem in polar coordinates, they seek for each  $\theta$  the corresponding position  $r_1$  and  $r_2$  of the endocardial and epicardial boundaries by minimizing a functional composed of 3 terms:

- a data attachment term where each region (blood, myocardium, surrounding tissues) is modelled by a Rayleigh distribution. This term is then expressed as a log-likelihood function to minimize.
- a spatial regularization term enforcing smooth variations of the contour.
- a prior term which include a myocardial thickness term, an endocardial volume term

and two temporal smoothness constraints (one for the endocardium and one for the epicardium). The second prior term forces the endocardial contour to move outward thus allowing to pass over artifacts inside the heart.

In [Chalana *et al.* (1996)], the authors proposed a coupled active contours technique based on snakes to segment the whole myocardium in parasternal short-axis sequences. Their model is an extension of the original snakes proposed by [Kass *et al.* (1988)] where the contour is represented as a set of 3D points where the 3rd dimension corresponds to the time dimension. Furthermore while the spatial components of the contours depend on two parameters  $s$  and  $r$ , the time component depends only on the second parameter  $r$ . In such a case, the active contour is represented as a sequence of planar contours with the second parameter  $r$  being the index of the plane. To segment the myocardium over the whole sequence, the authors then proposed to minimize an external energy composed by two terms:

- a gradient based term which will drives the contour towards high gradient area,
- a motion continuity term which enforces the contour to contract during systole and to expand during diastole.

Using this energy, the authors first segment the epicardium. The algorithm is initialized by replicating a coarse segmentation of the epicardium in end-diastole on all frames. Once the epicardial borders are detected, these borders are used to initialize the endocardial borders segmentation as well as to define a ROI to constraint the endocardial active contour evolution.

[Malassiotis and Srinatzis (1999)] proposed a temporal learning-filtering method for the segmentation of the left ventricle boundary in echocardiographic sequences using active contour model. Instead of creating a prior shape model using a PCA technique on a training dataset, the authors proposed to create and update their PCA model on the fly, *i.e.* directly from the images of the current sequence. A Kalman filtering strategy is used to merge the information provided by the active contour model from the current frame and the PCA analysis of the frames previously segmented. This is done in the following way:

- The current image is pre-processed using a despeckling procedure [Srinatzis *et al.* (1992)], in a coarse-to-fine framework. Using classical gradient-driven evolution, the active contour model then provides an estimation of the ventricular shape, which is expressed in the PCA space. This provides the measurement step of the Kalman filter;
- The shape of the ventricle is predicted from the contour segmented in the previous frame using a simple 0th order dynamic model. This provides the prediction step of the Kalman filter;
- The contour is then estimated from the measurement and prediction using the Kalman filter. In this filtering step, the model covariance matrix is built from the eigenvalues of the PCA analysis in order to give more weight to the predominant shape mode;

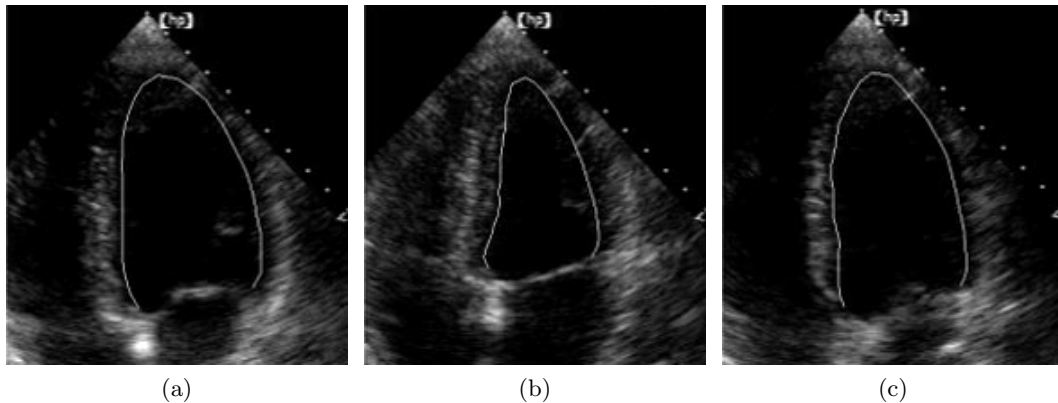


Figure 8.6: Example result of AAMM segmentation of an apical 4-chamber sequence. (a) Frame 1, (b) 9, (c) 16 (from [Bosch *et al.* (2002)]).

- The PCA is then updated using this final contour estimation. The method has been applied for the segmentation of sequences corresponding to a parasternal short-axis view.

In the same spirit [Jacob *et al.* (1999)] incorporates shape PCA and Kalman filtering in an active contour framework. In this work, PCA is performed on a training dataset that describes heart shape variation for one specific acquisition view. The measurement step is performed using a combination of spatio-temporal noise reduction filtering and feature detection from phase information. The dynamic model corresponds to a second order autoregressive model (AR). The parameters of the AR model are computed from the training dataset used to compute the PCA model. As in [Malassiotis and Strintzis (1999)], the Kalman filtering stage is finally used to track the shape model over time. Their method has been evaluated on both real normal and abnormal heart motion data sequences.

[Bosch *et al.* (2002)] used an adaptation of the active appearance model approach proposed by [Cootes *et al.* (2001)]. In their method called active appearance motion model (AAMM), in addition to the shape and appearance (intensity profile) of the object, the motion is also included in the model by considering a sequence as a stack of images. Moreover since applying PCA on the intensity assumes a Gaussian distribution which does not hold for echographic data, the authors proposed a non linear way to normalize the data based on a comparison between the cumulative intensity histogram and the normal distribution. This normalization proved to be very efficient in the segmentation process since the quality of matching was raised from 73% to 97%. Note however that due to the fact that a learning step is required, the model was only applied for the segmentation and tracking of the endocardium in apical 4-chamber sequences. Fig. 8.6 shows segmentation results of the AAMM.

[Comaniciu *et al.* (2004)] developed an information fusion framework to track the endocardium in parasternal short-axis and apical 4-chamber views. First, they formulate the



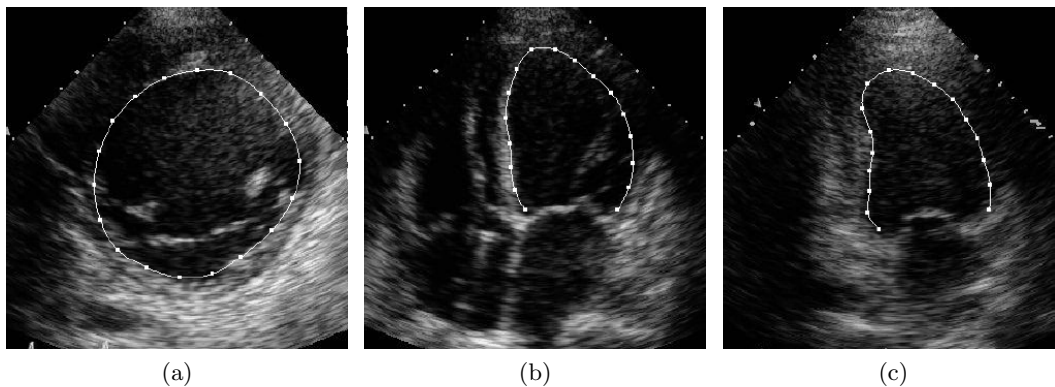


Figure 8.7: Example of segmentation results in different views: (a) SAX, (b) A4C, (c) A2C (from [Comaniciu *et al.* (2004)]).

tracking framework as an information fusion problem using Kalman filtering and strongly-adapted PCA (SA-PCA). SA-PCA uses the initial contour of the sequence to process to update a PCA model, thus taking into account shape variations that might not have been modelled through PCA. Secondly, during motion estimation, an uncertainty measure is also computed from the optical flow which is then used as a weight in the shape model constraining process. This allows to discard flows estimated from uncertain areas such as drop-out regions while giving more importance to flows with high confidence.

[Paragios *et al.* (2005)] proposed a parametric curve model dedicated to the extraction of the left ventricle for each frame of a cardiac cycle sequence. The proposed algorithm is based on two distinct phases: a training step and a segmentation step. The training phase consists in curves registration and parametric shape modeling. Their shape model is build from a linear combination of a diastolic and a systolic model obtained from a PCA applied to the registered curves. This shape model is thus an attempt to account for shape variation between diastole and systole. The segmentation step consists in two main steps. First an approximate segmentation of the left ventricle for each image in the sequence is performed using a parabolic description of the global shape of the endocardium. This allows registering the shape model in each frame by recovering the parameters of a similarity transformation. The segmentation can then be refined using the approximate segmentation as an initial solution. They tested the ability of their method for the segmentation and tracking of the left ventricle cavity using apical 4-chamber views.

[Sühling *et al.* (2005)] proposed an original optical flow-based method for the estimation of the heart motion from echocardiographic image sequences. The motion is estimated for the complete sequence using a local-affine model for the velocity in space and a linear model in time. The model parameters are estimated using a coarse-to-fine multiresolution approach and a sliding spatiotemporal B-spline windows. The derived velocity is then used to constrain the evolution of a parametric active contour on the whole sequence. The method has been evaluated from both simulation and a set of in vivo data from an animal study.

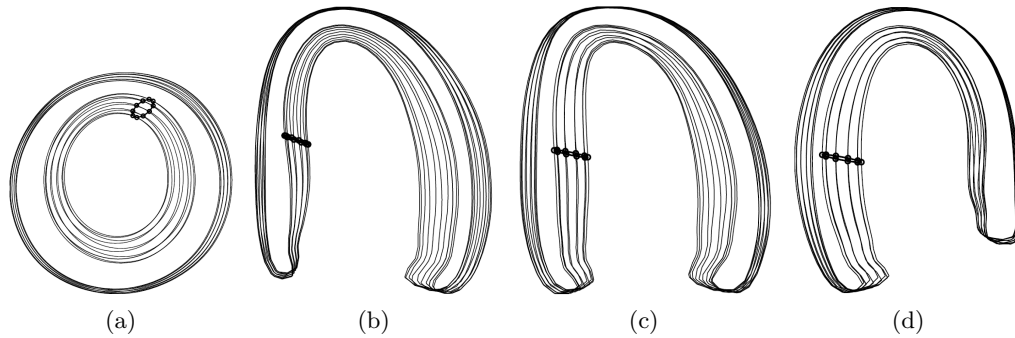


Figure 8.8: Examples of learned cyclic models (based on 21 sequences): (a) SAX, (b) A4C, (c) A2C, (d) A3C (from [Casero and Noble (2008)]). The dots correspond of the motion of an endocardial point during a cardiac cycle.

[Zhou *et al.* (2005)] proposed an optimized Kalman filtering approach which provides a unified fusion of three different sources of information: the system dynamics, a subspace model derived from a PCA technique and a measurement uncertainty. Their PCA model is built offline from training data represented in a Lagrangian formulation and is adapted to the current case using the initial contour drawn by the user. The measurement step is performed using an optimal Bayesian kernel matching algorithm [Comaniciu (2002)]. As in the approach used by [Malassiotis and Strintzis (1999)], the authors use 0th-order dynamics to impose a temporal smoothness constraint. The method has been successfully evaluated on both apical two/four chambers views and parasternal long/short axis views.

[Casero and Noble (2008)] proposed a framework to take into account the cyclic dynamics of the heart shape. To this end, the contours points are represented in a higher dimensional space as  $\mathbf{p} = [x, y, rt_1, rt_2]$ , where  $t_1 = \cos(2\pi t)$ ,  $t_2 = \sin(2\pi t)$ ,  $t \in [0; 1]$  is the time variable where  $t = 0$  and  $t = 1$  correspond to end diastole and  $r$  is a scaling factor. PCA is then applied on the dataset of sequences in a similar manner than [Cootes *et al.* (1995)], where the pose parameters are estimated using a modified Procrustes alignment in order not to remove temporal variability inside a sequence. Temporal models of the whole myocardium in parasternal short-axis (SAX, Fig. 8.8(a)), apical 4-chamber (A4C, Fig. 8.8(b)), apical 2-chamber (A2C, Fig. 8.8(c)) and apical 3-chamber (A3C, Fig. 8.8(d)) views are then learned using this technique. Note that in [Casero (2008)], the author use this model in an atlas-based segmentation algorithm.

[Nascimento and Marques (2008)] presented an algorithm for the tracking of the endocardial boundary in apical 4-chamber sequences. They first extract possible edges at  $t + 1$  by detecting strong intensity variations along lines orthogonal to the endocardial border at  $t$ . The evolution of the shape and motion parameters is then performed on this edge map using a bank of switched dynamic systems which is able to represent complex motion and shape dynamics. To deal with possible outliers and multiple dynamics, a filtering algorithm is proposed, which propagates the *a posteriori* density of the unknown shape and motion parameters using a tree of probability data association filters.

In [Hamou and El-Sakka (2010)], a GVF snake framework is used for the segmentation of the endocardium in apical 4-chamber view. The external energies are based on the optical flow and a shape prior. After a speckle reduction step, the optical flow is computed and an edge map is extracted. The shape prior is obtained by fitting two 3rd order hyperbola, one on the 2/3 upper part of the contour and the other one on the 1/3 lower part. The snake then evolve in 2 cycles, one where the external forces corresponds to the GVF generated from the optical flow edge map and the other based on the shape prior.

## 8.4 Conclusion

In this chapter, we reviewed the techniques using motion information to perform the segmentation of sequences. When considering motion as a prior, the model is almost always obtained through a learning step (*e.g.* PCA, deep learning) yielding similar problems as the ones mentioned in Chapter 5 (*e.g.* need of large number of training images, dependency of the model on the acquisition view, difficulty in modelling pathological behaviours). Note however that to avoid this learning procedure, some authors used an overall motion prior dedicated to the segmentation of the myocardium in 3D through the incompressibility constraint [Zhu *et al.* (2007), Lynch *et al.* (2008)].

When motion is used as an information, several approaches were proposed, namely using motion as a feature similar to the grey level and perform the segmentation based on the motion statistics [Cremers (2003), Herbulot *et al.* (2004)] or minimizing the optical flow in the sequence [Paragios and Deriche (2005), Brox *et al.* (2004), Ehrhardt *et al.* (2008)] in order to perform a joint motion estimation and segmentation. Some interesting approaches were proposed by [Papin *et al.* (2000), Unal *et al.* (2005)] where the active contour evolves according to the motion estimated prior to segmentation but these approaches did not rely on a variational framework.

In this context, we propose in the next chapter, a new energy criterion whose minimization constrains the implicit function to satisfy the OF condition. More particularly, this formulation yields a problem having a unique solution in contrary to the classical OF equation used for motion estimation. We then derive this energy to obtain an evolution term which is included in the algorithm described in the previous chapter to act as a motion prior forcing the level-set to move in accordance to the estimated motion.

---

# Our contribution: Segmentation of the whole myocardium in any view in 2D-echocardiographic sequences

---

### 9.1 Proposed scheme

In this chapter, we deal with the segmentation and tracking of the whole myocardium in any view in 2D-echocardiographic sequences. To this end, we have decided to use the motion information to guide the evolution of the active contour. This can be done in two different ways as discussed in the previous chapter: either considering motion as a data or as a prior knowledge.

However, in the latter case, the model is very often obtained through a learning step (*e.g.* PCA, deep learning) yielding similar problems as the one mentioned in Chapter 5. Indeed, in contrary to the myocardial borders where geometrical prior could be used, the heart motion is difficult to model through mathematical functions and it would thus require to learn a motion model per view as in [Casero and Noble (2008)]. Note that some authors [Zhu *et al.* (2007), Lynch *et al.* (2008)] proposed to use a mathematical framework based on the incompressibility constraint but this prior cannot be used in our case since we are working in 2D and not in 3D.

We thus choose to consider motion as an information and assume it has been estimated prior to segmentation. Indeed this solution (depicted in Fig. 9.1) is flexible since at any time, we can select the motion estimation method that produces the best results, while

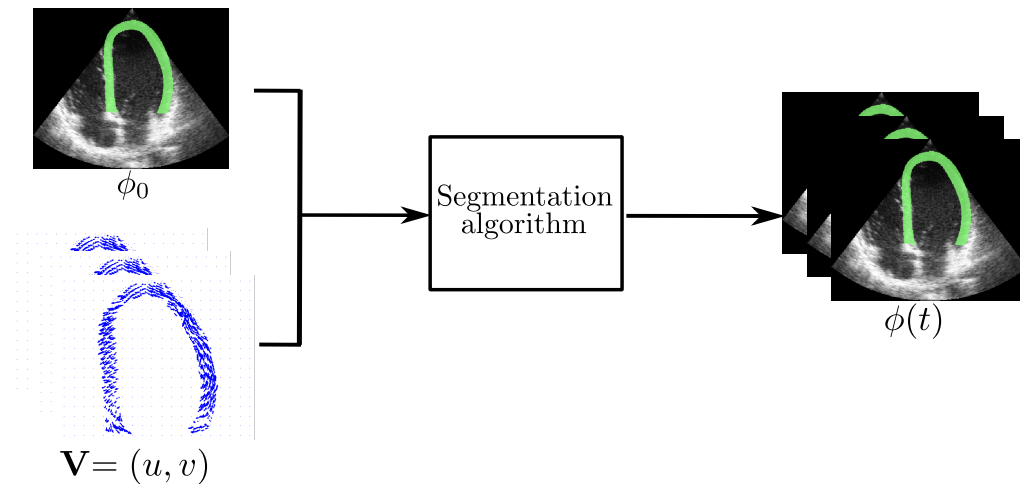


Figure 9.1: Proposed solution: the inputs of our algorithm are the motion estimated on the whole sequence and the segmentation of the first frame of the sequence.

keeping the same segmentation algorithm to be described in the sequel. For instance, one may note that recent work on transverse oscillations [Liebgott *et al.* (2009), Guo *et al.* (2012)] offers the perspective of providing a better estimation of the lateral motion which is a limitation of the current motion estimation algorithms.

## 9.2 Motion estimation

### 9.2.1 Review of motion estimation in echocardiographic images

Many approaches have been described that use speckle patterns to estimate motion from echocardiographic sequences [Mailloux *et al.* (1987), Baraldi *et al.* (1996)]. Since they rely on the local analysis of spatial and temporal gradients, these methods may fail at estimating large inter-frame cardiac motion. This implies multiscale strategies or a first stage of block-matching to provide a reliable displacement estimate [Behar *et al.* (2004), Sühling *et al.* (2005)]. Other approaches estimate cardiac motion by performing speckle tracking, which is generally done by comparing a block in the reference image and a block in the subsequent deformed image through a similarity measure [Strintzis and Kokkinidis (1997), Duan *et al.* (2007), Basarab *et al.* (2008)].

The above-described approaches were based on conventional B-mode images. However, some studies [Lubinski *et al.* (1999), D'hooge *et al.* (2002)] have proposed performing speckle tracking by using the RF signal to evaluate small displacements. Since the RF signal contains much higher frequencies, it is indeed better adapted to the estimation of small displacements (typically on the order of the emitted pulse wavelength). An interesting comparison between envelope-detected and RF-based echocardiographic speckle tracking has been made by [Yu *et al.* (2006)].

Finally, a recent study by [Touil *et al.* (2010)] suggested that speckle tracking from echocardiographic data should be performed from unconverted polar data. This is related

to the sectorial geometry of echocardiographic acquisition, which induces a sparser sampling far from the probe. Therefore, in the sequel, we will perform the motion estimation on the B-mode polar data and convert it to cartesian coordinates afterward.

### 9.2.2 Motion estimation using the monogenic signal

[Alessandrini *et al.* (2012)a] recently described an optical flow estimation algorithm based on the monogenic signal that was applied on 2D and 3D echocardiographic data. The monogenic signal extends the analytic signal concept to multiple dimensions data [Felsberg and Sommer (2001)] and is obtained, in 2D, from the responses to three 2D bandpass spherical quadrature filters (SQF). Following [Felsberg (2004)], they replace the brightness constancy assumption with the monogenic phase constancy assumption which has proven to be more robust. The complete algorithm is summarized in Alg. 2 and described in more details hereunder.

---

#### Algorithm 2: Multiscale Monogenic Optical Flow

---

**Input:** two subsequent frames:  $I_1, I_2$   
 parameters:  $\lambda_0, N_p, k$ .  
**Output:** displacement between  $I_1$  and  $I_2$ :  $\mathbf{d}$

```

 $\mathbf{d} = 0$ ;
for  $i = 1 : N_p$  do
     $[p_1, \mathbf{q}_1] = \text{MonogenSignal}(I_1, \lambda_0)$ 
     $[p_2, \mathbf{q}_2] = \text{MonogenSignal}(I_2, \lambda_0)$ 
     $\Delta \mathbf{d} = \text{Comp}\Delta \mathbf{d}(p_1, p_2, \mathbf{q}_1, \mathbf{q}_2)$ ;
     $\mathbf{d} = \mathbf{d} + \Delta \mathbf{d}$ ;
     $I_2 = \text{WarpImage}(I_2, \mathbf{d})$ ;
     $\lambda_0 = \lambda_0 / k$ ;

```

---

In order to be able to estimate large motion, the authors proposed a coarse to fine approach. The monogenic signal is first computed using the three 2D bandpass SQF with a small center frequency (*i.e.* a large value of  $\lambda_0$ ) adapted to capture displacement of coarse structures. Then assuming the motion to be locally affine in a small neighborhood, they estimate the motion using the optical flow applied on the monogenic phase (which is extracted from the monogenic framework). The choice of the neighborhood size (used to impose spatial regularization as in [Lucas and Kanade (1981)]) being a difficult issue, they apply an adaptive multiscale choice of the window size, as proposed in [Sühling *et al.* (2005)]. Specifically, at each scale, the local motion  $\Delta \mathbf{d}$  is computed as well as the residual error. Among the considered scales, the  $\Delta \mathbf{d}$  producing the smallest residual error is retained as displacement estimate. By doing so, the scale providing the most consistent motion estimate is selected.

The current estimate is then used to compensate the motion in the second frame and the monogenic signal of the two consecutive frames is recomputed using a smaller value

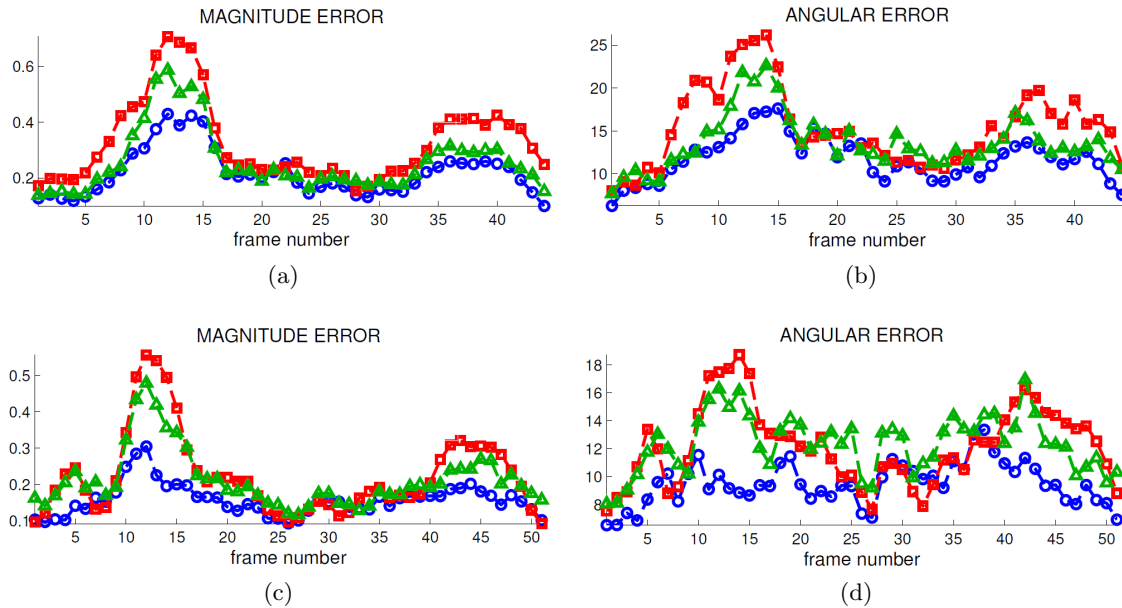


Figure 9.2: Motion estimation results from the method described in [Alessandrini *et al.* (2012)a] (blue), [Sühling *et al.* (2005)] (red) and [Felsberg (2004)] (green) on the SAx simulation (top row) and A4C simulation (bottom row) shown in Fig. 9.3 (from [Alessandrini *et al.* (2012)b]).

of  $\lambda_0$  (by dividing it by a factor  $k$ ) to capture finer details. The main process described above is then repeated  $N_p$  times.

This new motion estimation algorithm has been compared to two other methods [Sühling *et al.* (2005), Felsberg (2004)] on realistic echocardiographic simulations obtained using the simulation tool described in [Alessandrini *et al.* (2012)c]. The algorithm proved to be able to provide more accurate results than the two other methods as can be seen in Fig. 9.2. Indeed when compared to the algorithm proposed by [Sühling *et al.* (2005)], both algorithms use a coarse to fine motion estimation but the one proposed in [Alessandrini *et al.* (2012)a] produces better results in particular during cardiac phases associated with large magnitude motion, *e.g.* systole and early diastole, validating the choice of using phase instead of brightness consistency. Moreover when compared to the original monogenic motion estimator of [Felsberg (2004)], the better results provided by the algorithm of [Alessandrini *et al.* (2012)a] can be explain by the coarse to fine strategy, the affine motion model and the multiscale approach. Examples of motion field obtained on these simulations are shown in Fig. 9.3.

### 9.3 Motion term

Our motion term is inspired by the optical flow theory proposed by [Horn and Schunk (1981), Lucas and Kanade (1981)] with the following differences. Instead of applying the optical flow to the sequence to estimate the motion, we assume the motion to be known and constrain the level-set function to verify the optical flow hypothesis. These differences

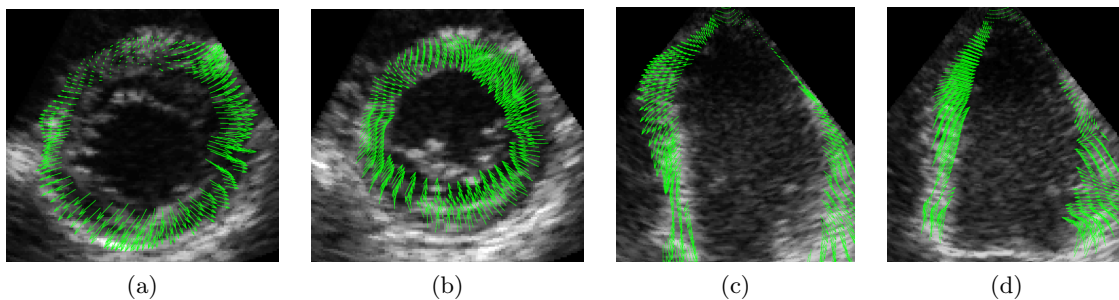


Figure 9.3: Diastolic and systolic frames from a synthetic parasternal short-axis ((a) and (b)) and apical 4-chamber ((c) and (d)) sequence. The motion estimated with the proposed algorithm is superimposed as green arrows (from [Alessandrini *et al.* (2012)b]).

are described in more details in Section 9.3.1. In Section 9.3.2, we describe the energy and the corresponding evolution equation derived from this hypothesis. We then provide the final algorithm we have designed for the segmentation and tracking of echocardiographic sequences

### 9.3.1 Hypothesis

As explained in Chapter 8, when estimating the motion in a sequence, the assumption is made that the grey level of a pixel remains constant in time. More formally, denoting by  $I : \mathbb{R}^2 \times \mathbb{R}^+ \mapsto \mathbb{R}$  the sequence, this can be written as  $I(\mathbf{p}) = I(\mathbf{p} + \mathbf{\Delta})$ , where  $I(\mathbf{p})$  is the grey level at point  $\mathbf{p} = (x, y, t)$  and  $\mathbf{\Delta} = (\Delta x, \Delta y, \Delta t)$  is the displacement between two consecutive frames. Assuming the displacement  $\mathbf{\Delta}$  to be small and using a Taylor series development

$$I(\mathbf{p} + \mathbf{\Delta}) = I(\mathbf{p}) + I_x \Delta x + I_y \Delta y + I_t \Delta t, \quad (9.1)$$

the following equation can be derived:

$$I_x \Delta x + I_y \Delta y + I_t \Delta t = 0, \quad (9.2)$$

where  $I_\alpha = \partial I / \partial \alpha$ . Dividing eq. (9.2) by the time step  $\Delta t$ , yield the optical flow constraint:

$$I_x u + I_y v + I_t = 0 \Leftrightarrow \nabla I \cdot \mathbf{V} + I_t = 0, \quad (9.3)$$

where  $\mathbf{V} = (u, v)$  is the interframe motion.

When performing motion estimation, the sequence  $I$  is given and the unknowns are the two components  $u$  and  $v$  of the motion. The problem is thus ill-posed since we have more unknowns than equations. To tackle this problem, various solutions have been proposed such as smooth variations of the motion field [Horn and Schunk (1981)] or constant motion in a small neighborhood [Lucas and Kanade (1981)].

In our case, we assume the motion to be estimated prior to segmentation. Furthermore, we make the hypothesis of the level conservation of the level-set function  $\phi$  instead of the



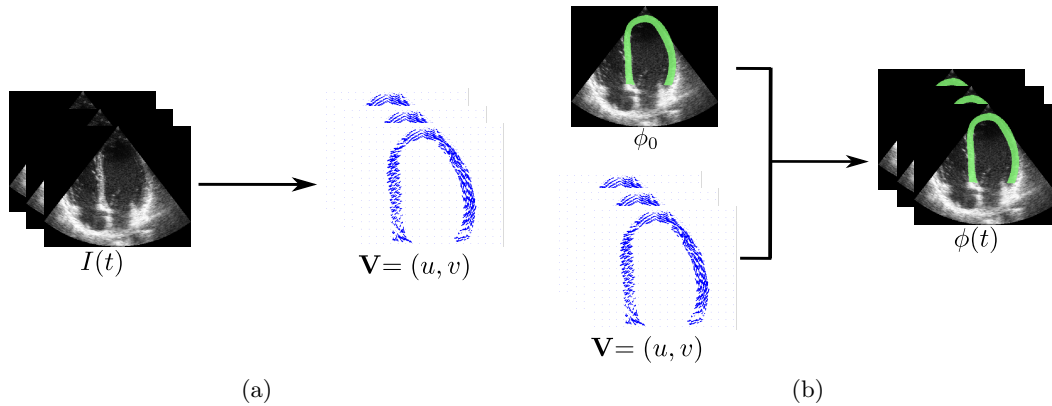


Figure 9.4: (a) Classical optical flow computation: the image sequence  $I$  is used to estimate the motion  $\mathbf{V} = (u, v)$ . (b) Optical flow guided level-set: the motion  $\mathbf{V}$  is estimated prior to segmentation and is used to guide the evolution of the level-set  $\phi$ .

grey level consistency. This assumption can be written as

$$\phi_x u + \phi_y v + \phi_t = 0 \Leftrightarrow \nabla \phi \cdot \mathbf{V} + \phi_t = 0. \quad (9.4)$$

Note that in this case, the motion is an input data as well as the segmentation of the first frame  $\phi_0$  while the level-set function is the unknown. Thus for each pixel  $\mathbf{p}$ , we still have one equation but only one unknown  $\phi(\mathbf{p})$  yielding a unique solution to the problem.

Fig. 9.4 depicts both schemes (motion estimation using OF and level-set segmentation based on level consistency), where the inputs are always on the left side and the unknown on the right side of the figure.

### 9.3.2 Energy formulation

We propose to minimize the following energy:

$$E_{motion}(\phi) = \int_{\Omega} (\nabla \phi(\mathbf{p}) \cdot \mathbf{V}(\mathbf{p}) + \phi_t(\mathbf{p}))^2 d\mathbf{p} \quad (9.5)$$

in order to impose the level consistency hypothesis (9.4). Indeed one can clearly see that the minimum of (9.5) is achieved when the levels of  $\phi$  in two successive frames satisfy the OF hypothesis.

Note however that if we minimize the energy (9.5), we will not be able to keep the signed distance property for  $\phi$  and thus may have numerical instabilities. To tackle this problem, we note that we only need the zero-level of  $\phi$  to satisfy the level consistency assumption. Thus we rewrite (9.5) as:

$$E_{motion}(\phi) = \int_{\Omega} \delta(\phi(\mathbf{p})) (\nabla \phi(\mathbf{p}) \cdot \mathbf{V}(\mathbf{p}))^2 d\mathbf{p}, \quad (9.6)$$

where  $\delta(\cdot)$  is the Dirac distribution allowing to consider only the zero-level of  $\phi$  and where homogeneous coordinates have been used, that is  $\nabla = (\partial/\partial x, \partial/\partial y, \partial/\partial t)$  and

$$\mathbf{V} = (u, v, 1).$$

The evolution equation is obtained by minimizing (9.6) with respect to  $\phi$  and is given by:

$$\frac{\partial \phi}{\partial \tau} = -\frac{\partial E}{\partial \phi} = 2\delta(\phi(\mathbf{p}))(\mathbf{V}^T \mathcal{H}(\phi)\mathbf{V} + \nabla \phi^T \mathcal{J}(\mathbf{V})\mathbf{V} + \text{Tr}(\mathcal{J}(\mathbf{V}))\nabla \phi^T \mathbf{V}) \quad (9.7)$$

where  $\tau$  is an artificial time parameter,  $\mathcal{H}(\phi)$  is the Hessian matrix of  $\phi$ ,  $\mathcal{J}(\mathbf{V})$  the Jacobian matrix of  $\mathbf{V}$  and  $\text{Tr}(A)$  is the trace of the matrix  $A$ . Note that the complete derivation is given in Appendix B.

To segment complete echocardiographic sequences, we propose to add the motion term (9.6) to the energy (7.1) described in Chapter 7 yielding the following general expression for the energy:

$$E = \nu_d E_{data} + \nu_s E_{shape} + \nu_t E_{thickness} + \nu_m E_{motion}, \quad (9.8)$$

where  $E_{data}$  represents the chosen data attachment term (7.2),  $E_{shape}$  embeds the shape prior (7.5),  $E_{thickness}$  is the anti-collision term (7.7) and  $E_{motion}$  is the motion term (9.6).  $\nu_i$  with  $i = \{d, s, t, m\}$  are hyperparameters weighting the influence of the different terms.

The level-set then evolves according to the following equation:

$$\frac{\partial \phi}{\partial \tau}(\mathbf{p}) = \nu_d f(\mathbf{p}) + \nu_s g(\mathbf{p}) + \nu_t h(\mathbf{p}) + \nu_m k(\mathbf{p}), \quad (9.9)$$

where  $f(\cdot)$  is the data attachment term given in equation (7.4),  $g(\cdot)$  is the shape prior term given in equation (7.6),  $h(\cdot)$  is the thickness term given in equation (7.8) and  $k(\cdot)$  is the motion term given in equation (9.7).

## 9.4 Implementation issues

### 9.4.1 Implementation of the evolution equation

As mentioned in Section 4.6, in order to avoid numerical instabilities, the derivatives of  $\phi$  should be computed using specific schemes called Upwind schemes [Osher and Sethian (1988), Osher and Fedkiw (2002)].

Considering (9.7), it can be seen that we have to compute the first and second order derivatives of  $\phi$  with respect to each dimension ( $x$ ,  $y$  and  $t$ ). Spatial derivatives can be easily computed using (4.23) to (4.27) though one may need to impose boundary conditions in order to compute the backward/forward derivatives on  $\partial\Omega$ . On the other hand, temporal derivatives (forward and 2nd order) require to use  $\phi(t+1)$  which is not available when segmenting the frame  $t$ .

A first solution would be to segment the whole sequence considering a 3D level-set:  $\phi : \mathbb{R}^2 \times \mathbb{R}^+ \mapsto \mathbb{R}$ . However, this solution has several drawback. First, due to the local nature of the data attachment term, the initial contour on each frame has to be close to

the true myocardial boundaries (as shown in Chapter 7). As will be shown in Section 9.5, tracking techniques which could be used to give the initial curves, fail to segment properly an entire sequence. A second drawback is that we would need to acquire the complete sequence before being able to process it making the algorithm unusable for on-line analysis.

This issue is solved by computing an rough approximation of  $\phi$  at  $t$  and  $t + 1$  from the knowledge of  $\phi(t - 1)$  and the available motion field: starting from the segmentation result at  $t - 1$ , we track the myocardial boundary using the estimated motion at  $t - 1$  and  $t$  to obtain a prediction of  $\phi$  at  $t + 1$  which is then used for the derivatives computation.

Note that the first derivatives of the velocity  $\mathbf{V}$  are computed using standard centered derivatives (4.25). This only implies that we need to compute the motion at time  $t + 1$  as well.

### 9.4.2 Level-set evolution

Similarly to the implementation of the algorithm described in Chapter 7, the implicit function is represented by a signed distance function  $\phi$  and is re-initialized every iteration using a fast marching scheme [Sussman *et al.* (1998)]. The neighbourhood  $N(\mathbf{p})$  defining the localization of the data attachment term is chosen in our case as a circular neighbourhood, with radius  $R_N$  chosen as the average thickness of the myocardium, *i.e.* 15 pixels in our case. In the same way, the value of  $R_T$  in the thickness term (7.7) was chosen to be set to 5 pixels.

The hyperparameters were set empirically and the same values were used in all experiments:  $\nu_d = 0.5$ ,  $\nu_s = 1$ ,  $\nu_t = 5$ . These values differ from the one given in 7.5.1 because of the introduction of the motion term and the fact that we now focus on the tracking of the myocardium. Regarding  $\nu_m$ , we used a different ponderation for the endocardial ( $\nu_m = 1.5$ ) and epicardial ( $\nu_m = 1$ ) border due to their different characteristics in the image. Indeed, the border of the endocardium is generally less smooth than the epicardial one and its segmentation implies the exclusion of the papillary muscles, which share similar intensity properties with the endocardium. Note that the hyperparameter  $\nu_t$  was set to a high value so that the thickness evolution term  $h(\mathbf{p})$  preponderate over the other evolution terms when the two contours are about to merge.

The following procedure is used to initialize the algorithm:

- the user is asked to enter 6 points (5 near the epicardium and 1 near the endocardium) and two ellipses are fitted on these points in a similar manner as described in Section 7.5.3.
- the static algorithm (Chapter 7) is used to segment the first frame of the sequence.
- the subsequent frames are then segmented using the proposed algorithm.

### 9.4.3 ROI tracking

When dealing with parasternal long-axis, apical 4-chamber or apical 2-chamber view, we need to update the ROI in order to make it corresponds to the part of the image where

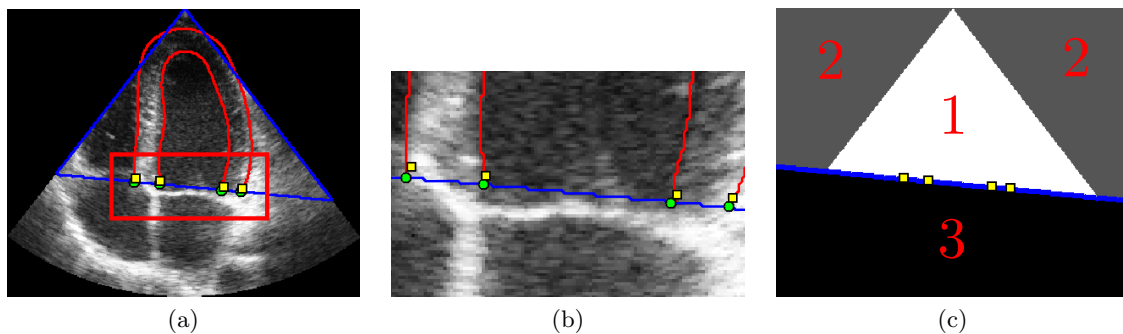


Figure 9.5: Example of a tracking of the ROI: (a) The image at  $t$ . Red: segmentation result; Blue: ROI; Green dots:  $\mathbf{p}_t$ ; Yellow dots:  $\mathbf{p}_{t+1}$  (b) Zoom of the region delineated red in (a). (c) ROI at  $t + 1$ ; Yellow dots:  $\mathbf{p}_{t+1}$ ; Blue: closest line to  $\mathbf{p}_{t+1}$

the myocardium is visible. This task is performed as follows:

1. the 4 intersection points  $\mathbf{p}_t$  between the segmentation result and the ROI at time  $t$  are computed (green points in Fig. 9.5(a) and (b));
2. the estimated motion is applied to these points to get their approximate position at  $t + 1$  denoted as  $\mathbf{p}_{t+1}$  (yellow points in Fig. 9.5);
3. least square fitting is used to estimate the closest line to  $\mathbf{p}_{t+1}$  (blue line in Fig. 9.5(c));
4. a mask is created in a similar manner as the one explained in Section 7.5.2 and is used as a ROI at  $t + 1$ .

This procedure is illustrated in Fig. 9.5.

## 9.5 Results

### 9.5.1 Comparison protocol

#### Experimental data

The reference dataset is composed of 20 echocardiographic sequences (5 per view) acquired from 14 healthy volunteers and imaging at least one cardiac cycle. The sequences were acquired using a GE Vivid E9 system equipped with a 2.5 MHz M5S probe (GE Vingmed Ultrasound, Horten, Norway). Two experts manually outlined the myocardium on one cardiac cycle per sequence resulting in the following reference distribution:

- 290 frames in parasternal short-axis view,
- 303 frames in parasternal long-axis view,
- 300 frames in apical 4-chamber view,
- 300 frames in apical 2-chamber view.

#### Error measures

To evaluate the accuracy of the algorithm, we measured the correspondence between the tracking results and the mean myocardial shape of the two experts contour obtained using the procedure described in [Chalana and Kim (1997)]. The three same metrics

|                        | Epicardium                                       |                  |                 | Endocardium                                      |                  |                 |
|------------------------|--|------------------|-----------------|--|------------------|-----------------|
|                        | $D^*$  | MAD              | HD              | $D^*$  | MAD              | HD              |
| Parasternal short-axis | $1.19 \cdot 10^{-2}$<br>( $2.55 \cdot 10^{-3}$ ) | 0.324<br>(0.061) | 1.11<br>(0.239) | $2.08 \cdot 10^{-2}$<br>( $1.14 \cdot 10^{-2}$ ) | 0.413<br>(0.223) | 1.11<br>(0.403) |
| Parasternal long-axis  | $8.59 \cdot 10^{-3}$<br>( $4.15 \cdot 10^{-3}$ ) | 0.445<br>(0.222) | 2.33<br>(1.57)  | $1.63 \cdot 10^{-2}$<br>( $5.66 \cdot 10^{-3}$ ) | 0.591<br>(0.228) | 3.03<br>(1.64)  |
| Apical 4-chamber       | $1.56 \cdot 10^{-2}$<br>( $6.57 \cdot 10^{-3}$ ) | 0.723<br>(0.262) | 2.47<br>(1.01)  | $2.97 \cdot 10^{-2}$<br>( $9.88 \cdot 10^{-3}$ ) | 0.844<br>(0.278) | 2.87<br>(0.994) |
| Apical 2-chamber       | $1.46 \cdot 10^{-2}$<br>( $9.04 \cdot 10^{-3}$ ) | 0.615<br>(0.295) | 2.9<br>(1.22)   | $3.47 \cdot 10^{-2}$<br>( $1.53 \cdot 10^{-2}$ ) | 0.949<br>(0.358) | 3.07<br>(1.34)  |

Table 9.1: Results of the fit of the hyperquadric prior on the mean curve of the epicardial and endocardial borders in term of modified Dice criterion ( $D^*$ ), Mean Absolute Distance (MAD) and Hausdorff distance (HD). The given values correspond to the mean (Standard deviation). HD and MAD are given in mm.

(modified Dice criterion  $D^*$ ,  $MAD$  and  $HD$ ) described in Section 6.5 were used with the following definition:

$$D^*(\Omega_R, \Omega_S) = \frac{1}{T} \sum_{t=1}^T D^*(\Omega_R(t), \Omega_S(t)). \quad (9.10)$$

$$MAD(R, S) = \frac{1}{T} \sum_{t=1}^T MAD(R(t), S(t)), \quad (9.11)$$

and

$$HD(R, S) = \frac{1}{T} \sum_{t=1}^T HD(R(t), S(t)) \quad (9.12)$$

where  $R$  and  $S$  are the reference contours and the tracking results,  $\Omega_S$  and  $\Omega_R$  are the sets of pixels within the segmented and the reference region and  $T$  is the number of frame in a given sequence.

## 9.5.2 Evaluation of the proposed scheme

### Hyperquadric shape prior

Since we will use the hyperquadric prior described in Chapters 6 and 7 to constrain the level-set evolution, we first demonstrate that hyperquadrics can be used to model the heart boundaries on whole sequence. To this end, we fit the hyperquadric model (with  $N_h = 4$ ) on the mean curve of the manual references drawn by two experts on the dataset and compared the error measures to the one obtained in Chapter 6. The results are given in Table 9.1.

From this Table, we can see that globally the mean error measures increase for hyperquadrics fit on whole sequence compared to the fitting on ED/ES images (*cf.* Table 6.1 and 6.2). This can be explained by the higher variability in the myocardial shape since we have to model the myocardium at ED and ES as well as all the shapes in between. However, we can note that this increase is moderate and that for example the mean MAD

|                          | Epicardium   |                           |                          | Endocardium                                      |                          |                          |
|--------------------------|--|---------------------------|--------------------------|--|--------------------------|--------------------------|
|                          | $D^*$  | MAD                       | HD                       | $D^*$  | MAD                      | HD                       |
| Tracking                 | $3.42 \cdot 10^{-2} \dagger$<br>( $1.78 \cdot 10^{-2}$ ) | $1.10 \dagger$<br>(0.552) | $6.04 \dagger$<br>(2.72) | $0.147 \dagger$<br>( $6.19 \cdot 10^{-2}$ )      | $3.58 \dagger$<br>(1.42) | $7.79 \dagger$<br>(2.81) |
| Multistatic segmentation | $7.12 \cdot 10^{-2} \dagger$<br>( $2.93 \cdot 10^{-2}$ ) | $2.14 \dagger$<br>(0.830) | $8.28 \dagger$<br>(3.10) | $0.182 \dagger$<br>(0.113)                       | $3.69 \dagger$<br>(2.24) | $14.4 \dagger$<br>(9.79) |
| Proposed method          | $2.33 \cdot 10^{-2}$<br>( $9.67 \cdot 10^{-3}$ )         | 0.753<br>(0.284)          | 3.77<br>(1.00)           | $5.03 \cdot 10^{-2}$<br>( $1.73 \cdot 10^{-2}$ ) | 1.13<br>(0.335)          | 4.16<br>(1.20)           |

Table 9.2: Results of the tracking of the myocardial border in an apical 4-chamber sequence in term of modified Dice criterion ( $D^*$ ), Mean Absolute Distance (MAD) and Hausdorff distance (HD). The given values correspond to the mean (Standard deviation). HD and MAD are given in mm.  $\dagger$  indicates that the difference was found significant ( $p < 0.05$ ) when compared to the proposed method.

never exceed 1mm showing that the fit results are overall close to the cardiologist references. This proves that hyperquadrics can accurately model the heart borders on whole sequences.

### Importance of the motion information

In order to show the efficiency of motion information in improving segmentation results, we segmented an apical 4-chamber sequence using three different methods:

1. pure tracking: the contour points are displaced using the estimated motion to track the myocardial border.
2. multistatic segmentation: the algorithm described in Chapter 7 is used successively on each frame. The initial contour at  $t + 1$  corresponds to the contour obtained after tracking of the segmentation result  $t$ .
3. our proposed method.

In all three methods, the monogenic motion estimation described in Section 9.2.2 was used. The results obtained on this sequence using these methods are given in Table 9.2 and a Friedman rank test ( $p = 0.05$ , [Chalana and Kim (1997)]) was applied to compare the results obtained using the proposed method and the two other ones.

From these figures, we can see that the proposed method outperformed the two others and that the differences are always statistically significant. Indeed, when compared to a pure tracking algorithm, our method has the advantage of using more information (*i.e.* intensity and shape) which allows it to better deal with areas where the motion is not a reliable information (such as low contrast or near-field areas). On the other hand, the motion can provide reliable information to follow moving structures or intensity changes in structures. Since these information are not taken into account in the static segmentation algorithm described in chapter 7, the proposed method manages to segment more robustly these structures.

### 9.5.3 Myocardial tracking results

We evaluate in this section the performance of our segmentation algorithm. The comparison protocol is the one described in 9.5.1 and the inter-observer distance (IOD) reported in the tables corresponds to the mean of the distances computed between the references of each expert. Tables 9.3 and 9.4 provide the mean and standard deviation of the error measures obtained for the complete data set on epicardial and endocardial borders, respectively. In each table, we give for each measure (modified Dice, MAD, Hausdorff) the IOD (three first columns), the error measures associated to the proposed method (three middle columns) and to Hamou's method (three last columns). Fig. 9.6 allows to visually compare these results for every view and for each border. To illustrate the quality of our results, we show examples of good tracking results and the associated mean reference contour of the cardiologists for parasternal (Fig. 9.7 and 9.8) and apical (Fig. 9.9 and 9.10) views. We also give some of the worst tracking results we obtained in Fig. 9.11 as well as the experts references on these images.

Considering, in a first step, the segmentation of the epicardium in parasternal short-axis view (first line in Table 9.3, Fig. 9.7), it may be observed that our method provides small values for all the criteria ( $D^* = 2.94 \cdot 10^{-2}$ , MAD = 0.83mm and HD = 2.19mm). This means that our segmentation results are close to the reference contours both on a global ( $D^*$  and MAD) and a local (HD) scale for this orientation. When compared to the corresponding IOD (three first columns in Table 9.3), it may be observed that the values obtained using the proposed method are slightly lower than the inter-observer ones ( $2.95 \cdot 10^{-2}$ , 0.852mm and 2.43mm for the modified Dice, the MAD and the HD respectively). This thus indicates that the segmentation provides consistent results in the sense that the difference with the experts' reference is comparable to the distance between experts.

The results associated with the endocardial borders in the same parasternal short-axis view (first line in Table 9.4), show that the errors are in the same order and slightly larger except for the HD:  $4.33 \cdot 10^{-2}$  for the modified Dice, 0.854mm for the MAD and 2.15mm for the HD. These higher values may come from the presence of the papillary muscles. Indeed these structures present intensity properties similar to the myocardium making them difficult to separate using the data attachment term. Moreover they also have a through-plan motion which means that they may not be present during the whole sequence. This, in turn, may imply a wrong motion estimation when these structures (dis)appear making them difficult to follow with the motion term. Note however that the same trend can be seen in the IOD and that our results are still in the same order and slightly lower than the corresponding IOD ( $6.94 \cdot 10^{-2}$  for  $D^*$ , 1.46mm for the MAD and 3.27mm for the HD).

If we now consider the other views (three last lines of Tables 9.3 and 9.4), we observe that in the parasternal views, the myocardium is better tracked than in apical views (*e.g.* the MAD for the epicardial border is 0.7mm smaller in parasternal long-axis than in apical views). This can be explained by a better image quality achieved in parasternal

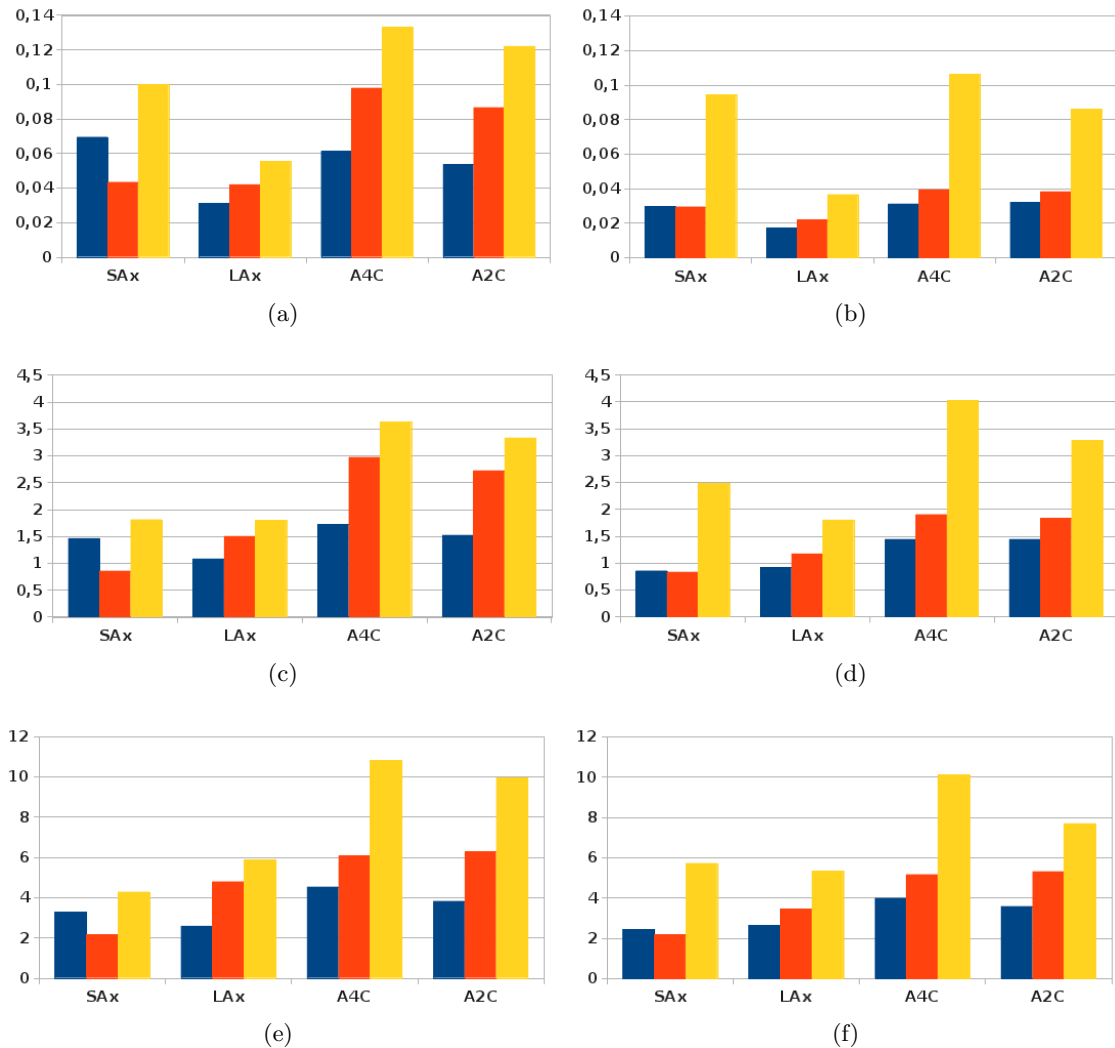


Figure 9.6: Results of the segmentation of the endocardial (left column) and epicardial (right column) borders in terms of  $D^*$  (first row), MAD (second row) and Hausdorff distance (third row). The MAD and Hausdorff distance are given in mm. Blue: Inter-Observers Distance; Red: results of our method; Yellow: results of [Hamou and El-Sakka (2010)].

views, where the myocardium is well-defined. On the other hand in apical views, the apex, commonly located in the near field of the probe, is usually blurred and the lateral wall is often poorly contrasted, yielding missing boundaries of significant size. In these cases, the multiscale motion estimator based on monogenic signal captures texture information at a coarse scale which combined to the shape prior, allows to cope with this missing information and provides meaningful results. This however induces a lower accuracy.



|                       | IOD  |  |                  | Our method                                       |  |                  | Hamou  |  |                             |
|-----------------------|--|--|------------------|--|--|------------------|--|--|-----------------------------|
|                       | $D^*$  | MAD  | HD               | $D^*$  | MAD  | HD               | $D^*$  | MAD  | HD                          |
|                       | Parasternal short-axis                           | $2.95 \cdot 10^{-2}$<br>( $1.35 \cdot 10^{-2}$ ) | 0.852<br>(0.402) | 2.43<br>(0.927)                                  | $2.94 \cdot 10^{-2}$<br>( $2.29 \cdot 10^{-2}$ ) | 0.830<br>(0.654) | 2.19<br>(1.59)                                   | $9.43 \cdot 10^{-2}$<br>( $9.60 \cdot 10^{-2}$ ) | 2.48 <sup>†</sup><br>(2.45) |
| Parasternal long-axis | $1.70 \cdot 10^{-2}$<br>( $1.06 \cdot 10^{-2}$ ) | 0.918<br>(0.593)                                 | 2.64<br>(1.67)   | $2.20 \cdot 10^{-2}$<br>( $1.34 \cdot 10^{-2}$ ) | 1.17<br>(0.719)                                  | 3.46<br>(2.05)   | $3.65 \cdot 10^{-2}$<br>( $4.39 \cdot 10^{-2}$ ) | 1.80 <sup>†</sup><br>(2.02)                      | 5.33 <sup>†</sup><br>(4.89) |
| Apical 4-chamber      | $3.11 \cdot 10^{-2}$<br>( $1.26 \cdot 10^{-2}$ ) | 1.44<br>(0.571)                                  | 3.99<br>(1.55)   | $3.93 \cdot 10^{-2}$<br>( $1.59 \cdot 10^{-2}$ ) | 1.90<br>(0.829)                                  | 5.16<br>(3.01)   | 0.106 <sup>†</sup><br>( $7.16 \cdot 10^{-2}$ )   | 4.02 <sup>†</sup><br>(2.48)                      | 10.1 <sup>†</sup><br>(6.1)  |
| Apical 2-chamber      | $3.21 \cdot 10^{-2}$<br>( $1.23 \cdot 10^{-2}$ ) | 1.44<br>(0.49)                                   | 3.58<br>(1.16)   | $3.82 \cdot 10^{-2}$<br>( $2.00 \cdot 10^{-2}$ ) | 1.83<br>(0.911)                                  | 5.31<br>(4.68)   | $8.59 \cdot 10^{-2}$<br>( $6.78 \cdot 10^{-2}$ ) | 3.28 <sup>†</sup><br>(2.14)                      | 7.69 <sup>†</sup><br>(4.97) |

Table 9.3: Results of the segmentation of the epicardial border. The results of our method and the one described in [Hamou and El-Sakka (2010)] as well as the Inter-Observers Distance (IOD) are shown in term of modified Dice criterion ( $D^*$ ), Mean Absolute Distance (MAD) and Hausdorff distance (HD). The given values correspond to the mean (Standard deviation). HD and MAD are given in mm. †indicates that the difference was found significant ( $p < 0.05$ ) when compared to our method.

|                       | IOD  |  |                 | Our method                                       |  |                  | Hamou  |                             |                             |
|-----------------------|--|--|-----------------|--|--|------------------|--|-----------------------------|-----------------------------|
|                       | $D^*$  | MAD  | HD              | $D^*$  | MAD  | HD               | $D^*$  | MAD                         | HD                          |
|                       | Parasternal short-axis                           | $6.94 \cdot 10^{-2}$<br>( $3.44 \cdot 10^{-2}$ ) | 1.46<br>(0.767) | 3.27<br>(1.26)                                   | $4.33 \cdot 10^{-2}$<br>( $3.72 \cdot 10^{-2}$ ) | 0.854<br>(0.746) | 2.15<br>(1.59)                                   | 0.1 <sup>†</sup><br>(0.101) | 1.81 <sup>†</sup><br>(1.62) |
| Parasternal long-axis | $3.10 \cdot 10^{-2}$<br>( $2.61 \cdot 10^{-2}$ ) | 1.08<br>(0.929)                                  | 2.58<br>(1.86)  | $4.19 \cdot 10^{-2}$<br>( $2.52 \cdot 10^{-2}$ ) | 1.5<br>(0.919)                                   | 4.78<br>(3.09)   | $5.52 \cdot 10^{-2}$<br>( $4.78 \cdot 10^{-2}$ ) | 1.8<br>(1.39)               | 5.87 <sup>†</sup><br>(4.49) |
| Apical 4-chamber      | $6.12 \cdot 10^{-2}$<br>( $3.06 \cdot 10^{-2}$ ) | 1.72<br>(0.847)                                  | 4.52<br>(1.73)  | $9.78 \cdot 10^{-2}$<br>( $5.05 \cdot 10^{-2}$ ) | 2.97<br>(1.57)                                   | 6.06<br>(2.52)   | 0.133 <sup>†</sup><br>( $7.09 \cdot 10^{-2}$ )   | 3.63 <sup>†</sup><br>(1.67) | 10.8 <sup>†</sup><br>(5.69) |
| Apical 2-chamber      | $5.34 \cdot 10^{-2}$<br>( $2.05 \cdot 10^{-2}$ ) | 1.52<br>(0.54)                                   | 3.81<br>(1.12)  | $8.65 \cdot 10^{-2}$<br>( $3.98 \cdot 10^{-2}$ ) | 2.72<br>(1.22)                                   | 6.27<br>(3.07)   | 0.122 <sup>†</sup><br>(0.135)                    | 3.33 <sup>†</sup><br>(3.15) | 9.94 <sup>†</sup><br>(9.22) |

Table 9.4: Results of the segmentation of the endocardial border. The results of our method and the one described in [Hamou and El-Sakka (2010)] as well as the Inter-Observers Distance (IOD) are shown in term of modified Dice criterion ( $D^*$ ), Mean Absolute Distance (MAD) and Hausdorff distance (HD). The given values correspond to the mean (Standard deviation). HD and MAD are given in mm. †indicates that the difference was found significant ( $p < 0.05$ ) when compared to our method.

The standard deviation for the epicardial border varies between  $1.3 \cdot 10^{-3}$  and  $2.3 \cdot 10^{-2}$  for  $D^*$ , 0.65 and 0.9 for the MAD and 1.6 and 4.7 for the HD. These values are in the same order than the standard deviation obtained for the experts' outline boundaries for the parasternal views while slightly higher in apical views, showing that the segmentation results do not deviate from the mean value more than the experts' outlined boundaries do. The same conclusion can be drawn for the endocardial detection where the standard deviation varies between  $2.5 \cdot 10^{-2}$  and  $5 \cdot 10^{-2}$  for  $D^*$ , 0.75 and 1.6 for the MAD and 1.6 and 3 for the HD.

Fig. 9.11 shows some of the worst tracking results and illustrates the difficulties encountered when tracking the myocardium. In parasternal long-axis views (Fig. 9.11(a) and (d)), an important part of the myocardium is usually out of the field of view during systole. Since the shape prior is only fitted on points inside the ROI, only few points are available and the hyperquadric fit is sometimes less reliable. The shape prior then tends to drive the contour to a wrong position yielding unsatisfactory results.

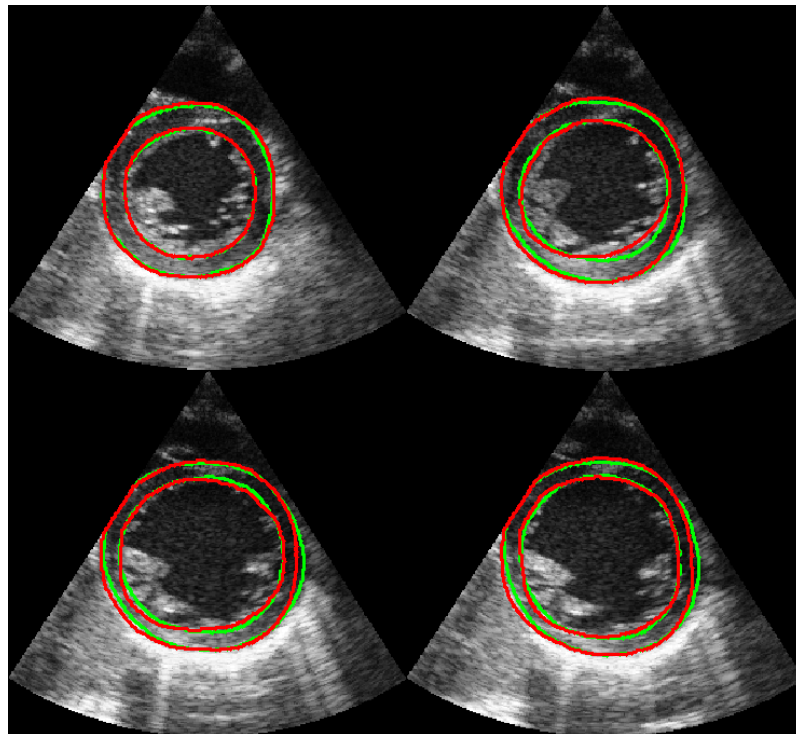
Another problem corresponds to the missing boundaries that are frequent in apical views for example (Fig. 9.11(b), (c), (e) and (f)). In Fig. 9.11(e), the apex is completely blurred and there is no image or motion information that can reliably drive the active contour. Thus the contour does not evolve from its initial position leading to high error values. Note however that our algorithm is able to correct this problem and provide satisfactory results in the next frames (Fig. 9.11(e) is taken out of the sequence shown in Fig. 9.9(a)). It can also be observed that our errors (*e.g.* 1.28mm for the MAD and 5.54mm for the HD of the endocardial border) are in the same order than the IOD (2.00mm for the MAD and 6.59mm for the HD of the endocardial border) and that the poor quality of the data also yield a higher inter-observer variability, confirming the difficulty to segment these data.

The figures provided in the last three columns of Tables 9.3 and 9.4 allow comparing the performance of the proposed method and Hamou's method. This method is close to ours since it uses both a motion and a shape term in a GVF-based snake framework. More specifically two edge maps are computed and used alternatively to evolve the curve: the first one is based on the optical flow computed between two subsequent frames while the second one is a shape prior based on  $3^{rd}$  order hyperbolas (see also Section 8.3).

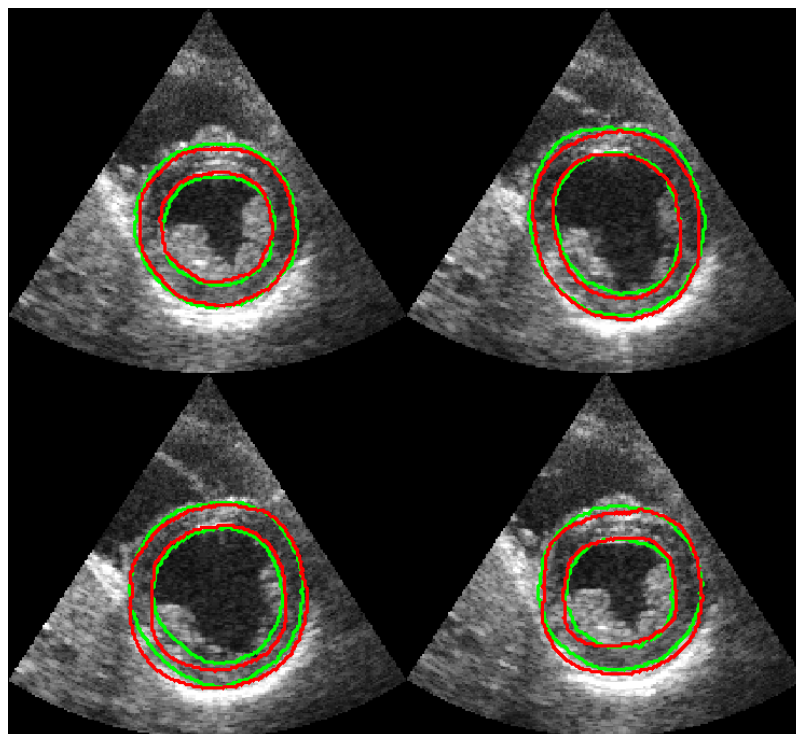
The results show that our method yields better results (difference statistically significant at a level  $p = 0.05$  for the Friedman rank test), except for the endocardial border in parasternal long-axis view, where the results are similar in term of MAD and  $D^*$ . Considering the mean differences between the error measures associated with the two approaches,  $D^*$  is on the average  $5 \cdot 10^{-2}$  ( $3.5 \cdot 10^{-2}$ ) lower, the MAD is 1.5mm (0.6mm) lower and the HD 3.2mm (2.9mm) lower which corresponds to at least a 44% (24%) improvement of the result for the epicardium (endocardium). This can be explained by the fact that our shape prior is better suited for the modelling of the heart boundaries as was shown in Section 6.5.2 and 7.6 but also by the fact that our motion term is more accurate than the classical OF hypothesis applied to B-mode images.

## 9.6 Conclusion

In this chapter, we proposed an algorithm to segment and track the whole myocardium in any of the classical views used in clinical routine. We proposed to add to the algorithm described in Chapter 7 a motion term that enforces the zero-level of the implicit function to satisfy the optical flow constraint. We then evaluated our method on a dataset of 20 sequences composed by more than 1000 images and showed that the tracking results were consistent with the references of 2 experts and compared favorably with a state-of-the-art algorithm.

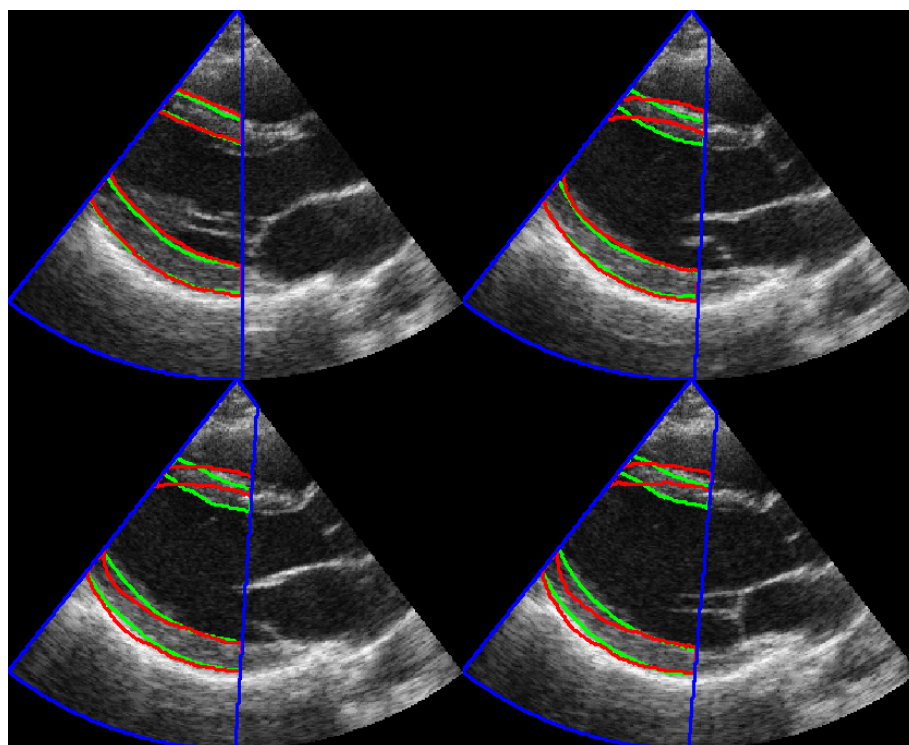


(a)  $MAD(\text{mm})$ :  $Endo = 0.715$ ,  $Epi = 0.792$ ,  
 $HD(\text{mm})$ :  $Endo = 2.13$ ,  $Epi = 2.24$

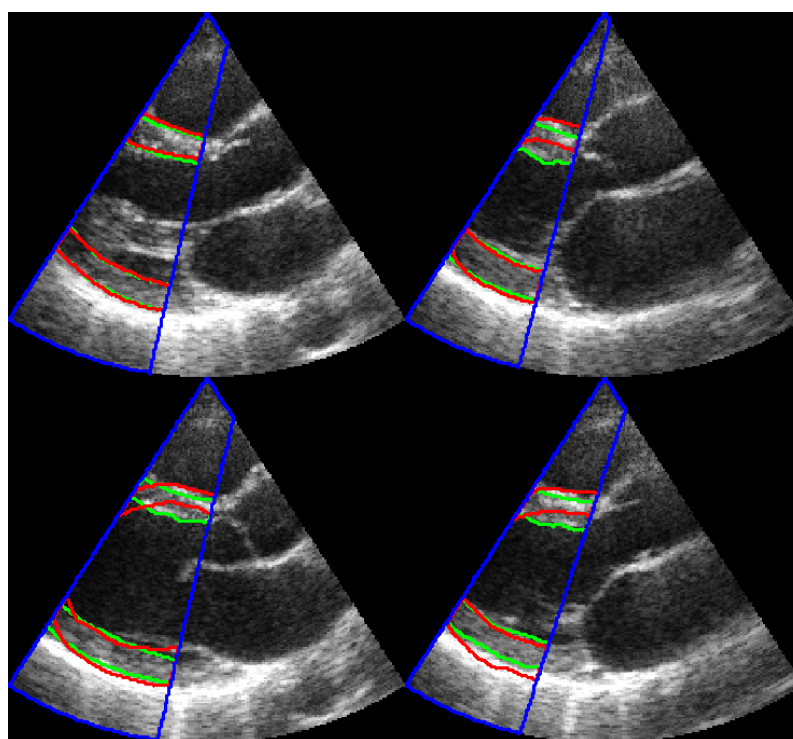


(b)  $MAD(\text{mm})$ :  $Endo = 1.03$ ,  $Epi = 1.09$ ,  
 $HD(\text{mm})$ :  $Endo = 3.11$ ,  $Epi = 2.99$

Figure 9.7: Results of the tracking of the whole myocardium at 4 time points in the cardiac cycle in parasternal short-axis views. Green: mean reference of the cardiologists; Red: our contour and Blue: region of interest. For each sequence, the MAD and HD (in mm) computed between the segmentation result and the mean contour is given.

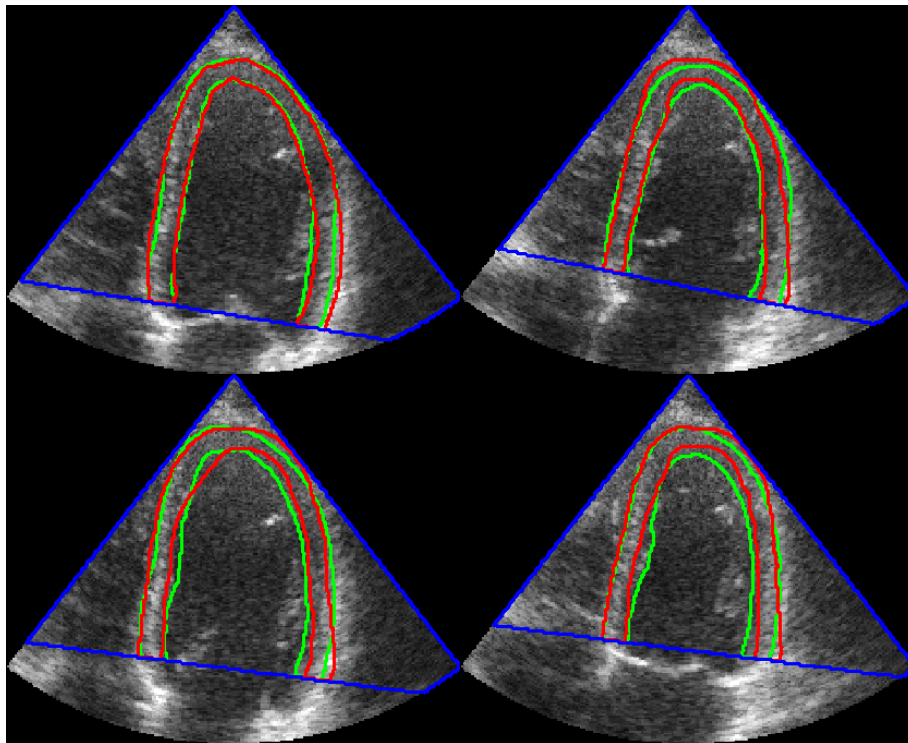


(a)  $MAD(\text{mm})$ :  $Endo = 1.93$ ,  $Epi = 1.35$ ,  
 $HD(\text{mm})$ :  $Endo = 5.45$ ,  $Epi = 4.27$

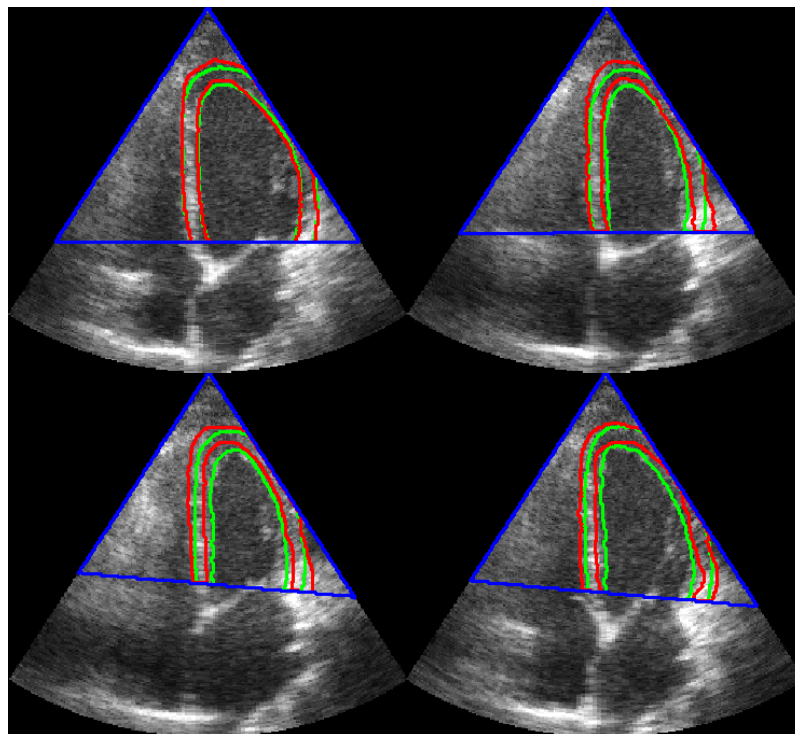


(b)  $MAD(\text{mm})$ :  $Endo = 1.86$ ,  $Epi = 1.77$ ,  
 $HD(\text{mm})$ :  $Endo = 5.29$ ,  $Epi = 3.69$

Figure 9.8: Results of the tracking of the whole myocardium at 4 time points in the cardiac cycle in parasternal long-axis views. Green: mean reference of the cardiologists; Red: our contour and Blue: region of interest. For each sequence, the MAD and HD (in mm) computed between the segmentation result and the mean contour is given.

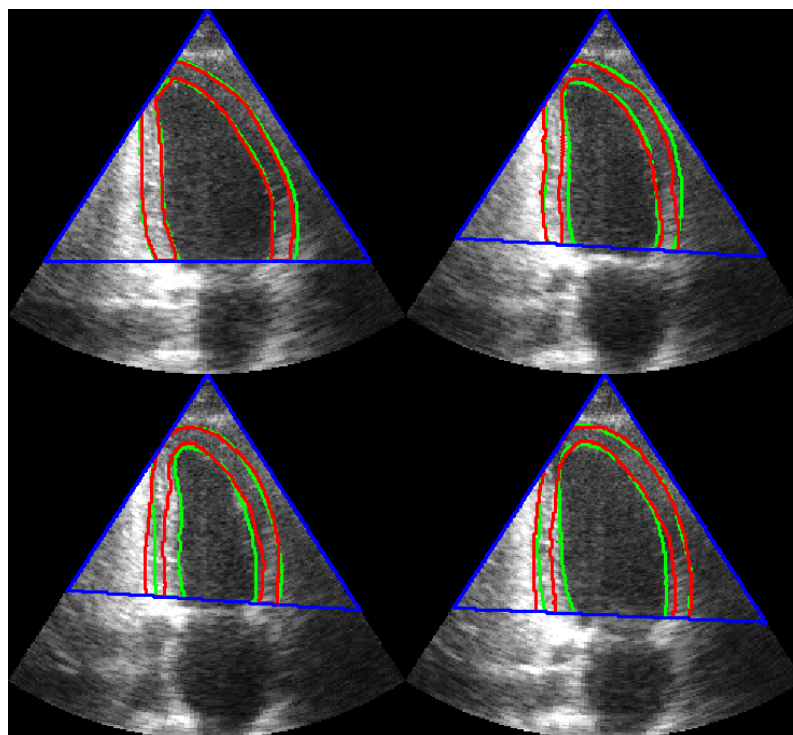


(a)  $MAD(\text{mm})$ :  $Endo = 1.53$ ,  $Epi = 1.27$ ,  
 $HD(\text{mm})$ :  $Endo = 4.11$ ,  $Epi = 3.67$

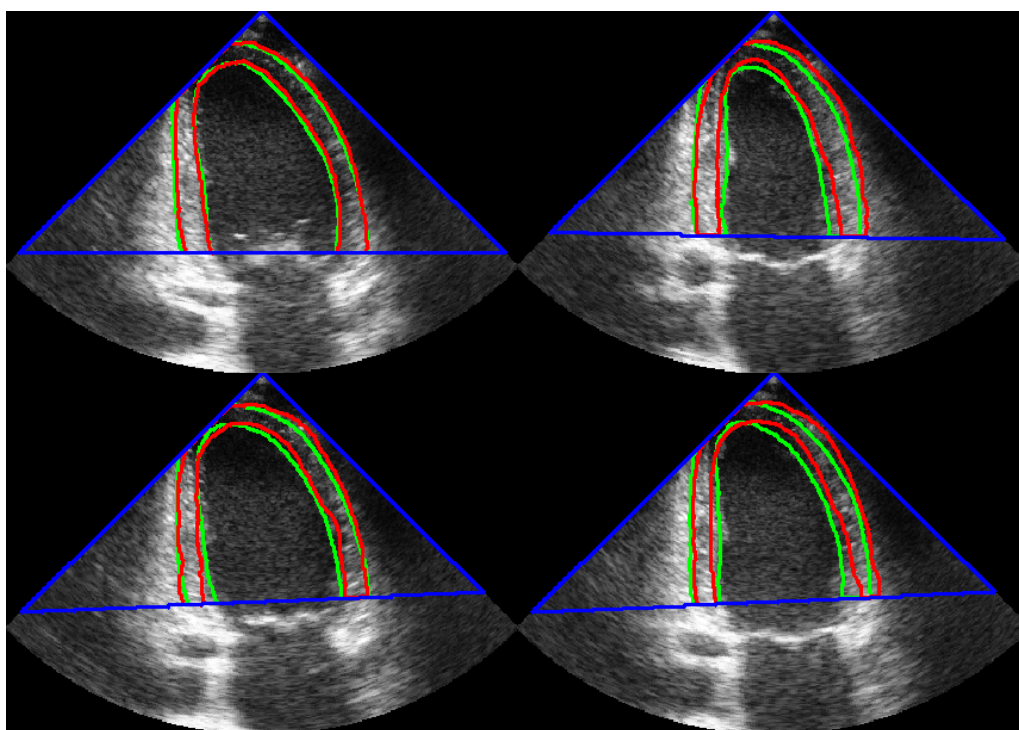


(b)  $MAD(\text{mm})$ :  $Endo = 2.06$ ,  $Epi = 1.81$ ,  
 $HD(\text{mm})$ :  $Endo = 4.77$ ,  $Epi = 4.95$

Figure 9.9: Results of the tracking of the whole myocardium at 4 time points in the cardiac cycle in apical views. Green: mean reference of the cardiologists; Red: our contour and Blue: region of interest. For each sequence, the MAD (in mm) computed between the segmentation result and the mean contour is given.

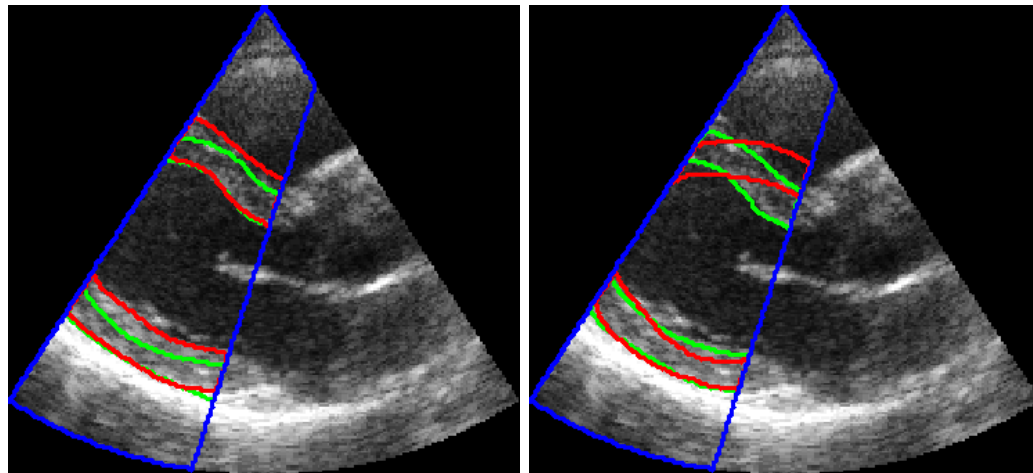


(a)  $MAD(\text{mm})$ :  $Endo = 1.94$ ,  $Epi = 1.09$   
 $HD(\text{mm})$ :  $Endo = 5.32$ ,  $Epi = 3.46$



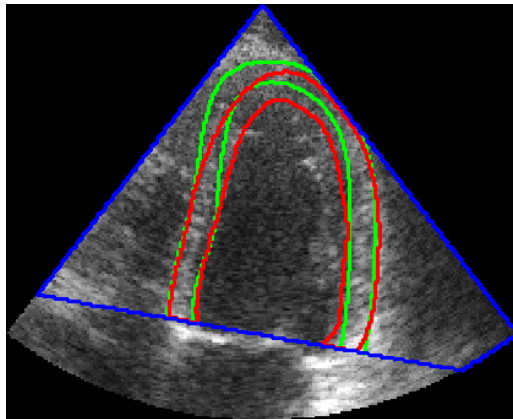
(b)  $MAD(\text{mm})$ :  $Endo = 2.05$ ,  $Epi = 1.56$ ,  
 $HD(\text{mm})$ :  $Endo = 4.87$ ,  $Epi = 3.62$

Figure 9.10: Results of the tracking of the whole myocardium at 4 time points in the cardiac cycle in apical views. Green: mean reference of the cardiologists; Red: our contour and Blue: region of interest. For each sequence, the MAD (in mm) computed between the segmentation result and the mean contour is given.

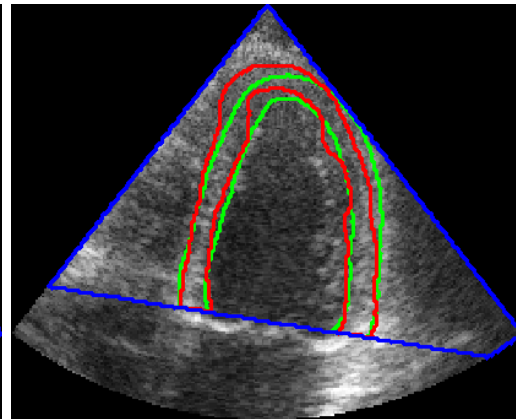


(a)  $MAD(mm)$ :  $Endo = 2.39$ ,  $Epi = 1.72$   
 $HD(mm)$ :  $Endo = 5.70$ ,  $Epi = 6.30$

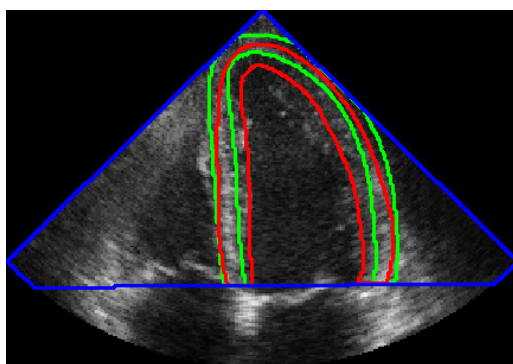
(b)  $MAD(mm)$ :  $Endo = 2.88$ ,  $Epi = 1.79$   
 $HD(mm)$ :  $Endo = 8.39$ ,  $Epi = 7.21$



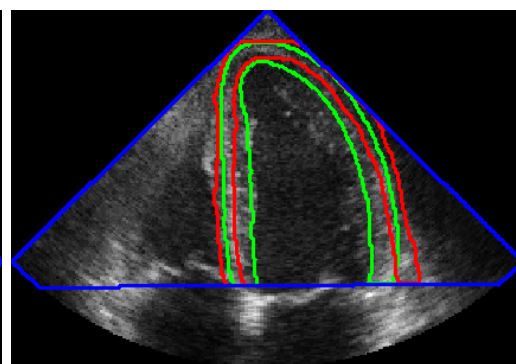
(c)  $MAD(mm)$ :  $Endo = 2.00$ ,  $Epi = 1.40$   
 $HD(mm)$ :  $Endo = 6.59$ ,  $Epi = 6.13$



(d)  $MAD(mm)$ :  $Endo = 1.28$ ,  $Epi = 1.80$   
 $HD(mm)$ :  $Endo = 5.54$ ,  $Epi = 5.54$



(e)  $MAD(mm)$ :  $Endo = 4.57$ ,  $Epi = 2.36$   
 $HD(mm)$ :  $Endo = 6.92$ ,  $Epi = 4.72$



(f)  $MAD(mm)$ :  $Endo = 4.62$ ,  $Epi = 2.57$   
 $HD(mm)$ :  $Endo = 9.37$ ,  $Epi = 8.62$

Figure 9.11: Example of some of the worst case of tracking of the whole myocardium. Left column: references of the two experts; Right column: tracking result with our contour in red, the mean cardiologist in green and the region of interest in blue. For each image, the MAD (in mm) computed between the two experts references or between the segmentation result and the mean contour is given.





## V Conclusion

---



---

---

# Conclusions et perspectives

---

Le but de ce travail de thèse était de proposer une méthode de segmentation et de suivi dans des séquences échocardiographiques. Cette méthode devait être capable de détecter le myocarde complet dans toutes les vues utilisées en routine clinique. Dans ce contexte, nous avons proposé un formalisme basé sur les ensembles de niveaux, où le contour est contraint par des *a priori* de forme et de mouvement. Les contributions principales de cette thèse sont développées dans la suite.

## Contributions principales

Nous avons tout d'abord proposé un nouveau modèle géométrique basé sur les hyperquadriques. Nous avons montré que chaque interface myocardique peut être approchée de manière précise par une hyperquadrique. Les deux contours sont alors intégrés dans une seule fonction implicite  $\psi$ . Cette représentation du myocarde est alors introduite dans un formalisme variationnel afin de contraindre un ensemble de niveaux et nous avons montré que cette formulation permet d'estimer les paramètres du modèle par une simple estimation par moindres carrés ce qui conduit à un algorithme rapide. Nous avons aussi montré que notre modèle était à même de modéliser les formes cardiaques de manière plus précise que d'autres modèles géométriques (ellipses, hyperboles de degré 3).

Dans un second temps, cet *a priori* de forme a été utilisé pour contraindre l'évolution d'un ensemble de niveaux pour la segmentation du myocarde complet sur des images en fin systole et en fin diastole. Pour ce faire, l'*a priori* de forme proposé est associé à un terme local d'attache aux données [Lankton and Tannenbaum (2008)]. De plus, comme une seule fonction implicite est utilisée pour segmenter l'endocarde et l'épicarde, un terme d'épaisseur est aussi inclus. Ce terme agit localement sur le contour afin d'éviter la fusion de celui-ci. L'algorithme a ensuite été évalué sur un jeu de données de 80 images en fin systole et en fin diastole pour lesquelles les références de 3 experts sont disponibles. Nous avons montré que ces performances étaient non seulement du même ordre

---

de grandeur que la variabilité inter-observateur mais qu'elles étaient également meilleures que celles d'une autre méthode récente [Hamou and El-Sakka (2010)].

Notre dernière contribution concerne l'inclusion de l'information de mouvement dans un formalisme variationnel afin de contraindre l'évolution d'un ensemble de niveaux. Nous avons proposé d'appliquer une contrainte de conservation des niveaux à la fonction implicite  $\phi$  similaire à l'hypothèse classiquement utilisée pour le flux optique, et nous l'avons exprimée sous la forme d'un terme d'énergie. Les résultats de suivi de notre algorithme sont à nouveau comparés aux références manuelles de 2 experts sur 20 séquences (soit environ 1200 images). Dans ce cas, bien que nos mesures d'erreur soient supérieures à la variabilité inter-observateur, elles restent cependant proches de celle-ci. De plus, les résultats obtenus avec notre méthode sont toujours meilleurs que ceux obtenus par l'algorithme proposé par [Hamou and El-Sakka (2010)].

## Perspectives

Notre travail de recherche en segmentation et suivi du myocarde dans des séquences échocardiographiques basés sur le formalisme des ensembles de niveaux contraints par *a priori* de forme et de mouvement offre plusieurs perspectives.

### Application en échocardiographie

Une des limitations de cette étude concerne la validation qui n'a été effectuée que sur des séquences de patients sains. Il est donc important de valider aussi les performances de notre méthode sur des cas pathologiques afin de s'assurer qu'elle y donne toujours des résultats corrects. En effet, dans des cas pathologiques, l'épaisseur du myocarde peut être faible ce qui pourrait être interprétée par le terme d'épaisseur comme un cas de fusion. De plus, les formes myocardiques peuvent varier significativement par rapport à des patients sains et il faut donc vérifier que celles-ci peuvent toujours être modélisées par des hyperquadriques.

D'un point de vue clinique, la segmentation et le suivi du myocarde complet dans toutes les vues ouvre des perspectives intéressantes. En effet, des paramètres mécaniques utiles au diagnostic peuvent être extraits de ce suivi et il serait intéressant d'étudier leurs variations au cours d'un cycle cardiaque dans des cas sains et pathologiques.

La segmentation d'une séquence prend environ 30 minutes (soit environ 30 secondes par images) avec l'implémentation Matlab actuelle et non optimisée. En particulier, dans cette implémentation, l'ensemble de niveaux évolue sur l'ensemble du domaine et est réinitialisé en carte de distance à chaque itération. Dans le but de rendre notre algorithme utilisable en routine clinique, il est primordial de le rendre temps réel. Dans cette optique, une solution envisageable est d'implémenter notre algorithme en utilisant des méthodes rapides et fonctionnant en bande étroite tel que la méthode Sparse Field [Whitaker (1998)], l'algorithme FTC [Shi and Karl (2008)] voire même une implémentation GPU [Lefohn *et al.* (2004)].

---

Nous avons aussi remarqué que selon la position le long de l'endocarde ou de l'épicarde, les résultats de segmentation étaient plus ou moins précis. Ceci peut être expliqué par le fait que les difficultés rencontrées lors de la segmentation d'une interface varient spatialement. Ainsi, lors de la segmentation de l'endocarde en parasternal petit axe par exemple, la paroi antéro-septale présente généralement un bon contraste entre le muscle et le sang, ce qui permet d'utiliser l'information d'intensité et de mouvement de manière fiable. En revanche, au niveau des parois inférieure, postérieure et latérale, le mouvement des muscles papillaires tend à faire évoluer le contour vers une position erronée. De plus, comme l'intensité de ces muscles est proche de celle du myocarde et supérieure à celle du sang, le terme d'attache aux données cherche à les inclure dans la segmentation. De ce fait, une pondération élevée de *l'a priori* de forme est nécessaire afin de contraindre l'ensemble de niveaux à exclure ces muscles de la segmentation. Cette forte pondération n'est en revanche pas nécessaire pour la paroi antéro-septale. Des considérations similaires peuvent être faites dans les vues apicales où le contraste entre le septum et la cavité est généralement élevé alors que l'apex est flou. Il serait donc intéressant de rendre les pondérations des différents termes d'énergie spatialement variantes afin de les adapter à ces différentes difficultés. Cela permettrait d'utiliser des termes d'énergie adaptés au contenu local de l'image ainsi qu'à ces propriétés anatomiques afin de faire évoluer le contour actif.

Enfin le choix des hyperparamètres a été fait empiriquement dans ces travaux et une étude plus approfondie de leur influence devrait être effectuée afin de caractériser notamment la robustesse de l'algorithme à des changements de pondération. Cette étude est d'autant plus importante si l'on considère des hyperparamètres spatialement variant puisqu'il est alors nécessaire de fixer plus de valeurs. Les travaux décrits dans [Martín-Fernández and Alberola-López (2005), Barbosa *et al.* (2012)a] procurent un cadre de travail intéressant pour effectuer cette caractérisation.

### Perspectives générales

Il est à noter que la formulation générale que nous avons proposée peut facilement être étendue à d'autres applications. La méthode décrite peut être appliquée facilement en trois dimensions, puisque le formalisme des ensembles de niveaux ainsi que le modèle hyperquadrique utilisé s'adaptent naturellement en 3D. De plus la méthode proposée peut aussi être adaptée à la segmentation du cœur dans d'autres modalités telles que l'imagerie par résonance magnétique (IRM) ou la tomodensitométrie (CT). Dans ce cas, cela peut cependant impliquer de modifier le terme local d'attache aux données par un autre type d'information pertinent vis à vis du type d'image traitée.

D'un point de vue méthodologique, l'introduction d'hyperparamètres spatialement (et temporellement) variant soulève d'intéressants problèmes théoriques. En effet, ces variations impliquent de considérer les hyperparamètres comme des variables lors de la dérivation des termes d'énergie par rapport à  $\phi$ .

L'introduction d'un modèle temporel pour les paramètres hyperquadriques pourrait aider à résoudre certains problèmes d'estimation dus à la faible quantité de muscle imagé en

---

parasternal grand axe. Des solutions envisageables seraient l'utilisation d'une approche de prédiction linéaire comme suggéré dans [Cremers (2006)] ou de techniques plus complexes comme du filtrage de Kalman [Guerrero *et al.* (2007)]. Ce modèle temporel pourrait aussi être utilisé pour la prédiction de la position du contour à  $t + 1$  afin de procurer une information supplémentaire à l'approximation obtenue par propagation dans notre algorithme.

Enfin, il est à noter que du fait de la faible complexité des formes myocardiques, la fonction implicite  $\phi$  pourrait être directement exprimée dans l'espace des hyperquadriques comme suggéré par d'autres auteurs pour d'autres *a priori* géométriques [Taron *et al.* (2004), Saroul *et al.* (2008)]. Le critère d'énergie serait alors minimisé par rapport aux paramètres de la forme au lieu de la fonction implicite. Cependant cette dérivation du critère d'énergie par rapport à ces paramètres n'est pas triviale du fait de l'expression complexe des hyperquadriques.

---

# Conclusions and perspectives

---

The aim of this work was to propose a method for the segmentation and tracking of echocardiographic sequences. The operational constraints set on this method were its ability to detect the whole myocardium in any of the 4 views used in clinical routine. We proposed a level-set formalism where the evolving contour is constrained by shape and motion priors. The main contributions of this thesis are summarized in the following.

### 10.1 Main contributions

We first proposed a new geometrical model for the whole myocardium based on hyperquadrics. We showed that each myocardial borders can be accurately approximated by one hyperquadric. We then derived a formulation allowing to embed both contours into a single implicit function  $\psi$ . This myocardial representation was introduced into a variational formalism to constrain a level-set function and we showed that this formulation allows estimating the model parameters through to simple least-square fitting procedure yielding a fast algorithm. We also showed that our proposed model was able to model more accurately the heart shapes than other geometrical model (ellipses, 3<sup>rd</sup> order hyperbolas).

In a second step, this shape prior was used to constrain an evolving level-set for the segmentation of the whole myocardium in ED and ES images. To this end, the proposed shape prior term was coupled to a local data-attachment term [Lankton and Tannenbaum (2008)]. Since we proposed to segment both the epicardium and the endocardium with a single level-set function, a thickness term was developed that acts locally on the contour and prevents its merging. The algorithm was then evaluated on a database of 80 ED or ES images with manual references of 3 experts. We showed that its performance was in the



same range than the inter-observer variability and that it moreover compares favorably with another state-of-the-art method [Hamou and El-Sakka (2010)].

Our last contribution was to include the motion information into a variational formalism to constrain the evolution of the level-set. Inspired by the classical optical flow constraint, we proposed to apply a level conservation constraint on the implicit function  $\phi$  and expressed this constraint as an energy term. The tracking results of the algorithm were again compared to the manual references of 2 experts on 20 sequences ( $\simeq$  1200 images). In this case, our error measures were higher than the inter-observer variability but remain close to it. Nevertheless, our method still provides better results than the one proposed by [Hamou and El-Sakka (2010)].

## 10.2 Perspectives

Our research on segmentation and tracking of the myocardium in echocardiographic sequences using shape and motion constrained level-set opens several perspectives.

### Echocardiographic application

One of the limitations of this study is that the validation has been performed on healthy patients. It is thus important to also evaluate the performance on pathological cases and see if our method still provides accurate results. Indeed, in pathological cases, the myocardial thickness can be small and the thickness term may interpret this situation as a merging case. Moreover, the myocardial shapes may vary significantly from healthy patients and we have to ensure that they can still be modelled by hyperquadrics.

From a clinical point of view, the segmentation and tracking of the whole myocardium in all views opens interesting perspectives. Indeed mechanical parameters relevant for diagnosis can be extracted from this tracking and it could be interesting to study their variations over time in both healthy and pathological cases.

The segmentation of a sequence takes around 30 minutes (*i.e.* roughly 30 seconds per frame) with the current unoptimized Matlab implementation. In particular, in this implementation, the level-set is evolved on the whole domain and reinitialized at every iteration. In order to make our algorithm usable in clinical routine, it is important to make it run in real time. Possible solutions are the implementation of the algorithm using fast, narrow-band method such as the sparse field method [Whitaker (1998)], the FTC algorithm [Shi and Karl (2008)] or a GPU implementation [Lefohn *et al.* (2004)].

We noticed that depending on the position along the endocardium or epicardium, the segmentation results were more or less accurate. This can be explained by the fact that the difficulties to segment a border vary spatially. When dealing with the segmentation of the endocardium in parasternal short-axis view for example, the antero-septal segment usually shows a high contrast between the muscle and the blood pool and both motion and intensity can be used reliably. On the other hand, in the inferior, posterior and lateral segments, the papillary muscles may appear, inducing false motion that may drive the

level-set toward a false contour. Moreover since the papillary muscles intensity is similar to the one of the myocardium and higher than the blood pool, the data attachment term also tends to include them in the segmentation. Thus a high ponderation of the shape prior is necessary to constraint the level-set to exclude these muscles from the segmentation which is not the case for the antero-septal segment. Similar conclusions can be drawn in apical views, where the contrast between the septum and the blood pool is usually high while the apex is blurred. It would thus be interesting to consider spatially varying ponderations of the different energy term to reflect these difficulties changes. This would allow to drive the active contour through energy terms that are adapted to the local image and anatomical properties.

The tuning of the hyperparameters was done empirically in this work and a more thorough study should be done in order to characterize the robustness of the algorithm with respect to these parameters. This would be even more important if we consider spatially varying ponderations since we would have even more parameters to set. The work described in [Martín-Fernández and Alberola-López (2005), Barbosa *et al.* (2012)a] provides a solid framework to perform such a characterization.

### General perspectives

It should be noted that the general formulation we developed may be easily extended to other applications. The described method can readily be applied to three dimensions, since the level-set formalism and the hyperquadric model we used are naturally adapted for 3D. Moreover, the proposed method may be easily adapted to the segmentation of the heart in other imaging modalities such as magnetic resonance imaging (MRI) or computed tomography (CT). This might just imply to replace our local data attachment term by any other kind of information relevant to the type of image to be processed.

From a methodological point of view, the introduction of spatially (and temporarily) varying hyperparameters raises interesting theoretical problems. Indeed, these variations imply that the hyperparameters have to be considered as variables when the derivative of the energy with respect to  $\phi$  is computed.

The introduction of a temporal model for the hyperquadric parameters may help solving some of the fitting issues we have due to the low amount of muscle imaged in parasternal long-axis views. This could be done through linear prediction approaches as suggested in [Cremers (2006)] or through more complex techniques such as Kalman filtering [Guerrero *et al.* (2007)]. This temporal model could also be used to predict the position of the contour at  $t + 1$  providing an additional information to the rough approximation obtained through tracking in our algorithm.

Finally, it can be noted that since the complexity of the myocardial shape is moderate, the implicit function  $\phi$  could be directly expressed in the hyperquadric space as suggested by other authors for other geometrical priors [Taron *et al.* (2004), Saroul *et al.* (2008)]. The energy criterion would then be minimized with respect to the shape parameters instead of the implicit function itself. However the derivation of the energy criterion with

respect to the corresponding parameters is not a trivial task, due to the complexity of the hyperquadrics expression.

# Appendix

---



---

## Derivation of the thickness term

---

Let us first recall our thickness energy:

$$E(\phi) = \int_{\Omega} \phi(\mathbf{p} + R_T \mathbf{N}) \cdot H(\phi(\mathbf{p} + R_T \mathbf{N})) \cdot \delta(\phi(\mathbf{p})) d\mathbf{p} = \int_{\Omega} L(\mathbf{p}, \phi(\mathbf{p})) d\mathbf{p}. \quad (\text{A.1})$$

To minimize this energy and obtain the evolution term, we derive  $L$  with respect to  $\phi$ , using variational calculus and the Euler-Lagrange theorem:

$$\begin{aligned} \frac{\partial L(\phi)}{\partial \phi} &= \frac{\partial}{\partial \phi} \phi(\mathbf{p}^*) \cdot H(\phi(\mathbf{p}^*)) \cdot \delta(\phi(\mathbf{p})) \\ &\quad + \phi(\mathbf{p}^*) \cdot \frac{\partial}{\partial \phi} H(\phi(\mathbf{p}^*)) \cdot \delta(\phi(\mathbf{p})) \\ &\quad + \phi(\mathbf{p}^*) \cdot H(\phi(\mathbf{p}^*)) \cdot \frac{\partial}{\partial \phi} \delta(\phi(\mathbf{p})), \end{aligned} \quad (\text{A.2})$$

where  $\mathbf{p}^* = \mathbf{p} + R_T \mathbf{N}$ .

As in [Lankton and Tannenbaum (2008)], we made the assumption that  $\frac{\partial}{\partial \phi} \delta(\phi(\mathbf{p})) \simeq 0$  near the zero-level and thus should not affect the evolution process. Thus equation (A.2) rewrites as:

$$\frac{\partial L(\phi)}{\partial \phi} = \frac{\partial}{\partial \phi} \phi(\mathbf{p}^*) \cdot \delta(\phi(\mathbf{p})) \cdot [H(\phi(\mathbf{p}^*)) + \phi(\mathbf{p}^*) \cdot \delta(\phi(\mathbf{p}^*))]. \quad (\text{A.3})$$

Since  $\frac{\partial}{\partial \phi} \phi(\mathbf{p}^*) = 1$  and

$$\begin{cases} \delta(\phi(\mathbf{p}^*)) = 1, & \text{if } \phi(\mathbf{p}^*) = 0 \\ \delta(\phi(\mathbf{p}^*)) = 0, & \text{otherwise} \end{cases} \Leftrightarrow \phi(\mathbf{p}^*) \cdot \delta(\phi(\mathbf{p}^*)) = 0, \forall \mathbf{p}^* \quad (\text{A.4})$$

we obtain

$$\frac{\partial L(\phi)}{\partial \phi} = H(\phi(\mathbf{p} + R_T \mathbf{N})) \cdot \delta(\phi(\mathbf{p})). \quad (\text{A.5})$$

Thus we get

$$\frac{\partial L(\phi)}{\partial \phi} = 0 \quad \Leftrightarrow \quad H(\phi(\mathbf{p} + R_T \mathbf{N})) \cdot \delta(\phi(\mathbf{p})) = 0, \quad (\text{A.6})$$

and the related evolution equation is thus given by

$$\frac{\partial \phi}{\partial \tau} = -H(\phi(\mathbf{p} + R_T \mathbf{N})) \cdot \delta(\phi(\mathbf{p})). \quad (\text{A.7})$$

---

## Derivation of the motion term

---

### B.1 Notation

Let  $\nabla\phi = \left(\frac{\partial\phi}{\partial x}, \frac{\partial\phi}{\partial y}, \frac{\partial\phi}{\partial t}\right)^T$  and  $\mathbf{V} = (u, v, 1)^T$  is the estimated motion (in homogeneous coordinates), where  $T$  denotes the transposition.

In the following, the derivative will be noted as  $f_\alpha = \frac{\partial f}{\partial \alpha}$ .

Let us also define the Hessian matrix of  $\phi$  as  $\mathcal{H}(\phi) = \begin{pmatrix} \phi_{xx} & \phi_{xy} & \phi_{xt} \\ \phi_{xy} & \phi_{yy} & \phi_{yt} \\ \phi_{xt} & \phi_{yt} & \phi_{tt} \end{pmatrix}$ , and the Jacobian

matrix of  $\mathbf{V}$  as  $\mathcal{J}(\mathbf{V}) = \begin{pmatrix} u_x & u_y & u_t \\ v_x & v_y & v_t \\ 0 & 0 & 0 \end{pmatrix}$ .

### B.2 Derivation of the motion term

Let us recall the motion prior term (9.6):

$$E(\phi) = \int_{\Omega} \delta(\phi(\mathbf{p})) (\nabla\phi^T \mathbf{V})^2 d\mathbf{p} = \int_{\Omega} \delta(\phi(\mathbf{p})) (\phi_t + u\phi_x + v\phi_y)^2 d\mathbf{p}. \quad (\text{B.1})$$

The evolution equation of the level-set is obtained by deriving (B.1) with respect to  $\phi$  using the Euler-Lagrange method [Gout *et al.* (2005)]. Considering a functional

$$E(\phi) = \int_{\Omega} L(x, y, t; \phi, \phi_x, \phi_y, \phi_t) d\mathbf{x}, \quad (\text{B.2})$$



its derivative with respect to  $\phi$  is given by:

$$\frac{\partial E}{\partial \phi}(\phi) = \frac{\partial L}{\partial \phi} - \left( \frac{\partial}{\partial x} \frac{\partial L}{\partial \phi_x} + \frac{\partial}{\partial y} \frac{\partial L}{\partial \phi_y} + \frac{\partial}{\partial t} \frac{\partial L}{\partial \phi_t} \right). \quad (\text{B.3})$$

Here we have  $L = \delta(\phi)(\phi_t + u\phi_x + v\phi_y)^2 = \delta(\phi)(\phi_t^2 + u^2\phi_x^2 + v^2\phi_y^2 + 2(u\phi_x\phi_t + v\phi_y\phi_t + uv\phi_x\phi_y))$ . Thus

$$\frac{\partial L}{\partial \phi} = \delta'(\phi)(\phi_t + u\phi_x + v\phi_y)^2 \simeq 0, \quad (\text{B.4})$$

$$\frac{\partial L}{\partial \phi_x} = \delta(\phi)(2u^2\phi_x + 2u\phi_t + 2uv\phi_y), \quad (\text{B.5})$$

$$\frac{\partial L}{\partial \phi_y} = \delta(\phi)(2v^2\phi_y + 2v\phi_t + 2uv\phi_x), \quad (\text{B.6})$$

$$\frac{\partial L}{\partial \phi_t} = \delta(\phi)(2\phi_t + 2u\phi_x + 2v\phi_y) \quad (\text{B.7})$$

and

$$\frac{\partial}{\partial x} \frac{\partial L}{\partial \phi_x} = 2\delta(\phi)(u^2\phi_{xx} + u\phi_{xt} + uv\phi_{xy} + 2u_xu\phi_x + u_x\phi_t + u_xv\phi_y + uv_x\phi_y), \quad (\text{B.8})$$

$$\frac{\partial}{\partial y} \frac{\partial L}{\partial \phi_y} = 2\delta(\phi)(v^2\phi_{yy} + v\phi_{yt} + uv\phi_{xy} + 2v_yv\phi_y + v_y\phi_t + u_yv\phi_x + uv_y\phi_x), \quad (\text{B.9})$$

$$\frac{\partial}{\partial t} \frac{\partial L}{\partial \phi_t} = 2\delta(\phi)(\phi_{tt} + u\phi_{xt} + v\phi_{yt} + u_t\phi_x + v_t\phi_y). \quad (\text{B.10})$$

where the assumption is made that  $\frac{\partial}{\partial \phi}\delta(\phi) \simeq 0$  near the zero-level and thus should not affect the evolution process (as in [Lankton and Tannenbaum (2008)]).

The derivative of (B.1) with respect to  $\phi$  thus writes

$$\begin{aligned} \frac{\partial E}{\partial \phi}(\phi) = & -2\delta(\phi)(u^2\phi_{xx} + u\phi_{xt} + uv\phi_{xy} + 2u_xu\phi_x + u_x\phi_t + u_xv\phi_y + uv_x\phi_y \\ & + v^2\phi_{yy} + v\phi_{yt} + uv\phi_{xy} + 2v_yv\phi_y + v_y\phi_t + u_yv\phi_x + uv_y\phi_x \\ & + \phi_{tt} + u\phi_{xt} + v\phi_{yt} + u_t\phi_x + v_t\phi_y) \end{aligned} \quad (\text{B.11})$$

$$\begin{aligned} \frac{\partial E}{\partial \phi}(\phi) = & -2\delta(\phi)(u^2\phi_{xx} + 2uv\phi_{xy} + v^2\phi_{yy} + 2u\phi_{xt} + 2v\phi_{yt} + \phi_{tt} + u(u_x\phi_x + v_x\phi_y) \\ & + v(u_y\phi_x + v_y\phi_y) + u_t\phi_x + v_t\phi_y + (u_x + v_y)(\phi_t + u\phi_x + v\phi_y)). \end{aligned} \quad (\text{B.12})$$

$$\frac{\partial E}{\partial \phi}(\phi) = -2\delta(\phi) \left( \mathbf{V}^T \mathcal{H}(\phi) \mathbf{V} + \nabla \phi^T \mathcal{J}(\mathbf{V}) \mathbf{V} + \text{Tr}(\mathcal{J}(\mathbf{V})) \nabla \phi^T \mathbf{V} \right), \quad (\text{B.13})$$

where  $\text{Tr}(A)$  denotes the trace of the matrix  $A$ .

The evolution equation is then given by:

$$\frac{\partial \phi}{\partial \tau} = -\frac{\partial E}{\partial \phi} = 2\delta(\phi) \left( \mathbf{V}^T \mathcal{H}(\phi) \mathbf{V} + \nabla \phi^T \mathcal{J}(\mathbf{V}) \mathbf{V} + \text{Tr}(\mathcal{J}(\mathbf{V})) \nabla \phi^T \mathbf{V} \right) \quad (\text{B.14})$$

where  $\tau$  is an artificial time parameter (that do not correspond to the “real” time dimension  $t$ ).

# Personal bibliography

## International journal

[Alessandrini *et al.* (2011)] M. Alessandrini, **T. Dietenbeck**, O. Basset, D. Friboulet and O. Bernard, “Using a geometric formulation of annular-like shape priors for constraining variational level-sets”, *Pattern Recognition Letters*, vol. 32, pp. 1240–1249, 2011.

[Barbosa *et al.* (2012)] D. C. Barbosa, **T. Dietenbeck**, J. Schaerer, J. D’hooge, D. Friboulet and O. Bernard, “B-Spline Explicit Active Surfaces: An efficient framework for real-time 3D region-based segmentation”, *IEEE Trans. Image Process.*, vol.21, no.1, pp. 241–251, 2012

[Dietenbeck *et al.* (2012)] **T. Dietenbeck**, D. Barbosa, J. D’hooge, D. Friboulet, O. Bernard, “Detection of the whole myocardium in 2D-echocardiography for multiple orientations using a geometrically constrained level-set”, *Medical Image Analysis*, vol. 16, pp. 386–401, 2012.

## International conferences

[Alessandrini *et al.* (2010a)] M. Alessandrini, **T. Dietenbeck**, O. Basset, D. Friboulet and O. Bernard, “Using a Geometric Formulation of Annular-like Shape Priors for Constraining Variational Level-Sets”, *IEEE International Conference On Image Processing (ICIP)*. Hong Kong, China, pp. 669–672, 2010.

[Alessandrini *et al.* (2010b)] M. Alessandrini, **T. Dietenbeck**, D. Barbosa, J. D’hooge, O. Basset, N. Speciale, D. Friboulet and O. Bernard, “Segmentation of the Full Myocardium in Echocardiography Using Constrained Level-Sets”, *Computing in Cardiology (CinC)*. Belfast, Northern Ireland, UK, pp.409–412, 2010.

[Barbosa *et al.* (2010)] D. C. Barbosa, O. Bernard, O. Savu, **T. Dietenbeck**, B. Heyde, P. Claus, D. Friboulet and J. D’hooge, “Coupled B-spline Active Geometric Functions for Myocardial Segmentation in Cardiac Ultrasound”, *IEEE International Ultrasonics Symposium*, San Diego, California, USA, pp. 1648–1651, 2010.

[Barbosa *et al.* (2011a)] D. C. Barbosa, **T. Dietenbeck**, D. Friboulet, J. D’hooge and O. Bernard, “Real-time region-based segmentation of 3D inhomogeneous objects in medical images“, *IEEE International Symposium on Biomedical Imaging (ISBI)*, Chicago, Illinois, USA, pp. 1986–1989, 2011.

[Barbosa *et al.* (2011b)] D. C. Barbosa, J. D’hooge, **T. Dietenbeck**, D. Friboulet and O. Bernard, “Towards real-time 3D region-based segmentation: B-spline explicit active surfaces”, *IEEE International Conference on Image Processing (ICIP)*, Bruxelles, Belgium, pp. 3121–3124, 2011.

[Barbosa *et al.* (2011c)] D. C. Barbosa, **T. Dietenbeck**, O. Bernard, D. Friboulet, H. Houle and J. D’hooge, “Fast 3D Echocardiographic Segmentation using B-Spline Explicit Active Surfaces: A validation study in a clinical setting”, *IEEE International Ultrasonics*

Symposium, Orlando, Florida, USA, pp. accepted, 2011.

[Dietenbeck *et al.* (2010)] **T. Dietenbeck**, M. Alessandrini, D. Friboulet, O. Bernard, “CREASEG: a free software for the evaluation of image segmentation algorithms based on level-set”, IEEE International Conference On Image Processing (ICIP). Hong Kong, China, pp. 665–668, 2010.

[Dietenbeck *et al.* (2011)] **T. Dietenbeck**, M. Alessandrini, D. Barbosa, J. D’hooge, D. Friboulet, O. Bernard, “Multiview Myocardial Segmentation In Echocardiographic Images Using a Piecewise Parametric Shape Prior”, IEEE International Symposium on Biomedical Imaging (ISBI). Chicago, USA, pp.645–648, 2011.

# Bibliography

- [Alberola-López *et al.* (2004)] Alberola-López, C., Martín-Fernández, M., and Ruiz-Alzola, J. (2004). Comments on: A methodology for evaluation of boundary detection algorithms on medical images. *IEEE Trans. Med. Imag.*, 23(5):658–660.
- [Alessandrini *et al.* (2009)] Alessandrini, M., Friboulet, D., Basset, O., D’hooge, J., and Bernard, O. (2009). Level-set segmentation of myocardium and epicardium in ultrasound images using localized bhattacharyya distance. In *IEEE International Ultrasonics Symposium, Roma, Italy*, pages 2468–2471.
- [Alessandrini *et al.* (2011)] Alessandrini, M., Dietenbeck, T., Basset, O., Friboulet, D., and Bernard, O. (2011). Using a geometric formulation of annular-like shape priors for constraining variational level-sets. *Pattern Recognition Letters*, 32:1240–1249.
- [Alessandrini *et al.* (2012)a] Alessandrini, M., Liebgott, H., and Bernard, O. (2012a). Monogenic phase based optical flow computation for myocardial motion analysis in 3D echocardiography. In *STACOM workshop at MICCAI 2012. Nice, France*, page in press.
- [Alessandrini *et al.* (2012)b] Alessandrini, M., Liebgott, H., Friboulet, D., and Bernard, O. (2012b). Monogenic phase based myocardium motion analysis from cardiac ultrasound with transverse oscillations. In *IEEE International Ultrasonic Symposium (IUS). Dresden, Germany*, page in press.
- [Alessandrini *et al.* (2012)c] Alessandrini, M., Liebgott, H., Friboulet, D., and Bernard, O. (2012c). Simulation of realistic echocardiographic sequences for ground truth validation of motion estimation. In *IEEE International Conference on Image Processing (ICIP). Orlando, USA*, page in press.
- [Angelsen (2000)] Angelsen, B. (2000). *Ultrasound Imaging: Waves, Signals, and Signal Processing*. Emantec, Norway.
- [Aubert *et al.* (2003)] Aubert, G., Barlaud, M., Faugeras, O., and Jehan-Besson, S. (2003). Image segmentation using active contours: Calculus of variations or shape gradients? *SIAM Applied Mathematics*, 63(6):2128–2154.
- [Baraldi *et al.* (1996)] Baraldi, P., Sarti, A., Lamberti, C., Prandini, A., and Sgallari, F. (1996). Evaluation of differential optical flow techniques on synthesized echo images. *IEEE Trans. Biomedical Engineering*, 43(3):259–272.
- [Barbosa *et al.* (2012)a] Barbosa, D., Dietenbeck, T., Heyde, B., Houle, H., Friboulet, D., D’hooge, J., and Bernard, O. (2012a). Fast and Fully Automatic 3D Echocardiographic Segmentation Using B-Spline Explicit Active Surfaces: Feasibility Study and Validation in a Clinical Setting. *Ultrasound in Medicine and Biology*, page accepted.

- [Barbosa *et al.* (2012)b] Barbosa, D. C., Dietenbeck, T., Schaerer, J., D’hooge, J., Friboulet, D., and Bernard, O. (2012b). B-Spline Explicit Active Surfaces: An efficient framework for real-time 3D region-based segmentation. *IEEE Trans. Image Process.*, 21(1):241–251.
- [Basarab *et al.* (2008)] Basarab, A., Liebgott, H., Morestin, F., Lyshchik, A., Higashi, T., Asato, R., and Delachartre, P. (2008). A method for vector displacement estimation with ultrasound images and its application for thyroid nodular disease. *Medical Image Analysis*, 12(3):259–274.
- [Behar *et al.* (2004)] Behar, V., Adam, D., Lysyansky, P., and Friedman, Z. (2004). The combined effect of nonlinear filtration and window size on the accuracy of tissue displacement estimation using detected echo signals. *Ultrasonics*, 41(9):743–753.
- [Belaid *et al.* (2011)a] Belaid, A., Boukerroui, D., Maingourd, Y., and Lerallut, J.-F. (2011a). Implicit active contours for ultrasound images segmentation driven by phase information and local maximum likelihood. In *IEEE International Symposium on Biomedical Imaging (ISBI)*. Chicago, USA, pages 630–635.
- [Belaid *et al.* (2011)b] Belaid, A., Boukerroui, D., Maingourd, Y., and Lerallut, J.-F. (2011b). Phase-based level set segmentation of ultrasound images. *IEEE Trans. Information Technology in Biomedicine*, 15(1):138–147.
- [Berg (1998)] Berg, J. M. (1998). On parameter estimation using level sets. *SIAM J. on Control and Optimization*, 37:1372–1393.
- [Bernard *et al.* (2007)a] Bernard, O., Touil, B., Gelas, A., Prost, R., and Friboulet, D. (2007a). A RBF-based multiphase level set method for segmentation in echocardiography using the statistics of the radiofrequency signal. In *IEEE International Conference On Image Processing (ICIP)*. San Antonio, Texas, USA, pages 157–160.
- [Bernard *et al.* (2007)b] Bernard, O., Touil, B., Gelas, A., Prost, R., and Friboulet, D. (2007b). Segmentation of myocardial regions in echocardiography using the statistics of the radio-frequency signal. In *Functional Imaging and Modeling of the Heart (FIMH’07)*. Metro Washington DC, USA, pages 433–442.
- [Bernard *et al.* (2009)] Bernard, O., Friboulet, D., Thévenaz, P., and Unser, M. (2009). Variational B-Spline Level-Set: A Linear Filtering Approach for Fast Deformable Model Evolution. *IEEE Trans. Image Process.*, 18:1179–1191.
- [Binder *et al.* (1999)] Binder, T., Sussner, M., Moertl, D., Strohmer, H., T., T. B., Maurer, G., and Porenta, G. (1999). Artificial neural networks and spatial temporal contour linking for automated endocardial contour detection on echocardiograms: A novel approach to determine left ventricular contractile function. *Ultrasound in Medicine and Biology*, 25(7):1069–1076.
- [Bland and Altman (1986)] Bland, J. and Altman, A. (1986). Statistical methods for assessing agreement between two methods of clinical measurement. *Lancet*, 1(8476):307–310.
- [Bosch *et al.* (2002)] Bosch, J., Mitchell, S., Lelieveldt, B., Nijland, F., Kamp, O., Sonka, M., and Reiber, J. (2002). Automatic segmentation of echocardiographic sequences by active appearance motion models. *IEEE Trans. Med. Imag.*, 21:1374–1383.

- [Boukerroui *et al.* (2003)] Boukerroui, D., Baskurt, A., Noble, J., and Basset, O. (2003). Segmentation of ultrasound images multiresolution 2d and 3d algorithm based on global and local statistics. *Pattern Recognition Letters*, 24(4-5):779–790.
- [Bresson *et al.* (2006)] Bresson, X., Vandergheynst, P., and Thiran, J. (2006). A variational model for object segmentation using boundary information and shape prior driven by the mumford-shah functional. *Int. J. of Computer Vision*, 68:145–162.
- [Brox *et al.* (2004)] Brox, T., A. Bruhn, N. P., and Weickert, J. (2004). High accuracy optical flow estimation based on a theory for warping. In *European Conference on Computer Vision (ECCV), Prague, Czech Republic, Springer, LNCS*, pages 25–36.
- [Brox *et al.* (2006)] Brox, T., Bruhn, A., and Weickert, J. (2006). Variational motion segmentation with level sets. In *European Conference on Computer Vision (ECCV), Graz, Austria, Springer, LNCS*, volume 3951, pages 471–483.
- [Carneiro *et al.* (2012)] Carneiro, G., Nascimento, J., and Freitas, A. (2012). The segmentation of the left ventricle of the heart from ultrasound data using deep learning architectures and derivative-based search methods. *IEEE Trans. Image Process.*, 21(3):968–982.
- [Caselles *et al.* (1997)] Caselles, V., Kimmel, R., and Sapiro, G. (1997). Geodesic active contours. *Int. J. of Computer Vision*, 22:61–79.
- [Casero (2008)] Casero, R. (2008). *Left ventricle functional analysis in 2D+t contrast echocardiography within an atlas-based deformable template model framework*. PhD thesis, University of Oxford.
- [Casero and Noble (2008)] Casero, R. and Noble, J. (2008). A novel explicit 2d+t cyclic shape model applied to echocardiography. In *Medical Image Computing and Computer-Assisted Intervention – MICCAI’2008*, pages 527–534.
- [Chalana *et al.* (1996)] Chalana, V., Linker, D., Haynor, D., and Kim, Y. (1996). A multiple active contour model for cardiac boundary detection on echocardiographic sequences. *IEEE Trans. Med. Imag.*, 15(3):290–298.
- [Chalana and Kim (1997)] Chalana, V. and Kim, Y. (1997). A methodology for evaluation of boundary detection algorithms on medical images. *IEEE Trans. Med. Imag.*, 16(5):642–652.
- [Chan and Vese (2001)] Chan, T. and Vese, L. (2001). Active contours without edges. *IEEE Trans. Image Process.*, 10:266–277.
- [Chan and Zhu (2005)] Chan, T. and Zhu, W. (2005). Level set based shape prior segmentation. In *IEEE Conference on Computer Vision and Pattern Recognition (CVPR)*, pages 1164–1170.
- [Chen *et al.* (2002)] Chen, Y., Tagare, H. D., Thiruvenkadam, S., Hunag, F., Wilson, D., Gopinath, K. S., Briggs, R. W., and Geiser, E. A. (2002). Using prior shapes in geometric active contours in a variational framework. *Int. J. of Computer Vision*, 50:315–328.
- [Chen *et al.* (2007)] Chen, Y., Huang, F., Tagare, H. D., and Rao, M. (2007). A coupled minimization problem for medical image segmentation with priors. *Int. J. of Computer Vision*, 71(3):259–272.

- [Chen *et al.* (2008)] Chen, T., Babb, J., Kellman, P., Axel, L., and Kim, D. (2008). Semiautomated segmentation of myocardial contours for fast strain analysis in cine displacement-encoded mri. *IEEE Trans. Med. Imag.*, 27(8):1084–1094.
- [Clifford *et al.* (1993)] Clifford, L., Fitzgerald, P., and James, D. (1993). Non-rayleigh first-order statistics of ultrasonic backscatter from normal myocardium. *Ultrasound in Medicine and Biology*, 19:487–495.
- [Cohen and Cohen (1996)] Cohen, I. and Cohen, L. (1996). A Hybrid Hyperquadric Model for 2-D and 3-D Data Fitting. *Computer Vision and Image Understanding*, 63(3):527–541.
- [Comaniciu (2002)] Comaniciu, D. (2002). Bayesian kernel tracking. In *Ann. Conf. German Soc. for Pattern Recognition*, pages 438–445.
- [Comaniciu *et al.* (2004)] Comaniciu, D., Zhou, X. S., and Krishnan, S. (2004). Robust real-time myocardial border tracking for echocardiography: An information fusion approach. *IEEE Trans. Med. Imag.*, 23:849–860.
- [Cootes *et al.* (1995)] Cootes, T., Taylor, C., Cooper, D., and Graham, J. (1995). Active shape models - their training and application. *Computer Vision and Image Understanding*, 61:38–59.
- [Cootes *et al.* (2001)] Cootes, T., Edwards, G., and Taylor, C. (2001). Active appearance models. *IEEE Trans. Pattern Anal. Machine Intell.*, 23(6):681–685.
- [Cootes and Taylor (1999)] Cootes, T. and Taylor, C. (1999). Statistical models of appearance for computer vision. Technical report, University of Manchester.
- [Cremers (2003)] Cremers, D. (2003). A variational framework for image segmentation combining motion estimation and shape regularization. In *IEEE Conference on Computer Vision and Pattern Recognition (CVPR)*.
- [Cremers (2006)] Cremers, D. (2006). Dynamical statistical shape priors for level set-based tracking. *IEEE Trans. Pattern Anal. Machine Intell.*, 28:1262–1273.
- [Cremers *et al.* (2003)] Cremers, D., Sochen, N., and Schnörr, C. (2003). Towards recognition-based variational segmentation using shape priors and dynamic labeling. In Griffith, L., editor, *Int. Conf. on Scale Space Theories in Computer Vision*, volume 2695 of LNCS. Springer.
- [Cremers *et al.* (2006)] Cremers, D., Kohlberger, T., and Schnörr, C. (2006). A multiphase dynamic labeling model for variational recognition-driven image segmentation. *Int. J. of Computer Vision*, 66:67–81.
- [Cremers *et al.* (2007)] Cremers, D., Rousson, M., and Deriche, R. (2007). A review of statistical approaches to level set segmentation: Integrating color, texture, motion and shape. *Int. J. of Computer Vision*, 72(2):195–215.
- [Cremers and Funka-Lea (2005)] Cremers, D. and Funka-Lea, G. (2005). Dynamical statistical shape priors for level set based sequence segmentation. In *Intl. Workshop on Variational and Level Set Methods*, volume 3752 of LNCS, pages 210–221.

- [Cremers and Soatto (2005)] Cremers, D. and Soatto, S. (2005). Motion competition: A variational approach to piecewise parametric motion segmentation. *Int. J. of Computer Vision*, 62:249–265.
- [D’hooge *et al.* (2002)] D’hooge, J., Bijnens, B., Thoen, J., de Werf, F. V., Sutherland, G., and Suetens, P. (2002). Echocardiographic strain and strain-rate imaging: a new tool to study regional myocardial function. *IEEE Trans. Med. Imag.*, 21(9):1022–1030.
- [Deriche and Monga (1988)] Deriche, R. and Monga, O. (1988). 3d edge detection using recursive filtering: Application to scanner images. Technical report, INRIA.
- [Dias and Leitao (1996)] Dias, J. M. B. and Leitao, J. M. N. (1996). Wall position and thickness estimation from sequences of echocardiographic images. *IEEE Trans. Med. Imag.*, 15:25–38.
- [Dice (1945)] Dice, L. (1945). Measures of the amount of ecologic association between species. *Ecology*, 26:297–302.
- [Duan *et al.* (2007)] Duan, Q., Angelini, E., Homma, S., and Laine, A. (2007). Validation of optical-flow for quantification of myocardial deformations on simulated RT3D ultrasound. In *International Symposium on Biomedical Imaging (ISBI’07)*. Metro Washington, DC, USA, pages 49–52.
- [Duan *et al.* (2010)] Duan, Q., Angelini, E., and Laine, A. (2010). Real-time segmentation by active geometric functions. *Computer Methods and Programs in Biomedicine*, 98(3):223–230.
- [Dydenko *et al.* (2006)] Dydenko, I., Jamal, F., Bernard, O., D’hooge, J., Magnin, I., and Friboulet, D. (2006). A level set framework with a shape and motion prior for segmentation and region tracking in echocardiography. *Medical Image Analysis*, 10:162–177.
- [Ehrhardt *et al.* (2008)] Ehrhardt, J., Schmidt-Richberg, A., and Handels, H. (2008). Simultaneous Segmentation and Motion Estimation in 4D-CT Data Using a Variational Approach. In *SPIE Medical Imaging 2008*, volume 6914.
- [Epstein and Gage (1987)] Epstein, C. and Gage, M. (1987). The curve shortening flow. In *Wave Motion: Theory, Modeling, and Computation*. New York: Springer-Verlag.
- [Felsberg (2004)] Felsberg, M. (2004). Optical flow estimation from monogenic phase. In *Proceedings of the 1st International Conference on Complex motion*, pages 1–13.
- [Felsberg and Sommer (2001)] Felsberg, M. and Sommer, G. (2001). The monogenic signal. *IEEE Trans. Signal Process.*, 49(12):3136–3144.
- [Feng *et al.* (1991)] Feng, J., Lin, W., and Chen, C. (1991). Epicardial boundary detection using fuzzy reasoning. *IEEE Trans. Med. Imag.*, 10:187–199.
- [Foulonneau *et al.* (2006)] Foulonneau, A., Charbonnier, P., and Heitz, F. (2006). Affine-invariant geometric shape priors for region-based active contours. *IEEE Trans. Pattern Anal. Machine Intell.*, 28:1352–1357.
- [Friedland and Adam (1989)] Friedland, N. and Adam, D. (1989). Automatic ventricular cavity boundary detection from sequential ultrasound images using simulated annealing. *IEEE Trans. Med. Imag.*, 8(4):344–353.



- [Gelas *et al.* (2007)] Gelas, A., Bernard, O., Friboulet, D., and Prost, R. (2007). Compactly supported radial basis functions based collocation method for level-set evolution in image segmentation. *IEEE Trans. Image Process.*, 16(7):1873–1887.
- [Giachetti (1998)] Giachetti, A. (1998). On-line analysis of echocardiographic image sequences. *Medical Image Analysis*, 2(3):261–284.
- [Gong *et al.* (2004)] Gong, L., Pathak, S., Haynor, D., Cho, P., and Kim, Y. (2004). Parametric shape modeling using deformable superellipses for prostate segmentation. *IEEE Trans. Med. Imag.*, 23(3):340–349.
- [Gout *et al.* (2005)] Gout, C., LeGuyader, C., and Vese, L. (2005). Segmentation under geometrical conditions using geodesic active contours and interpolation using level set methods. *Numerical Algorithms*, 39:155–173.
- [Gower (1975)] Gower, J. (1975). Generalized procrustes analysis. *Psychometrika*, 40:33–51.
- [Guerrero *et al.* (2007)] Guerrero, J., Salcudean, S., McEwen, J., Masri, B., and Nicolaou, S. (2007). Real-Time Vessel Segmentation and Tracking for Ultrasound Imaging Applications. *IEEE Trans. Med. Imag.*, 26:1079–1090.
- [Guo *et al.* (2012)] Guo, X., Friboulet, D., and Liebgott, H. (2012). Transverse oscillations beamformer design for sector scan using back-propagation. In *IEEE International Symposium on Biomedical Imaging (ISBI). Barcelona, Spain*.
- [Hamou and El-Sakka (2010)] Hamou, A. and El-Sakka, M. (2010). Optical flow active contours with primitive shape priors for echocardiography. *EURASIP Journal on Advances in Signal Processing*, 2010.
- [Han *et al.* (1993)] Han, S., Goldgof, D., and Bowyer, K. (1993). Using hyperquadrics for shape recovery from range data. In *ICCV'93*, pages 492–496.
- [Hanson (1988)] Hanson, A. (1988). Hyperquadrics: Smoothly deformable shapes with convex polyhedral bounds. *CVGIP*, 44:191–210.
- [Harker and O’Leary (2006)] Harker, M. and O’Leary, P. (2006). First order geometric distance (the myth of sampsonus). In *Proc. BMVC*, pages 10.1–10.10.
- [Herbulot *et al.* (2004)] Herbulot, A., Jehan-Besson, S., Barlaud, M., and Aubert, G. (2004). Shape gradient for image segmentation using information theory. In *International Conference on Acoustics, Speech and Signal Processing (ICASSP). Montreal, Canada*.
- [Herbulot *et al.* (2006)] Herbulot, A., Jehan-Besson, S., Duffner, S., Barlaud, M., and Aubert, G. (2006). Segmentation of vectorial image features using shape gradients and information measures. *J. of Math Imaging Vis*, 25:365–386.
- [Herlin *et al.* (1994)] Herlin, L., Bereziat, D., Giraudon, G., Nguyen, C., and Graffigne, C. (1994). Segmentation of echocardiographic images with markov random fields. In *European Conference on Computer Vision (ECCV), Springer, LNCS, Lecture Notes in Computer Science*, pages 200–206.
- [Horn and Schunk (1981)] Horn, B. and Schunk, B. (1981). Determining optical flow. *Artificial Intelligence*, 17:185–203.

- [Huttenlocher *et al.* (1993)] Huttenlocher, D., Klanderman, G., and Rucklidge, W. (1993). Comparing images using the Hausdorff Distance. *IEEE Trans. Pattern Anal. Machine Intell.*, 15(9):850–863.
- [Jacob *et al.* (1999)] Jacob, G., Noble, J., Mulet-Parada, M., and Blake, A. (1999). Evaluating a robust contour tracker on echocardiographic sequences. *Medical Image Analysis*, 3(1):63–75.
- [Jehan-Besson *et al.* (2003)] Jehan-Besson, S., Barlaud, M., and Aubert, G. (2003). Dream2s: Deformable regions driven by an eulerian accurate minimization method for image and video segmentation. *Int. J. of Computer Vision*, 53(1):45–70.
- [Kass *et al.* (1988)] Kass, M., Witkin, A., and Terzopoulos, D. (1988). Snakes : Active contour models. *Int. J. of Computer Vision*, 1:321–332.
- [Kohlberger *et al.* (2006)] Kohlberger, T., Cremers, D., Rousson, M., Ramaraj, R., and Funka-Lea, G. (2006). 4d shape priors for a level set segmentation of the left myocardium in spect sequences. In *Medical Image Computing and Computer-Assisted Intervention – MICCAI’06*, number 92–100.
- [Kumar *et al.* (1995)] Kumar, S., Han, S., Goldgof, D., and Bowyer, K. (1995). On recovering hyperquadrics from range data. *IEEE Trans. Pattern Anal. Machine Intell.*, 17:1079–1083.
- [Lankton and Tannenbaum (2008)] Lankton, S. and Tannenbaum, A. (2008). Localizing region-based active contours. *IEEE Trans. Image Process.*, 17:2029–2039.
- [Lefohn *et al.* (2004)] Lefohn, A., Kniss, J., Hansen, C., and Whitaker, R. (2004). A streaming narrow-band algorithm: interactive computation and visualization of level sets. *IEEE Trans. Visualization and Computer Graphics*, 10(4):422–433.
- [Leung *et al.* (2011)] Leung, K., Danilouchkine, M., van Stralen, M., de Jong, N., van der Steen, A., and Bosch, J. (2011). Left ventricular border tracking using cardiac motion models and optical flow. *Ultrasound in Medicine and Biology*, 37(4):605–616.
- [Leventon *et al.* (2000)] Leventon, M., Grimson, W., and Faugeras, O. (2000). Statistical shape influence in geodesic active contours. In *Proc. IEEE Conf. Comp. Vision and Patt. Recog.*, pages 316–323.
- [Li *et al.* (2005)] Li, C., Xu, C., Gui, C., and Fox, M. D. (2005). Level set evolution without re-initialization: A new variational formulation. In *Proc. IEEE Conf. Computer Vision and Pattern Recognition*, volume 1, pages 430–436.
- [Li *et al.* (2008)] Li, C., Kao, C.-Y., Gore, J. C., and Ding, Z. (2008). Minimization of region-scalable fitting energy for image segmentation. *IEEE Trans. Image Process.*, 17:1940–1949.
- [Liebgott (2005)] Liebgott, H. (2005). *Impulse response synthesis in ultrasound imaging for vectorial displacement estimation*. PhD thesis, INSA Lyon (Villeurbanne, France).
- [Liebgott *et al.* (2009)] Liebgott, H., Salem, A. B., Basarab, A., Gao, H., Claus, P., D’hooge, J., Delachartre, P., and Friboulet, D. (2009). Tangential sound field oscillations for 2D motion estimation in echocardiography. In *IEEE International Ultrasonics Symposium. Roma, Italy*, pages 498–501.

- [Lin *et al.* (2003)] Lin, N., Yu, W., and Duncan, J. S. (2003). Combinative multi-scale level set framework for echocardiographic image segmentation. *Medical Image Analysis*, 7:529–537.
- [Lubinski *et al.* (1999)] Lubinski, M., Emelianov, S., and O'Donnell, M. (1999). Speckle tracking methods for ultrasonic elasticity imaging using short-time correlation. *IEEE Trans. Ultrasonics, Ferroelectricity and Frequency Control*, 46(1):82–96.
- [Lucas and Kanade (1981)] Lucas, B. and Kanade, T. (1981). An iterative image restoration technique with an application to stereo vision. In *Proc. of Imaging Understanding Workshop*, pages 121–130.
- [Lynch *et al.* (2006)] Lynch, M., Ghita, O., and Whelan, P. (2006). Left-ventricle myocardium segmentation using a coupled level-set with a priori knowledge. *Computerized Medical Imaging and Graphics*, 30(4):255–262.
- [Lynch *et al.* (2008)] Lynch, M., Ghita, O., and Whelan, P. (2008). Segmentation of the Left Ventricle of the Heart in 3-D+t MRI Data Using an Optimized Nonrigid Temporal Model. *IEEE Trans. Med. Imag.*, 27:195–203.
- [Mailloux *et al.* (1987)] Mailloux, G., Bleau, A., and adn P. Petitclerc, M. B. (1987). Computer analysis of heart motion from two-dimensional echocardiograms. *IEEE Trans. Biomedical Engineering*, 34(5):356–364.
- [Malassiotis and Strintzis (1999)] Malassiotis, S. and Strintzis, M. (1999). Tracking the left ventricle in echocardiographic images by learning heart dynamics. *IEEE Trans. Med. Imag.*, 18:282–290.
- [Malladi *et al.* (1995)] Malladi, R., Sethian, J., and Vemuri, B. (1995). Shape modeling with front propagation: a level set approach. *IEEE Trans. Pattern Anal. Machine Intell.*, 17(2):158–175.
- [Marquina and Osher (2000)] Marquina, A. and Osher, S. (2000). Explicit algorithms for a new time dependent model based on level set motion for nonlinear deblurring and noise removal. *SIAM J. on Scientific Computing*, 22:387–405.
- [Martín-Fernández and Alberola-López (2005)] Martín-Fernández, M. and Alberola-López, C. (2005). An approach for contour detection of human kidneys from ultrasound images using Markov random fields and active contours. *Medical Image Analysis*, 9:1–23.
- [Mignotte *et al.* (2001)] Mignotte, M., Meunier, J., and Tardiff, J. (2001). Endocardial Boundary Estimation and Tracking in Echocardiographic Images using Deformable Templates and Markov Random Fields. *Pattern Analysis & Applications*, 4:256–271.
- [Mikić *et al.* (1998)] Mikić, I., Krucinski, S., and Thomas, J. (1998). Segmentation and tracking in echocardiographic sequences: active contours guided by optical flow estimate. *IEEE Trans. Med. Imag.*, 17(2):274–284.
- [Mulet-Parada and Noble (2000)] Mulet-Parada, M. and Noble, J. (2000). 2d+t acoustic boundary detection in echocardiography. *Medical Image Analysis*, 4(1):21–30.
- [Mumford and Shah (1989)] Mumford, D. and Shah, J. (1989). Optimal approximations by piecewise smooth functions and associated variational problems. *Comm. Pure Appl. Math.*, 42:577–685.

- [Nascimento and Marques (2008)] Nascimento, J. and Marques, J. (2008). Robust shape tracking with multiple models in ultrasound images. *IEEE Trans. Image Process.*, 17(3):392–406.
- [Noble and Boukerroui (2006)] Noble, J. A. and Boukerroui, D. (2006). Ultrasound image segmentation: A survey. *IEEE Trans. Med. Imag.*, 25(11):987–1010.
- [Ohuchi *et al.* (2003)] Ohuchi, M., Kudo, H., and Saito, T. (2003). Shape representation using extended hyperquadrics. In *Electronics and Communications in Japan*, volume 86, pages 42–51.
- [Osher and Fedkiw (2002)] Osher, S. and Fedkiw, R. (2002). *Level Set Methods and Dynamic Implicit Surfaces*. Springer Verlag.
- [Osher and Paragios (2003)] Osher, S. and Paragios, N. (2003). *Geometric Level Set Methods in Imaging, Vision, and Graphics*. Springer Verlag.
- [Osher and Sethian (1988)] Osher, S. and Sethian, J. (1988). Fronts propagating with curvature-dependent speed : Algorithms based on Hamilton-Jacobi formulation. *J. of Comp. Phys.*, 79:12–49.
- [Papin *et al.* (2000)] Papin, C., Bouthemy, P., Mémin, E., and Rochard, G. (2000). Tracking and characterization of highly deformable cloud structures. In *ECCV*, volume LNCS 1843, pages 428–442.
- [Paragios (2002)] Paragios, N. (2002). A variational approach for the segmentation of the left ventricle in cardiac image analysis. *Int. J. of Computer Vision*, 50(3):345–362.
- [Paragios *et al.* (2002)] Paragios, N., Rousson, M., and Ramesh, V. (2002). Matching Distance Functions: A Shape-to-Area Variational Approach for Global-to-Local Registration. In *European Conference on Computer Vision (ECCV)*, pages 775–789.
- [Paragios *et al.* (2004)] Paragios, N., Mellina-Gottardo, O., and Ramesh, V. (2004). Gradient vector flow fast geometric active contours. *IEEE Trans. Pattern Anal. Machine Intell.*, 26(3):402–407.
- [Paragios *et al.* (2005)] Paragios, N., Jolly, M., Taron, M., and Ramaraj, R. (2005). Active shape models and segmentation of the left ventricle in echocardiography. In *Scale-Space 2005, LNCS 3459*, pages pp. 131–142.
- [Paragios and Deriche (1999)] Paragios, N. and Deriche, R. (1999). Geodesic active regions for motion estimation and tracking. In *IEEE International Conf. Computer Vision (ICCV)*, pages 688–674.
- [Paragios and Deriche (2005)] Paragios, N. and Deriche, R. (2005). Geodesic active regions and level set methods for motion estimation and tracking. *Computer Vision and Image Understanding*, 97:259–282.
- [Peng *et al.* (1999)] Peng, D., Merriman, B., Osher, S., Zhao, H., and Kang, M. (1999). A PDE-Based Fast Local Level Set Method. *J. of Comp. Phys.*, 155(2):410–438.
- [Press *et al.* (1992)] Press, W., Teukolsky, S., Vetterling, W., and Flannery, B. (1992). *Numerical Recipes in C*. Cambridge, England:Cambridge Univ. Press.

- [Rousson *et al.* (2004)] Rousson, M., Paragios, N., and Deriche, R. (2004). Implicit Active Shape Models for 3D Segmentation in MR Imaging. In *Medical Image Computing and Computer-Assisted Intervention – MICCAI’04*, pages 209–216.
- [Rousson and Paragios (2002)] Rousson, M. and Paragios, N. (2002). Shape priors for level set representations. In Griffith, L., editor, *Proc. of the Europ. Conf. on Comp. Vis.*, pages 78–92. Springer.
- [Sühling *et al.* (2005)] Sühling, M., Arigovindan, M., Jansen, C., Hunziker, P., and Unser, M. (2005). Myocardial motion analysis from b-mode echocardiograms. *IEEE Trans. Image Process.*, 14(4):525–536.
- [Sampson (1982)] Sampson, P. (1982). Fitting conic sections to ‘very scattered’ data: An iterative refinement of the bookstein algorithm. *Computer Graphics and Image Processing*, 18(1):97–108.
- [Saroul *et al.* (2008)] Saroul, L., Bernard, O., Vray, D., and Friboulet, D. (2008). Prostate segmentation in echographic images: a variational approach using deformable super-ellipse and rayleigh distribution. In *IEEE International Symposium on Biomedical Imaging (ISBI), Paris, France*, pages 129–132.
- [Sarti *et al.* (2005)] Sarti, A., Corsi, C., Mazzini, E., and Lamberti, C. (2005). Maximum likelihood segmentation of ultrasound images with rayleigh distribution. *IEEE Trans. Ultrasonics, Ferroelectricity and Frequency Control*, 41(4):435–440.
- [Shankar (1995)] Shankar, P. (1995). A model for ultrasonic scattering from tissues based on the k distribution,. *Phys. Med. Biol.*, 40:1633–1649.
- [Sheng *et al.* (2006)] Sheng, C., Xin, Y., Liping, Y., and Kun, S. (2006). Segmentation in Echocardiographic Sequences using Shape-based Snake Model Combined with Generalized Hough Transformation. *Int. J. of Cardiovascular Imaging*, 22:33–46.
- [Shi and Karl (2008)] Shi, Y. and Karl, W. C. (2008). A real-time algorithm for the approximation of level-set based curve evolution. *IEEE Trans. Image Process.*, 17:645–656.
- [Strintzis *et al.* (1992)] Strintzis, M., Magnisalis, X., Kotropoulos, C., Pitas, I., and Maglaveras, N. (1992). Maximum likelihood signal adaptive filtering of speckle in ultrasound b-mode images. In *IEEE Engineering Medicine Biology Society Conference*, volume 14, pages 1870–1871.
- [Strintzis and Kokkinidis (1997)] Strintzis, M. and Kokkinidis, I. (1997). Maximum likelihood motion estimation in ultrasound image sequences. *IEEE Signal Processing Letters*, 4(6):156–157.
- [Suri *et al.* (2002)] Suri, J., Liu, K., Singh, S., Laxminarayan, S., Zeng, X., and Reden, L. (2002). Shape recovery algorithms using level sets in 2-d/3-d medical imagery: A state-of-the-art review. *IEEE Trans. Information Technology In Biomedicine*, 6(1):8–28.
- [Sussman *et al.* (1998)] Sussman, M., Fatemi, E., Smereka, P., and Osher, S. (1998). An improved level set method for incompressible two-phase flows. *J. of Computers and Fluids*, 27:663–680,.

- [Tao and Tagare (2007)] Tao, Z. and Tagare, H. D. (2007). Tunneling descent for M.A.P. active contours in ultrasound segmentation. *Medical Image Analysis*, 11:266–281.
- [Taron *et al.* (2004)] Taron, M., Paragios, N., and Jolly, M. (2004). Border detection on short axis echocardiographic views using a region based ellipse-driven framework. In *Medical Image Computing and Computer-Assisted Intervention – MICCAI’04*, pages 443–450.
- [Touil *et al.* (2010)] Touil, B., Basarab, A., Delachartre, P., Bernard, O., and Friboulet, D. (2010). Analysis of motion tracking in echocardiographic image sequences: influence of system geometry and point-spread function. *Ultrasonics*, 50(3):373–386.
- [Tsai *et al.* (2003)] Tsai, A., A.Yezzi, Wells, W., Tempany, C., Tucker, D., Fan, A., Grimson, W., and Willsky, A. (2003). A shape-based approach to the segmentation of medical imagery using level sets. *IEEE Trans. Med. Imag.*, 22:137–154.
- [Tsai and Osher (2003)] Tsai, R. and Osher, S. (2003). Level set methods an their applications in image science. *Comm. Math. Sci.*, 1(4):623–656.
- [Unal *et al.* (2005)] Unal, G., Krim, H., and Yezzi, A. (2005). Fast incorporation of optical flow into active polygons. *IEEE Trans. Image Process.*, 14(6):745–759.
- [Vallet *et al.* (2006)] Vallet, B., Angelini, E., and Laine, A. (2006). Variational segmentation framework in prolate spheroidal coordinates for 3D real-time echocardiography. In *SPIE Medical Imaging Conference, San Diego, CA, USA*, pages 61444A.1–61511A.
- [Wagner *et al.* (1983)] Wagner, R., Smith, S., Sandrik, J., and Lopez, H. (1983). Statistics of Speckle in Ultrasound B-Scans. *IEEE Trans. Sonics and Ultrasonics*, 30:156 – 163.
- [Whitaker (1998)] Whitaker, R. (1998). A level-set approach to 3d reconstruction from range data. *Int. J. of Computer Vision*, 29:203–231.
- [Yezzi *et al.* (1997)] Yezzi, A., Kichenassamy, S., Kumar, A., Olver, P., and Tannenbaum, A. (1997). A geometric snake model for segmentation of medical imagery. *IEEE Trans. Med. Imag.*, 16(2):199–209.
- [Yu *et al.* (2006)] Yu, W., Yan, P., Sinusas, A., Thiele, K., and Duncan, J. (2006). Towards pointwise motion tracking in echocardiographic image sequences - comparing the reliability of different features for speckle tracking. *Medical Image Analysis*, 10(4):495–508.
- [Zeng *et al.* (1998)] Zeng, X., Staib, L., Schultz, R., and Duncan, J. (1998). Segmentation and measurement of the cortex from 3D MR images. In *Medical Image Computing and Computer-Assisted Intervention – MICCAI’98*, pages 519–530.
- [Zhang and Lu (2004)] Zhang, D. and Lu, G. (2004). Review of shape representation and description techniques. *Pattern Recognition*, 37(1):1–19.
- [Zhang and Pless (2005)] Zhang, Q. and Pless, R. (2005). Segmenting cardiopulmonary images using manifold learning with level sets. In *CVBIA*, volume LNCS 3765, pages 479–488.
- [Zhao *et al.* (1996)] Zhao, H.-K., Chan, T., Merriman, B., and Osher, S. (1996). A variational level set approach to multiphase motion. *J. of Comp. Phys.*, 127:179–195.

- [Zhou (2010)] Zhou, S. (2010). Shape regression machine and efficient segmentation of left ventricle endocardium from 2D B-mode echocardiogram. *Medical Image Analysis*, 14:563–581.
- [Zhou *et al.* (2005)] Zhou, X., Comaniciu, D., and Gupta, A. (2005). An information fusion framework for robust shape tracking. *IEEE Trans. Pattern Anal. Machine Intell.*, 27:115–129.
- [Zhu *et al.* (2007)] Zhu, Y., Papademetris, X., Sinusas, A., and Duncan, J. (2007). Segmentation of myocardial volumes from real-time 3d echocardiography using an incompressibility constraint. In *Medical Image Computing and Computer-Assisted Intervention – MICCAI’07*, pages 44–51.
- [Zhu *et al.* (2010)] Zhu, Y., Papademetris, X., Sinusas, A. J., and Duncan, J. S. (2010). A coupled deformable model for tracking myocardial borders from real-time echocardiography using an incompressibility constraint. *Medical Image Analysis*, 14:429–448.
- [Zhu and Yuille (1996)] Zhu, S. and Yuille, A. (1996). Region competition : unifying snakes, region growing, and Bayes/MDL for multiband image segmentation. *IEEE Trans. Pattern Anal. Machine Intell.*, 18:884–900.